Felix Kolpak

Anisotropic Hardening in Cold Forging
Characterization, Simulation and Consequences

Yield stress in MPa

900

600

300

Anisotropic Hardening in Cold Forging:
Characterization, Simulation and Consequences

Zur Erlangung des akademischen Grades eines

Dr.-Ing.

von der Fakultät Maschinenbau
der Technischen Universität Dortmund

genehmigte Dissertation

vorgelegt von

Felix Kolpak, M. Sc.

aus

Duisburg

Dortmund, 2021

Dortmunder Umformtechnik

Band 115

Felix Kolpak

Anisotropic Hardening in Cold Forging

Characterization, Simulation and Consequences

Vorwort und Danksagung

Duisburg, im Februar 2022   **Felix Kolpak**

Abstract

The goals of metal forming process design have long exceeded the mere shaping of components. Changes of the component properties which are caused by forming, including residual stresses, damage and work-hardening have received increasing attention in the last years. If done right, the incorporation and control of property changes of cold forged components in terms of numerical process simulations could significantly improve the energy- and resource-efficiency of metal forming processes as well as the components' service life and performance. To predict and exploit the property changes by means of numerical simulations, the exact incorporation of the workpiece material behavior is of utmost importance. Up to now, anisotropic hardening is rarely considered in the field of cold bulk metal forming making impossible a flawless prediction of a component's properties and its performance.

In the scope of this thesis, typical cold forging materials are characterized with regard to their anisotropic work-hardening behavior exhibited at large strains. Tension, torsion and upsetting of material specimens pre-strained by forward rod extrusion reveal the material's work-hardening behavior under a variety of different strain paths. It was shown that all investigated materials exhibit an extensive Bauschinger effect, work-hardening stagnation and permanent softening which, up to now, are rarely considered in cold forging simulations. All anisotropic hardening phenomena intensify drastically, with the pre-strain.

The experimental data is utilized to select, modify, and fit constitutive models of increasing complexity with the goal to capture all relevant work-hardening phenomena exhibited in the course of strain path changes. A modified version of the Yoshida-Uemori multi-surface model is successfully implemented and applied to improve the prediction accuracy of cold forging simulations. Various hardening models were applied to the simulation of basic single-stage cold forging processes, revealing, that the flow stress and residual stresses as well as the ejector forces are strongly affected by strain path changes, which cannot be captured with the common assumption of isotropic work-hardening.

While the forming forces of single-stage cold forging processes are hardly affected by anisotropic hardening, despite the occurrence of intrinsic strain path changes, the forming forces in multi-stage forming operations are reduced significantly, if large regions of the workpiece experience a strain path reversal. Lastly, it was shown that heat-treatments subsequent to cold forging at temperatures between 300 °C and 600 °C lead to a decrease of the Bauschinger effect, whereas work-hardening stagnation and permanent softening decrease only at larger temperatures.

Zusammenfassung

Die Ziele bei der Gestaltung von Umformprozessen gehen längst über die reine Formgebung hinaus. Die Vorhersage von Produkteigenschaften wie Eigenspannungen, Schädigung und Kaltverfestigung, welche durch die Umformung verändert werden, hat in den letzten Jahren zunehmend an Bedeutung gewonnen. Eine aktive Beeinflussung und Ausnutzung der veränderten Bauteileigenschaften würde die Ressourcen- und Energie-Effizienz von Kaltumformprozessen sowie die Leistungsfähigkeit der erzeugten Produkte deutlich steigern. Um diese Änderungen der Eigenschaften mittels Simulationen vorherzusagen und auszunutzen ist die exakte Einbeziehung des Werkstoffverhaltens der Werkstücke während der Umformung von größter Bedeutung. Das anisotrope Verfestigungsverhalten wird im Bereich der Kaltmassivumformung aktuell nur selten berücksichtigt, wodurch eine Vorhersage der Bauteilleistungsfähigkeit nicht möglich ist.

Im Rahmen dieser Arbeit werden typische Werkstoffe der Kaltmassivumformung hinsichtlich ihres anisotropen Verfestigungsverhaltens bei großen Umformgraden charakterisiert. Durch Zug-, Torsions- und Stauchversuchen an Werkstoffproben, die durch Voll-Vorwärts-Fließpressen umgeformt wurden, konnte das anisotrope Verfestigungsverhalten unter einer Vielzahl unterschiedlicher Dehnpfade charakterisiert werden. Alle untersuchten Werkstoffe zeigen dabei einen ausgeprägten Bauschingereffekt, Verfestigungsstagnierung und eine bleibende Entfestigung, welche in der Kaltmassivumformung bisher nicht berücksichtigt wurden. Sämtliche Effekte intensivieren sich drastisch mit der Vordehnung.

Die experimentellen Daten werden verwendet, um konstitutive Modelle mit zunehmender Komplexität auszuwählen, zu modifizieren und anzupassen, mit dem Ziel, alle relevanten Verfestigungsphänomene zu erfassen. Das Mehrflächenmodell von Yoshida-Uemori wird genutzt, um die Vorhersagegenauigkeit von Kaltumformsimulationen zu steigern. Bei Verwendung des Verfestigungsmodells in Simulationen einstufiger Kaltumformprozesse wurde gezeigt, dass die Fließspannung, Eigenspannungen und Auswerferkräfte stark von einer Dehnpfadumkehr beeinflusst werden, welche durch konventionelle isotrope Verfestigungsmodelle nicht abgebildet werden können.

Während die Prozesskräfte bei einstufigen Kaltumformverfahren, trotz intrinsischer Dehnpfadwechsel, kaum von anisotroper Verfestigung beeinflusst werden, führt eine Dehnpfadumkehr bei mehrstufigen Umformvorgängen zu einer deutlichen Verringerung der Umformkräfte. Weiterhin wurde gezeigt, dass eine Wärmebehandlung in Temperaturbereichen zwischen 300 °C und 600 °C zu einer Verringerung des Bauschingereffektes führt, während die Verfestigungsstagnation und bleibende Entfestigung erst bei höheren Temperaturen abnehmen.

Table of contents

Previous publication of contents

Listed below are the publications that were created during the work on this dissertation. The previous publication of the research results was done with the approval of the doctoral committee.

Kolpak, F., Schwane, M., Dahnke, C., Tekkaya, A. E., 2017. Improved property prediction of cold forged components by means of enhanced material models. In: Proceedings of the Conference on Steels in Cars and Trucks 2017, Amsterdam, Netherlands.

Kolpak, F., Dahnke, C., Tekkaya, A. E., 2018. Prediction of Product Properties in Cold Forging Considering the Bauschinger Effect. In: Proceedings of the 51st ICFG Plenary Meeting, Columbus, USA, pp. 159-166.

Kolpak, F., Dahnke, C., Tekkaya, A. E., 2018. Influence of the Bauschinger Effect on the Product Properties of Cold Forged Parts. In: Proceedings of the 8th International Seminar on Precision Forging 2018, Nagoya, Japan.

Kolpak, F., Dahnke, C., Tekkaya, A. E., 2019. Forming-induced anisotropy of product properties in cold extrusion. In: Proceedings of the METEC and 4th European Steel Technology and Application Days 2019, Düsseldorf, Germany.

Hering, O., Kolpak, F., Tekkaya, A. E., 2019. Flow curves up to high strains considering load reversal and damage. International Journal of Material Forming 12, pp. 955-972.

Hering, O., Kolpak, F., Dahnke, C., Tekkaya, A. E., 2019. High Strain Flow Curves by Mechanical Tests on Specimens Pre-strained by Forward Rod Extrusion. In: Proceedings of the 52nd ICFG Plenary Meeting 2019, Donostia-San Sebastian, Spain.

Kolpak, F., Hering, O., Tekkaya, A. E., 2019. Verfahren und Vorrichtung zur Herstellung von Proben aus metallischen Werkstoffen mit bekannten plastischen Vordehnungen für die Werkstoffcharakterisierung. DPMA patent application DE 10 2020 005 670.9 (16.09.2020).

Kolpak, F., Hering, O., Traphöner, H., Tekkaya, A. E., 2021. Large strain flow curves of sheet metals by sheet extrusion. CIRP Annals – Manufacturing Technology 70 (1), pp. 247-250.

Kolpak, F., Hering, O., Tekkaya, A. E., 2021. Consequences of large strain anisotropic work-hardening in cold forging. International Journal of Material Forming (Article in press).

Symbols and abbreviations

Symbols

Symbol	Unit	Description
A	mm^2	Area
B	MPa	Radius of bounding surface (Yoshida-Uemori model)
b	-	Saturated value of kinematic hardening of the bounding surface (Yoshida-Uemori model)
C	MPa	Linear hardening factor (Swift-type hardening)
c	-	Material parameter (Yoshida-Uemori model)
$C_{1,2}$	MPa	Kinematic hardening rate (Chaboche model)
dA	-	Increment of generic variable A
d	mm	Diameter
D	mm	Outer diameter
$d\lambda$	-	Plastic multiplier
E	MPa	Young's modulus
e_u	%	Uniform elongation
f	-	Yield function
F	N	Force
F_c	kN	Counter-force (forward extrusion)
F_ε	kN	External force considering true strain distribution
F_{ε_m}	kN	External force considering average strain
h	-	Material parameter (Yoshida-Uemori model)
h_0	mm	Initial height
i	-	Index (i = 1, 2, …, n)
I	-	Unit tensor (2. order tensor)
k	MPa	Shear flow stress

Symbol	Unit	Description
k	-	Saturation rate of hardening (Voce-type hardening)
k_2	-	Material parameter (Modified Yoshida-Uemori model)
k_{HAH}	-	Material parameter (HAH-model)
k_i	-	Material parameters ($i = 1, 2, …, 5$) (HAH-model)
l	mm	Contact surface length in forward rod extrusion
m	-	Strain rate exponent
M	Nm	Torque
n	-	Hardening exponent (Swift-type hardening)
p	MPa	Hydrostatic pressure
$\bar{p}$	MPa	Total pressure in the forming zone (forward extrusion)
p_c	MPa	Superposed hydrostatic pressure (forward extrusion)
p_0	-	Correction parameter in the flow stress calculation for torsion of cylindrical specimens
R	mm	Outer specimen diameter
$R_{p0.05}$	MPa	0.05 % proof stress
$R_{p0.1}$	MPa	0.1 % proof stress
$R_{p0.2}$	MPa	0.2 % proof stress
R_{sat}	MPa	Saturated value of isotropic hardening
q	-	Material parameter of the HAH-model
r	mm	Radius
r'	-	Lankford coefficient
r^*	mm	Critical evaluation radius in torsion of cylindrical specimens
r_{ex}	mm	Tool radius of extrusion dies (forward extrusion)
R_{sat}	MPa	Maximum value of saturating component in isotropic hardening
t	s	Time

Symbol	Unit	Description
T	°C	Temperature
V	mm^3	Volume
w	-	Weighting factor of saturating and non-saturating isotropic hardening components
x	-	x-coordinate in the Cartesian coordinate system
Y	MPa	Flow stress (Yoshida-Uemori model)
y	-	y-coordinate in the Cartesian coordinate system
z	-	z-coordinate in the Cartesian / cylindrical coordinate system
$\boldsymbol{\alpha}$	MPa	Kinematic back stress tensor (Second order tensor)
α	°	Shear angle in torsion of bars
2α	°	Cone angle of extrusion dies
γ	-	Shear strain, kinematic hardening rate in the Chaboche model
$\dot{\gamma}_R$	1 / s	Twisting angle rate at $r = R$
$\Delta\varepsilon_{\mathrm{m}}$	-	Strain inhomogeneity
ε	%	Relative elongation
$\bar{\varepsilon}$	-	Effective strain
$\boldsymbol{\varepsilon}$	-	Total strain tensor
$\dot{\bar{\varepsilon}}$	-	Effective plastic strain rate
ε_{w}	-	Strain in width direction of a thin specimen
ε_{t}	-	Strain in thickness direction of a thin specimen
$\varepsilon_{\mathrm{ex}}$	-	Logarithmic extrusion strain (forward rod extrusion)
$\varepsilon_{\mathrm{pre}}$	-	Pre-strain
$\varepsilon_{\mathrm{tens}}$	-	True strain in tension
$\varepsilon_{\mathrm{comp}}$	-	True strain in compression

Symbol	Unit	Description
ε_m	-	Area-weighted average strain
ε_0	-	Hardening parameter (Swift-type hardening)
θ	rad	Twisting angle in torsion of bars
$\dot{\theta}$	$\mathrm{rad} \cdot \mathrm{s}^{-1}$	Twisting rate
$\bar{\theta}$	-	Strain path change parameter
μ	-	Friction coefficient (Coulomb)
ρ	$\mathrm{kg} \cdot \mathrm{m}^{-3}$	Density
σ	MPa	Stress
$\bar{\sigma}$	MPa	Equivalent stress (von Mises)
σ_f	MPa	Flow stress
σ_m	MPa	Ultimate tensile strength
$\boldsymbol{\sigma}$	MPa	Cauchy stress tensor (2nd order)
$\sigma^{I/II/III}$	MPa	1. / 2. / 3. principal stress
τ	MPa	Shear stress
χ	-	Bauschinger coefficient
$(\boldsymbol{A})_{ij}$	-	*ij*-th component of the tensor $\boldsymbol{A}$
$\boldsymbol{A}^\mathrm{h}$	-	Hydrostatic part of $\boldsymbol{A}$
$\boldsymbol{A}'$	-	Deviatoric part of $\boldsymbol{A}$

Indices

Index	Description
0	Initial configuration
1	Deformed configuration
bc	Backward can extrusion

Index	Description
C	Counter
comp	Compression
ex	Forward rod extrusion
exp	Experiment
hold	Holding (annealing)
iso	Isotropic
max	Maximum
min	Minimum
P	Punch
p	Plastic
pre	Pre-strain
sim	Simulation
tens	Tension
tot	Total
+	Under tensile loading
-	Under compressive loading

Abbreviations

Abbreviation	Description
ASCII	American Standard Code for Information Interchange
DIN	Deutsches Institut für Normung (German Institute for Standardization)
EN	Europäische Norm (European Standard)
FEM	Finite-Element-Method
ISO	International Organization of Standardization
HAH	Homogeneous anisotropic hardening model

Abbreviation	Description
MSE	Mean-Square-Error
ODB	Output Database File (Abaqus)
TEM	Transmission electron microscopy
UMAT	User material subroutine (Abaqus)
YU	Yoshida-Uemori model

1 Introduction

The climate change makes necessary increasing efforts in the fields of resource and energy efficiency and the reduction of CO_2 emissions in all fields of the industry including the production sector and more specifically metal forming. The European Commission has set the goal to keep global warming below an increase of 2 °C as compared to the pre-industrial state. To reach this, the target is to reduce overall emissions by 55 % as compared to the state of 1990 (European Commission, 2021). The reduction of component weight and thus, the increase of resource efficiency can be reached in terms of lightweight design approaches. Especially the reduction of moving masses contributes to a decrease of energy consumption of the components in service and thus to a reduction of CO_2 emissions (Isogawa, 2016).

To exploit the lightweight potential of components produced by metal forming processes, the production must be designed in a way that allows for a decrease of component weight, while maintaining the required performance in service. With this in mind, the goals of metal forming process design have long exceeded the mere shaping of components. In the recent years, the alteration and improvement of a components' properties caused by microstructural changes during cold forging has gained increasing attention. This includes the alteration of the mechanical properties (Tekkaya et al., 2015), the evolution of ductile damage (Tekkaya et al., 2017) and its influence on a components' performance (Hering and Tekkaya, 2020). If done right, the incorporation and control of property changes of cold forged components in terms of numerical process simulations can significantly improve the energy- and resource-efficiency of metal forming processes (**Figure 1.1**).
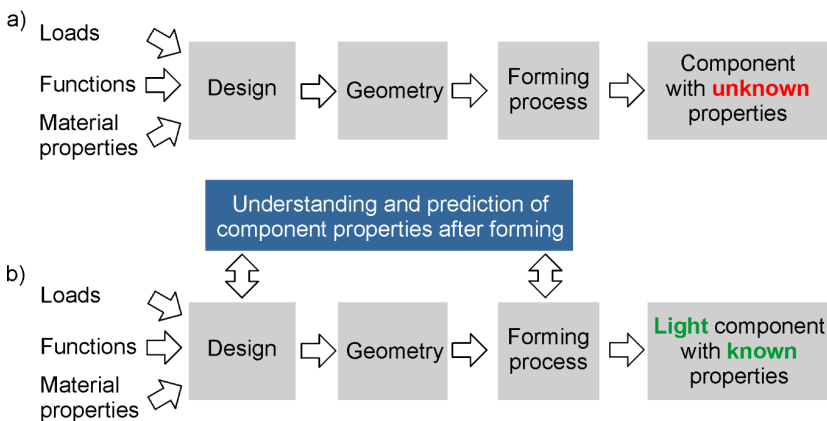
Figure 1.1: a) Conventional component design process, b) targeted component design process (based on Tekkaya et al., 2015)

While many aspects of property changes triggered during cold forging have been investigated in the past, one major aspect has been nearly ignored up to now: anisotropic work-hardening. In contrast to the geometric anisotropy, introduced during the production of initial material e. g. by rolling or drawing, anisotropic work-hardening can be understood as the translation or distortion of a metal's yield surface, as described by the phenomenological concepts of kinematic or distortive hardening. After a complete strain path reversal, several work-hardening phenomena are known to manifest, including the classical Bauschinger effect, transient hardening, work-hardening stagnation and permanent softening, all of which are functions of the pre-strain. In the field of sheet metal forming simulation, the consideration of anisotropic hardening has been investigated extensively, e. g. to increase the accuracy of springback predictions. As work-hardening, in general, has a major impact on process forces, tool loads and the resulting components' properties after forming, the current ignorance of the work-hardening anisotropy in state-of-the-art cold forging simulations is expected to lead to large errors and uncertainties.

There exist many possible reasons for the limited consideration of anisotropic work-hardening in the field of cold forging, including the lack of suitable characterization methods to determine the anisotropic work-hardening behavior of metals at large effective strains and pre-strains as well as the lack of suitable constitutive models to simulate the material behavior with the required accuracy. To quantify and explain the influence of anisotropic hardening, such advanced material models must be applied in cold forging simulations with the goal to identify and understand the consequences of anisotropic hardening on the outcome of metal forming processes.

The current state-of-the-art is evaluated in order to identify blank spots regarding the aspects of the characterization, constitutive modelling and consequences of anisotropic work-hardening in the field of cold forging. Based on the results of this study, new methods are derived to quantify the various anisotropic work-hardening effects exhibited during different types of strain path changes with a focus on complete strain path reversals. In order to identify possible variations in the manifestation or intensity of the corresponding effects, the methods are applied to different types of cold forging materials. By consideration and comparison of conventional isotropic and advanced anisotropic constitutive models in cold forging simulations, the impact of the evolving work-hardening anisotropy can be isolated and interpreted.

The new knowledge is expected to contribute to the prediction accuracy of cold forging simulations and thus to increase the opportunities for a targeted process design, allowing an active control of the resulting component properties. In additions to this, the vision of a performance prediction of cold forged components becomes more tangible with every new phenomenological aspect that is fully grasped.

2 State of the art

In the first section, a basic understanding of the mechanical behavior of plastically deforming metals under complex strain paths is established. In this scope, the different anisotropic work-hardening phenomena exhibited during strain path reversals are described and their micromechanical origins are illustrated. Phenomenological constitutive models are presented, which are capable of simulating the anisotropic hardening behavior focusing on combined isotropic-kinematic hardening models. Lastly, the known consequences of anisotropic hardening in metal forming processes, including sheet metal forming and incremental metal forming, are summarized.

In the second section, the basics of cold forging are presented and deepened by the example of forward rod extrusion which is utilized to characterize cold forging materials under complex strain paths in the scope of this thesis. The most important compnent properties of cold forged components are described, and examples of multi-stage cold forging processes are presented which include strain path reversals. Lastly, the literature findings are summarized and linked with the aim to identify the gaps in the state of the art regarding the consequences of anisotropic hardening in cold forging.

2.1 Anisotropic hardening

Commonly, when anisotropy is discussed in the field of metal forming, it relates to the geometric anisotropy, i.e. the direction-dependence, of the mechanical properties of metal sheets, caused by the preferred direction of the crystallographic structure which is typically generated during rolling. The geometric anisotropy plays an important role to determine a sheet metal's formability under certain stress-states. It can be quantified by a various experimentally determined parameters, e.g. the Lankford parameter or anisotropy coefficient

$$r' = \frac{\varepsilon_w}{\varepsilon_t}, \tag{2.1}$$

which describes the materials tendency to flow either from the width or the thickness during uniaxial testing. Herein, ε_w and ε_t describe the logarithmic strain in width and thickness direction, respectively (Banabic et al., 2000). In contrast to this definition of anisotropy in the field of metal forming, in this thesis, the term "anisotropic hardening" refers to the transition of a material's initially isotropic yield locus into an anisotropic one (Baltov and Sawczuk, 1965). This becomes especially relevant if strain path changes are considered, which are described and classified in the following section.

2.1.1 Basics of anisotropic hardening

Strain path changes can be classified using the strain path change indicator defined by Schmitt et al. (1985):

$$\cos(\bar{\theta}) = \frac{\Delta\boldsymbol{\varepsilon}_1^p : \Delta\boldsymbol{\varepsilon}_2^p}{|\Delta\boldsymbol{\varepsilon}_1^p||\Delta\boldsymbol{\varepsilon}_2^p|}. \tag{2.2}$$

Herein, $\Delta\boldsymbol{\varepsilon}_1^p$ and $\Delta\boldsymbol{\varepsilon}_2^p$ are the incremental strain tensors (2nd order) before and after a strain path change, respectively. Various ranges of $\bar{\theta}$ are visualized in **Figure 2.1**, assuming a coordinate base that has no shear strain entries (principal strain space). Strain sequences along a straight line in the principal strain space are referred to as monotonic proportional ($\bar{\theta} = 1$). Under this condition, most metals show a continuous work-hardening curve.
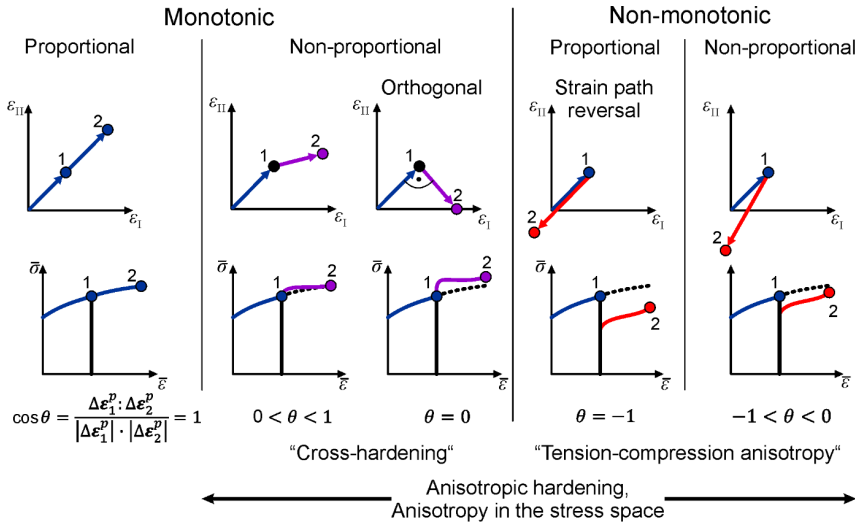
Figure 2.1: Distinction of strain path changes and their consequences for the work-hardening behavior (visual representation based on Schmitt et al., 1985; the third principal strain component ε_{III} is suppressed to improve visualization)

Strain paths with $0 < \bar{\theta} < 1$ are referred to as monotonic non-proportional. In this range, many metals reveal a so-called cross-hardening effect, which is caused by the formation of microbands within which the new plastic strains are localize e. g. under shearing of previously elongated material (Thuillier and Rauch, 1994). The effect is most pronounced for $\bar{\theta} = 0$, at which many metals show a significant overshoot of the flow curve with respect to the monotonic flow curve. A strain path indicator of $-1 < \bar{\theta} < 0$ corresponds to non-monotonic strain paths, i. e. strain path reversals. The best-known anisotropic hardening phenomenon revealed after a full strain path reversal ($\bar{\theta} = -1$) is the Bauschinger effect. In the following the Bauschinger effect and other anisotropic hardening phenomena are presented.

Bauschinger (1886) conducted tensile and upsetting tests on wrought iron. He found, that when a material is plastically deformed under tension and then compressed, the yield stress under compression is lower than the flow stress before unloading. In his case, the yield stress under compression was even lower than the initial yield stress under tension. Consequently, the common assumption of isotropic hardening is flawed, whenever a region of material undergoes a load reversal. In addition to the Bauschinger effect, which only describes the difference of the yield stress in tensile and compressive direction, a plastically deformed material exhibits additional effects, when the load is reversed. In the literature all such effects are directly associated with the Bauschinger effect (Boger, 2006).

The known anisotropic hardening phenomena revealed after strain path reversal are summarized in **Figure 2.2**.
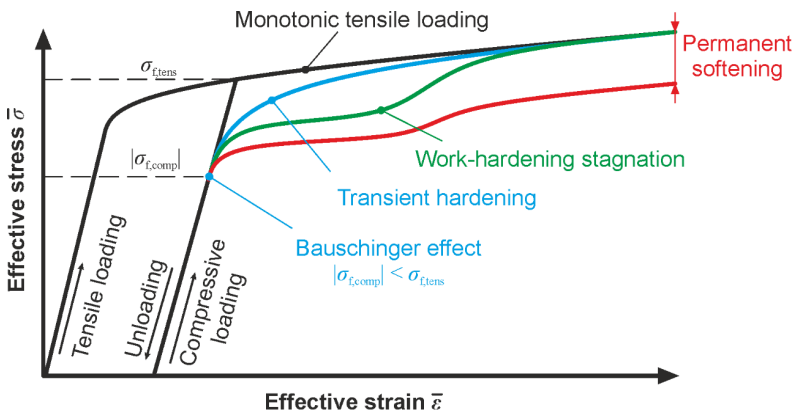
Figure 2.2: Work-hardening phenomena exhibited after strain path reversals (based on Yoshida and Uemori, 2002)

The above effects include the Bauschinger effect in its original form ($|\sigma_{f,comp}| < \sigma_{f,tens}$), the smooth transition from the elastic into the elastic-plastic state, referred to as transient hardening, work-hardening stagnation and a permanent softening, as compared to the monotonic flow curve (Yoshida and Uemori, 2002). In the following the known microstructural explanations of individual anisotropic hardening phenomena are summarized.

Bauschinger effect and transient hardening

Masing (1923) explained the Bauschinger effect with differences in the orientation of individual crystals within a polycrystal, leading to differences in the yield strength in different directions. The residual stresses resulting from plastic strain, lead to variances in the global yield stress during load reversal. In contrast to these theories, Mughrabi (1983) pointed out that the Bauschinger effect can also be observed in single crystals. A

possibility to generalize the idea of Masing is to consider residual stress field within single crystals, caused by regions with varying dislocation density (Margolin et al., 1978). Orowan (1959) proposed that the origin of the Bauschinger effect is connected to the interrelation of dislocations with obstacles, which hinder dislocation movements. Such obstacles can be clusters of interstitial atoms of a secondary phase. During initial loading, these obstacles must be sliced or bypassed depending on the size, type, and lattice structure. In both cases, elastic stresses, often referred to as back stresses, remain in the vicinity of the obstacle, adding up to the load stresses during reverse deformation. In the case of slicing, the sliced obstacle leads to an eased dislocation motion upon load reversal.

Work-hardening stagnation

Hasegawa et al. (1975) showed by transmission electron micrography of plastically deformed pure aluminium specimens, that the stagnation of the work-hardening curve after load reversal is related to the dissolution of dislocation structures upon reverse plastic deformation, while new dislocations are created simultaneously (**Figure 2.3**).
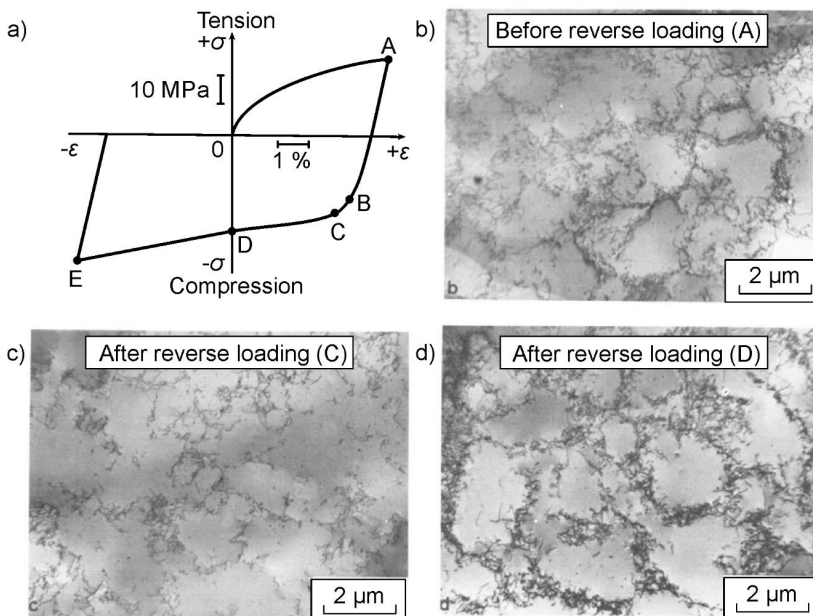
Figure 2.3: a) Cyclic stress-strain curve of pure aluminium at room temperature, b) through d) TEM-images of thin foils prepared from specimens subjected to deformation up to points A through D (Hasegawa et al., 1975)

The authors have reported a drop of dislocation density by 16 % directly after the strain path reversal. At increasing reverse strains the increase of dislocation density resumes. Stoltz and Pelloux (1976) found that aluminium alloys with non-shearable precipitations show a unique hysteresis loop with convex curvature after load reversal, caused by internal elastic stresses exerted by the strong precipitates on the matrix. Sillekens et al. (1988) explained the lowered flow curve with the unpiling of dislocation structures that do not encounter any new obstacles when moving in reverse direction.

Permanent softening

By plastically loading and reverse loading single crystal zinc specimens Edwards and Washburn (1954) observed that, even at large reverse strains, the flow stress remained permanently below than the large strain flow stress under monotonic loading. The authors reported that this - what they called "permanently lost strain" - increases almost linearly with the pre-strain. They explained this behavior with the annihilation of dislocations trapped in the crystal during first straining. Wilson (1965) performed tests on aluminium alloy specimens and concluded that permanent softening is mainly attributed to internal stresses. In contrast, Sleeswyk et al. (1986) explained the Bauschinger effect and the accompanying transient hardening by a "loss of strain" after reloading, based on an observed decrease of dislocation density when dislocations move between barriers. Similarly, Sillekens et al. (1988) attributed the linear correlation between the pre-strain and the magnitude of permanent softening of Ck45 steel to the gradually obstacle-free slip-planes in the reverse dislocation moving direction.

Factors influencing anisotropic hardening

To summarize the above findings, the anisotropic hardening phenomena exhibited at small reverse strains, i. e. the Bauschinger effect and transient hardening are associated with small-range residual stresses, whereas the phenomena observed at larger reverse strains, i. e. work-hardening stagnation and permanent softening are driven by the formation, movement and increasingly heterogeneous structure of dislocation clusters. Based on these explanations, there exist a number of factors potentially affecting the intensity of anisotropic hardening phenomena, which are discussed in the following (**Table 2.1**).

Table 2.1: Factors influencing the anisotropic work-hardening behavior

Factors influencing monotonic work-hardening		Additional factors influencing non-monotonic work-hardening
• Material	• Strain rate	• Pre-strain
• Temperature	• Hydrostatic pressure	• Strain path (loading sequence)

The most significant factor influencing the intensity of the Bauschinger effect for a given metal or alloy has been reported to be the pre-strain. Sowerby et al. (1979) observed for

three types of steel that the amount of permanent softening correlates with the square root of the pre-strain. Scholtes et al. (1980) reported by the example of normalized Ck45 steel that the Bauschinger coefficient saturates with increasing pre-strain. However, he observed that permanent softening increases drastically to about 160 MPa, even at a small-pre-strain of 2 %. Sillekens et al. (1988) conducted similar tests on C45 steel and found a linear correlation between the pre-strain and the magnitude of permanent softening, leading to a loss of 120 MPa at a pre-strain of 0.2. Yoshida et al. (2002) performed forward-reverse tensile tests on stacked sheet specimens. They reported only about 2.5 % permanent softening for a mild steel, but up to 7.5 % for an advanced high strength steel. Han et al. (2005a) investigated the influence of the strength of various steels in the form of sheets as well as the influence of the flow stress before reverse loading on the intensity of the Bauschinger effect. They found that the $R_{p0.05\%}$ yield strength in reverse direction is significantly lower than the flow stress before unloading. For steels with strengths greater than 710 MPa, the reverse yield strength even approaches an asymptotic value, which means that no more hardening takes place in the reverse direction.

Hasegawa et al. (1976) investigated the influence of temperature on various stress- and strain-related Bauschinger parameters by conducting tension-compression tests on pure aluminium polycrystalline specimens at temperatures up to 250 °C (**Figure 2.4**). While stress-related parameters, which are associated with small pre-strains decrease with increasing temperatures, the strain-related parameters associated with large reverse strains even undergo a drastic increase at temperatures above 250 °C. These findings underline the postulated origins of individual anisotropic hardening phenomena, as residual stresses are released at relatively low temperatures due to microscopic plastic deformations, whereas dislocation structures are not affected up to recrystallization.
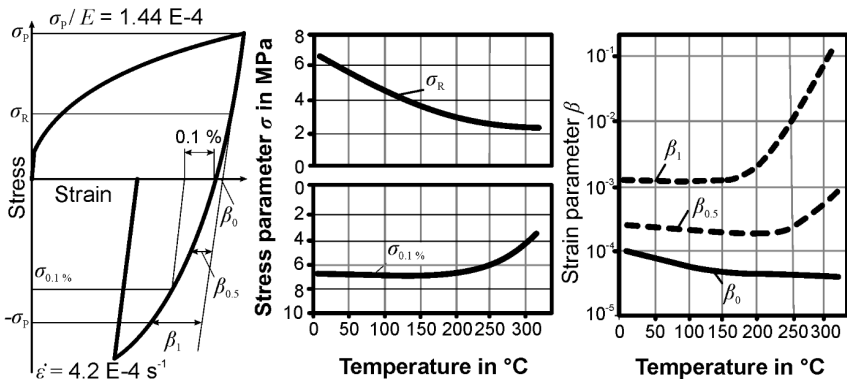
Figure 2.4: Influence of temperature on stress- and strain related Bauschinger parameters of pure aluminium specimens (Hasegawa et al., 1976)

Similarly, Hahn (2003) showed by cyclic torsion of 20MoCrS4 specimens at elevated temperatures, that the Bauschinger effect, transient hardening and permanent softening persist up to the maximum investigated temperature of 500 °C.

Hahn (2003) performed cyclic torsion tests on 20MoCrS4 specimens with varying shear strain rates ranging from 0.07 s^{-1} to 7 s^{-1}, finding no significant influence on the cyclic hardening behavior. While he observed differences in the evolving dislocation structures, he explained these rather with the influence of the temperature increase at higher strain rates, as no temperature balance was reached in the experiments. Han et al. (2005b) investigated the influence of the strain rate on the Bauschinger effect for three types of steels. Up to the maximum strain rate of 0.01 s^{-1} they found no significant influence of the strain rate on the Bauschinger effect. Similar results were reported by Mahato et al. (2014) for annealed OFHC copper, which showed no stress rate dependence of the Bauschinger effect even at large stress rates up to 500 MPa/s.

Bridgman (1945) conducted tensile tests on specimens subjected to large hydrostatic pressures by immersing them in a pressurized fluid. He found that the ductility and the flow stress increase with the hydrostatic pressure. When the pressure is released and the specimens are loaded again at atmospheric pressure, no "pressure memory" could be observed. Similar tests were conducted by Spitzig et al. (1975) on AISI 4310 and 4330 steel. While the initial flow stress is significantly increased during the applied pressure, the strain hardening behavior and the ultimate tensile strength were not affected permanently.

Scholtes et al. (1980) investigated the influence of the loading sequence on the load reversal behavior of Ck45 by pre-straining it under tension as well as compression and reloading it in opposite direction, showing that the Bauschinger effect manifests similarly in both cases. Sun et al. (2009) pre-strained specimens made of the dual phase steel DP560 by 6 % under tension and compression and plastically reloaded it in the opposite direction. In accordance to the results by Scholtes et al. (1980), an identical hardening behavior was reported for both investigated loading sequences.

2.1.2 Characterization of anisotropic hardening

To characterize the material behavior under strain path reversals, continuous or interrupted characterization methods can be applied. The term "continuous" refers to the fact that the specimens are loaded subsequently in two opposing directions without intermediate processing.

In the past, most experimental methods to quantify anisotropic hardening were focused on the characterization of thin specimens extracted from metal sheets. Consequently, most characterization methods focus on the characterization of thin specimens extracted from metal sheets. The most common method to characterize sheet material is the utilization of tensile tests with an abrupt reversal of the loading direction after a certain

amount of tensile strain has been applied. This type of continuous test is referred to as the conventional tension-compression test (Abel and Ham, 1966) (**Figure 2.5a**). Due to the low bending stiffness of the specimens, the achievable tensile pre-strains are highly limited (Tan et al., 1994). To deal with this drawback Kuwabara et al. (2001) have introduced a supporting device, while Boger et al. (2005) focused on adapted specimen geometries. Other continuous procedures include the cyclic planar shear test (Hu et al., 1992) and the cyclic bending test (Yoshida et al., 1998). While the former procedure introduces a stress inhomogeneity at the groove edges (Bouvier et al., 2006), the latter relies on force-displacement data which cannot directly be transformed into the necessary stress-strain data and must instead be evaluated by means of inverse methods. Galdos et al. (2019b) investigated the load reversal behavior of 42CrMoS4Al case-hardening steel by means of cyclic torsion tests on cylindrical specimens. While torsion of solid round specimens does not lead to structural instabilities, the local stress and strain is not uniform over the specimen radius and a transformation of torque measurements into flow stress data is only possible with assumptions regarding the hardening curve or by means of inverse methods. The authors were able to characterize the material for large pre-strains up to $\varepsilon_{pre} = 0.7$ and observed the classical Bauschinger effect, transient hardening, work-hardening stagnation and permanent softening (**Figure 2.5b**). Yin et al. (2015b) performed cyclic in-plane torsion tests on metal sheets to obtain cyclic flow curves of DP600, DP800 and DX54D and AA5182. He was able to obtain Bauschinger coefficients with maximum pre-strains of $\varepsilon_{pre} > 0.6$ (**Figure 2.5c**).
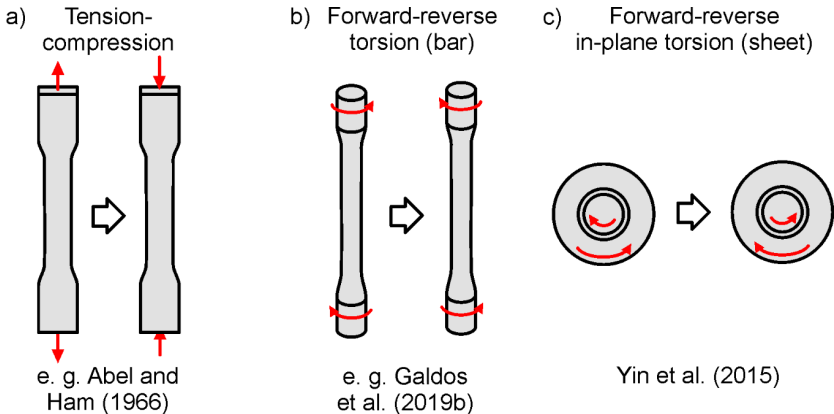
Figure 2.5: Continuous characterization methods to obtain the anisotropic hardening behavior of metals

In the field of bulk metal forming, only few publications exist on the characterization of anisotropic hardening. Here, the material typically comes in the form of bars or slabs.

Analogously to the characterization of sheet specimens, a common method to characterize material in the form of bars is the tension-compression test of cylindrical specimens. Due to the high length to diameter ratio and the low bending stiffness, standardized tensile specimens according to the international standard DIN EN ISO 6892-1 or the American standard ASTM E8/E8M are not suited for large strain cyclic testing. Different types of alternative specimen geometries and test apparatuses were utilized to overcome this problem (Scholtes et al., 1980). Despite the special precautions, the achievable pre-strains were limited due to the constrained end faces, resulting in an unknown non-uniform stress distribution (**Figure 2.6**).
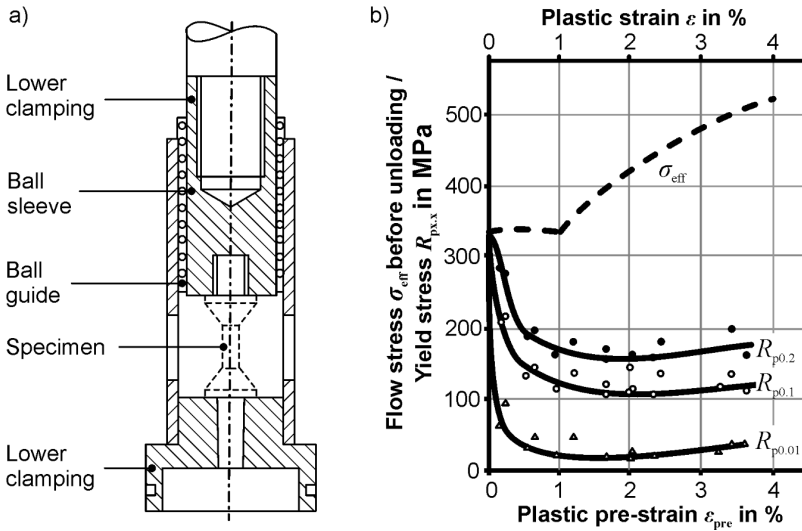
Figure 2.6: a) Special test apparatus and specimen geometry for tension-compression tests, b) Flow stress of pre-strained specimens (Scholtes et al., 1980)

In the technological practice of bulk metal forming, large strains are frequently attained. As the material is typically deformed under hydrostatic pressure the maximum attainable strain is only limited by the ductility of the material rather than structural instabilities (Gil Sevillano et al., 1980). They define the term "large strain" as strains above $\bar{\varepsilon} > 1$, as these strains are significantly higher than those attainable in conventional characterization tests. To determine flow curves up to large strains, interrupted characterization procedures were applied, including

- upsetting with intermediate machining to restore the initial height-to-diameter ratio (e. g. Krause, 1963 and Hockett and Sherby, 1975),
- tensile tests on drawn wires (Langford and Cohen, 1969),
- and tensile tests on rolled sheets (e. g. Krause, 1963).

Generally, interrupted procedures can also be utilized to obtain large pre-strains for the investigation of a subsequent strain path reversals. Some examples of interrupted procedures are shown in **Figure 2.7**.
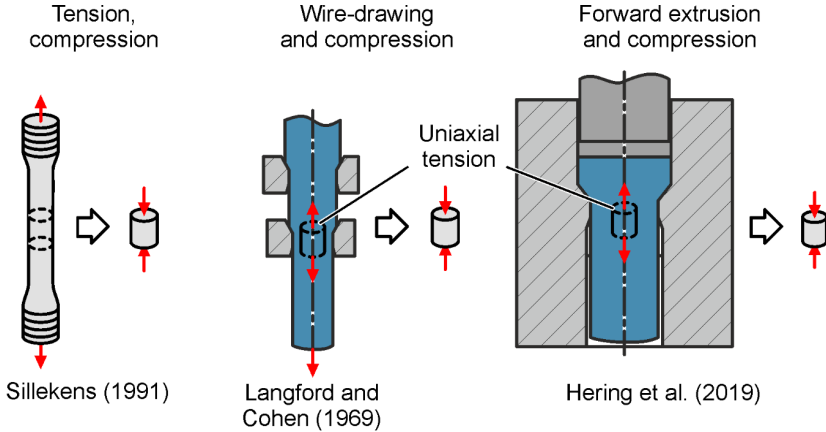
Figure 2.7: Interrupted characterization methods to obtain the anisotropic hardening behavior of metals

Sillekens et al. (1991) conducted upsetting tests on cylindrical specimens machined from previously elongated bars made of C22 steel and CuZn37 brass. They were able to achieve pre-strains of $\varepsilon_{pre} > 0.3$, showing that the flow stress and hardening rate in reverse direction drops significantly with increasing pre-strain. Langford and Cohen (1969) conducted upsetting tests on drawn iron wires with large pre-strains of $\varepsilon_{pre} = 4.5$, demonstrating that the material starts exhibiting extensive softening after the strain path reversal. Pöhlandt (1979) performed upsetting tests on cold-extruded steel shafts of QSt32-3 to obtain large strain flow curves. He observed an "abnormal" hardening slope, which Doege et al. (1986) attributed to the change in strain direction between extrusion and upsetting. Similarly, Nehl (1983) investigated the influence of the extrusion strain in forward rod extrusion on the flow stress in subsequent compression for various types of machining steels and found that even at the lowest investigated pre-strain of $\varepsilon_{pre} = 0.5$ all materials exhibit softening in subsequent upsetting.

A summary of literature results on the effect of strain path reversals with a focus on large pre-strains is given in **Table 2.2**. The main objective of most of the studies was the determination of large strain flow curves, however, the published described methods can also be applied to gain insights into the work-hardening behavior after strain path reversals for various types of materials.

Table 2.2: Literature summary of experiments on the influence of strain path reversals with focus on large pre-strains

Authors	Test setup	Specimen type	Materials	Pre-strain
(Ellermann, 2013)	Tension – compression	Round bars	42CrMoS4, 100Cr6	0.04
(Scholtes et al., 1980)	Tension – compression	Round bars	Ck 45	0.04
(Sillekens et al., 1988)	Tension – compression	Round bars	C45	0.10
(Sillekens et al., 1991)	Tension – machining – compression	Round bars	CuZn37, C22	0.30
(Galdos et al., 2019a)	Forward-reverse torsion	Round bars	42CrMoS4Al	0.70
(Pöhlandt, 1979)	Extrusion – compression	Round bars	QSt32-3	1.30
(Nehl, 1983)	Extrusion – compression	Round bars	C15, 9SMn28, 10S20, 35S20	1.60
(Langford and Cohen, 1969)	Drawing – compression	Wire	Pure iron	4.50

All materials included in Table 2.2 exhibit the Bauschinger effect, transient hardening, work-hardening stagnation and permanent softening, however, none of the effects were quantified systematically as they were not the focus of the underlying investigations and in some cases they were even actively regarded as measurement errors (Pöhlandt, 1979).

2.1.3 Constitutive modelling of anisotropic hardening

For the phenomenological modelling of work-hardening of metallic materials during plastic deformation, the concept of the yield surface is commonly used. The yield surface is defined as the mathematical relation in the form of

$$f(\boldsymbol{\sigma}) = \bar{\sigma}(\boldsymbol{\sigma}) - \sigma_f \leq 0. \tag{2.3}$$

Herein, $\bar{\sigma}$ is a function which maps the stress tensor $\boldsymbol{\sigma}$ onto a stress-like scalar value. In case of the von-Mises-yield criterion, this function corresponds to the second invariant of the deviatoric stress tensor. The current flow stress of the material is given by σ_f. The yield cylinder with the radius σ_f defined in the stress space limits all stress states that lead to a purely elastic shape change ($f < 0$). If the stress lies on the surface of the yield cylinder, plastic deformation takes place ($f = 0$).

The exact definition of the quantities $\bar{\sigma}$ and σ_f depends on the underlying hardening approach. Typically, it is differentiated between three basic hardening concepts, which are discussed in the following:

I.   Isotropic hardening: A plastic deformation leads to an isotropic expansion of the yield surface according to

$$\sigma_f = \sigma_f(\bar{\varepsilon}, \dots). \qquad (2.4)$$

The current flow stress σ_f, which according to **Eq. (2.4)** corresponds to the radius of the yield cylinder, depends on the accumulated or equivalent plastic strain $\bar{\varepsilon}$ (**Figure 2.8a**). The physical interpretation of this quantity is connected to the accumulated number of dislocations with increasing plastic deformation. In general, the connection between σ_y and $\bar{\varepsilon}$ is arbitrary and can either be in the form of an experimentally obtained flow curve or be defined in the form of a material dependent mathematical function as given by Ludwik (1909), Swift (1952) or Voce (1956). Additionally, the flow stress can be given as a function of the strain rate $\dot{\bar{\varepsilon}}$ (visco-plasticity) or temperature T. Per definition, the use of isotropic hardening assumes that hardening evolves equal in all directions. Consequently, modelling of the Bauschinger effect is not possible, which means that utilization of isotropic hardening is strictly suited for the simulation of monotonic loading paths.

II. Kinematic hardening: Plastic deformations lead to a translation of the yield surface without altering its shape. The translation is symbolized by the relation

$$f = \bar{\sigma}(\boldsymbol{\sigma} - \boldsymbol{\alpha}). \qquad (2.5)$$

Herein, the back stress tensor $\boldsymbol{\alpha}$ corresponds to the current position of the yield surface centre in the stress space. The term back stress corresponds to the microscopic residual stress fields created during plastic deformation, referring to the common explanation of the Bauschinger effect (**Figure 2.8b**).

III. Distortional hardening: Plastic deformation causes a distortion of the yield surface (**Figure 2.8d**). Tozawa (1979) reported for several metals including brass and different types of steels, that a plastic deformation in a certain load direction, causes flattening of the yield surface in the opposite direction. A consideration of distortional hardening allows modelling of the Bauschinger effect as well as additional loading-direction dependent material phenomena like cross-hardening.

Most metals exhibit a combination of isotropic and kinematic hardening, according to

$$f = \bar{\sigma}(\boldsymbol{\sigma} - \boldsymbol{\alpha}) - \sigma_f(\bar{\varepsilon}, \dots) \le 0. \qquad (2.6)$$

This type of hardening is most frequently referred to as mixed or combined hardening (**Figure 2.8c**). The exact hardening behavior is defined by the evolution equations of the back stress tensor $\boldsymbol{\alpha}$ (kinematic hardening part) and the current flow stress σ_f (isotropic hardening part). In the following some kinematic and distortional material models are presented which are able to capture the Bauschinger effect.
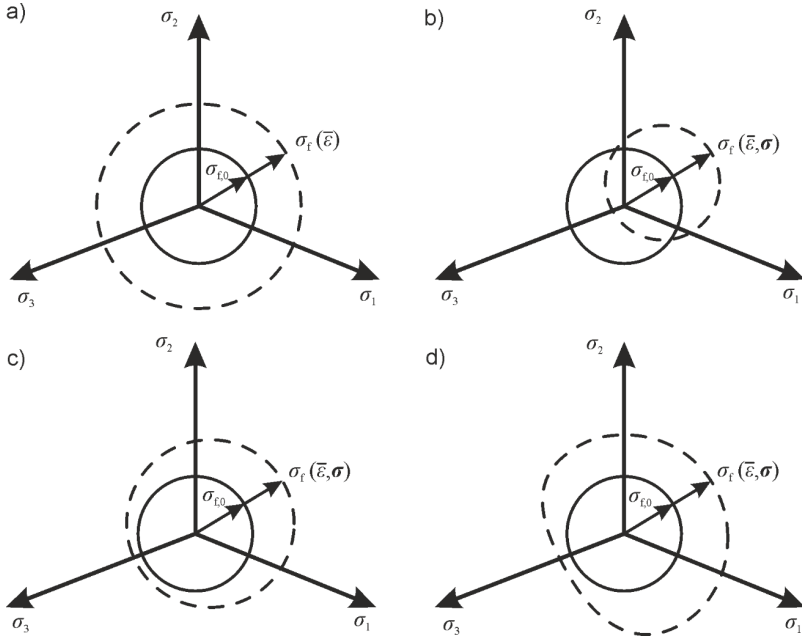
Figure 2.8: a) Isotropic hardening, b) Kinematic hardening, c) Combined isotropic-
kinematic hardening, d) distortional hardening

Kinematic hardening

The main difference between individual kinematic hardening models lies in the defini-
tion of the evolution equation of the back stress tensor $\boldsymbol{\alpha}$. The first kinematic hardening
model was introduced by Prager (1945) and later modified by Ziegler (1959). In Prager's
model, the increment of the back stress tensor $d\boldsymbol{\alpha}$ evolves according to the relation

$$d\boldsymbol{\alpha} = c\, d\bar{\boldsymbol{\varepsilon}} \tag{2.7}$$

into the direction of the plastic strain increment tensor $d\bar{\boldsymbol{\varepsilon}}$. Herein, c is a material pa-
rameter referring to the linear slope of the kinematic hardening function. Ziegler noted
that this relation gives inconsistent results between 2D- and 3D-load cases and modified
it according to

$$d\boldsymbol{\alpha} = \frac{c}{\sigma_{f,0}}\, (\boldsymbol{\sigma} - \boldsymbol{\alpha})\, d\bar{\varepsilon}. \tag{2.8}$$

With this modification, the increment of the back stress tensor points in the direction of
the connecting line between the current stress and the back stress tensor $(\boldsymbol{\sigma} - \boldsymbol{\alpha})$ and
thus, outward of the yield surface. The term $1/\sigma_{f,0}$ serves as a normalization with respect
to the initial flow stress.

As most materials exhibit nonlinear hardening behavior, linear models mainly served as a theoretical basis for advanced modelling approaches. One class of approaches utilizes a series of yield surfaces, in between which kinematic hardening evolves linearly with the plastic strain, however, the slope changes in between yield surfaces. The approach was first introduced by Mróz (1967). Based on this approach, Krieg (1975) and Dafalias and Popov (1976) created so-called *Two-Surface* models, in which additionally to the yield surface, a limiting surface is defined. Between the yield surface and the limiting surface, the hardening evolution is defined by a continuous function of the plastic strain. Frederick and Armstrong (2007) enhanced the Prager-model by an additional term:

$$d\boldsymbol{\alpha} = C \, d\bar{\boldsymbol{\varepsilon}} - \gamma \, \boldsymbol{\alpha} \, d\bar{\varepsilon}. \tag{2.9}$$

While the increment of plastic strain tensor $d\bar{\boldsymbol{\varepsilon}}$ can point in any direction in the stress space, the plastic strain increment $d\bar{\varepsilon}$ can only increase, which assures, that kinematic hardening saturates with the plastic strain. The speed of saturation is given by the material parameter γ. The maximum yield surface translation in the stress space can be calculated by the relation C/γ. On this basis, the Armstrong-Frederick-model can be interpreted as a *Two-Surface* model with a limiting surface with the radius C/γ. In the case of monotonically increasing one-dimensional loading, the differential **Eq. (2.9)** can be solved explicitly in terms of the total accumulated plastic strain $\bar{\varepsilon}$ as

$$\alpha(\bar{\varepsilon}) = \frac{C}{\gamma} \, (1 - e^{-\gamma \, \bar{\varepsilon}}). \tag{2.10}$$

Chaboche (1986) generalized the Armstrong-Frederick-model by superposition of an arbitrary number of back stresses according to

$$\boldsymbol{\alpha} = \sum_{i=1}^{m} \boldsymbol{\alpha}_i \tag{2.11}$$

where each back stress tensor $\boldsymbol{\alpha}_i$ is calculated as

$$d\boldsymbol{\alpha_i} = C_i \, d\boldsymbol{\varepsilon}^p - \gamma_i \, \boldsymbol{\alpha}_i \, d\bar{\varepsilon}. \tag{2.12}$$

The superposition of several back stress tensors allows for a flexible definition of the kinematic hardening slope. In addition to this, setting one term $\gamma_k = 0$ prevents the hardening saturation and allows for consideration of continuous hardening.

Yoshida and Uemori (2002) presented a mixed isotropic-kinematic hardening model for application in sheet metal forming, allowing the simulation of all strain path reversal related phenomena shown in Figure 2.2. The basic idea of the model is summarized in **Figure 2.9**.
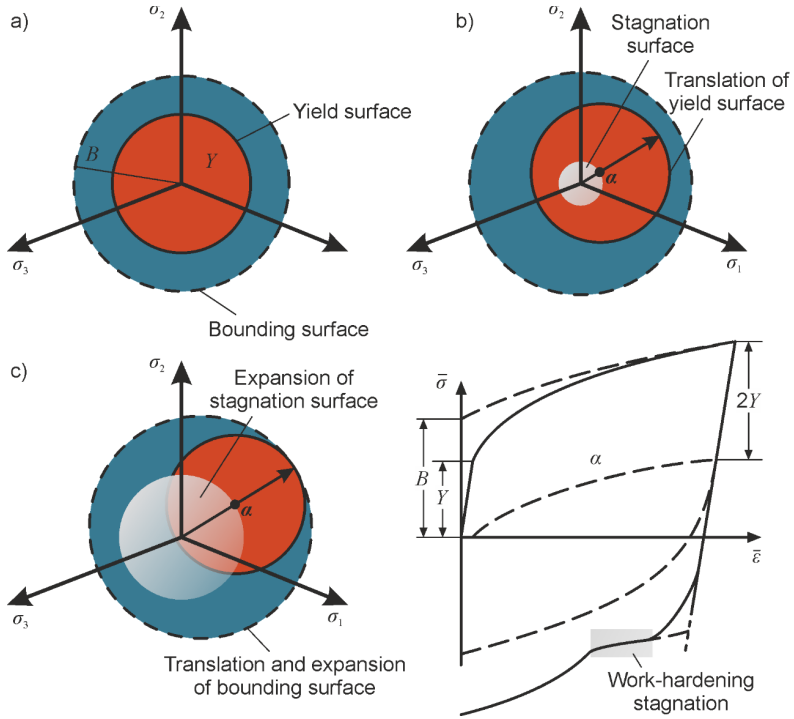
Figure 2.9: Description of hardening model by Yoshida and Uemori (2002)

The model consists of an inner yield surface with the radius Y which is located within a bounding surface with a radius of B. If the loading stress exceeds Y, a translation of the yield surface (kinematic hardening) is triggered, which is captured by a shift of the yield surface center $\boldsymbol{\alpha}$. When the boundary of the yield surface reaches outer bounding surface, the bounding surface translates and expands simultaneously (combined hardening). To account for work-hardening stagnation, work-hardening only occurs when the center of the yield surface lies on the edge of a third surface, the so-called stagnation surface, which translates and expands during plastic flow. The ratio between the rate of translation and expansion of the stagnation surface prescribe the intensity of work-hardening stagnation.

In its original form, the Yoshida-Uemori model includes six material parameters which are associated with kinematic hardening and work-hardening stagnation (**Table 2.3**).

Table 2.3: Material parameters of the original Yoshida and Uemori (2002) model

	Symbol	Description	Unit
Yield surface (kinematic hardening)	Y	Initial flow stress	MPa
	c	Rate of kinematic hardening of yield surface	-
Bounding surface (Isotropic & kinematic hardening)	B	Initial radius of bounding surface	-
	b	Threshold of kinematic hardening of bounding surface	MPa
	R_{sat}	Saturated value of isotropic hardening of bounding surface	MPa
	k	Rate of isotropic & kinematic hardening of bounding surface	-
Stagnation surface	h	Intensity of work-hardening stagnation	-

While Yoshida and Uemori have given no information on the numerical implementation of their hardening model, Ghaei et al. (2010) have presented a detailed return-mapping algorithm with a semi-implicit implementation approach in which the plastic strain evolution equation is solved implicitly and all internal variables are solved explicitly. Later Ghaei and Green (2010) have also published a fully-implicit integration procedure of the Yoshida-Uemori model. Recently, Jia (2014) presented an alternative fully-implicit integration procedure and an accompanying sub-stepping algorithm for the Yoshida-Uemori model, to achieve fast convergence even with large strain increments.

Despite the relatively low number of material parameters, the Yoshida-Uemori hardening model is capable of modelling a large variety of different materials under monotonic and cyclic loading, with exceptional accuracy. Shi et al. (2008) utilized the Yoshida-Uemori hardening model to capture the hardening behavior of DP980, DP780, HSLA and DDQ steel sheets at multiple subsequent strain path reversals. They showed that the model accuracy can be increased by considering non-saturating isotropic hardening. Zhu et al. (2013) have recently used the Yoshida-Uemori model to simulate springback after rotary-draw bending of a complex three-dimensional part, achieving high accuracy in comparison with experimental results. In the field of bulk metal forming, the only publication on utilization of the Yoshida-Uemori model was presented by Narita et al. (2016), showing that the use of the model leads to an improvement of the prediction accuracy of the resulting strength of a bolt after cold forging.

Detailed reviews on the application of various kinematic hardening models in metal forming processes were given by Chaboche (2008) and Eggertsen and Mattiasson (2009).

Distortional hardening

Tozawa (1979) performed tensile and compression tests on glued stacks of sheet specimens (**Figure 2.10a**). By exposing the specimens to different types of strain path changes, he observed, that plastic deformations lead to a distortion of the yield surface rather than a translation or expansion (**Figure 2.10b**). Typically, a pre-strained material shows the lowest flow stress in the loading direction opposite to the previous loading, which is symbolized by the flattening of the back of the yield surface along the x-axis.
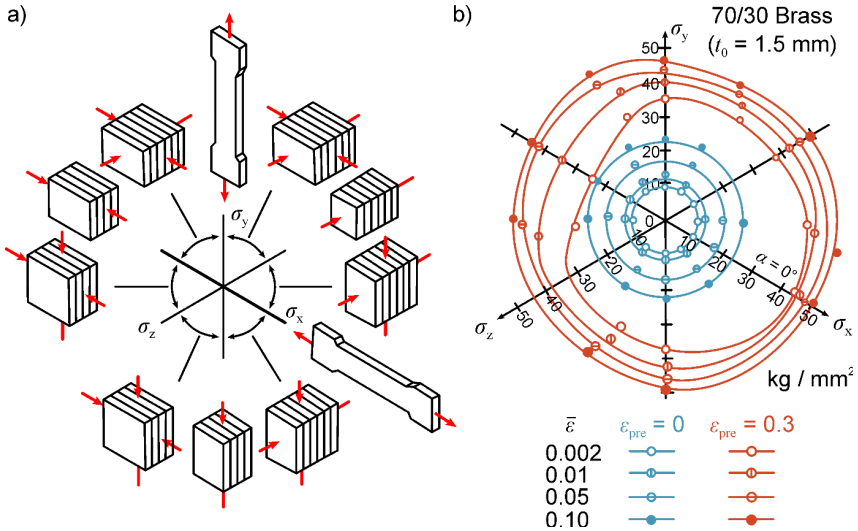
Figure 2.10: a) Schematic representation of the experimental methods to determine yield loci in the normal stress plane, b) Yield loci before and after pre-straining in x-direction (Tozawa, 1979)

Several researchers have proposed constitutive models to incorporate distortional hardening, including the HAH-model ("homogeneous anisotropic hardening") proposed by Barlat et al. (2011). In its original form, the HAH-model is capable to capture the Bauschinger effect, transient hardening, and permanent softening over multiple loading cycles. Additionally, the distortion of the yield surface allows modelling of cross-hardening effects. The model was applied by Lee et al. (2012) in draw bending simulations, showing that springback can be modelled with an improved accuracy as compared to isotropic and combined isotropic-kinematic hardening models.

Lee et al. (2013) further extended the model by incorporating the change in Young's modulus with regard to loading and unloading. Recently Yoon et al. (2018) implemented the HAH-model applying a straightforward numerical differentiation scheme and

showed that a similar computation time can be achieved compared to the classical ana-
lytical differentiation approach. Currently, – to the knowledge of the author – there exist
no publications on the application of distortional hardening models in bulk metal form-
ing simulations.

2.1.4 Anisotropic hardening in sheet and incremental metal forming

In the field of sheet metal forming, the anisotropic hardening phenomena receive fre-
quent attention, as springback, a major concern in this field of forming, is strongly af-
fected by non-proportional strain paths and the hardening phenomena exhibited at such
(Sun et al., 2009). This is important especially when material regions are bent and unbent
multiple times, e.g. in deep drawing with draw beads (Ghaei and Green, 2010). The
authors showed by the example of the NumiSheet 2005 Benchmark, that the accuracy
of springback prediction can be drastically increased by use of the combined isotropic-
kinematic Yoshida and Uemori (2002) hardening model when compared to standard
isotropic hardening (**Figure 2.11**).
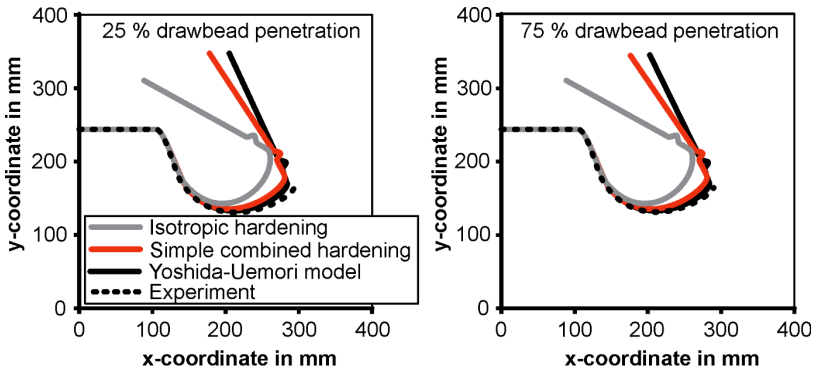
Figure 2.11: Comparison of experimental and simulated springback using different
constitutive models (adapted from Ghaei and Green, 2010)

A comprehensive review on the influence of anisotropic hardening on springback was
given by Wagoner et al. (2013), who name anisotropic hardening and more specifically
the Bauschinger effect a material feature that must be considered in the accurate predic-
tion of springback.

In incremental metal forming processes, the material is formed locally and in several
consecutive steps. The repeated forming of material regions is oftentimes accompanied
by strain path reversals, triggering the Bauschinger effect and other effects connected to
strain path changes. Hahn (2003) investigated the influence of the Bauschinger effect
on the forming work in spin extrusion. He was able to show that it has a major impact
on the plastic work.

The consideration of the Bauschinger effect by means of an analytical model led to an improved prediction of the forming work. Awiszus et al. (2009) investigated potential influencing factors to be considered in the simulation of roller spinning processes. They showed that the investigated material 42CrMo4 shows a pronounced Bauschinger effect which is triggered by the frequent changes of the loading direction. Investigations on the longitudinal tooth forming with oscillating rams were conducted by Schultheis (2007). The oscillation movement of the ram leads to a decrease of the maximum forming loads of up to 40 %. According to the authors, this phenomenon can be partly ascribed to the Bauschinger effect.

Wernicke et al. (2021) investigated the influence of the indentation depth on the required forming force during radial edge thickening of DC04 sheets by edge rolling. They observed that the plastic work required to reach a prescribed total indentation depth is significantly lower for smaller indentation increments per revolution. They explained this with the larger number of strain path reversals occurring at lower indentation increments, triggering the so-called ratcheting which is associated with anisotropic hardening. To prove their hypothesis, they performed cyclic in-plane torsion tests of grooved specimens with different angle increments, showing that the plastic work required to reach a prescribed total strain decreases significantly at smaller angle increments (**Figure 2.12**). By considering the saturated cyclic flow curves instead of the monotonic flow curve they were able to significantly improve the accuracy of the force prediction via numerical simulations of the edge thickening process.
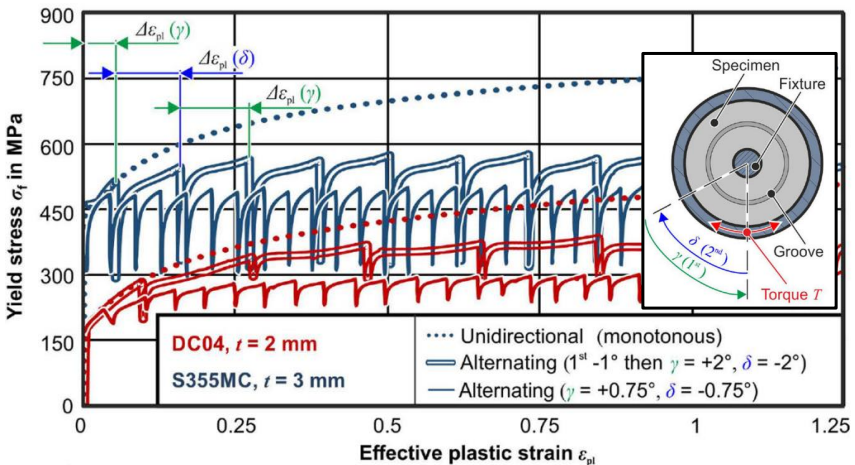
Figure 2.12: Influence of torsion angle increment on the cyclic flow curve of DC04 and S355MC sheets (Wernicke et al., 2021)

2.2 Cold forging

According to DIN 8582 and DIN 8583-6 cold extrusion processes are a subcategory of bulk forming, belonging to the process family of extrusion in which a typically cylindrical workpiece is pushed through a form giving die by a moving punch, while being fully or partially enclosed by a stationary container.

In the literature cold extrusion is further classified according the type of part produced and the direction of material flow relative to the direction of the punch movement. In this regard, it is differentiated between rod, hollow and can extrusion as well as between forward, backward and lateral extrusion (Lange, 1988). The different types of basic cold forging processes according to the above definition are illustrated in **Figure 2.13**.
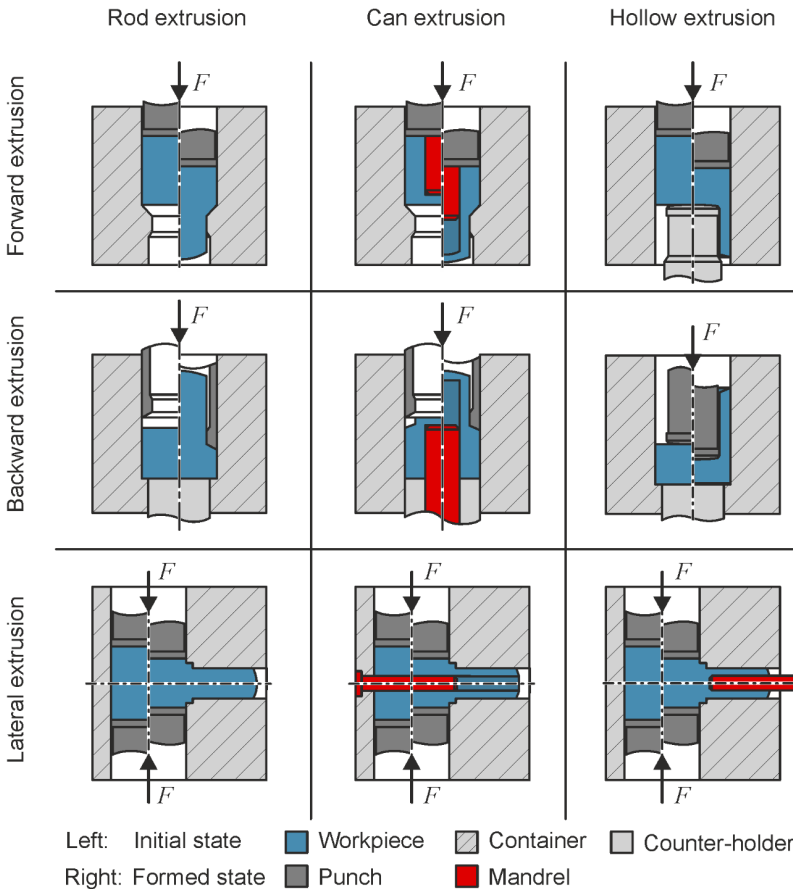
Figure 2.13: Basic cold forging processes (DIN 8583-6)

Typically, in cold forging the billets or slugs are not heated actively and extruded at room temperature. The main advantage of cold extruded parts over hot forged parts is the high surface quality, the high dimensional accuracy as well as the work-hardening, which leads to an increase of the parts' strength (Lange, 1988). For some special applications and materials, the parts are heated to 200 °C to 850 °C. This process modification is referred to as warm extrusion and is used to reduce the forming loads for complex parts, e.g. trispheres (Lange, 1988). When even higher temperatures are used, the process is referred to as hot forging (DIN 8580).

At the beginning of the 19th century cold extrusion was used for the production of lead tubes and projectile bodies (Lange, 1988). Since 1886 can extrusion is known to be used for the production sleeves and tubes made of lead (Feldmann, 1959). Nowadays, cold extrusion of steel is mainly applied due to its advantageous characteristics for the mass production of parts with high mechanical quality and dimensional accuracy. Nearly 90 percent of parts produced by cold forging are used in the automotive sector. In average each passenger car includes 50 kg of cold forged components. In 2008, Germany was the third largest manufacturer of cold forged components with 150.000 t. Despite the ongoing progression of fast and fully automated machining technologies, the increasing demand for metal and steel parts will increase in the future, especially with respect to the high material utilization in the range of over 90 % (Lange et al., 2008).

2.2.1 Basics of forward rod extrusion

In forward rod extrusion a cylindrical billet is pushed through a die, leading to a reduction of the initial cross-section. In contrast to reduction, the typically higher area reduction in forward extrusion makes necessary the use of a container which limits the buckling of the workpiece und pressure. Forward rod extrusion is a steady-state process, meaning that after an initial transient material flow into the die cavity, the material flow is nearly constant over time leading to a homogeneous distribution of component properties over the parts length. Besides cold heading and upsetting, forward extrusion is the most widely used cold forging process (Hoffmann et al., 2012).

Due to the large stresses the tools are subjected to, the dies are supported by shrink-fit or press-fit rings, causing favorable initial compressive stresses. The elastic deflection of the tools under pressure causes tool springback during unloading, which makes necessary an ejector to push the part out of the die after forming (Lange et al., 2008).

Strain measures in forward rod extrusion

In order to compare the shape change in cold extrusion two measures of strain have prevailed in the literature, namely the relative cross-section reduction ε_A and the geometric or extrusion strain ε_{ex}. The relative cross section reduction is defined as

$$\varepsilon_A = \frac{A_0 - A_1}{A_0},\tag{2.13}$$

where A_0 is the initial cross-section of the cylindrical billet and A_1 is the reduced cross-section after extrusion. The extrusion strain, also called logarithmic strain is calculated by the relation

$$\varepsilon_{ex} = \int_{A_0}^{A_1} \frac{\delta A}{A} = \ln A_1 - \ln A_0 = \ln \frac{A_1}{A_0} = 2 \ln \frac{d_1}{d_0}.\tag{2.14}$$

While both strain measures can be used for comparison of similar forming processes, the main advantage of the logarithmic extrusion strain is the fact that it corresponds exactly to the true effective strain of material along the central axis of the extrudate. Both strain measures are used in the literature with respect to the process limits, i. e. the recommended maximum strains for a given material and process with regard to a cost-efficient tool life (Lange et al., 2008).

Figure 2.14 shows the material flow during forward rod extrusion made visible with the visio-plastic method applied by Ossenkemper (2018). For this, a billet is sectioned longitudinally and marked with a grid. The two sections are assembled and extruded together. After extrusion and ejection, the two halves are separated manually, and the material flow becomes visible.
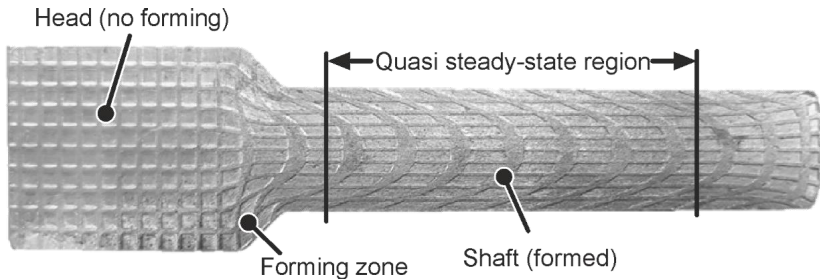
Figure 2.14: Material distortion in forward rod extrusion (Ossenkemper, 2018)

At the shaft tip, the transient material deformation at the beginning of the process becomes visible. Once the tip exits the die, the quasi steady-state leads to homogeneous material distortion over the length of the shaft up to the extrudate shoulders. While in the center of the extrudate shaft the material is mainly stretched, toward the surface it is sheared additionally. The amount of shear deformation is subject to the die geometry, including the extrusion ratio, the shoulder opening angle and the tool radii, as well as the friction conditions.

Stresses

The material flow during forward extrusion allows for a qualitative assessment of the stress state in the forming zone with help of the "Elementary Plasticity Theory" according to Sachs (1927b) and Siebel (1924). By use of the slab method, which assumes that plane cross-sections remain plane over the complete forming history, it is possible to describe the three-dimensional stress evolution qualitatively (**Figure 2.15**).

When the forming zone is in the cone region, where the cross section is reduced from A_0 to A_1 and the highest principal strain occurs in axial direction, the axial stress σ_z reaches its maximum at the cone entry line. Toward the cone or die exit line, the axial stress σ_z drops to zero. Due to axisymmetry, along the center line, the radial stress σ_r and tangential stress σ_t must be equal. Assuming isotropy, the relation between the radial stress σ_r and the axial stress σ_z is given as

$$\sigma_z - \sigma_r = \sigma_f. \tag{2.15}$$
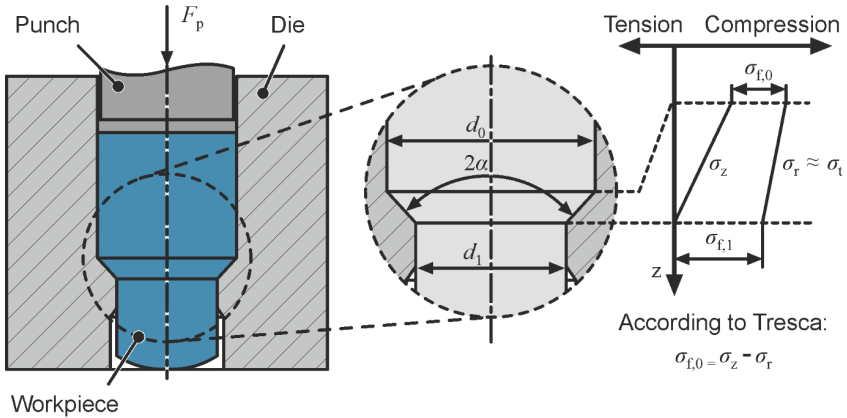
Figure 2.15: Stress distribution in the forming zone in forward rod extrusion according to the "Elementary Plasticity Theory" by Siebel (1924) (Lange, 1988)

Since the Elementary Plasticity Theory is based on a number of assumptions, the described stress state should only be interpreted qualitatively. In terms of integral calculations, i. e. for approximate calculations of the necessary forming loads the analytical theory has shown to be remarkably accurate. A local description of stresses, strains and failure mechanisms, is not possible without the use of numerical methods (Roll and Tekkaya, 1993).

Forming force

For an efficient tool design, knowledge of the expected forming forces especially the maximum forming force is essential. **Figure 2.16** shows a typical force-displacement curve of forward rod extrusion.
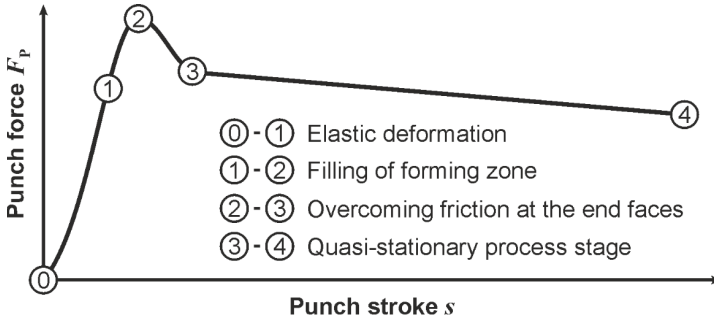
Figure 2.16: Force-stroke curve in forward rod extrusion (based on Lange et al., 2008)

At the beginning of extrusion the force increases drastically, in a near linear fashion up to Point ①. In this stage, the material is upset elastically, contact with the tool is established, and the die is filled until reaching the force maximum F_{max} at Point ②. The subsequent drop of the forming force to Point ③ results from the change in the frictional behavior when the lower end face of the workpiece exits the forming zone. The region between Points ③ and ④ marks the quasi steady-state material flow. From here the force decreases steadily, as the friction surface decreases with increasing punch stroke.

The analytical force estimation according to Siebel (1932) is based on the Elementary Plasticity Theory. Herein, the total force F_{tot} is the sum of the ideal forming force F_{id}, the force resulting from friction at the die shoulder $F_{\mu s}$, the force resulting from the friction at the container $F_{\mu c}$, and the force associated with redundant shearing F_{sh}:

$$F_{tot} = A_0 \cdot \sigma_{fm} \cdot \varepsilon_{ex} \cdot \left(1 + \frac{2 \cdot \mu}{\sin 2\alpha} + \frac{2}{3} \cdot \frac{\hat{\alpha}}{\varepsilon_{max}}\right) + \pi \cdot d_0 \cdot \mu \cdot \sigma_{f0} \cdot l. \qquad (2.16)$$

Herein, ε_{ex} is the extrusion ratio, σ_{fm} is a mean flow stress of the material before and after extrusion, 2α is the shoulder opening angle of the die, μ is the friction coefficient according to the Coulomb friction model and l is the current length of the contact surface between workpiece and container.

2.2.2 Workpiece material and preparation

Workpiece materials used for cold forging should ideally possess a low initial flow stress, a low work-hardening tendency as well as a high formability (Hoffmann et al., 2012). Historically, these requirements were mainly met by non-ferrous metals such as

copper and aluminium. However, since the patent by Singer (1934) on the phosphating of steel surfaces which allowed the application of a new group of lubrication systems preventing welding between the workpiece and the tools, the use of steel as cold forging material has become possible for the first time. Nowadays, steels are the most applied workpiece materials in cold forging (Lange et al., 2008).

The requirements for cold extrudability are especially met by unalloyed steels with low carbon contents of C < 0.5 %. The initial flow stress of a material can be drastically increased by work-hardening during cold forging, leading to strengths comparable to quenched and tempered Ck45. If a higher strength is necessary, alloyed steels, especially case-hardening steels are used, which are typically heat-treated after cold forging. **Table 2.4** shows an excerpt of steels typically used in the field of cold forging.

Table 2.4: Excerpt of cold forging steels (adapted from Lange et al., 2008)

| Naming (DIN ISO) | Strength in MPa | | | | Applications |
| | Annealed | | Cold-worked | | |
	σ_f	σ_m	σ_y	σ_m	
Case-hardening steels					
Ck15	280	400-450	500	600-700	Spindles
16MnCr5	340	420-500	500	650-750	Small gears
Heat-treatable steels					
Ck22	300	420-500	550	650-750	Moderately Loaded parts
Ck45	340	500-600	650	750-850	Engine parts
Low-alloyed heat-treatable steels					
40Mn4	350	600-750	550	700-800	Gears
42MnV7	350	650-800	650	800-950	Ball pins
Corrosion-resistant steels					
X10Cr13	450	600	600	750	
X5CrNi1810	220	550-700	600	800-900	

Among the non-ferrous metals, aluminium alloys are still most frequently applied in cold forging, especially in the scope of current weight reduction efforts for automotive applications (Hilleke and Baumgart, 2010).

Since cold extrusion is mainly used in the automatic or semi-automatic mass production, the preparation of the semi-finished parts is essential to reduce forming forces and enhance tool life. The preparation stages regard the shape, the dimensional tolerances, the microstructure as well as the surface properties (Lange et al., 2008). **Figure 2.8** illustrates the necessary preparation steps to ensure optimal billet properties for subsequent cold forging.

Figure 2.17: Billet preparation steps in cold forging (based on Lange et al., 2008**)**

In order to ensure high formability, the materials should have a low initial flow stress and high ductility. To achieve this, parts are commonly heat-treated before or in between cold forging steps to prescribe a certain microstructure or reduce work-hardening. In the case of steels, this is usually achieved by full annealing, where an initially lamellar pearlite is transformed into spherically shaped grains (Lange et al., 2008). Depending on the application, one can choose between soft annealing, normalization and stress relief annealing (Hoffmann et al., 2012). Due to the high costs resulting from heat treatments, the amount of heat treatment steps should be minimized (Lange, 1988).

Before extrusion, the workpieces are coated to improve the tribological conditions with the aim to maximize formability, save forming steps, improve form filling, reduce tool loads, reach good surface properties and in the case of steel, prevent pressure welding with the tools (Lange et al., 2008). In order to prepare the billet surface, numerous preparation steps are necessary for material removal, cleaning, degreasing, washing as well as mechanical and chemical descaling (Lange, 1988). When extruding steels, a permanent cohesion of lubricant and semi-finished part must be assured by applying a lubricant carrying layer (ICFG, 1991). For steels, the most frequently used carrying layer is zinc phosphate. However, in the last years dry-film coatings including polyolefin and acrylic polymers have gained acceptance as a result of their environmental benefits as well as the eased cleaning when compared to conventional zinc phosphate (Semiatin, 2005). The choice of the ideal lubricant generally depends on the expected contact pressure, surface expansion and the forming conditions. Traditionally used lubricants include soaps or molybdenum disulfide (MoS2) (Lange et al., 2008). By utilization of such lubricant systems, low friction coefficients in the range of $0.04 < \mu < 0.08$ can be achieved in cold forging (Hoffmann et al., 2012).

2.2.3 Material properties after cold forging

Metal forming leads to a significant alteration of the properties of the initial material. However, the influence of the manufacturing process on the material properties is rarely considered in the product design stage (Tekkaya et al., 2015) and only recently gains momentum. In this context, it is differentiated between microstructural properties, macroscopic material properties as well as the resulting product performance (**Table 2.5**).

Table 2.5: Differentiation between microstructural mechanisms, phenomenological material properties and resulting product performance

Microstructural properties	Material properties after cold forming	Product performance
• Dislocation density • Grain size & orientation • Lattice strain • Void volume fraction	• Flow stress • Residual stresses • Ductile damage	• Stiffness • Hardness • Static strength • Impact strength

The control of material properties during cold forging has been the focus of multiple investigations in the past, which are summarized in the following.

Work-hardening

Work-hardening (also strain-hardening or cold-working) is the increase of the strength observed in materials possessing crystal structures, caused by interactions between individual dislocations and dislocation groups with other dislocations and barriers. The number of dislocations increases with increasing plastic strain, which amplifies the before mentioned effects (Dieter, 1961). As large strains are achieved in cold forging processes, work-hardening has a major influence on the product properties of cold forged parts. Depending on the material and the extrusion ratio, work-hardening can increase the strength of a part in terms of its initial yield stress and ultimate tensile strength to more than thrice its initial value (Feldmann, 1959). If the parts are not heat-treated after cold forging, work-hardening can be beneficial. For some materials, work-hardening leads to a strength increase, comparable to that of subsequent quenching and tempering (Lange, 1988). For the same reason, work-hardening leads to an increase of tool loads and thus reduces tool life. Work-hardening can also be exploited to avoid the necessity of subsequent heat-treatment steps. **Figure 2.18** illustrates how different cold forging sequences to produce a screw lead to different flow stress distributions in the final part.

Schmoeckel (1973) showed by the example of the production of a safety-relevant hollow shaft, that work-hardening by cold forging can be exploited to reach a required strength of 650 MPa, without the necessity of subsequent heat-treatment processes. When a prevention of subsequent heat-treatment stages is desired with the aim of a time- and cost-optimization, the material choice must receive particular attention to guarantee the required strength of the final part (Schmoeckel, 1976).
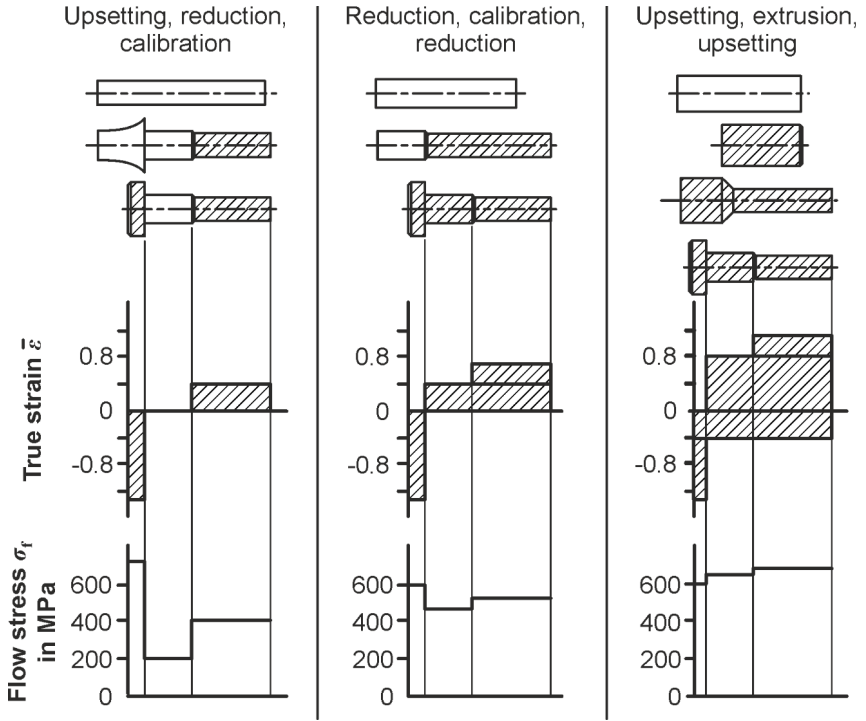
Figure 2.18: Influence of the cold forging sequence for the production of a screw on the resulting yield strength distribution (adapted from VDI 3171)

Scholtes et al. (1980) showed by the example of Ck45, that the Bauschinger effect leads to an introduction of a significant direction-dependence of work-hardening and noted that the ignorance of anisotropic hardening in cold forging processes must be compensated by the use of large safety margins in the product and process design.

Work-hardening has a direct impact on hardness, which can also be an important product property. Nehl (1983) illustrated the local work-hardening distribution by hardness measurements of cold extruded rods. The hardness increases along the central axis of the extrudates as the material is stretched axially. A similar increase can be observed over the radius as the material is increasingly sheared toward the surface. Based on results by Tabor (2000), Tekkaya and Lange (2000) have presented a procedure to obtain large strain flow curves by correlating hardness and flow stress values of forward extruded parts with a known local strain.

Residual stresses

Residual stresses are elastic stresses within a closed system, that is not subjected to external loads (Macherauch et al., 1973). The main origins of residual stresses are

- inhomogeneous elastic-plastic deformations and
- inhomogeneous temperature changes.

After inhomogeneous elastic-plastic deformations, unloading leads to inhomogeneous elastic springback. This is accompanied by internal stresses, referred to as residual stresses. Residual stresses can be differentiated by their spatial resolution. Macroscopic residual stress, called residual stresses of type I (σ^I), are homogenous over multiple grains. Macroscopic residual stress regions may exist over a cross-section and possess infinitesimal thickness. The forces and torques resulting from these residual stresses are in equilibrium over any arbitrary plane within the body. Any disruption of this equilibrium by external forces will necessarily lead to a shape change or geometric distortion (Peiter, 1966). Microscopic residual stresses are the sum of residual stresses of type II (σ^{II}) and type III (σ^{III}). The former are nearly homogenous over small material regions (single grains or grain clusters), latter exist on the level of the smallest material regions (multiple atom spacings). **Figure 2.19** illustrates the residual stress superposition considering three neighboring grains. Residual stresses of type I are always averaged over multiple grains, i. e. when the body subjected to residual stress is considered as continuum, only macroscopic residual stresses can be modelled per definition (Tekkaya, 1986). Residual stresses lead to an alteration of the product performance. For example, negative residual stresses near the surface of a part can increase the fatigue life of a component (Dieter, 1961).
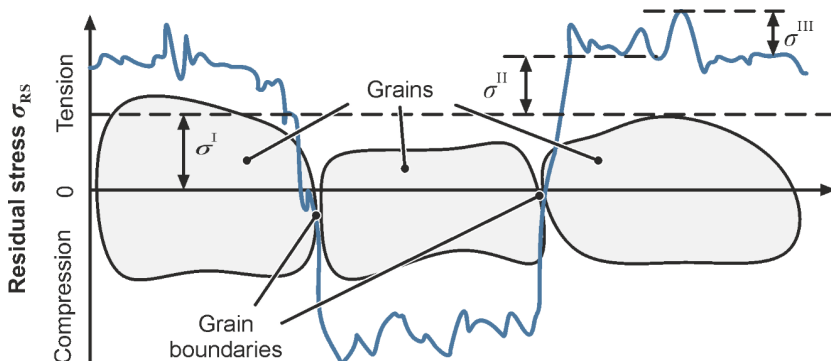
Figure 2.19: Residual stress superposition (adapted from Macherauch et al., 1973)

For brittle materials, residual stresses significantly alter the fracture behavior, as a superposition of external loads and residual stresses can lead to premature failure (Muster

and Hochhaus, 1983). Ductile steels are less affected by this, as any plastic deformation preceding fracture will lead to a residual stress relief (Macherauch et al., 1973). To reach a high quality of the produced part, residual stresses must be predicted and controlled. Most procedures to reach this are of mechanical or thermal nature. In the field of cold forging, it was shown by Tekkaya (1986) that a significant residual stress relaxation is achieved by relatively small plastic deformations. It was shown experimentally and numerically that part ejection after forward extrusion leads to a significant reduction of residual stresses (**Figure 2.20**). Similar observations were made for larger extrusion strains up to $\varepsilon_{ex} = 1.6$ by Zucko et al. (1997) who investigated the influence of the forward extrusion parameters on extruded parts made of C15 steel.
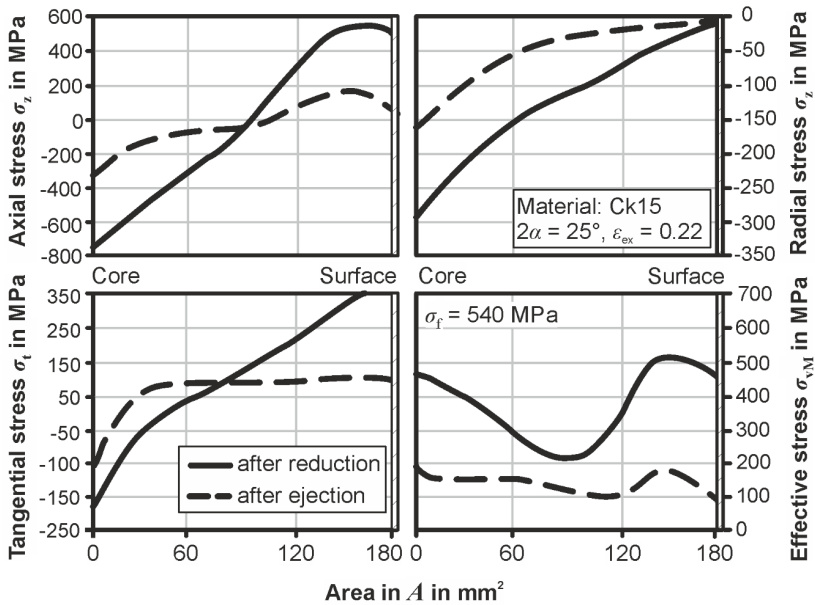
Figure 2.20: Numerically determined distribution of residual stresses in cold extruded parts, before and after part ejection (Tekkaya et al., 1985)

When cold forged parts are stress relief annealed, geometric distortion can occur (Berns, 1977). Geometric distortion is defined as the "change of shape and dimension of a workpiece caused by heat treatment". Volkmuth (1996) and Zoch (2006) named over 200 influencing factors on the intensity of workpiece distortion, appearing over the whole production chain, exceeding the process related factors arising from cold forging. However, the high residual stresses caused by cold forging were found to have a significant influence, making necessary the consideration of residual stresses in the design of cold forging processes to produce highly accurate parts.

Ductile damage and failure

The main defect mechanism in cold drawing and forward extrusion is the formation of Chevron cracks in the extrudate center. Numerous research efforts have been dedicated to the prediction and prevention of Chevron cracks, dating back to works by Jennison (1930), who pointed out the importance of the die design in wire drawing, to prevent central bursts and surface defects. Avitzur (1968) and Zimerman and Avitzur (1970) presented an analytical procedure based on admissible velocity fields, to consider the influence of reduction ratio, die angle and work-hardening on the likelihood of Chevron crack occurrence. The progress in numerical modelling of forming processes has allowed to consider the local stress and strain conditions in the forming zone and predict material failure with a high accuracy. Landgrebe (2000) showed that the process sequence in cold forging has a major impact on the damage accumulation and material failure in multi-stage cold forging. The most recent works on failure in cold forging have been conducted by Mcallen and Phelan (2005) for wire drawing of aluminium and Soyarslan et al. (2008) for forward rod extrusion of steel. Both research groups where able to correctly predict the number, location and shape of central burst defects.

Research on damage evolution and its effects on product performance of cold forged parts in terms of the nucleation, growth and coalescence of voids has just recently gained momentum. Tekkaya et al. (2017) showed that the extrusion ratio in cold extrusion, which prescribes the amount of hydrostatic stress in the forming zone, can lead to varying damage levels in the extrudates. Later, Hering and Tekkaya (2020) demonstrated that the die design in forward rod extrusion can be adapted to decrease the hydrostatic stress in the forming zone, and thus to control damage in terms of void volume, which has a considerable impact on the resulting performance of cold forged products e. g. in terms of the number of cycles to failure, impact energy and stiffness (**Figure 2.21**).
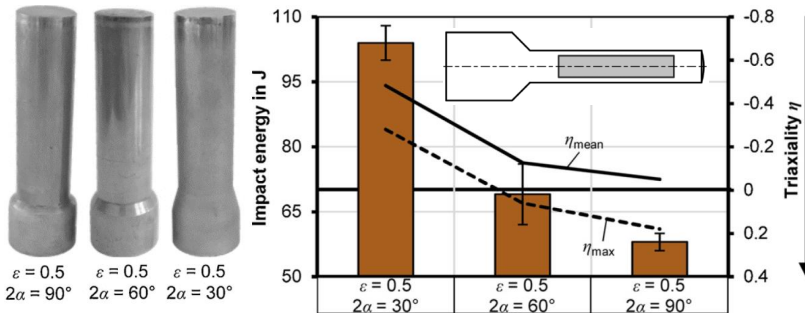
Figure 2.21: Influence of die angle in forward rod extrusion on the mean and maximum triaxiality (η_{mean} and η_{max}) in the forming zone and resulting impact energy at room temperature (Hering and Tekkaya, 2020)

2.2.4 Multi-stage and combined cold forging

A large variety of part geometries can be produced by cold forging. For parts of high geometric complexity, cold forging processes are oftentimes designed with multiple subsequent forming stages. **Figure 2.22** illustrates a variety of cold forged parts produced via different combinations of basic cold forging processes.

Figure 2.22: Parts produced by cold forging process combinations (Semiatin, 2005)

Figure 2.23 shows an example of a typical cold forging sequence to produce a tie rod casing. In between each individual forming stages, the surface of the intermediate parts are treated. Between upsetting and backward can extrusion, the part is also annealed, to reduce the work-hardening and increase the tool life in the subsequent forming stages.
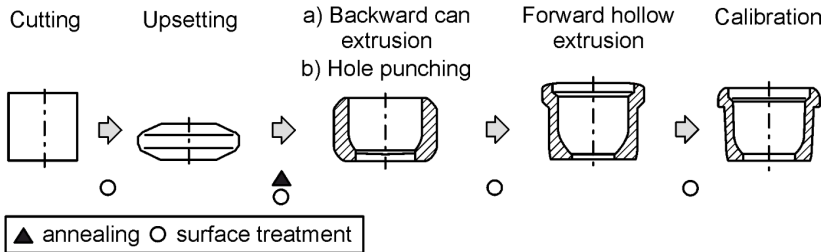
Figure 2.23: Cold forging and heat treatment sequence for the production of a tie rod casing (adapted from Lange, 1988, simplified illustration)

Before the establishment of numerical process simulation, process sequence design was a tedious iterative procedure, which required tremendous experience and costly experimental tryouts (Schmoeckel, 1973). While the advancements in the field of computational process design have reduced the necessary workload significantly, however, final process sequences are still well-kept company secrets. For the design of forming sequences, the flow stress and formability of the material play an important role to assure a cost-effective production with an adequate tool life (Feldmann, 1959).

In addition to cold forging sequences, basic cold forging processes can be combined in a single stage. **Figure 2.24** shows parts produced by different process combinations.

While in many combined processes the material is formed only once (**Figure 2.24a**), in some special cases some regions of workpiece are subjected to multiple forming stages and may undergo strain path reversals (**Figure 2.24b**).
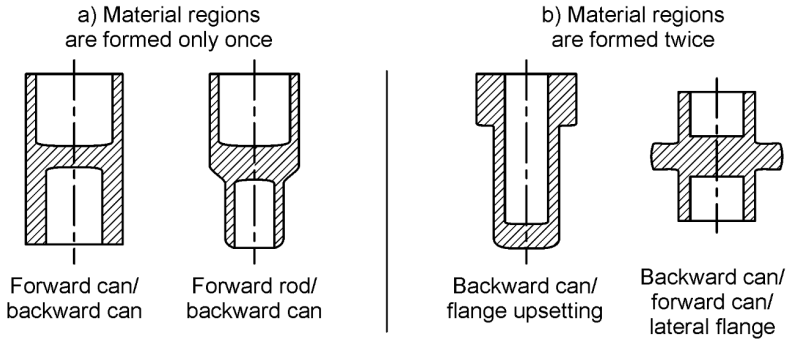
Figure 2.24: Cold forging process combinations (adapted from Lange, 1988)

Based on the state of knowledge on the influence of anisotropic hardening in sheet and incremental metal forming processes presented in the previous section, the frequent application of multi-stage cold forging sequences raises the question on the influence of anisotropic hardening in cold forging especially for parts which undergo strain path reversals. A prominent example of a cold forging sequence including an intrinsic strain path reversal, which affects a large region of the workpiece, is the production of trisphere joints (or ball spiders) by cold forging (**Figure 2.25a**). To produce a trisphere, the material is first extruded laterally into a closed cavity, which is directly followed by upsetting (Lange, 1988).
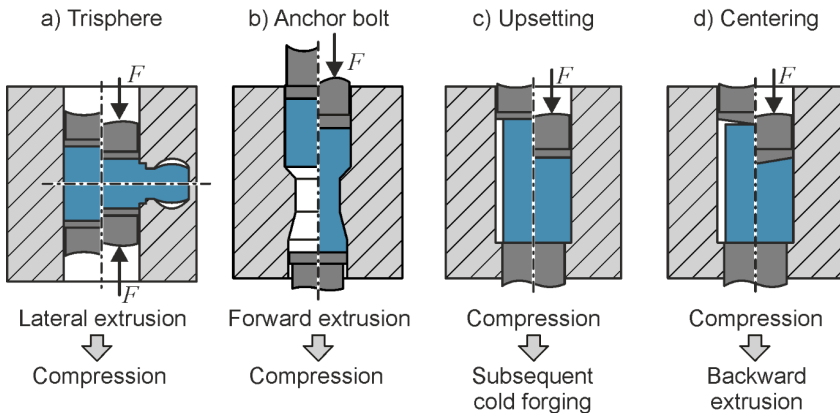
Figure 2.25: Cold forging processes which include strain path reversals (Sources: a) Lange, 1988; b) Ningbo Anchors, 2021, c) & d) Lange et al., 2008)

Another example of a forging sequence which includes an intrinsic strain path reversal is the production of anchor bolt precursors by forward rod extrusion directly followed by upsetting within an enclosed die (**Figure 2.25b**) (Ningbo Anchors, 2021). Shearing of workpieces from bars can lead to significant angularity of the cut surface. To restore parallel end faces, parts are frequently upset in a closed container before the actual cold forging stages. In addition to this, wires with a small diameter are oftentimes processed by upsetting, which leads to an increase of the initial diameter (**Figure 2.25c**). Workpiece centering is another application of initial upsetting, which is applied to prevent a punch deflection and fracture in subsequent backward can extrusion (**Figure 2.25d**) (Lange et al., 2008). If cold forged parts are processed in any of these ways, subsequent cold forging stages will introduce a significant strain path reversal.

2.2.5   Anisotropic hardening in cold forging

Publications on the influence of anisotropic hardening in bulk forming are rare and focus mainly on the application of pre-drawn wire in subsequent forming. Tozawa and Kojima (1971) conducted cold heading tests on three different steels that were pre-drawn at different drawing angles and reduction ratios. They found that higher reduction ratios lead to an increasing region of work-hardening stagnation, which leads to an increased upsetting limit in subsequent cold heading. Havranek (1984) showed that pre-drawing leads the two investigated steels AISI K1020 and AISI K1040 to exhibit work-hardening stagnation and permanent softening under subsequent cold heading, causing the required forming work to be lower than that of spheroidized material. Miki and Toda (1988) investigated the evolution of anisotropic hardening in the process sequences of drawing and upsetting and drawing and forward rod extrusion. They found, that the manifestation of the Bauschinger effect depends strongly on the strain path, which can have a significant impact on the flow stress and must consequently considered for an accurate tool life prediction. Ma (2007) showed that consideration of the Bauschinger effect in cold heading simulations leads to a significant improvement of formability predictions.

Tekkaya (1986) named the neglection of the Bauschinger effect as one possible source for the deviations in numerically and experimentally observed residual stresses in cold extruded shafts. Suh et al. (1991) investigated the influence of kinematic hardening on the residual stress evolution during forward rod extrusion using a simple kinematic hardening model with generic material parameters. They supported Tekkaya's assumption, that the residual stresses in forward extruded parts can only be simulated correctly if the Bauschinger effect is considered in the forming simulations.

Narita et al. (2016) compared different process sequences for the production of cold forged bolts made of the corrosion-resistant steel SUS304 (**Figure 2.26a**). They showed that the strength of the finished bolt under tension and the residual stress distribution depend on the process sequence which they attributed to the differences in the strain paths and the evolution of anisotropic hardening. The assumption of isotropic hardening

has led to a significant overestimation of the bolt strength, which could be improved by the use of the Yoshida-Uemori kinematic hardening model (**Figure 2.26b**).
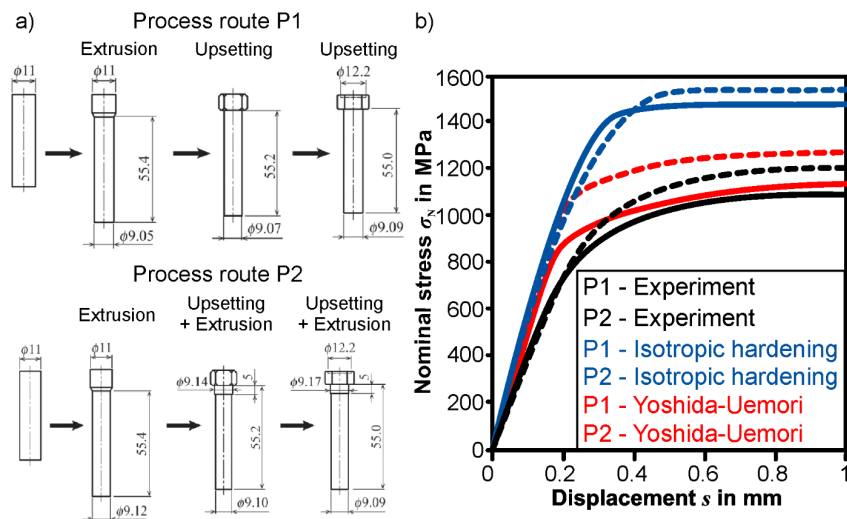
Figure 2.26: a) Investigated process routes for the production of cold forged SUS304 bolts, b) Numerically obtained stress-strain curves of cold forged bolts and comparison with experiments (based on Narita et al., 2016)

Narita et al. (2017) investigated if anisotropic hardening has an effect on the diameter change of forward extruded rods after die springback and after ejection, finding no note-worthy deviations between isotropic and kinematic hardening models.

Galdos et al. (2019a) analyzed the influence of anisotropic hardening on the evolution of residual stresses in the production of ball pins by cold forging. They modelled the cyclic plastic material behavior by means of the Chaboche and Lemaítre (1990) harden-ing model and observed that the material flow is only weakly affected by the anisotropic hardening. As most material regions are only formed once in the production of ball pins they did neither observe an influence on residual stresses nor on the resulting process forces, however, the authors did not consider part ejection, which is known to alter the residual stress distribution significantly (Tekkaya et al., 1985).

2.3 Summary

In the numerical design of metal forming processes, a comprehensive knowledge of the elastic-plastic material behavior of the part is of utmost importance. In the production of complex parts via metal forming processes, the material can undergo complex non-monotonic or non-proportional strain paths including complete strain path reversals or cross-loading sequences. Under such strain paths, anisotropic work-hardening phenomena are exhibited, which can have a significant effect on forming forces, tool loads and component properties. Anisotropic hardening phenomena include the well-known Bauschinger effect, i. e. premature re-yielding, a smooth transition from the elastic- to the elastic-plastic region, work-hardening stagnation and permanent softening. The origins of these phenomena is based mainly on the generation of short- and long-range residual stresses and the polarization of dislocation structures upon plastic deformation.

While the consequences of anisotropic hardening are well known and understood in the field of sheet metal forming, no comprehensive investigations exists on their influence in bulk metal forming processes. As a comparison, the scientific publication data base *Web of Science* lists nearly 500 publications under the keyphrases "anisotropic hardening sheet metal forming", whereas the keyphrases "anisotropic hardening bulk metal forming / cold forging" yields less than 15 publications (as of September 20th, 2021). The literature review suggests that the ignorance of anisotropic work-hardening in cold forging may lead to a flawed prediction of tool loads, forming forces and component properties. For parts that are not heat-treated after cold forging, strain path reversals trigger a tension-compression anisotropy, which is not conventionally considered in the design of cold forged parts or the process sequence design.

A possible reason for the ignorance of anisotropic hardening in cold forging may be the lack of suitable experimental characterization methods to obtain data on the intensity of work-hardening phenomena exhibited after strain path reversals under cold forging conditions, mainly due to the restrictions regarding the achievable pre-strains and total strains. In this context, interrupted procedures, in which large pre-strains are generated before the actual testing, are promising to obtain the corresponding experimental data. Additionally, constitutive material models that allow for a consideration of all relevant anisotropic hardening effects must yet be validated and optimized for their application in bulk metal forming simulations with the aim of an optimized prediction of material properties like work-hardening and residual stresses or forming forces and tool loads in single and multi-stage cold forging processes.

3 Aim and scope

The state-of-the-art shows that anisotropic hardening and, most prominently the Bauschinger effect, can have a significant influence on the outcome of a metal forming process. This includes the process forces as well as product properties in terms of work-hardening and residual stresses. Up to now, the majority of publications on the influence of anisotropic hardening were focused on the field of sheet metal forming and incremental forming processes: In sheet metal forming anisotropic hardening and especially the Bauschinger effect as described by kinematic hardening has been shown to have a major impact on spring back, whereas in incremental metal forming, it was observed that process forces are highly affected by frequent strain path reversals as the material exhibits permanent softening.

In the field of cold forging only few publications exist so far regarding the influence of anisotropic hardening on process forces and component properties. The aim of this work is the analysis and assessment of the influence of the material behavior under non proportional strain path changes in cold forging processes focusing on strain path reversals. The goals and structure of this work are illustrated in **Figure 3.1** and described in the following.
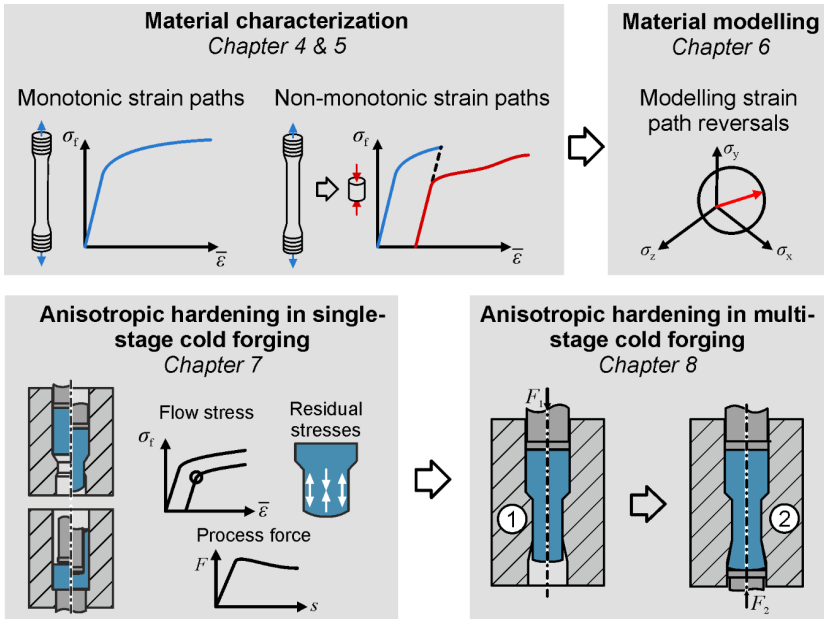
Figure 3.1: Procedure to assess the influence of strain path reversals in cold forging

In **Chapter 4** new experimental methods are presented to characterize the work-hardening behavior of metals under monotonic (proportional) strain paths up to large strains. For this, continuous procedures as well as interrupted procedures are applied. The methods are conducted on three typical cold forging steels with different anisotropic hardening behaviors as well as one aluminum alloy.

Up to now, there exist no standardized experimental methods to characterize the anisotropic hardening behavior at large pre-strains. In addition to this, conventional methods are highly limited with regard to the achievable pre-strains due to structural instabilities of the specimens under the subjected loads. In **Chapter 5**, the experimental methods presented in Chapter 4 are extended to capture the material behavior under non-monotonic strain paths with a focus on full strain path reversals. For this, conventional and new characterization methods are utilized to characterize and quantify the intensity of strain path reversal effects including the Bauschinger effect, work-hardening stagnation, and permanent softening with respect to the pre-strain over a large strain regime.

Chapter 6 deals with the assessment of numerical constitutive models that include all facets of the material behavior observed in the characterization in the preceding chapters. Constitutive models of varying degrees of complexity are selected, implemented and adapted according to the actual material behavior. The parameters of each model are determined by means of an inverse parameter identification procedure and the models are validated with respect to their capability to capture anisotropic hardening of 16MnCrS5 over a large pre-strain regime.

In **Chapter 7** the material models are utilized and compared by conducting cold forging simulations of basic single-stage cold forging processes, to assess the influence of anisotropic hardening on process forces as well as the resulting part properties with regard to flow stress and forming-induced residual stresses.

Chapter 8 is focused on the influence of anisotropic hardening in combined and multi-stage cold forging processes. Three multi-stage cold forging sequences are investigated in this scope. The new knowledge is utilized to derive methods to prevent negative influences of strain path reversal effects on the product properties or to exploit the material behavior exhibited under strain path reversals, e. g. exploitation of permanent softening by pre-compression targeting a reduction of process forces in subsequent cold forging. As a large fraction of cold forged parts are heat-treated between and after individual cold forging stages, the influence of typical heat-treatments on the anisotropic work-hardening is discussed.

Lastly, in **Chapter 9**, the new knowledge of the thesis is summarized and directions for future research topics in the field of anisotropic hardening in cold forging are given.

4 Work-hardening behavior under monotonic strain paths

In this chapter, the material characterization procedures are presented and discussed to quantify the large strain monotonic work-hardening behavior of metals. The characterization procedures are applied to three typical cold forging steels and one aluminum alloy. As a reference, the flow curve of the investigated materials was determined under proportional loading by means of conventional tensile and upsetting tests (**Figure 4.1a** and **b**). To identify the influence of the stress state on the flow stress, the plastic material behavior was further characterized under monotonic shearing by means of torsion tests on round bars (**Figure 4.1c**) and in-plane torsion tests on thin sheet specimens extracted from the as-received steel bars (**Figure 4.1d**). Since the achievable strains are highly limited in conventional characterization methods, a new interrupted procedure is presented and discussed in which specimens with a known pre-strain are produced by forward rod extrusion and subsequently tested under uniaxial tension (**Figure 4.1e**). The new method is first analyzed analytically and numerically and the resulting procedure to generate flow curves for high strains are presented and compared to the flow curves generated by conventional characterization approaches.
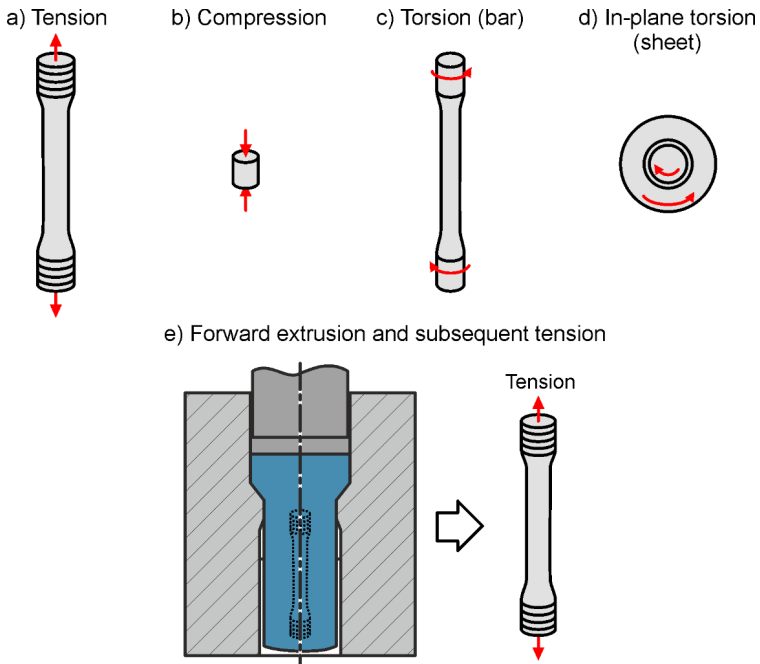
Figure 4.1: Applied methods to characterize the materials under monotonic loading

4.1 Investigated materials

Three steels were investigated in the scope of this thesis: The case-hardening steel DIN 16MnCrS5 (1.7139), that finds regular application in the field of cold forging of highly loaded parts like gear shafts, the lower strength case-hardening steel DIN C15 (1.0401), and DIN 100Cr6 (1.3505), which is mainly used as a rolling bearing steel. The measured chemical composition of the three investigated steels are shown in **Table 4.1**.

Table 4.1: Investigated steels

| Steel grade | | Chemical composition (mass-%) | | | | | | | Heat- |
DIN	EN	C	Si	Mn	P	S	Cr	Mo	treatment
16MnCrS5	1.7139	0.152	0.172	1.194	0.013	0.027	1.040	0.042	Ferrite-pearl-ite annealed
C15	1.0401	0.153	0.231	0.570	0.123	0.018	0.093	0.036	Ferrite-pearl-ite annealed
100Cr6	1.3505	0.967	0.178	0.351	0.009	0.017	1.478	0.019	Quenched & tempered

All three steels were present in the form of bars, with 16MnCrS5 having a diameter of 40 mm and C15 and 100Cr6 having a diameter of 30 mm. The materials were selected with the intention to achieve a broad range of different anisotropic work-hardening behaviors. **Figure 4.2** shows the micro-structure of the three investigated steels in longitudinal and transverse direction.
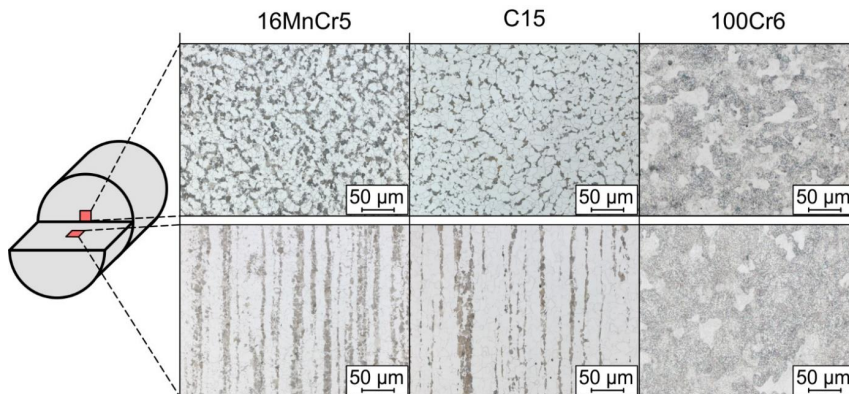
Figure 4.2: Grain-structure of the three investigated steels grades

In the industrial practice of cold forging, aluminum alloys gain increasing attention due to their special density-to-strength ratio. Consequently, the common aluminum alloy AA6060 was investigated in the scope of this thesis. The chemical composition ranges of AA6060 according to DIN EN 573-3 are summarized in **Table 4.2**.

Table 4.2: Chemical composition of AA6060 aluminium alloy (DIN EN 573-3)

Mg	Si	Fe	Cr	Cu	Mn	Ti	Zn	Other
0.35 – 0.5	0.3 – 0.6	0.1 – 0.3	< 0.05	< 0.1	0.1	< 0.1	< 0.15	< 0.15

The aluminium alloy AA6060 was present in the form of hot extruded bars with a diameter of 30 mm. The aluminium was present in the T6-state (peak-aged).

4.2   Characterization via conventional methods

4.2.1   Tensile and upsetting tests

The investigated steels were tested under monotonic tensile and compressive loading utilizing conventional tensile and upsetting tests. Tensile and upsetting test specimens were extracted from the center of bars by turning according to **Figure 4.3**.
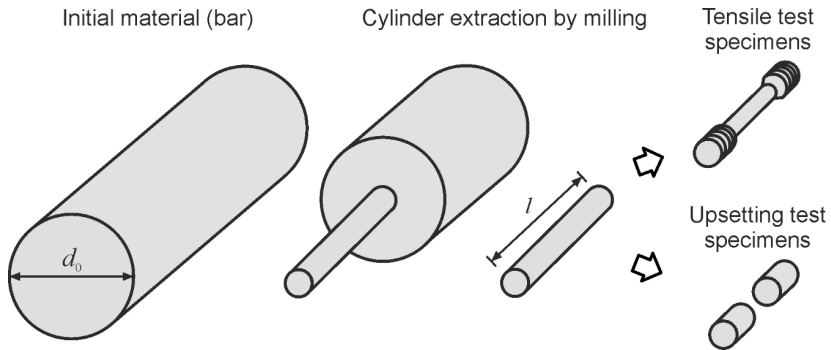
Figure 4.3: Extraction of tensile and upsetting test specimens from round bars

The tensile test specimens were produced according to DIN 50125 (specimen type B) with a diameter of 8 mm (**Figure 4.4a**). The cylindrical test specimens were produced according to DIN 50106 with a height of $h_0 = 12$ mm and the diameter as $d_0 = 8$ mm (**Figure 4.4b**). A Zwick/Roell universal testing machine with a maximum force of 250 kN was utilized for all tests.

Tensile tests were conducted according to DIN EN ISO 6892-1. The strain was measured directly at the specimens by means of tactile frictional strain gauges with an initial gauge length of 40 mm. The upsetting tests were performed according to DIN 50106. To reduce friction and delay buckling, the contacting surfaces between the specimens and dies were cleaned and lubricated with Teflon spray before each test. To account for the significant elastic deflections of the test setup under compressive loading, a correction curve was recorded prior to the upsetting. For this, the dies were pressed together and the elastic deflection in terms of crossbeam travel was measured and recorded over

the corresponding force up to the maximum force of 250 kN. To account for settling effects this procedure was repeated until no significant deviations could be observed between each individual curve. The measured deflection curve was considered inline during the actual upsetting tests, in order to correct the measured stroke by the deflection corresponding to the current force.
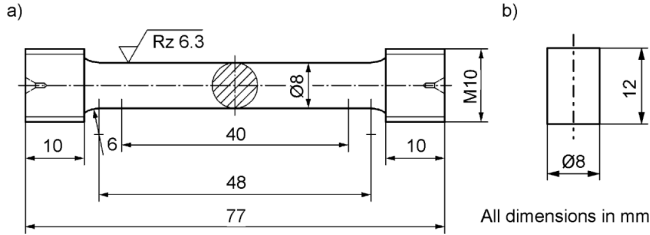
Figure 4.4: a) Tensile test specimens according to DIN 50125, b) upsetting test specimens according to DIN 50106

If not mentioned differently, both tensile and upsetting tests were performed at room temperature and at a constant strain rate of $\dot{\bar{\varepsilon}} = 0.0067$ 1/s. The testing setups for tension and compression are shown in **Figure 4.5a** and **Figure 4.5b**, respectively.
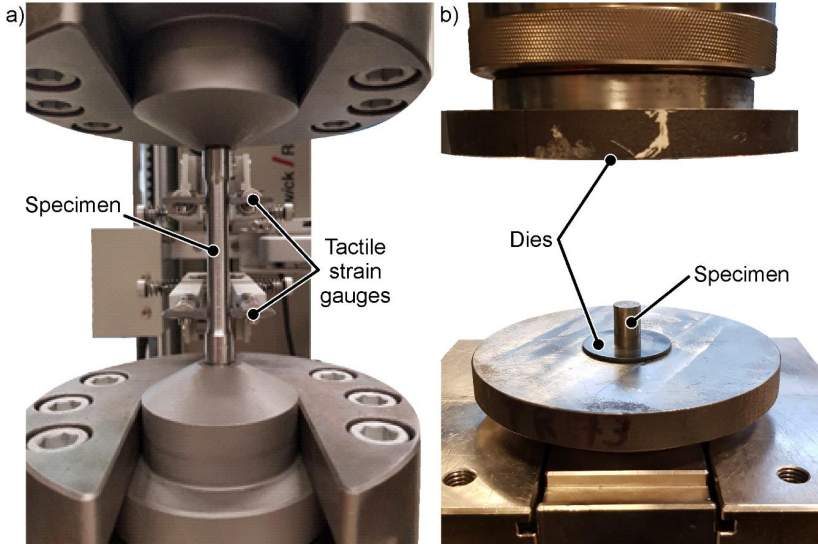
Figure 4.5: Test setups: a) uniaxial tensile test and b) upsetting test

Each test was repeated at least three times. All measured force-stroke curves obtained by tensile or compression tests were averaged. For this, all neighboring data points of a

curve were linearly interpolated, and the interpolated data was evaluated for 1000 pre-defined x-increments shared by each curve. For each x-increment, the mean value as well as the standard deviation of the measured force was determined.

To determine the influence of the strain rate on the resulting work-hardening behavior, tensile tests have been conducted at different strain rates. To maximize the achievable strain rates, some tests have been conducted with a lower gauge length of 20 mm. The highest reached strain rates amounted to $\dot{\varepsilon} = 0.2$ 1/s.

4.2.2 Torsion of cylindrical specimens

Torsion tests on cylindrical specimens were conducted to determine the flow curve of the investigated materials under shear loading. The parameter definitions in torsion testing are shown in **Figure 4.6**.

l	Gauge length
R	Specimen diameter
r	Radius at which the flow stress is evaluated
α	Shear angle at r
θ	Twisting angle
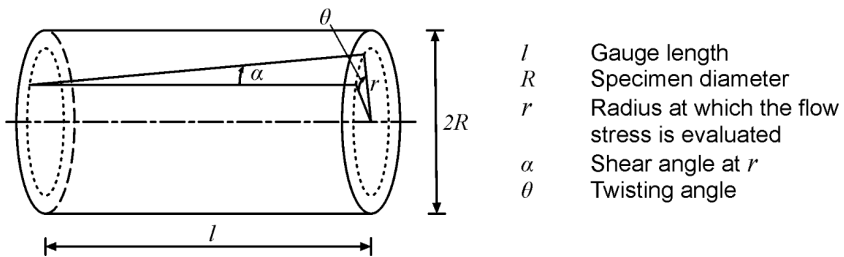
Figure 4.6: Parameters in the torsion test of cylindrical specimens (Pöhlandt et al., 1983)

In contrast to tensile and compression testing, calculation of stress-strain data from measured data in torsion is not a straightforward process. This is mainly due the inhomogeneous stress and strain distribution over the specimen radius. In the literature, various methods have been proposed to deal with this challenge. Two different approaches were applied to obtain flow curves by torsion on cylindrical specimens:

- Method by Fields and Backofen (1957)
- Method by Pöhlandt et al. (1983)

In the method by Fields and Backofen (1957) both stress and strain are evaluated at the specimen surface, where the shear strain γ_R is calculated as

$$\gamma(r = R) = \gamma_R = \frac{R \cdot \theta}{l}. \tag{4.1}$$

Herein, R is the outer radius of the torsion specimen, θ is the twisting angle in radians, and l is the length of the plasticized region. Assuming the von Mises flow criterion the flow stress can be calculated from the twisting angle and torque data as

$$\sigma_f = \frac{\sqrt{3}}{2\pi R^3}\left(3M + \gamma_R \frac{\delta M}{\delta \gamma_R} + \dot{\gamma}_R \frac{\delta M}{\delta \dot{\gamma}_R}\right),$$ (4.2)

where $\dot{\gamma}_R$ is the shear strain rate at the surface ($r = R$) and M is the torque. The main challenge in this formulation is that the surface region of the specimen is highly affected by notch effects and the presence of the partial differential terms is unfavorable regarding error propagation. To overcome these drawbacks, Pöhlandt et al. (1983) presented a method, in which the flow stress is evaluated at a critical inner radius of $r^* = \frac{3}{4} R$, at which the shear stress depends only weakly on the slope of the flow curve. In addition, the stress and strain at this inner radius are nearly independent of notch effects. The flow stress can be calculated according to

$$\sigma_f = \frac{\sqrt{3}M}{2\pi R^3} \cdot \left(\frac{3 + p_0}{e^{p_0/(3+p_0)}}\right).$$ (4.3)

The parameter p_0 represents the sum of the initial hardening exponent n_0 and the strain rate sensitivity m_0 according to the hardening relation

$$\sigma_f(\bar{\varepsilon}, \dot{\bar{\varepsilon}}) = C \cdot \bar{\varepsilon}^n \cdot \dot{\bar{\varepsilon}}^m.$$ (4.4)

By insertion of an approximated realistic value of p_0 into Eq. (4.3), the flow stress can be evaluated. It is noted that Eq. (4.3) depends only weakly on p_0. In the present case it is assumed that $p_0 = 0.3$.

An electro-mechanical axial-torsional testing system by the company walter+bai LFM was used to perform the torsion tests. The testing machine has a maximum torque of 200 Nm and an operation twisting angle range of $\pm 270°$. The twisting angle and torque was recorded throughout the test and exported into an ASCII file. The utilized tensile test specimen geometry is shown in **Figure 4.7**.
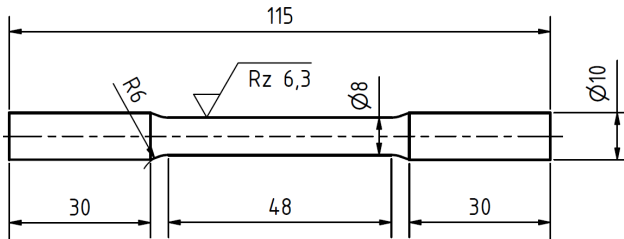
Figure 4.7: Specimen geometry for torsion tests according to DIN 50125

The twisting rate was set to a low value of $\dot{\theta} = 2$ °/s, representing near quasi-static loading, to rule out any strain rate related effects. According to the relation

$$\dot{\gamma}_R = \frac{R \cdot \dot{\theta}}{l}$$ (4.5)

this corresponds to a shear strain rate at the surface of the specimen of $\dot{\gamma}_R = 0.006$ s^{-1} ($\dot{\bar{\varepsilon}} = 0.003$ s^{-1}). Due to the low strain rate, the strain rate term in Eq. (4.2) was approximated as zero. The specimens were twisted up to the maximum possible total twisting angle of 540°, which corresponds to an effective strain of $\bar{\varepsilon} = 0.4$ ("Backofen method") and $\bar{\varepsilon} = 0.35$ ("Pöhland method"). Each test was repeated at least five times. The measured torque-angle curves were averaged over each corresponding data set. To identify regions of strain localization, all specimens were marked with a vertical line, which was controlled during and after testing.

4.3 Characterization via new methods

The achievable strains are highly limited in conventional material testing methods. To overcome these limits two new approaches were derived and assessed. The first idea is the production of pre-strained specimens by forward rod extrusion and the subsequent tensile testing of said specimens, which possess a very large known strain that can be determined analytically. The second new approach is the utilization of the in-plane torsion test of sheet specimens extracted from as-received steel bars. In the following the two methods are described in detail.

4.3.1 Tensile tests on forward extruded material

The idea is to produce pre-strained specimens by forward rod extrusion, where in the core of the produced parts, there exists a known pre-strain. The subsequent extraction and testing of specimens is expected to reveal the flow stress of the pre-strained material. For the presented procedure to generate reliable results the following requirements must be fulfilled:

- The stress state in terms of deviatoric stress in the forming zone must equal the deviatoric stress of the subsequent testing method.
- The strain distribution over the specimen radius must be known.
- The strain distribution must be uniformly distributed along the central axis to prevent stress concentrations in subsequent testing of the extracted specimens.
- An influence of residual stresses in the produced specimens must be ruled out.
- Possible influences of the change in conditions between forward rod extrusion and subsequent testing of specimens on the flow stress must be ruled out. This includes the change in pressure, temperature, strain rate and strain aging effects.

In the following, each of these requirements is addressed individually by means of analytical and numerical investigations. Experimental details regarding the production of specimens by forward rod extrusion are given in **Appendix A**.

Analytical description of the stress state in forward rod extrusion

To determine the stress state evolution in forward rod extrusion an infinitesimal volume element dV travelling along the central axis through the forming zone is considered according to **Figure 4.8**. By defining the coordinates in the forming zone accordingly and considering that no shear stresses exist on the central axis of the extrudate, the components of the strain increments $d\varepsilon_{ij}$ read (cylinder coordinates):

$$d\varepsilon_{ij} = \begin{pmatrix} d\varepsilon_r & 0 & 0 \\ 0 & d\varepsilon_\theta & 0 \\ 0 & 0 & d\varepsilon_z \end{pmatrix}. \tag{4.6}$$

From axisymmetry it follows further, that the strain increments in radial and circumferential direction must be equal ($d\varepsilon_r = d\varepsilon_\theta$).
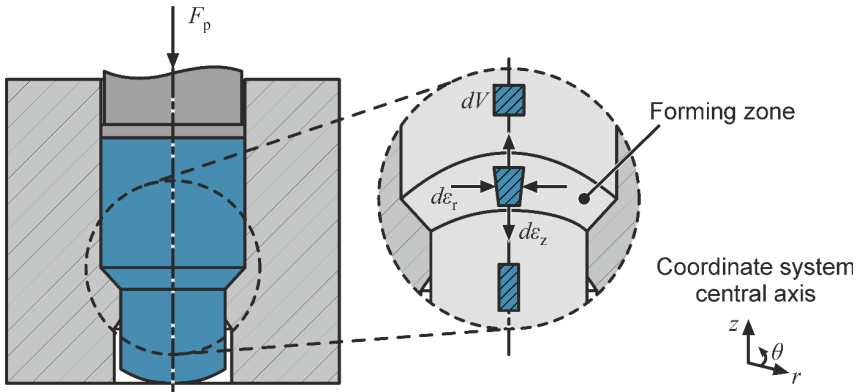
Figure 4.8: Schematic of the strain history of an infinitesimal area element dA moving through the forming zone in forward rod extrusion

The infinitesimal volume element dV is contracted radially and tangentially when moving through the forming zone (i. e. $d\varepsilon_r = d\varepsilon_\theta < 0$). The volume constancy of plastic deformations prescribes that the sum of the normal strain increments must vanish ($\sum d\varepsilon_{ii} = 0$), thus it follows that $d\varepsilon_z = -2d\varepsilon_r$ and

$$d\varepsilon_{ij} = d\varepsilon_r \begin{pmatrix} -1 & 0 & 0 \\ 0 & -1 & 0 \\ 0 & 0 & 2 \end{pmatrix}. \tag{4.7}$$

Eq. (4.7) can be reorganized in terms of the principal strains $\varepsilon_{I/II/III}$ according to

$$(d\varepsilon)_{ij} = d\varepsilon_r \begin{pmatrix} 2 & 0 & 0 \\ 0 & -1 & 0 \\ 0 & 0 & -1 \end{pmatrix}. \tag{4.8}$$

The components of the stress tensor within the volume element dV then read

$$(\sigma)_{ij} = \begin{pmatrix} \sigma_z & 0 & 0 \\ 0 & \sigma_r & 0 \\ 0 & 0 & \sigma_\theta \end{pmatrix} = \begin{pmatrix} \sigma_z & 0 & 0 \\ 0 & \sigma_r & 0 \\ 0 & 0 & \sigma_r \end{pmatrix}. \tag{4.9}$$

The stress tensor can be subdivided into its deviatoric and hydrostatic parts $\boldsymbol{\sigma'}$ and $\boldsymbol{\sigma^h} = \sigma^h \boldsymbol{I}$, respectively. From Eq. (4.9) it follows for the hydrostatic stress that

$$\sigma^h = \frac{1}{3}(\sigma_z + 2\sigma_r) \tag{4.10}$$

Lastly, by subtracting the mean stress from the total stress tensor it follows for the deviatoric stress components:

$$(\sigma')_{ij} = \frac{1}{3}(\sigma_z - \sigma_r) \begin{pmatrix} 2 & 0 & 0 \\ 0 & -1 & 0 \\ 0 & 0 & -1 \end{pmatrix}. \tag{4.11}$$

By considering the Levy-Mises flow rule ($d\bar{\varepsilon}_{ij} = d\lambda \cdot (\sigma')_{ij}$) the chosen order of stress components in Eq. (4.6) is validated. Considering an isotropic flow condition, the kinematically necessary absence of shear stresses along the central axis leads to

$$\sigma_f = (\sigma_z - \sigma_r). \tag{4.12}$$

It follows for the hydrostatic and deviatoric stress components:

$$\sigma^h = \frac{\sigma_f}{3} + \sigma_r \tag{4.13}$$

$$(\sigma')_{ij} = \frac{1}{3} \cdot \sigma_f \cdot \begin{pmatrix} 2 & 0 & 0 \\ 0 & -1 & 0 \\ 0 & 0 & -1 \end{pmatrix}. \tag{4.14}$$

In a uniaxial tensile test of a round bar, the stress state can be simply described by

$$(\sigma)_{ij} = \begin{pmatrix} \sigma_z & 0 & 0 \\ 0 & 0 & 0 \\ 0 & 0 & 0 \end{pmatrix}. \tag{4.15}$$

Herein, the stress tensor is already sorted according to the principal stresses. With $\sigma_z = \sigma_f$ it follows for the hydrostatic and deviatoric stress components that

$$\sigma^h = \frac{\sigma_f}{3} \tag{4.16}$$

$$(\sigma')_{ij} = \frac{1}{3} \cdot \sigma_f \cdot \begin{pmatrix} 2 & 0 & 0 \\ 0 & -1 & 0 \\ 0 & 0 & -1 \end{pmatrix} \tag{4.17}$$

Counterintuitively, the deviatoric stresses in a uniaxial tensile test (**Table 4.3**) and in the forming zone during forward extrusion are equal. The only difference lies in the hydrostatic stress, which is superposed by the radial stress σ_r.

Table 4.3: Comparison of stress states during uniaxial tensile loading and the stress
state along the central axis of forward rod extrusion

	Deviatoric stress	Hydrostatic stress
Tensile test	$(\sigma')_{ij} = \dfrac{1}{3} \cdot \sigma_f \cdot \begin{pmatrix} 2 & 0 & 0 \\ 0 & -1 & 0 \\ 0 & 0 & -1 \end{pmatrix}$	$\sigma^h = \dfrac{\sigma_f}{3}$
Forward rod extrusion (central axis)	$(\sigma')_{ij} = \dfrac{1}{3} \cdot \sigma_f \cdot \begin{pmatrix} 2 & 0 & 0 \\ 0 & -1 & 0 \\ 0 & 0 & -1 \end{pmatrix}$	$\sigma^h = \dfrac{\sigma_f}{3} + \sigma_r$

The radial stress σ_r depends on the material's hardening behavior as well as the extrusion parameters. For typical extrusion strains ($\varepsilon_{ex} > 0.5$), the hydrostatic pressure is negative and has a large magnitude. This leads to a suppression of material defects which allows forward rod extrusion to generate large strains without the occurrence of material failure. However, for materials exhibiting little work-hardening, the use of low extrusion ratios and high die angles can lead to low hydrostatic pressure or even positive hydrostatic stresses, causing the occurrence of Chevron cracks, as reported by Avitzur (1968). As the main goal of the proposed method is to characterize the plastic behavior for large strains, the possible occurrence of Chevron cracks plays only a minor role.

Strain distribution over extrudate radius

As the material flow is delayed in the region of the die shoulders the material is subjected to shear strains. This must be considered for the specimen extraction, as any extracted geometry with a finite radial dimension will contain such sheared regions. The amount of shear strain is generally unknown and depends on a variety of material and process dependent parameters. To minimize the error that originates from the unknown shear strain distribution, the diameter of the extracted specimens should be significantly smaller than the extrudate diameter.

To determine the strain inhomogeneity over the specimen radius forward extrusion simulations have been conducted in *Abaqus Standard*. Detailed descriptions regarding the numerical model setup can be found in **Appendix B**. The effective strain distributions are shown for various extrusion strains (**Figure 4.9**). The results are plotted over the squared radius r^2, as the influence of work-hardening in subsequent tensile testing acts on the corresponding cross-section. Along the central axis, the calculated strain nearly equals the theoretical strain. Small deviations are connected to the additional strain achieved during initial upsetting, which is added to the effective strain after extrusion. The remaining deviations are related to the differences of the elastic deflections of the container and the die.
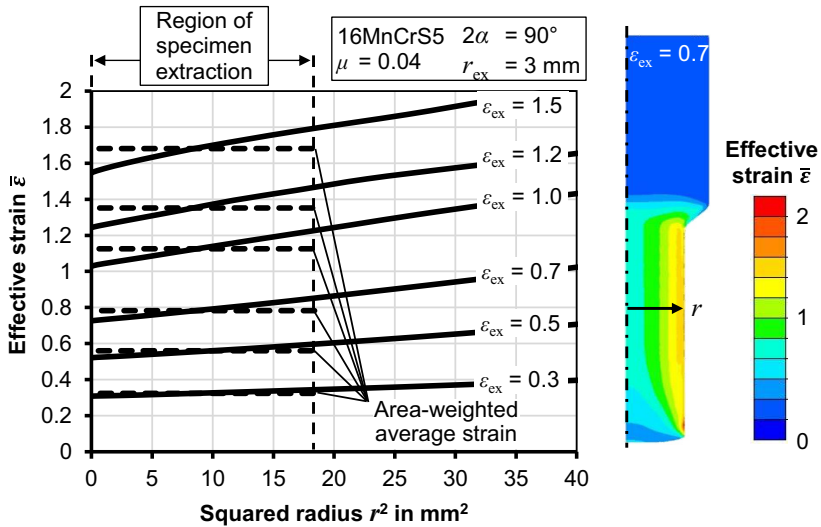
Figure 4.9: Strain distribution over the shaft radius for various extrusion strains

The difference between the area-weighted average strain and the extrusion strain was determined numerically for a specimen with a diameter of $D = 8$ mm (**Figure 4.10**).
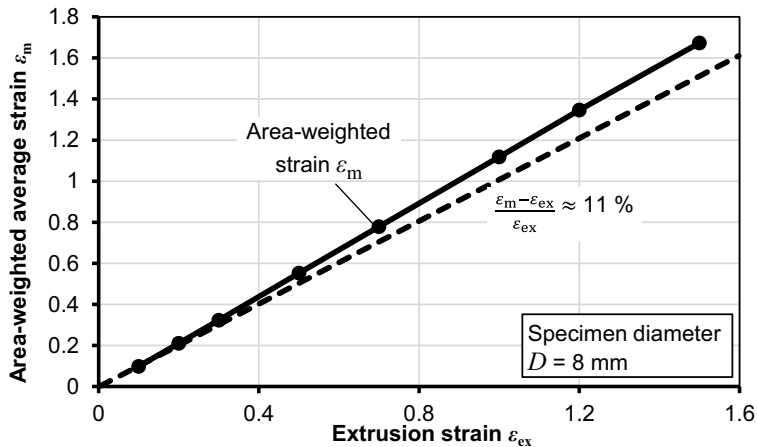
Figure 4.10: Area-weighted average strain and the theoretical (extrusion) strain

The area-weighted average strain is linearly connected to the extrusion strain. For the specimen diameter of $D = 8$ mm, the area-weighted average strain supersedes the extrusion strain by about 11 % over the entire investigated strain range.

To quantify the error associated with considering the area-weighted average strain as the overall effective strain within an extracted test specimen with a diameter of $D = 2R$, geometrical parameters and strain measures were defined according to **Figure 4.11**.
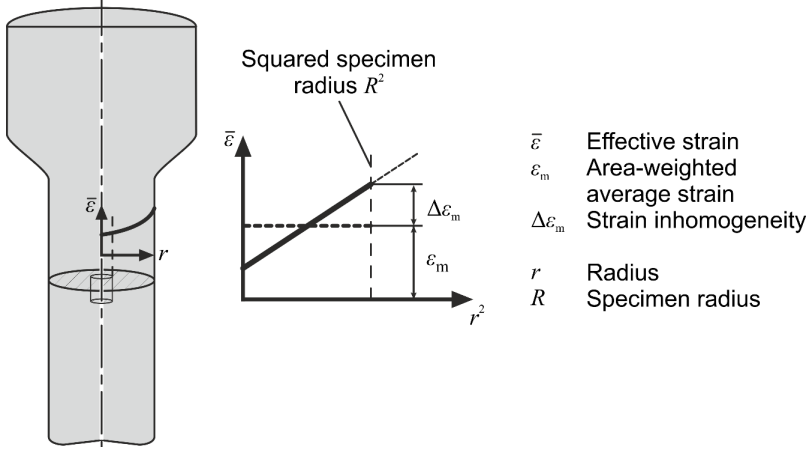
Figure 4.11: Approximate strain distribution in cylindrical specimens extracted from forward extruded parts

Within a specimen with a diameter that is significantly lower than the shaft diameter ($D < d_1 / 2$), the effective strain distribution can be approximated by a linear relation in respect to the squared radius r^2 according to:

$$\bar{\varepsilon}(r^2) = \frac{2 \cdot \Delta\varepsilon_m}{R^2} r^2 + \varepsilon_m - \Delta\varepsilon_m \tag{4.18}$$

When the pre-strained specimen is loaded in subsequent tension (or compression) and full plasticization is assumed, the necessary external force F_ε can be calculated as

$$F_\varepsilon = 2\pi \cdot \int_0^R \sigma_f(\bar{\varepsilon}(r)) \cdot r \cdot dr. \tag{4.19}$$

Herein, σ_f is the current local flow stress as a function of the effective strain $\bar{\varepsilon}$, which itself is a function of the radius r according to Eq. (4.18). Considering isotropic hardening according to the Swift-hardening relation with

$$\sigma_f(\bar{\varepsilon}) = C \cdot (\bar{\varepsilon} + \varepsilon_0)^n, \tag{4.20}$$

the necessary external force F_ε can be written in terms of the geometrical and material dependent parameters as

$$F_\varepsilon = \pi R^2 \cdot C \left[\frac{(\varepsilon_m + \Delta\varepsilon_m + \varepsilon_0)^{n+1} - (\varepsilon_m - \Delta\varepsilon_m + \varepsilon_0)^{n+1}}{2 \cdot \Delta\varepsilon_m \cdot (n+1)} \right]. \tag{4.21}$$

If a constant strain of $\varepsilon = \varepsilon_m$ is assumed instead of the actual linearly increasing strain distribution, the necessary external force for plasticisation F_{ε_m} can be written as

$$F_{\varepsilon_m} = 2\pi R^2 \cdot \int_0^R \sigma_f(\varepsilon_m) \cdot r \cdot dr, \tag{4.22}$$

$$F_{\varepsilon_m} = \pi R^2 \cdot C \cdot (\varepsilon_m + \varepsilon_0)^n. \tag{4.23}$$

The difference between the force calculated from the actual strain distribution F_ε and the approximated "mean" strain distribution F_{ε_m} was calculated as

$$\left| \frac{F_{\varepsilon_m} - F_\varepsilon}{F_\varepsilon} \right| = f(\varepsilon_m, \Delta\varepsilon_m, \varepsilon_0, n) \tag{4.24}$$

as a function of the material and process dependent parameters. Interestingly, for a given specimen geometry and the corresponding strain inhomogeneity $\Delta\varepsilon_m$, the specimen radius R does not appear in this relationship explicitly. In addition, the error connected to the negligence of the true strain distribution is not affected by the scaling factor C. Eq. (4.24) was evaluated for a fixed set of material and extrusion parameters (**Table 4.4**).

Table 4.4: Reference sets for the evaluation of Eq. (4.24)

Swift hardening			Extrusion parameters		
Parameter	**Symbol**	**Value**	**Parameter**	**Symbol**	**Value**
Flow curve translation	ε_0	0.1	Area weighted average strain	ε_m	0.5
Hardening coefficient	n	0.2	Strain inhomogeneity	$\Delta\varepsilon_m$	20 %

The influences of some selected parameters of Eq. (4.24) on the resulting force deviation are shown in **Figure 4.12**.
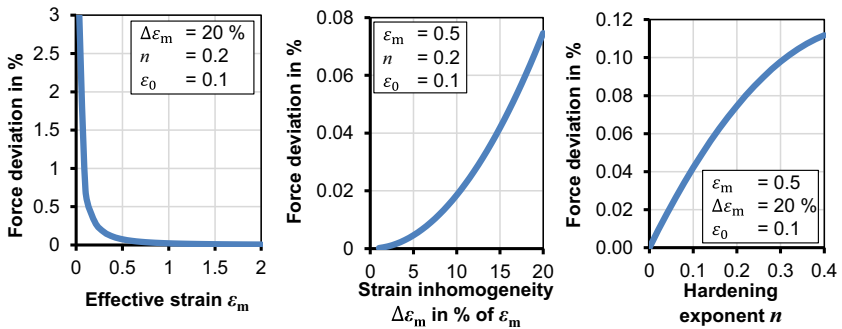
Figure 4.12: Difference between the force to plasticize specimens considering the actual pre-strain distribution $\bar{\varepsilon}(r)$ and the corresponding constant mean strain ε_m

The above results imply that the force deviation increases with the hardening exponent n and the strain inhomogeneity $\Delta\varepsilon_m$ and decreases with the flow curve translation ε_0 and the mean effective strain ε_m. These relations can be explained by the fact, that both n and $\Delta\varepsilon_m$ increase the flow stress inhomogeneity, whereas ε_0 and ε_m decrease the flow stress inhomogeneity. Even in the worst-case scenario the total error arising from the combination of all investigated influencing factors is lower than 1.2 %, which is considered insignificant for the flow stress evaluation.

To validate the above results, simulations of tensile tests have been conducted on a specimen with the strain distribution corresponding to a specimen extracted from a forward extruded part with $\bar{\varepsilon} = f(\varepsilon_{ex} = 1.5) = f(r)$ as well as on specimens with the corresponding constant average strain of $\bar{\varepsilon} = \varepsilon_m = 1.67$. The corresponding contour plots and strain-strain curves calculated from the force-stroke data is shown in **Figure 4.13**.
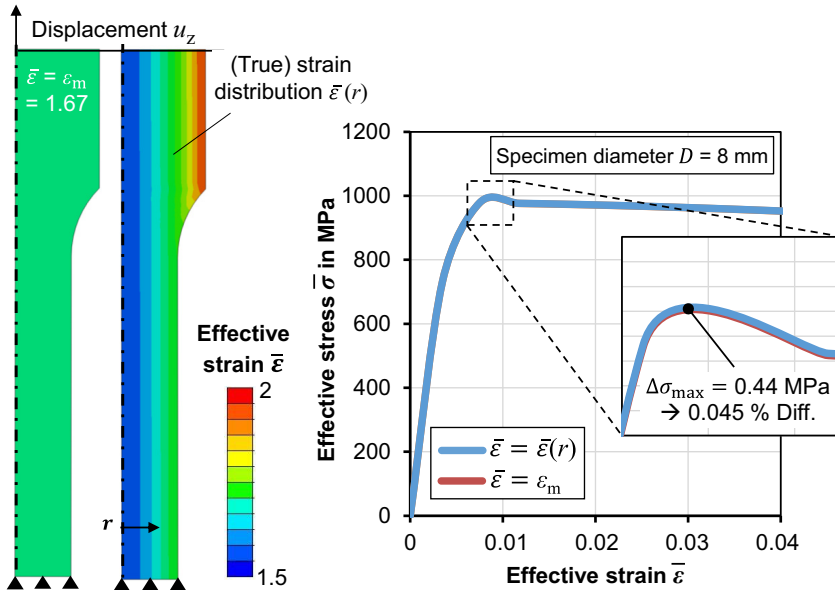
Figure 4.13: Numerically determined stress-strain curves of pre-strained specimens with actual pre-strain distribution caused during forward extrusion and corresponding specimen with constant pre-strain distribution

The maximum deviation between the two curves amounts to $\Delta\sigma_{max} \approx 0.045$ %, which means that no significant differences are observed during tensile testing, regardless of whether the actual pre-strain distribution $\bar{\varepsilon}(r)$ or the average strain ε_m is considered. The same observations apply for upsetting of specimens with the same initial diameter.

As a conclusion of the analytical and numerical results presented in this section, the pre-strain specimens extracted from forward extruded parts can be approximated by considering the theoretical extrusion strain and correcting it by a shear factor, which takes into account the radial increase of the strain connected to shearing. This factor merely depends on the diameter of the extracted specimens, whereas material dependent influencing factors can be neglected. For the investigated specimen diameter of $2 \cdot R = D = 8$ mm considered in this work, the correction factor amounts to approximately 11 %.

Strain distribution over extrudate length

Strain inhomogeneity over the length of specimens extracted from forward extruded parts would cause unwanted stress concentrations in subsequent testing. This would cause instabilities and induce premature failure preventing a correct evaluation of the flow stress. Therefore, the strain distribution must be constant along central axis. As forward rod extrusion is a quasi-static process, this property is generally given, if the length of the shaft is sufficiently long to allow an extraction of specimens whose imposed strain is constant in the tested region.

To validate the requirement, forward extrusion simulations were conducted in Abaqus CAE. A detailed description on the model setup is given in Appendix B. **Figure 4.14a** shows the strain distribution of forward extruded rods along the center line.
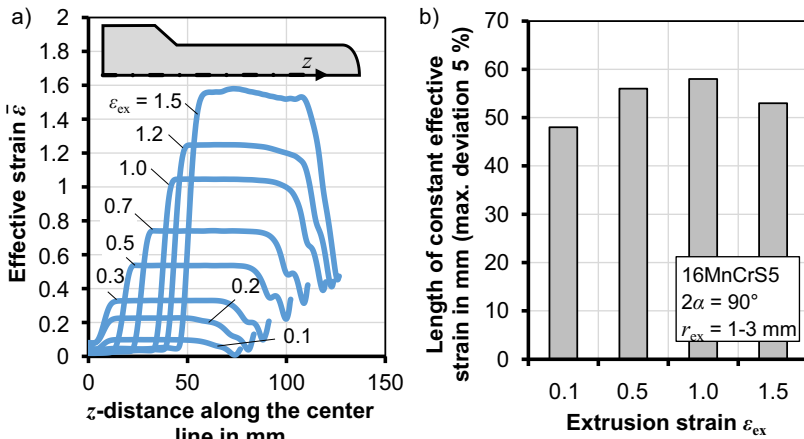
Figure 4.14: a) Numerically obtained effective strain distribution in forward extruded parts along the center line, b) Lengths of "constant effective strain" along the center line

All parts were extruded until a shaft length of 80 mm was reached. The maximum lengths in which the strain distribution varies within ±5 % of the corresponding average strain ("length of constant extrusion strain") is plotted for four extrusion strains (**Figure**

4.14b). The minimum length of constant extrusion strain amounts to 48 mm ($\varepsilon_{ex} = 0.1$). This value coincides with the gauge length of the chosen standardized tensile test specimens (Figure 4.4), which means that extraction of specimens with this geometry does not violate the requirement for a constant strain over the specimen length. The same applies for the chosen upsetting test specimens with a much lower height of 12 mm.

Residual stresses

Inhomogeneous plastic flow causes residual stresses in the finished workpiece after cold forging. In some cases, the individual residual stress components can be larger than the flow stress of the material. Since the residual stresses add up to the loading stresses in subsequent testing, the apparent flow stress may be influenced by the residual stress. While cold forging can generally cause large residual stresses, the processes of ejection and specimen extraction are expected to lower the residual stresses significantly.

To quantify the amount of residual stress, forward rod extrusion simulations were conducted with Abaqus CAE, according to Appendix B. The influence of the extrusion strain on the residual stress components over the specimen radius was evaluated after three individual steps:

- forming,
- ejection,
- machining.

The axial residual stress distribution after each step depending on the extrusion strain is shown in **Figure 4.15**. To model the specimen extraction, the residual stresses after ejection are mapped onto the tensile specimen geometry and an equilibrium calculation is conducted to find the residual stress distribution in the new reduced domain.
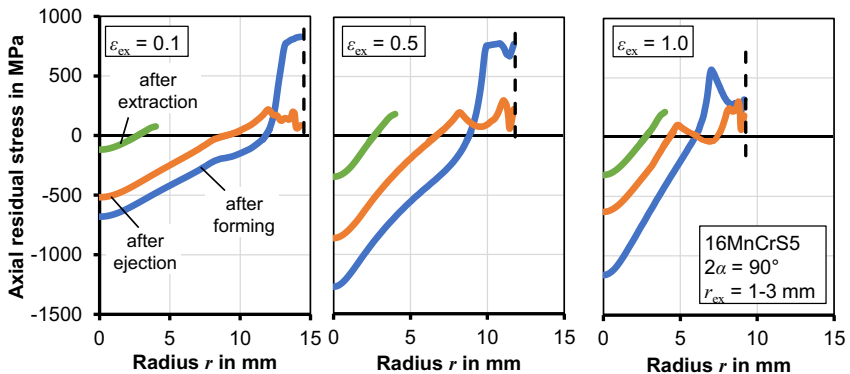
Figure 4.15: Axial residual stress components after forming, after ejection and after specimen extraction with $D = 8$ mm for three different extrusion strains

After forming, high residual stresses are present over the whole shaft radius. In the core, the axial stresses are negative (compressive stress), whereas in the outer region, the stresses become highly positive (tensile stress). During ejection, a large part of the residual stresses in the outer region are released due to small plastic deformations induced by the die spring back after unloading. Due to the equilibrating nature of residual stresses, this leads to an overall reduction of residual stresses. In the last stage, the extraction of specimens with a diameter of $D = 8$ mm leads to another decrease of the residual stresses, as the regions containing positive stresses are completely removed.

The largest remaining stresses (-350 MPa) are present in the specimen extracted from the shaft with an extrusion strain of $\varepsilon_{ex} = 0.5$ (**Figure 4.16a**). To quantify their influence on the apparent flow stress during tensile testing, the apparent flow curve of the specimen with $\varepsilon_{ex} = 0.5$ was compared with the apparent flow stress of an initially stress-free specimen with the same pre-strain distribution (**Figure 4.16b**).
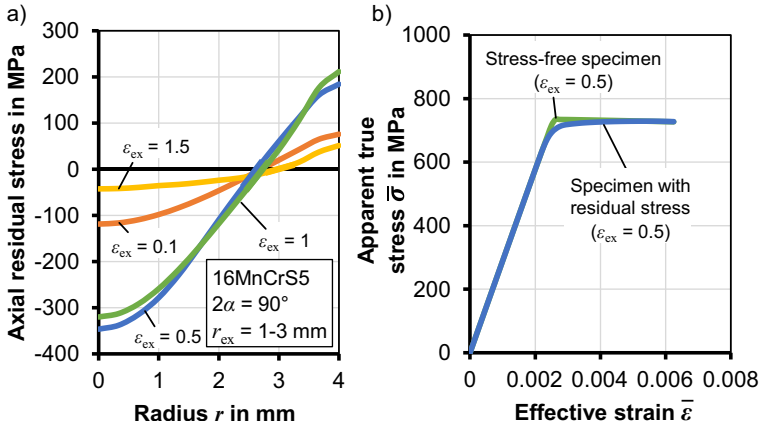
Figure 4.16: a) Residual stress distribution in specimens depending on the extrusion strain, b) Apparent true stress-strain curves of specimens with and without residual stresses from previous forward rod extrusion

The tensile residual stresses in the specimens add up to the tensile stress during loading, which leads to a lowered initial apparent flow stress. The local plasticization leads to a residual stress release, causing the apparent flow stress to converge toward the real flow stress. In the present case, evaluation of the $R_{p0.2\%}$ proof stress reveals a difference of less than 0.2 %. Consequently, residual stresses resulting from previous cold forging do not significantly alter the apparent flow stress in subsequent testing as the residual stresses are released during initial plasticization of the material.

Changing forming conditions between forward extrusion and subsequent testing

The method of tensile test on extruded specimens is assessed further to exclude effects connected to the interrupted nature of the procedure which could potentially falsify the results in the subsequent flow stress determination. To assess possible influences of changes of the forming conditions, the following aspects were investigated experimentally:

- Pressure change,
- temperature change,
- strain rate change,
- strain aging.

In the following sections, each of the above aspects is discussed individually.

Hydrostatic pressure variation

It was shown previously that the deviatoric part of the stress a material point is subjected to along the central axis in the forming zone of forward extrusion is equal to that of the uniaxial tensile test. However, the hydrostatic stress depends on the extrusion parameters. While hydrostatic stress by itself cannot cause plastic flow, several authors have reported a pressure dependence of the current flow stress.

To verify whether the pressure during forward extrusion permanently influences the flow stress during subsequent loading, specimens have been produced under varying hydrostatic pressures. For this, a constant counter-holder force F_C was applied by the ejector during forward extrusion (**Figure 4.17**). As the material is fully enclosed in the container and the punch the amount of counter-pressure superposed onto the pressure p in the forming zone p_c can be approximated by by F_c / A_1. This leads to an overall increased pressure in the forming zone amounting to $\bar{p} = p + p_c$.
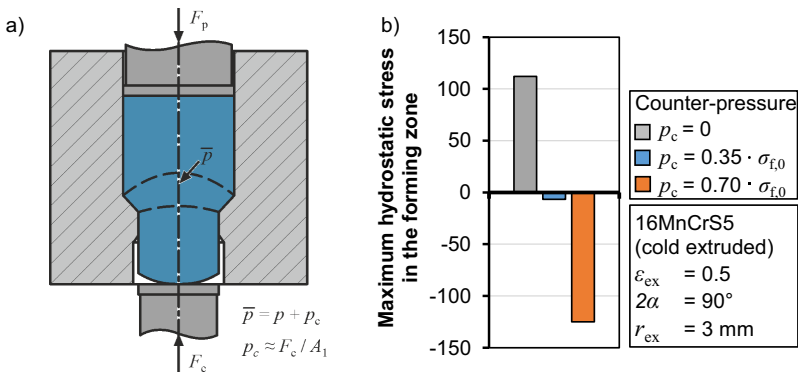
Figure 4.17: a) Location of maximum hydrostatic stress in the forming zone, b) Influence of counter-force on maximum hydrostatic stress

It was determined numerically that a counterforce of 50 kN (100 kN), corresponding to a pressure of $0.35 \cdot \sigma_{f,0}$ $(0.70 \cdot \sigma_{f,0})$, leads to a maximum hydrostatic stress in the forming zone of -6.6. MPa (-125 MPa) ($\varepsilon_{ex} = 0.5$, $2\alpha = 90°$, $r_{ex} = 3$ mm) (**Figure 4.17b**). The achievable hydrostatic stresses thus include large positive to large negative values, which addresses a range of possible local conditions representative for various cold forging processes.

To investigate the influence of the hydrostatic stress variation on the work-hardening, tensile test specimens were extracted from the extruded shafts produced under varying hydrostatic stresses. The resulting stress-strain curves of the extruded specimens as well as the corresponding flow stress and ultimate tensile strength are shown in **Figure 4.18**.
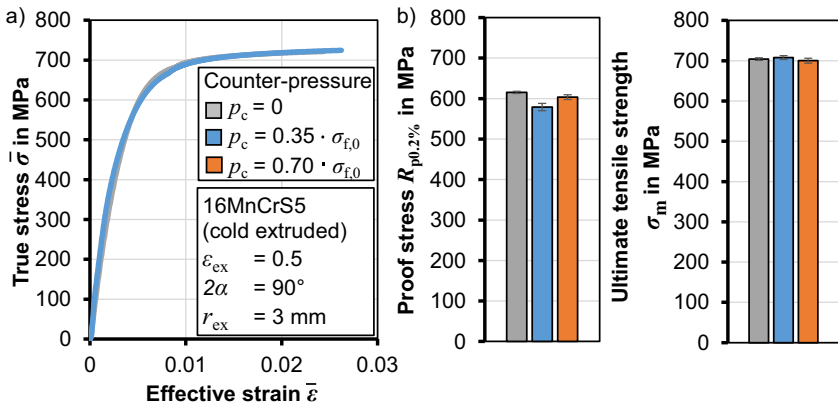
Figure 4.18: a) Influence of hydrostatic stress in the forming zone on the resulting work-hardening behavior of specimens extracted from the central axis of the extrudates, b) $R_{p0.2\%}$-proof stress and ultimate tensile strength

The results suggest that the hydrostatic pressure in the forming zone has no visible effect on the flow stress, which means that the hydrostatic stress during pre-straining does not lead to a permanent alteration of the dislocation density or structure, which would manifest in a measurable effect on the macroscopic mechanical behavior. As a consequence a possible influence of the hydrostatic stress history can be disregarded for the new interrupted characterization method.

Temperature change

Increased temperatures can trigger microstructural recovery, recrystallization and consequently lead to a reduction of dislocation density. This causes softening of a previously work-hardened material. During extrusion, the dissipated plastic work can lead to

a temperature increase of up to 400 °C. Temperature-induced changes of the microstructure or dislocation density can potentially lead to deviations in the subsequent testing of cold extruded material, i.e. the strain is not the only factor influencing the observed work-hardening behavior.

To determine the relevant temperature range, the expected temperature increase ΔT due to cold forging was estimated by the analytical relation according to Farren and Taylor (1925) under the assumption of adiabatic conditions:

$$\Delta T = \frac{\sigma_{f,m} \cdot \bar{\varepsilon} \cdot \beta}{c \cdot \rho}, \tag{4.25}$$

where $\sigma_{f,m}$ is the mean flow stress, β is the fraction of plastic work that is transformed into heat, c is the specific heat and ρ the density of the material. According to Farren and Taylor (1925) the factor β can be assumed as 86.5 % for steels. The influence of the extrusion strain on the temperature increase during forward extrusion is shown by the example of 16MnCrS5 (**Figure 4.19**). The highest calculated temperature increase of 250 K is present for the highest investigated extrusion strain of $\varepsilon_{ex} = 1.5$.
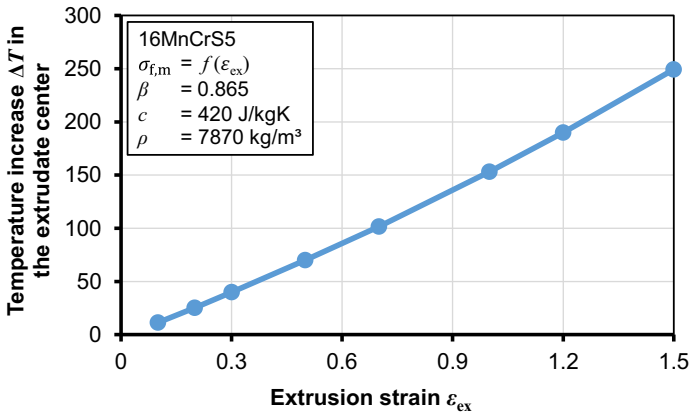
Figure 4.19: Influence of extrusion strain on the temperature increase in core of the extrudate under adiabatic conditions, calculated with Eq. (4.25)

To determine the influence of the temperature increase on the flow stress, tensile specimens were elongated at room temperature up to a strain of $\bar{\varepsilon} = 0.07$ and then unloaded. The specimens were then exposed to temperatures of 100 °C, 200 °C, 300 °C and 400 °C in a convection furnace and held at each temperature for 5 minutes. Afterwards, the specimens were air-cooled at room temperature and reloaded under tension up to fracture (**Figure 4.20**).

The specimens heated to 100 °C and 200 °C show no significant deviations from the the tensile test results obtained at room temperature. Specimens heated to 300 °C show clear signs of annealing effects, as the yield stress increases to about 530 MPa (+9 %).
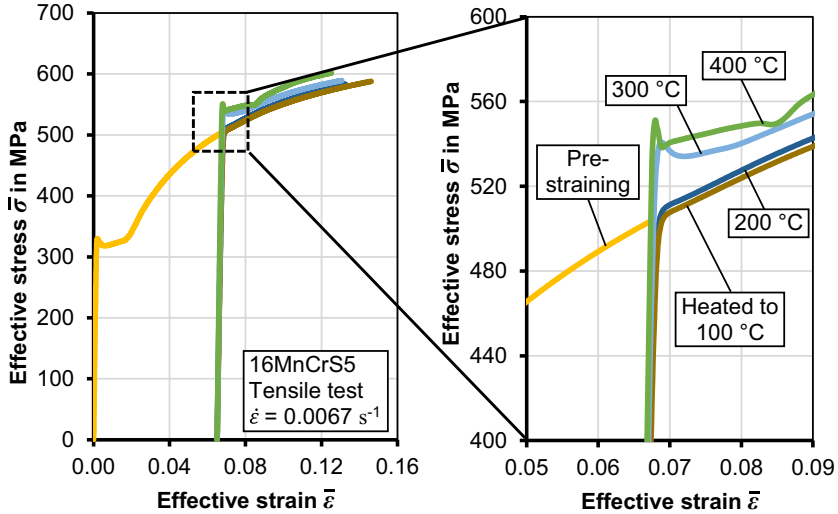
Figure 4.20: Influence of intermediate temperature increase on the hardening behavior of 16MnCrS5

The results suggest that annealing effects starts at temperatures above 200 °C. This temperature range is reached only for the part with the highest extrusion ratio $\varepsilon_{ex} = 1.5$. It is noted, however, that the calculation according to Eq. (4.25) considers adiabatic conditions, which is likely to lead to an overestimation of the actual temperature increase. In addition, the holding time of 5 minutes overestimates the actual time of elevated temperature during extrusion. A permanent effect of the temperature increase caused by the plasticity-induced heat dissipation on the flow stress is thus unlikely. The existence of a yield plateau gives an additional indication on whether annealing effects have occurred.

Strain rate change

The strain rate history of a particle travelling through the forming zone in forward rod extrusion is highly irregular and exceeds the strain rates achieved in quasi-static material characterization. This leads to the question, whether the strain rate history has a permanent effect on the plastic behavior of subsequently tested specimens. To analyze this, flow curves of 16MnCrS5 were determined by tensile tests at a strain rate of $\dot{\bar{\varepsilon}} = 2 \cdot 10^{-1} \text{ s}^{-1}$ and a quasi-static strain rate of $\dot{\bar{\varepsilon}} = 6.7 \cdot 10^{-3}$ as well as with an intermediate strain rate change at $\bar{\varepsilon} = 0.07$ (**Figure 4.21**).
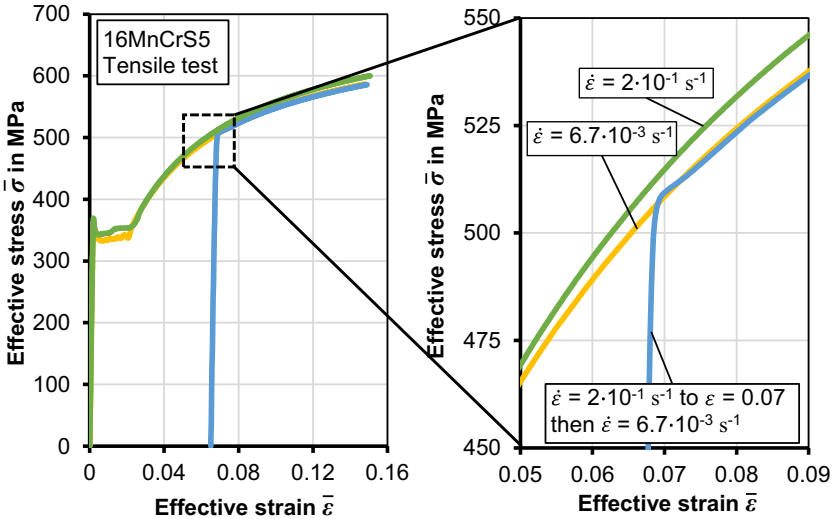
Figure 4.21: Influence of strain rate change on the hardening behavior of 16MnCrS5

While there exists a small influence of the strain rate on the flow curve, no influence of the strain rate change can be observed, as the flow curve corresponding to the test with a strain rate change converges toward the flow curve corresponding conducted under a constant strain rate of $\dot{\bar{\varepsilon}} = 6.7 \cdot 10^{-3} \text{ s}^{-1}$.

Yoshino and Shirakashi (1997) conducted compressive tests on the steel SUS430F utilizing a Split-Hopkinson bar tester. They conducted tests at strain rate of $\dot{\varepsilon} = 1500 \text{ s}^{-1}$ up to a plastic strain of $\varepsilon = 0.1$, then unloaded the specimens and continued the tests at a much lower strain rate of $\dot{\varepsilon} = 10^{-3} \text{ s}^{-1}$. In this setup the resulting flow stress curve did not converge to the flow curve obtained by tensile tests on virgin material tested with a constant strain rate of $\dot{\varepsilon} = 10^{-3} \text{ s}^{-1}$, showing that the strain rate history may affect the plastic material behavior. The present results suggest, that a permanent influence of the strain rate history on the flow stress only becomes active at much larger strain rate differences, leading to the assumption that the strain rate history of the extruded material has no permanent effect on the flow curve measured in subsequent tension

Strain aging

Between forward extrusion, specimen extraction and subsequent tensile testing a certain amount of time passes, leading to the question whether natural strain aging processes affect the properties of the extracted specimens after forward extrusion. To simulate this, tensile test specimens were pre-strained by $\bar{\varepsilon} = 0.07$ and unloaded. The specimens were

then reloaded after periods of 5 minutes, 1 month and 3 months. The resulting stress-strain curves are shown in **Figure 4.22**.
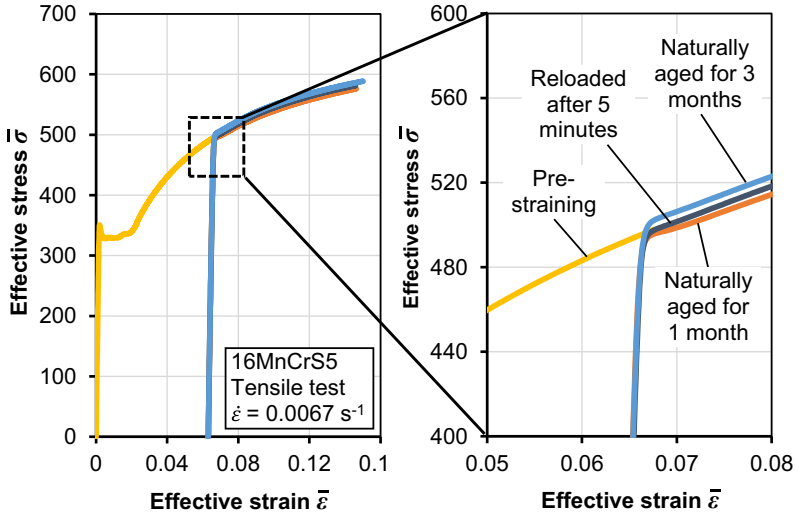
Figure 4.22: Influence of natural strain aging on the hardening behavior of 16MnCrS5

The maximum deviation between the curves amounts to less than 1 %, which is less than the general data scatter of the tensile tests ($\approx$ 3 %). From the fundamental experiments, it is concluded that natural strain aging has no significant effect on the resulting flow stress in the subsequent testing of extruded 16MnCrS5 specimens.

Conclusion on the influence of abrupt changes of the forming conditions

The results of this subsection indicate that the flow stress of forward extruded material is not influenced by the occurring changes in the forming conditions between cold forging, specimen extraction and testing. This leaves the strain to be the only factor permanently influencing the flow stress, which underlines the applicability of the new characterization method.

4.3.2 In-plane torsion of material extracted from metal bars

The in-plane torsion test on sheet metal was first presented by Marciniak and Kolodziesjki (1972) in order to determine the hardening exponent *n* and formability under shear stresses. The method was later extended by Tekkaya et al. (1982) in order to obtain flow curves for arbitrary hardening models. Due to the favorable hydrostatic pressure of $\sigma_h = 0$, the characterization method allows for much higher strains than those achieved in tensile tests, where the specimens are prone to instabilities like necking. With the

advancements in optical strain measurements, the procedure has gained increased atten-
tion in the recent years (Yin et al., 2011). Yin et al. (2015a) presented a variation of the
in-plane torsion test, utilizing metal sheets specimens with circular grooves, which pre-
vents fracture at the clamping area, increasing the achievable strains. While the in-plane
torsion test was originally invented to characterize the elastic-plastic behavior of metals
in the form of sheets, the idea was adapted to characterize the investigated materials in
the form of bars by machining thin specimens from the center (**Figure 4.23**).
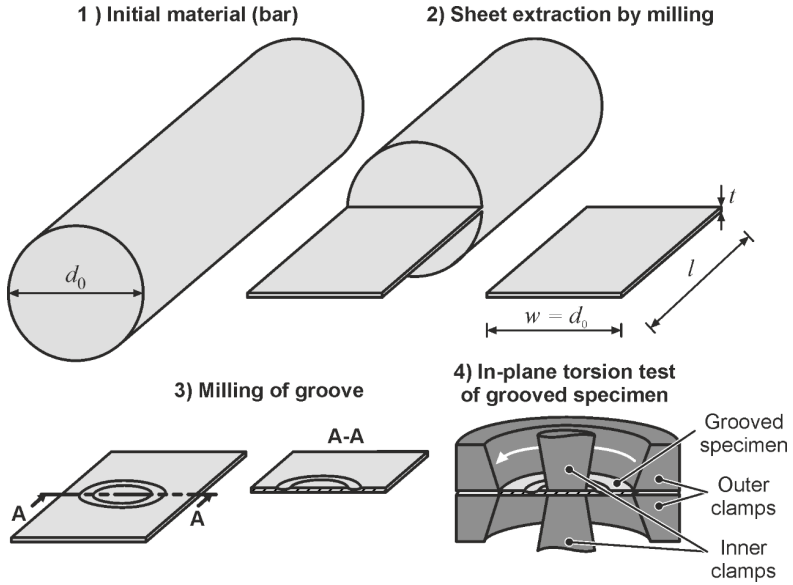
Figure 4.23: Specimen preparation for the in-plane torsion test on bulk material

The rod material was machined to produce thin sheet-like specimens. A circular groove
is then machined into the specimen. The produced in-plane torsion specimen is shown
in **Figure 4.24**. The clamped portion is indicated by the hatched regions.
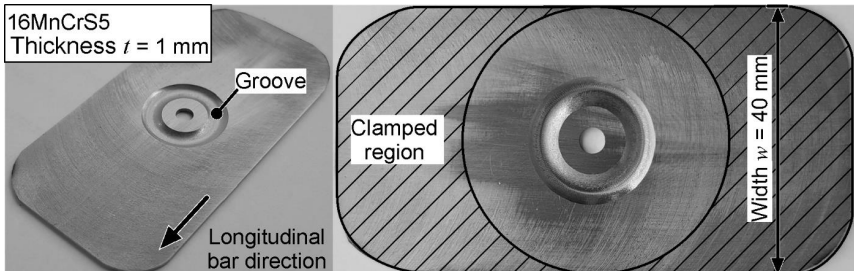
Figure 4.24: In-plane torsion test specimen extracted from a steel bar

The local strains are continuously determined by means of optical measurements, utilizing the measurement setup ARAMIS by GOM. To improve the contrast and thus support the strain measurement by gray value analysis specimens were sprayed with a white base layer and a stochastically distributed black pattern. The torque and displacement data are recorded and transformed into flow stress and effective strain by means of the Von-Mises-yield criterion. A sketch of the longitudinal section along with the actual test setup in action is shown in **Figure 4.25**.
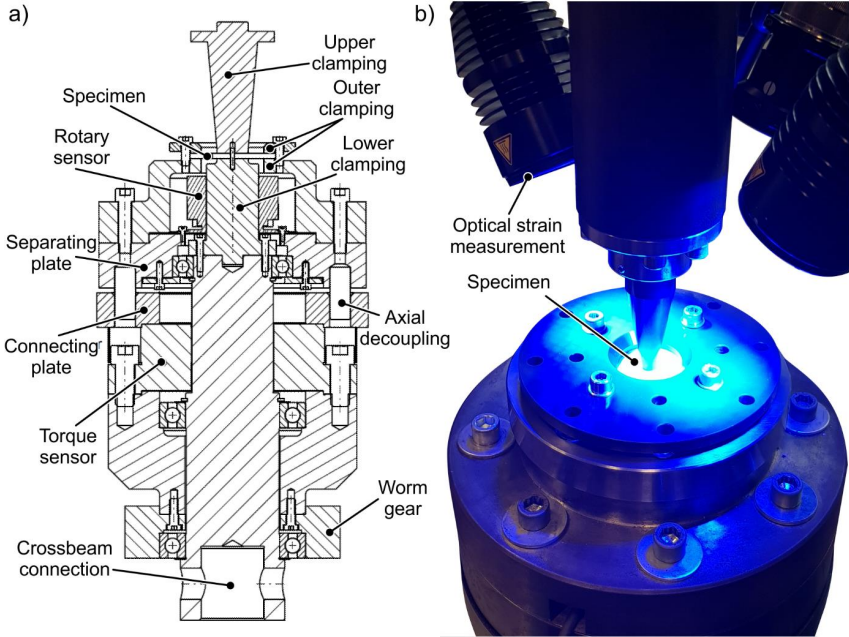
Figure 4.25: a) Longitudinal section of the in-plane torsion test setup, b) Test setup of the in-plane torsion test in action

4.4 Results on the monotonic work-hardening behavior

In this subsection, the results of the monotonic loading tests are presented. The resulting flow curves of the investigated steels determined by conventional characterization methods as well as by the new proposed methods are presented. To prove the applicability of subsequent testing of forward extruded material to characterize the material behavior at large strains, the influence of changes in temperature, strain rate and hydrostatic pressure between the pre-extrusion and subsequent testing is evaluated and a possible effect of strain aging on the mechanical properties of the three investigated steels is determined

4.4.1 Tension and upsetting

The flow curves determined by tensile and upsetting tests of all investigated materials are plotted in **Figure 4.26**. In all cases, the effective strains obtained by upsetting tests are significantly higher than those obtained under tension. All materials show the typical work-hardening behavior at room temperature with a rapid increase of the flow stress in the small strain regime following by a degressive increase at larger strains. While the tensile and upsetting flow curves of 16MnCrS5 are nearly identical, as is typical for FP-annealed material, both 100Cr6 and C15 show visible differences in the work-hardening behavior under tension and compression. As for both steels, the tensile flow curve lies above the flow curve measured by upsetting, the results indicate the existence of an initial Bauschinger effect. While for C15, the two flow curves approach each other at increasing effective strains, 100Cr6 even exhibits a work-hardening plateau under compression, which supports the existence of initial anisotropic hardening, caused by plastic deformations in the bar production via cold rolling or drawing, which was not fully removed by the subsequent heat-treatment. For the aluminium alloy AA6060 no significant differences can be observed between the flow curves obtained under tension and compression.
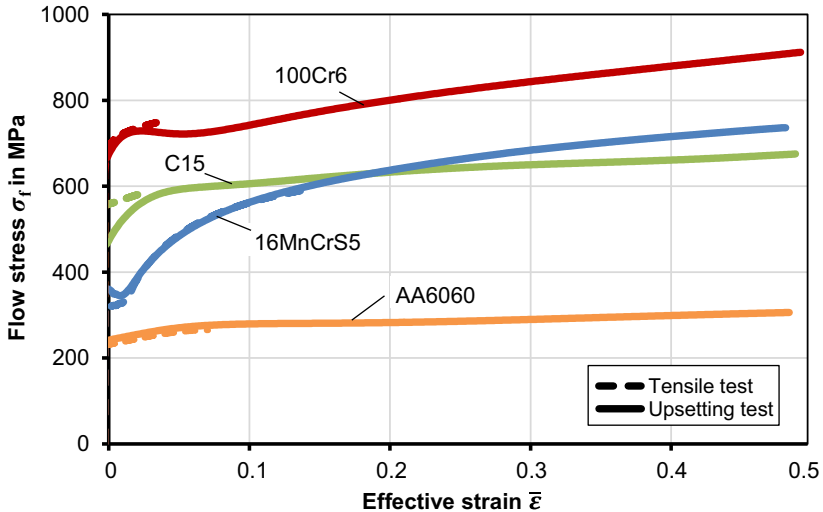
Figure 4.26: Flow curves determined by tension and upsetting tests

4.4.2 Torsion of cylindrical specimens

The torque-angle data determined by torsion of cylindrical specimens was evaluated by two different methods to obtain flow curves as described in Section 4.2.2. The results for 16MnCrS5 are presented in **Figure 4.27**.
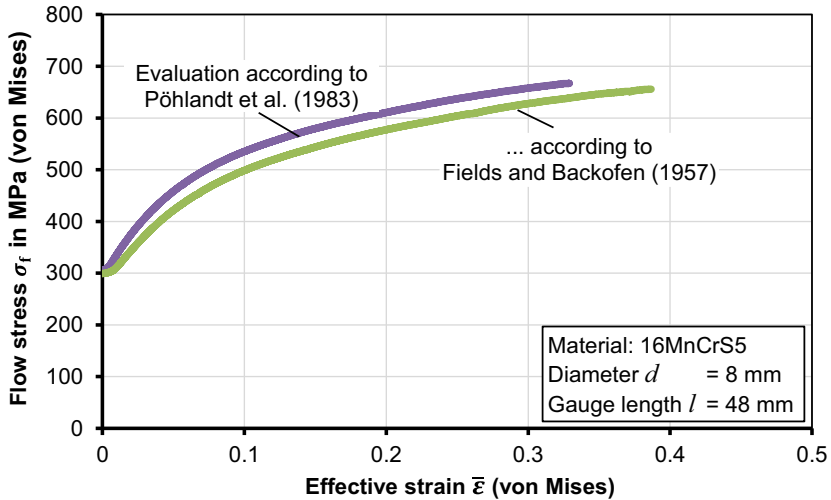
Figure 4.27: Effective stress-strain curves determined by torsion of cylindrical speci-
mens using different evaluation methods

The achievable strains in torsion of cylindrical specimens where only limited by the operating twisting angle of the utilized testing equipment. In the case of the Backofen-method, this has led to an achievable surface strain of $\bar{\varepsilon} = 0.4$. With the Pöhlandt-method a maximum strain of $\bar{\varepsilon} = 0.35$ could be reached, as it is evaluated inside the specimen where the strain is lower. At the highest achieved strain, the specimen surface showed first signs of surface degradations, which is a possible explanation of the lower flow curve calculated by the Backofen-method, which is evaluated at the surface.

4.4.3 Tensile tests on forward extruded material

The evaluable flow stress data in tension and upsetting is limited by the occurrence of necking and barreling, respectively. To achieve larger strains, tensile tests have been conducted on specimens extracted from forward extruded material as described in Section 4.2.1. The results of the new method are shown by the example of 16MnCrS5 (**Figure 4.28**). Each stress-strain curve is translated along the x-axis by the corresponding amount of effective strain as described in Section 4.3.1. For each individual pre-strain, only one curve (median) is shown in the diagram.

The flow curve of the lowest investigated pre-strain of $\varepsilon_{pre} = 0.1$ converges into that of the initially annealed material, which supports the consistency of the new approach with the conventional tensile test. The results indicate that even for strains of $\bar{\varepsilon} > 1.7$, no work-hardening saturation can be observed. On the contrary, the rate of work-hardening appears to increase at strains above 1.3.
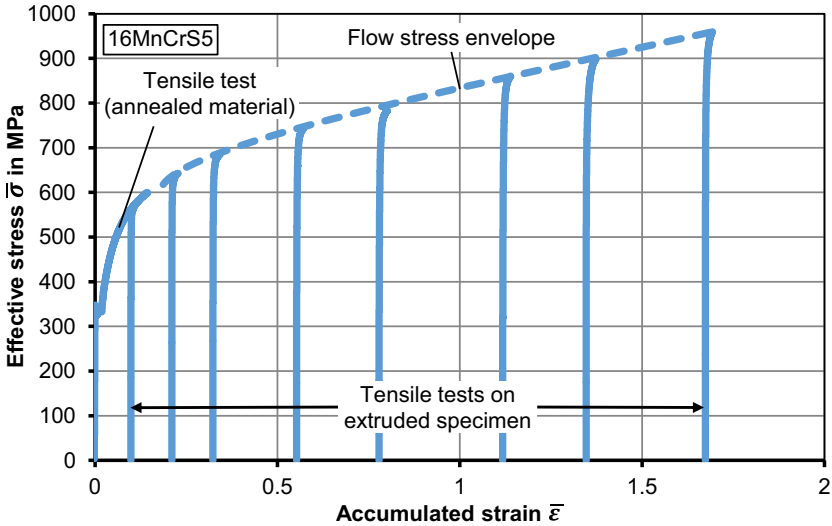
Figure 4.28: Stress-strain curve obtained by tensile tests of extruded material (the curves of the extruded material are shifted by the effective pre-strain achieved by forward rod extrusion, see Section 4.3.1)

For strains below 0.7 the flow curve of 16MnCrS5 is well described by typical degressively increasing hardening formulations e. g. according to Ludwik (1909) or Swift (1952). For strains above 0.7, the flow curve shows a linearly increasing behavior that cannot be captured well by these formulations.

To obtain flow curves from the discrete data, the peak values of the stress-strain curves of the extruded material were used as support points for interpolation. For the flow curve interpolation, splines were adjusted manually to find the best fit with the experimental data. The resulting flow curves of all investigated materials are compared in **Figure 4.29**. Only the maximum points of each flow curve generated by tensile tests on cold extruded materials are evaluated and indicated as rectangles.

All investigated materials exhibit near linear work-hardening after the typical rapid increase of the flow curve in the small strain regime. In the literature, a linear hardening behavior at large strains was also observed e. g. by Langford and Cohen (1969) for iron and by Verhoeven (1966) on steels with various carbon contents. Both researchers conducted tensile tests on wires with large pre-drawing strains between 4 and 8. The authors explained the transition from the curved into the linear hardening behavior by a change of the dominating hardening mechanism as the influence of the developing fibrous microstructure increasingly hinders dislocation movements along the active slip systems.
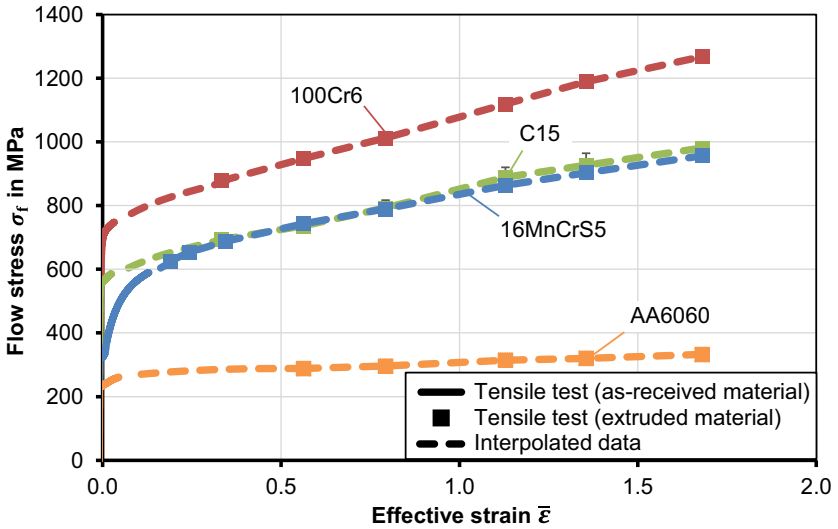
Figure 4.29: Flow curves determined by tensile tests on forward extruded material for various materials

4.4.4 In-plane torsion

The flow curve of 16MnCrS5 was evaluated by in-plane torsion tests on sheet specimens extracted from round bars as described in Section 4.3.2. All specimen fractured in the grooved region at an approximate maximum effective strain of $\bar{\varepsilon} = 0.8$ (**Figure 4.30**).
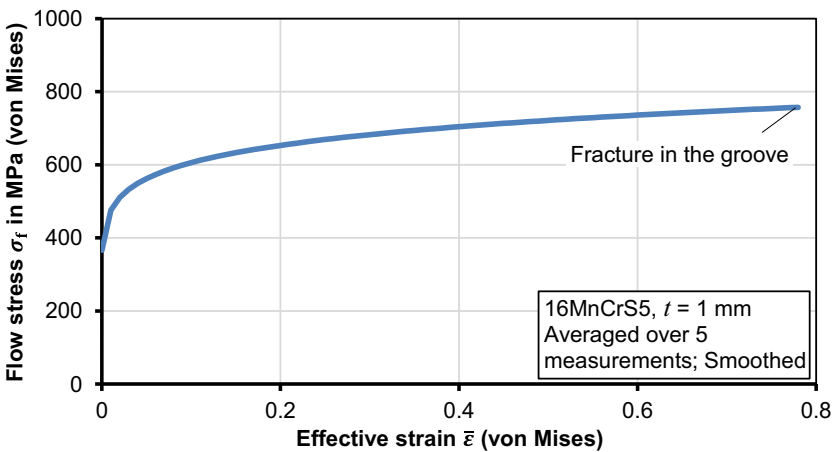
Figure 4.30: Flow curves obtained by in-plane torsion tests

4.4.5 Comparison of characterization methods

It is reported that different types of characterization methods lead to variations in the measured flow curves. Gil Sevillano et al. (1980) observed that the hardening behavior in tension and torsion deviates at large strains. While the hardening rate of wire-drawn polycrystalline BCC iron was nearly constant at large strains up to $\bar{\varepsilon} = 10$, a saturation is observed under torsion at $\bar{\varepsilon} = 4$. Langford and Cohen (1969) have discussed that the constant hardening rate of drawn material is due to the increasingly axially-oriented grains at increasing strains. Other researchers have discussed that the differences in tension, torsion and compression are connected to the general hydrostatic pressure dependence of the flow stress of metals (Spitzig et al., 1975).

In order to identify differences in the hardening behavior at large strains, the methods of upsetting ($\eta = -0.33$), in-plane torsion ($\eta = 0$) and tension after extrusion ($\eta = 0.33$) are compared by the example of 16MnCrS5 (**Figure 4.31**). The maximum achieved strains for each characterization method are indicated by the vertical lines.

In the small strain regime, all characterization methods show a good correlation, with exception of torsion of cylindrical specimens, which yields a lower flow curve. In the large strain regime ($\bar{\varepsilon} > 0.7$), the flow curve determined by in-plane torsion deviates from the curve measured by tensile tests on extruded material.
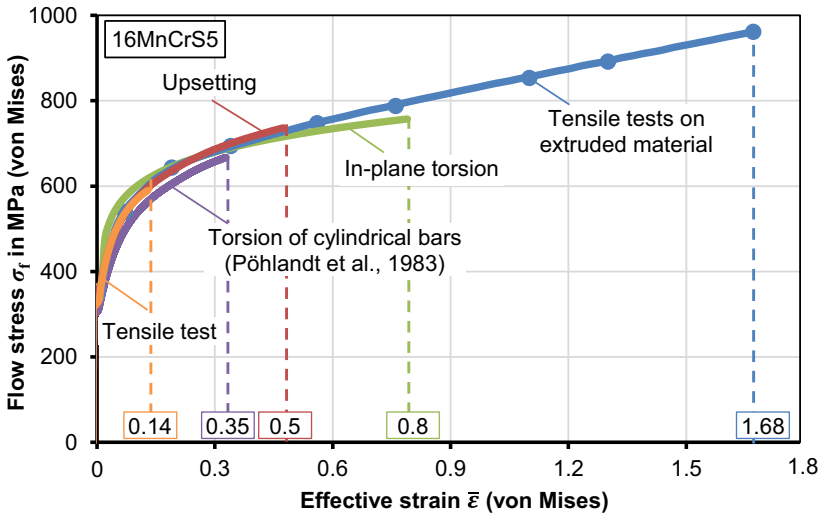
Figure 4.31: Comparison of flow curves determined by different characterization approaches (vertical lines indicate highest achieved strain for each method)

The observed discrepancy was reported by several other researchers as well, who discussed that the large strain work-hardening behavior under tension is increasingly driven by the evolving fibrous microstructure rather than by the formation and mutual obstruction of dislocations (Langford and Cohen, 1969). A summary of the characterization results for 16MnCrS5 is given in **Table 4.5**.

Table 4.5: Results of different characterization methods to determine flow curves (16MnCrS5)

Method	Maximum strain	Limiting factor	Swift hardening parameters		
			C in MPa	ε_0	n
Tensile test	0.14	Necking	950	0	0.23
Torsion of cylinders	0.35	Machine limit	825	0.003	0.20
Upsetting test	0.5	Barreling	856	0	0.19
In-plane torsion test	0.8	Fracture	778	0.001	0.11
Tensile test on extruded material	1.68	Maximum extrusion strain	Swift hardening relation not recommended for $\bar{\varepsilon} > 0.7$		

It is concluded that the new method of tensile tests on extruded material is very promising with regard to the maximum achievable strains as well as the capability to capture the actual work-hardening behavior under cold forging conditions and the present mode of deformation. It is noted, however, that interrupted procedures must be used with care due to possible changes in the forming conditions between the pre-straining method and subsequent testing.

4.5 Summary

In this chapter, various metals were characterized with regard to their monotonic work-hardening behavior up to large strains. For this, new characterization methods were derived and compared with conventional methods and the results were discussed.

A new characterization method was developed, in which specimens are pre-strained by forward rod extrusion. Tensile test specimens are then extracted from the core of the extrudates were the strain is known exactly. The specimens are then tested to obtain large strain flow curve points at pre-determined initial strains. The new method was assessed by means of numerical methods in order to assure the required homogeneous strain distribution over the length and radius of the produced extrudates and the stress state in the forming zone was analyzed, which equals that of a conventional tensile test superposed by hydrostatic pressure. Furthermore, it was shown experimentally, that the changes of forming conditions between forward rod extrusion and subsequent tensile testing do not have a permanent effect on the resulting flow curves. These aspects include the temperature increase and the hydrostatic pressure during extrusion as well as

the strain rate change between extrusion and tensile testing. Additionally, it was shown that 16MnCrS does not exhibit strain aging effects at room temperature during the time between specimen pre-straining and testing. It was concluded, that the strain achieved during forward extrusion is the only relevant parameter affecting the flow stress permanently, which underlines the suitability of the new experimental procedure.

The new characterization method was applied to obtain flow curves of 16MnCrS5, 100Cr6 and C15 steels as well as of the aluminium alloy AA6060. By combining flow stress data obtained by tensile tests on annealed material with the data obtained by tensile tests on forward extruded material, large strain flow curves were generated successfully. Maximum strains of up to 1.7 could be achieved for each material, exceeding the strains reached by conventional tensile tests by a factor of 10 and the strains reached by upsetting tests by a factor of 2-3.

As an additional experimental procedure, in-plane torsion tests were conducted on sheet-like specimens extracted from the as-received 16MnCrS5 steel bars to determine the work-hardening behavior under shear loading. The investigations revealed that the work-hardening behavior under shear deviates from that of tensile tests on pre-strained material especially at larger strains. A possible explanation of this deviation is given by the difference in the microstructure evolution at different stress states which was also reported by other researchers.

In order to investigate the anisotropic work-hardening behavior, a promising characterization method is given by the possibility to conduct upsetting tests on material pre-strained by forward rod extrusion. According to the analytical evaluation of the stress state in the forming zone of forward rod extrusion the change of loading direction corresponds to a complete strain path reversal. Evaluation of the data promises to reveal the anisotropic work-hardening behavior under strain path reversals at large pre-strains, which is dealt with in the following chapter.

5   Work-hardening behavior under non-monotonic strain paths

In this chapter, the material behavior under non-monotonic strain paths is investigated. To analyze the forward-reverse hardening behavior in the small pre-strain upsetting tests on elongated material were conducted (**Figure 5.1a**). To account for forward-reverse shear loading sequences forward-reverse torsion tests (**Figure 5.1b**) and in-plane torsion tests of metal sheets extracted from steel bars were applied (**Figure 5.1c**). To investigate the large pre-strain regime material was pre-strained by forward rod extrusion to extract upsetting specimens to account for forward-reverse loading sequences (**Figure 5.1d**) and torsion test specimens to cover cross-loading sequences (**Figure 5.1e**).
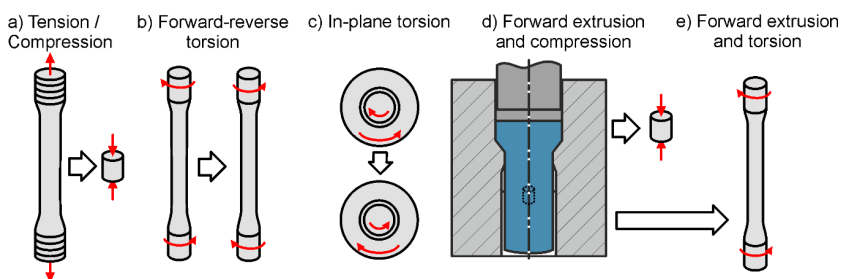
Figure 5.1: Methods to characterize the materials under forward-reverse strain paths

The chapter is divided into a section on conventional characterization methods "tension with subsequent compression" and "forward-reverse torsion" and a section on the new characterization methods "forward reverse in-plane torsion of sheets extracted from metal bars" and "compression of extruded material". Lastly, the results are discussed and the methods are compared with regard to their capability to capture the work-hardening behavior in varying pre-strain regimes.

5.1   Characterization via conventional methods

5.1.1   Upsetting of elongated material

The conventional tension-compression test is highly limited with regard to the achievable pre-strain due to the early buckling of the typically slender specimens under compressive loading (**Figure 5.2a**). While some modifications of the procedure are presented in the literature to mitigate or delay the occurrence of buckling of sheet specimens, systematic investigations of bulk specimens (e. g. cylindrical specimens) are rare. In order to reach higher pre-strains without buckling, an interrupted testing method was

conducted, in which cylindrical tests specimens were machined out of pre-strained specimens (**Figure 5.2b**). A similar method has been applied by Sillekens (1992), who reached pre-strains up to $\varepsilon_{pre} = 0.2$ for C45 steel.
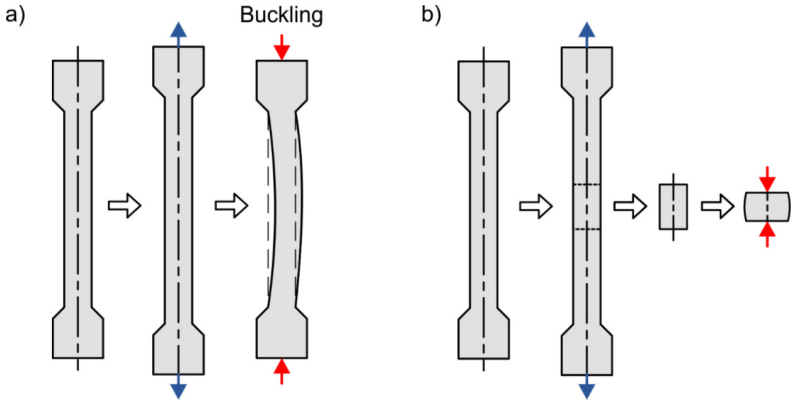
Figure 5.2:   a) Conventional tension-compression test and b) Upsetting test on elongated material to characterize the material behavior after a strain reversal

Each elongated tensile specimen was sawed into three upsetting specimens and compressed to 50 % of its initial height ($\varepsilon_{comp} = 0.7$) (**Figure 5.3**).
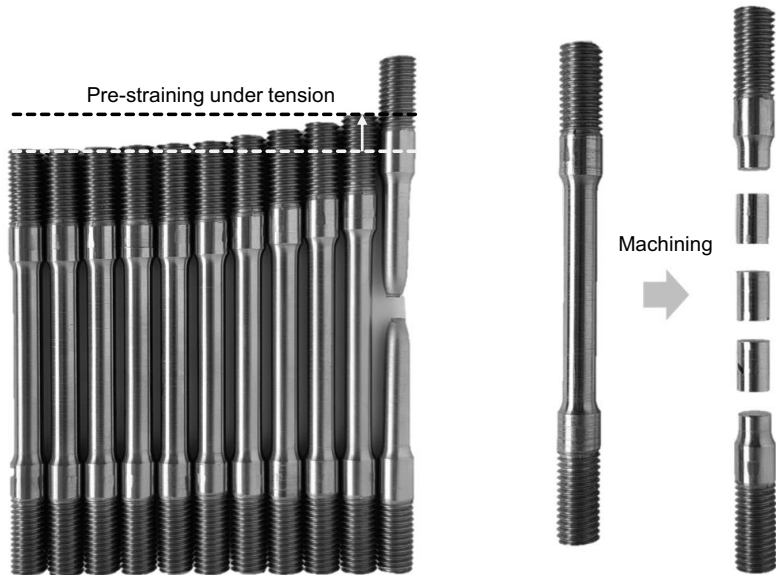
Figure 5.3: Extraction of compression specimens from pre-strained material

The maximum evaluable pre-strain in tension is prescribed by the uniform elongation of the material. After the maximum tensile force is reached, the tensile specimens start necking leading the stress state to deviate from uniaxial tension. On the basis of the uniform elongation, each material was pre-strained by the amounts summarized in **Table 5.1**.

Table 5.1: Investigated pre-strains generated under tensile loading

Material	Pre-strain in tension in %										Uniform elongation $e_{u\ in\ \%}$
16MnCrS5	0	0.5	1	1.5	2	3	5	7	10	14	14.5
C15	0		0.5	1		1.5	2	3		3.8	4.1
100Cr6	0		0.5	1		1.5	2	3		3.8	4.4
AA6060	0		0.5	1		1.5	2	3		5	7

5.1.2 Forward-reverse torsion of cylindrical specimens

The torsion test on cylindrical specimens described in Section 4.2.2 was adapted by reversing the twisting direction at prescribed angles of 270°, 405° and 540°, corresponding to pre-strains at the evaluated critical radius r^* of $\varepsilon_{pre} = 0.16, 0.25$ and 0.35. The results of the investigation are presented in Section 5.3.3.

5.2 Characterization via new methods

5.2.1 Upsetting of forward extruded material

The method of tensile tests on extruded material presented in Section 4.4.3 is adapted to identify the anisotropic work-hardening behavior under forward-reverse strain paths by extracting compression test specimens according to **Figure 5.4**.
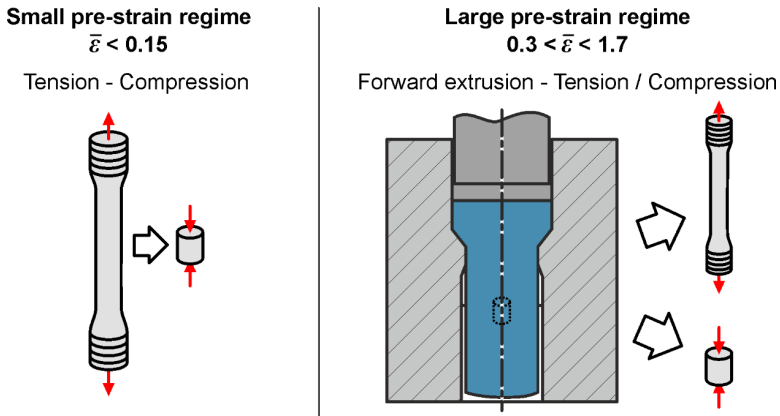
Figure 5.4: Methods to assess strain path reversal effects over a large pre-strain region

It was shown that the deviatoric stress state the material experiences along the central line during forward rod extrusion, equals uniaxial tension. Consequently, the application of subsequent compression corresponds to a full strain path reversal, where the reachable pre-strain is only limited by the maximum effective strain in the core of the extrudates ($\bar{\varepsilon} = 1.7$).

5.2.2   Forward-reverse in-plane torsion

The forward-reverse in-plane torsion test was utilized in order to characterize the cyclic work-hardening behavior according to Yin et al. (2015b). Grooved sheet specimens are twisted up to a certain twisting angle after which the twisting direction is reversed. By evaluating the local strain at various radii, multiple pre-strains can be achieved within one test. To apply the method to material in the form of bars, sheet specimens were extracted analogously to the method presented in Section 4.3.2. The results are presented in Section 5.3.3.

5.2.3   Torsion of forward extruded material

Anisotropic work-hardening has been reported to be exhibited during cross-loading. In this case, the yield locus can exhibit excessive expansion in the regions orthogonal to the original strain direction. In analogy to strain path reversals, the existence and intensity of cross-hardening effects depends on the material as well as on the amount of pre-strain. Cross-hardening is reported to be highest when the following condition is fulfilled.

$$\dot{\boldsymbol{\varepsilon}}_{n-1} : \dot{\boldsymbol{\varepsilon}}_n \ = \ 0. \tag{5.1}$$

Herein, $\dot{\boldsymbol{\varepsilon}}$ refers to the tensor of plastic strain increments and the indices $n-1$ and n refer to the time step before and after the orthogonal strain path change. To assess potential cross-hardening effects, cylindrical specimens were extracted from the center of forward extruded bars with a pre-strain of $\varepsilon_{ex} = 0.5$ and subsequently loaded under torsion as described in Section 4.2.2.

5.3   Results on the forward-reverse work-hardening behavior

In the following section, the results on the forward-reverse work-hardening behavior are presented. The known anisotropic hardening phenomena are defined. Tension-compression loading sequences as well as forward-reverse shear loading sequences are compared by the example of 16MnCrS5 to identify a possible influence of the stress state on the forward-reverse work-hardening behavior. Lastly, various materials are compared with regard to the intensity of anisotropic work-hardening phenomena.

5.3.1 Quantification of forward-reverse work-hardening characteristics

No generally accepted quantification methods exist in the literature to describe the forward-reverse work-hardening effects such as work-hardening stagnation or permanent softening. In the scope of this thesis, the definitions according to **Figure 5.5** were chosen which are described in more detail in the following.
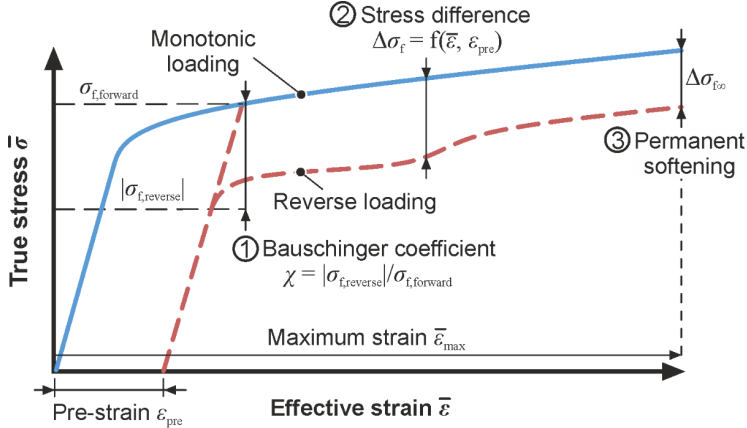
Figure 5.5: Definition of strain path reversal-related hardening phenomena

Bauschinger coefficient

The Bauschinger effect in terms of the relative flow stress difference in tension and compression is commonly described by the Bauschinger coefficient:

$$\chi = \left| \frac{\sigma_{f,reverse}}{\sigma_{f,forward}} \right|. \tag{5.2}$$

Herein, $\sigma_{f,forward}$ is the flow stress under tension before unloading and $\sigma_{f,reverse}$ is the flow stress under subsequent compression. In the following this measure will be used to describe the intensity of the Bauschinger effect for different pre-strain ranges. As the exact transition from the elastic to the elastic-plastic state is not clear once a material has been plastically deformed, the three proof stress definitions $R_{p0.2\%}$, $R_{p0.1\%}$ and $R_{p0.05\%}$ at the offset strains $\varepsilon_{offset} = 0.2\,\%$, $0.1\,\%$ and $0.05\,\%$ were evaluated as an approximation of the actual flow stress. The Bauschinger coefficient was redefined as:

$$\chi \approx \left| \frac{R_{pX.X\%,reverse}}{R_{pX.X\%,forward}} \right|, \tag{5.3}$$

where the expression X.X% corresponds to the corresponding offset strain.

Transient hardening and work-hardening stagnation

Both transient hardening and work-hardening evolve over the course of a plastic deformation after previous deformation in opposite direction. Consequently, the two effects are best quantified by a functional relation according to

$$\Delta\sigma_f(\bar\varepsilon, \varepsilon_{pre}) = \sigma_{f,tens}(\bar\varepsilon) - \left|\sigma_{f,comp}(\bar\varepsilon - \varepsilon_{pre}, \varepsilon_{pre})\right|, \qquad (5.4)$$

which describes the difference between the monotonic flow curve $\sigma_{f,tens}(\bar\varepsilon)$ and the flow curve corresponding to reverse loading $\sigma_{f,comp}(\bar\varepsilon - \varepsilon_{pre}, \varepsilon_{pre})$ with respect to the amount of reverse strain $\bar\varepsilon$ and the pre-strain in tension ε_{pre}. The resulting curves reveal any deviations from the regular work-hardening behavior observed at monotonic deformation. The functional relation $\Delta\sigma_f(\bar\varepsilon, \varepsilon_{pre})$ is hence called "stress-difference curve".

Permanent softening

Permanent softening is regarded as the permanent loss of resistance to plastic flow observed in a reverse loaded material, in comparison to the flow resistance during monotonic loading. In theory, permanent softening $\Delta\sigma'_{f\infty}(\bar\varepsilon = \infty)$ is the difference between the flow stress levels in forward and reverse loading at an infinitely large strain. In practice, quantification of permanent softening in terms of a scalar value is not trivial, as there exists no defined strain at which the stress difference between the monotonic flow curve and the flow curve corresponding to the strain path reversal. For the present investigation, the softening is evaluated at the highest effective strain that is reached during reverse loading ($\Delta\sigma_{f\infty}$). If the stress difference curve $\Delta\sigma_f(\bar\varepsilon, \varepsilon_{pre})$ reveals an existence of an asymptotic value, it is assumed that the stress difference at the highest evaluated strain is a sufficient approximation of the permanent softening ($\Delta\sigma_{f\infty} \approx \Delta\sigma'_{f\infty}$).

5.3.2 Tension-compression

For 16MnCrS5 pre-strains up to 14 % were achieved by means of tensile tests according to Section 5.1.1. The compressive flow stress was determined by compression of previously elongated material. The true stress-strain curves of the pre-strained material over the total accumulated strain $\bar\varepsilon$ (the sum of the effective strain in tension ε_{tens} and compression ε_{comp}) are shown in **Figure 5.6**. All reverse curves are mirrored into the first quadrant to allow better comparison. The results reveal that the flow curves after strain path reversal are significantly lower than the monotonic flow curve under compression of annealed material. However, the flow curves determined by upsetting after tension exceed the flow curve generated by monotonic tension of annealed material. It is assumed that the deviation between the tensile and the compressive flow curves is caused by the hydrostatic pressure influence of the flow stress. In addition, the flow curves generated by upsetting tests may be influenced by unwanted friction forces at the ends faces of the upsetting specimens which lead to an increase of the apparent flow stress.
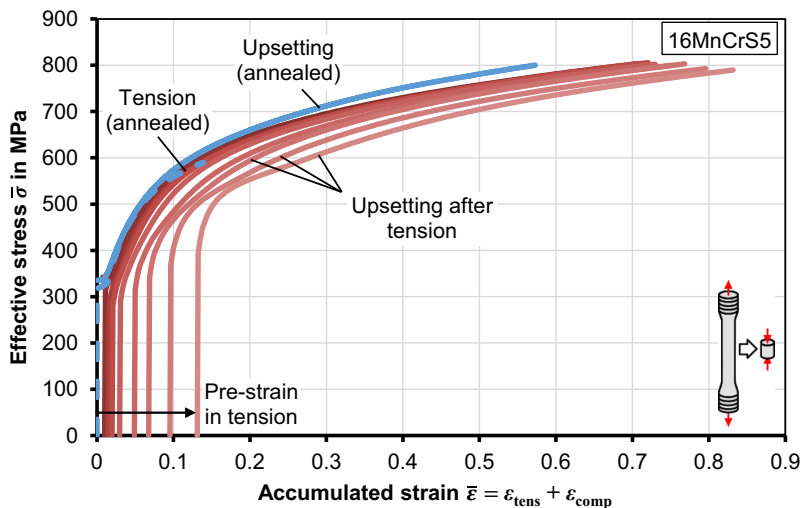
Figure 5.6: Stress-strain curves obtained by upsetting of specimens pre-strained by tensile testing with respect to the amount of pre-strain in tension

To explore the anisotropic work-hardening behavior for larger pre-strains compression tests were conducted on material pre-strained by forward rod extrusion (**Figure 5.7**).
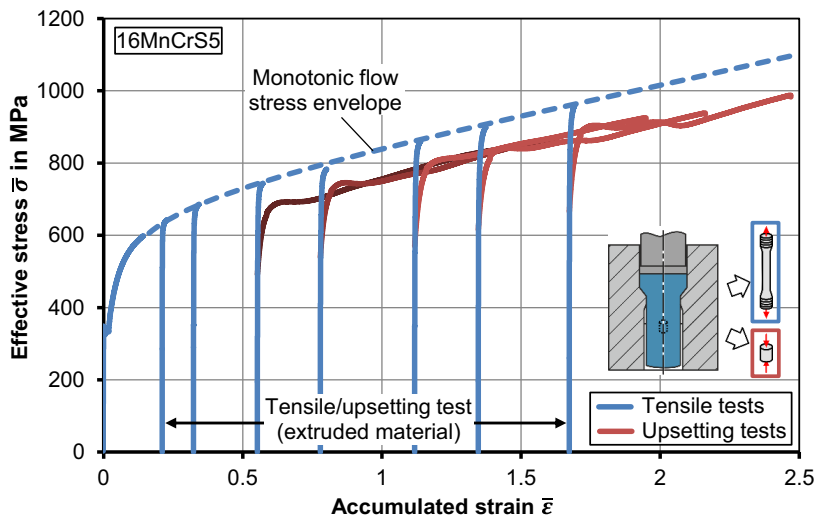
Figure 5.7: Stress-strain curves obtained by compression of specimens pre-strained by forward rod extrusion depending on the amount of pre-strain

To allow a better comparison of the flow curves under tension and compression subsequent to extrusion, the monotonic flow stress envelope is plotted, additionally. The comparison reveals that the intensity of the Bauschinger effect, work-hardening stagnation and permanent softening increase with the pre-strain. In the following the evolution of the anisotropic work-hardening effects with the pre-strain are quantified and discussed.

Bauschinger effect

Figure 5.8a shows the influence of the pre-strain in tension on the proof stresses in subsequent compression utilizing three different proof-stress definitions according to Eq. (5.3). The resulting Bauschinger coefficients are plotted over the corresponding pre-strains (**Figure 5.8b**).
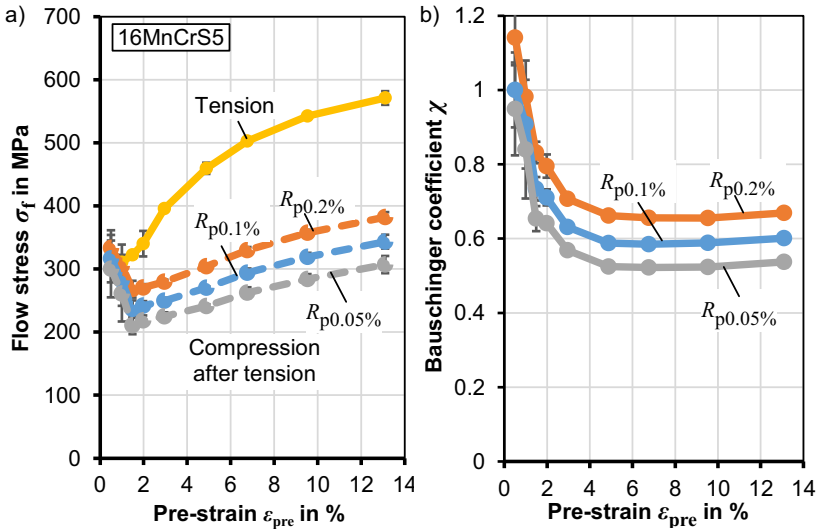
Figure 5.8: a) Flow stress under tension and subsequent compression, b) Influence of proof-stress definitions on the Bauschinger coefficient

The Bauschinger coefficients start at a value of around $\chi = 1$, indicating that there exists no initial Bauschinger effect, which is in accordance with the results on the flow curves under tension and compression presented in Section 4.2.1. The Bauschinger coefficients then converges to a constant value of $\chi \approx 0.6$. To evaluate the Bauschinger coefficients in the large pre-strain regime upsetting tests have been conducted on extruded material as described in Section 5.2.1 (**Figure 5.9**). The data in the pre-strain regime between $\varepsilon_{pre} = 0.1$ and $\varepsilon_{pre} = 0.3$ has been interpolated (dashed lines). The results indicate that the saturation of the Bauschinger effect observed in the low pre-strain regime continues with increasing pre-strains.
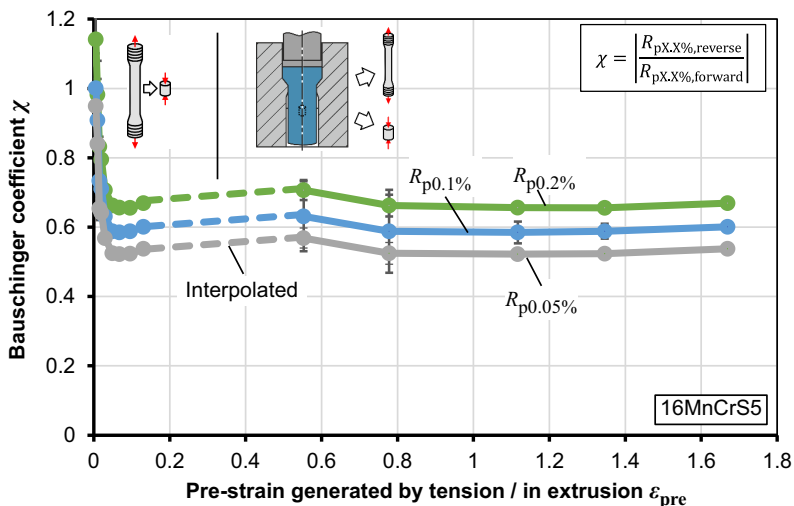
Figure 5.9: Bauschinger coefficients using different proof stress definitions

Work-hardening stagnation

Figure 5.10 shows, that 16MnCrS5 exhibits first signs of work-hardening stagnation at a pre-strain of 7 %. For pre-strains above 10 % the intensity of work-hardening stagnation increases visibly. The work-hardening slope is constant over a small part of the reverse flow curve and then resumes to the expected saturating hardening behavior.
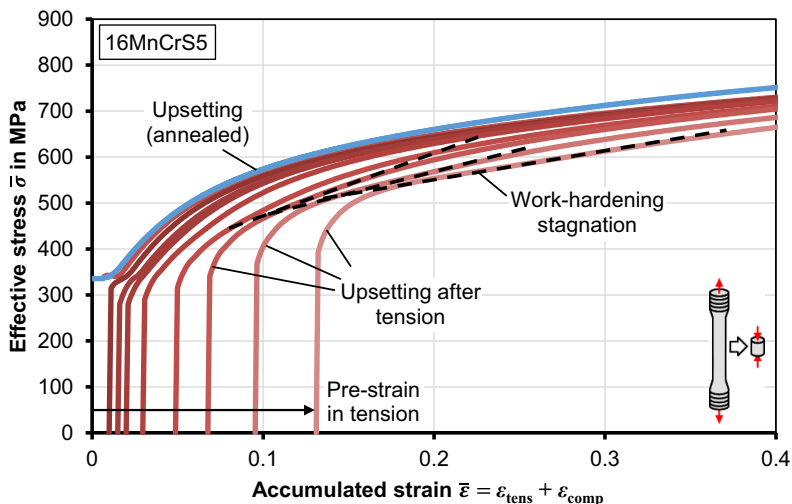
Figure 5.10: Work-hardening stagnation during compression of elongated material

The intensity of work-hardening stagnation and permanent softening can be visualized more clearly by evaluation of stress-difference curves as defined in Eq. (5.4). **Figure 5.11** shows the stress-difference curves of 16MnCrS5 over the complete investigated pre-strain regime.
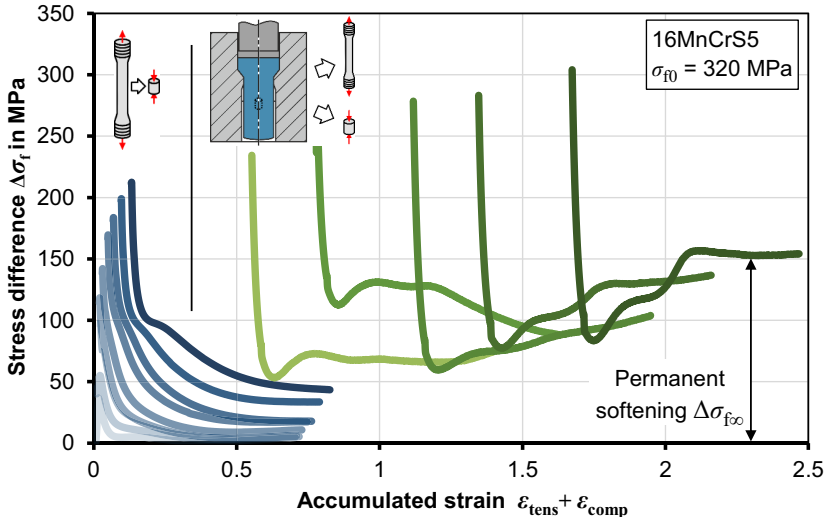
Figure 5.11: Stress difference curves over small and large pre-strain regimes

The stagnation of the work-hardening slope is indicated by the small bend after initial yielding observed for specimens with pre-strains above 7 %. For the specimens pre-strained by forward rod extrusion, the intensity of work-hardening stagnation increases drastically. Starting from the smallest pre-strain realized by extrusion ($\varepsilon_{ex} = 0.5$) work-hardening stagnation creates a yield plateau which is indicated by the increase of the stress difference after the first initial drop. For specimens with extrusion strains above 0.7 an oscillating work-hardening behavior exists whose intensity depends on the pre-strain as well. With increasing strain in compression, the stress difference curves converge toward constant levels corresponding to the permanent softening.

Permanent softening

The permanent softening $\Delta\sigma_{f\infty}$ was evaluated utilizing the stress difference curves defined in Eq. (5.4) and approximated by the flow stress difference at the highest evaluated total strain (corresponding to the last point of the stress difference curves). The resulting curves depending on the corresponding amount of pre-strain in tension are shown by the example of 16MnCrS5 (**Figure 5.12**).
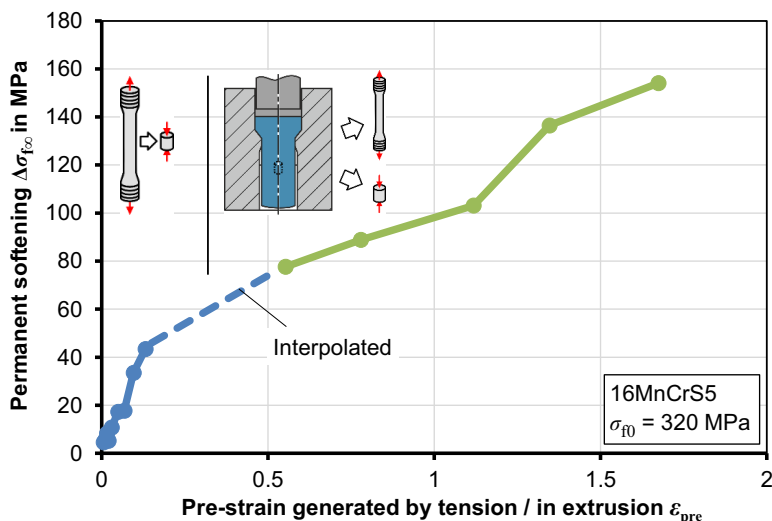
Figure 5.12: Influence of pre-strain on permanent softening after strain path reversal

The increase of permanent softening continues at large pre-strains, however, the slope of the curve decreases from 319 MPa to 71 MPa. The maximum permanent softening at the highest investigated pre-strain amounts to approximately 160 MPa, which corresponds to 50 % of the initial flow stress of the material ($\sigma_{f0} = 320$ MPa).

5.3.3   Forward-reverse torsion

To identify the work-hardening behavior under forward-reverse shear loading, two characterization methods were applied by the example of the case-hardening steel 16MnCrS5, namely forward-reverse torsion of cylindrical specimens and forward-reverse in-plane torsion of sheet specimens extracted from bars. In the following, the results of the two methods are discussed.

Forward-reverse torsion of cylindrical specimens

The results of forward-reverse torsion of cylindrical 16MnCrS5 bars are shown in **Figure 5.13a**. In analogy to tension-compression, the flow curves after load reversal are significantly lower than the monotonic flow curve. The maximum achievable shear pre-strain of $\varepsilon_{pre} = 0.35$ was limited by first signs of surface degradation of the torsion specimens. The flow stress values needed to calculate the Bauschinger coefficients were evaluated at a reverse plastic strain of 0.2 % (**Figure 5.13b**). The region between the measured values was manually interpolated by means of a smoothly transitioning spline.
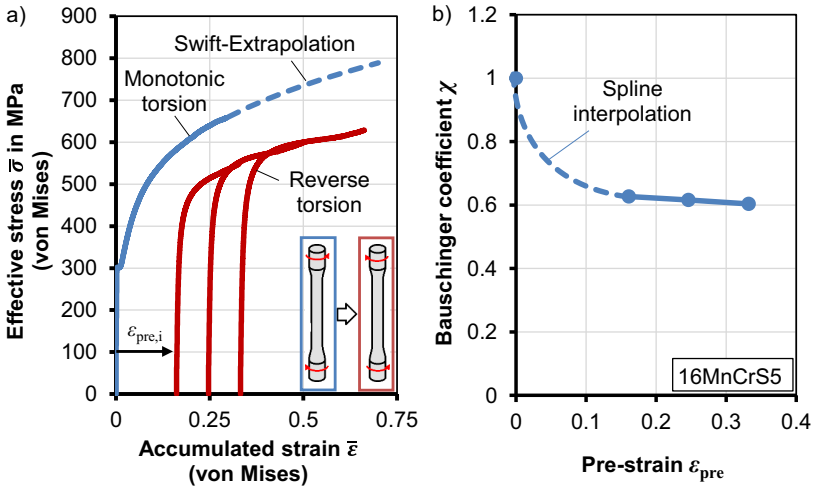
Figure 5.13: a) Stress-strain curves obtained by forward-reverse torsion of cylindrical specimens, b) Effect of pre-strain on the Bauschinger coefficient

Forward-reverse in-plane torsion

The results of the forward-reverse in-plane torsion test on a sheet specimen extracted from the center plane of a 16MnCrS5 steel bar are shown in **Figure 5.14a**.
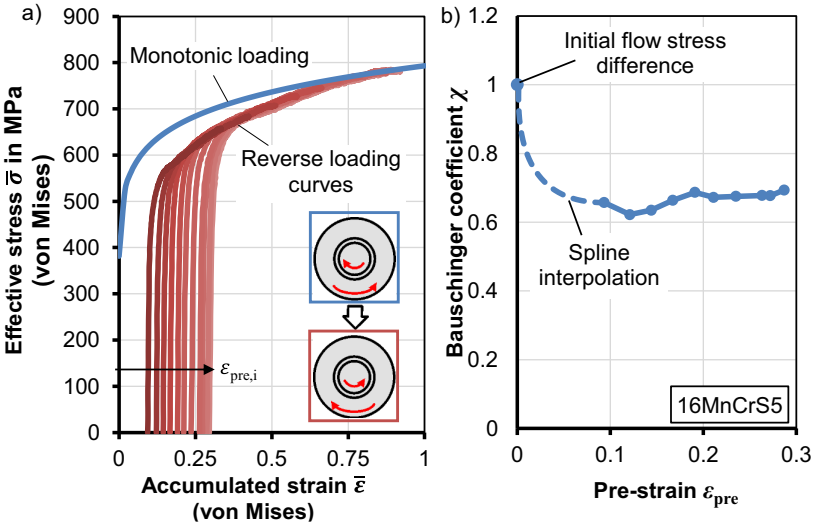
Figure 5.14: a) Stress-strain curves obtained by forward-reverse in-plane torsion, b) Effect of pre-strain on Bauschinger coefficient

The achievable accumulated strain by forward-reverse in-plane torsion ($\bar{\varepsilon} = 0.9$) was limited by specimen fracture. The flow stress values used to calculate the Bauschinger coefficients were evaluated at a reverse plastic strain of 0.2 % (**Figure 5.14b**). While the initial material does not show an initial Bauschinger effect ($\chi = 1$), the flow stress in reverse loading drops to a constant value of 66 % of the flow stress prior to unloading, even at the smallest evaluated pre-strain of $\varepsilon_{pre} = 0.1$. The region between the measured values was interpolated by a smoothly transitioning spline. While the results indicate the existence of work-hardening stagnation even at the smaller pre-strains, permanent softening could not be observed within the investigated pre-strain regime.

5.3.4 Comparison of characterization methods

Several continuous as well as interrupted characterization procedures were applied to analyze the anisotropic work-hardening behavior of 16MnCrS5 shown during strain paths reversals. The influence of the pre-strain on the Bauschinger coefficient and permanent softening as determined by the different methods are shown in **Figure 5.15**.
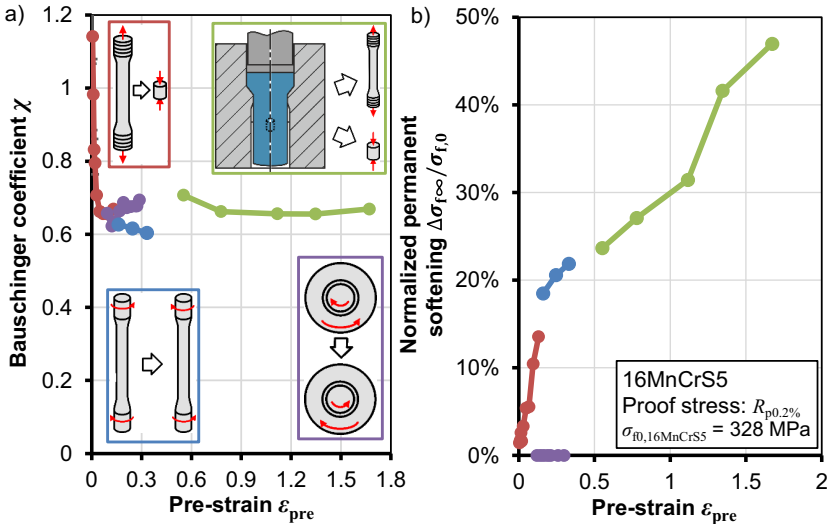
Figure 5.15: a) Bauschinger coefficients and b) normalized permanent softening of 16MnCrS5 as determined by different characterization methods

In terms of the Bauschinger coefficients, all characterization methods show the typical steep drop with increasing pre-strain and the subsequent plateau. The different methods yield Bauschinger coefficients in the range between $0.65 < \chi < 0.70$. The deviation of the results generated by torsion of cylindrical specimens can potentially be explained by

uncertainties in the flow stress calculation from torsion-angle data as well as the transformation of shear flow stress and strain into the respective effective quantities. In the case of in-plane torsion the complete lack of permanent softening is most notable. These observations suggest, that the intensity and even the existence of certain anisotropic work-hardening phenomena may depend on the type of the stress state, which can differ significantly between different characterization methods.

5.3.5 Additional materials

The interrupted procedure of upsetting tests on extruded specimens has been applied to all investigated materials, as the method has been proven to be reliable for the characterization of strain path reversal effects over a large pre-strain regime. **Figure 5.16** and **Figure 5.17** show the corresponding stress-strain curves for 100Cr6 and C15, respectively. The monotonic flow stress envelope, indicated by the dashed line, is generated by fitting a linear function to the flow stress points obtained by tensile tests.
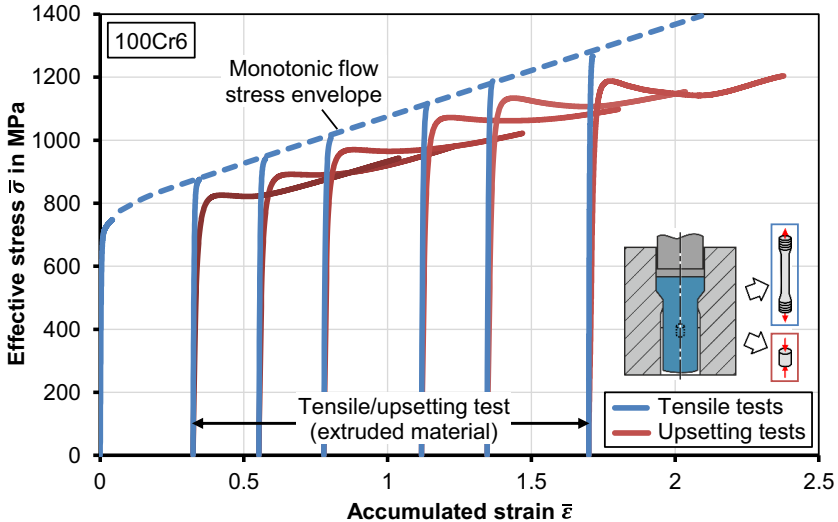
Figure 5.16: Effect of pre-strain on the tensile and compressive stress-strain curves of 100Cr6 after forward rod extrusion

Both 100Cr6 and C15 show linear work-hardening under proportional loading, whereas the flow stress after strain path reversal is consistently lower. Both steels are subject to significant work-hardening stagnation and permanent softening, becoming more pronounced with increasing pre-strains. After the initial flow stress drop and hardening stagnation, all compression flow curves approach a shared flow stress level. While the monotonic flow curves of 16MnCrS5 and C15 are similar, C15 appears to lose its work-hardening potential in the loading direction opposite to the pre-straining.
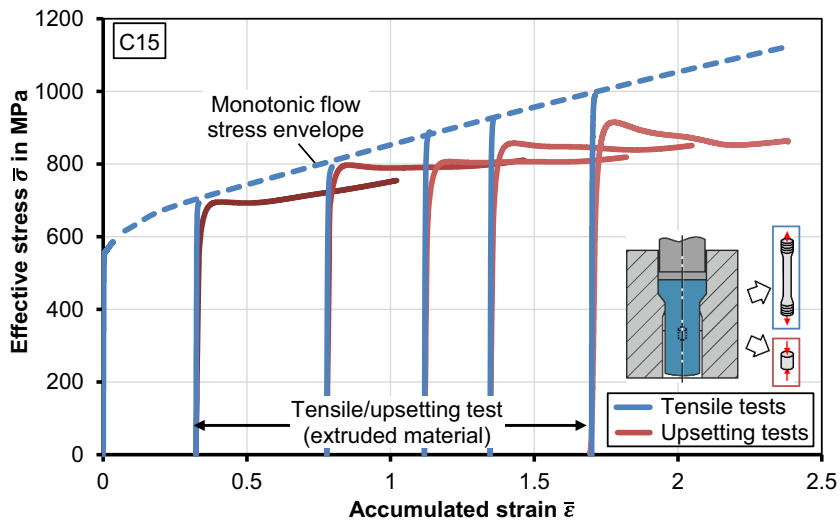
Figure 5.17: Effect of pre-strain on the tensile and compressive stress-strain curves of C15 after forward rod extrusion

Figure 5.18 illustrates the influence of the pre-strain on the resulting stress-strain curves of AA6060 under tension and compression after forward extrusion.
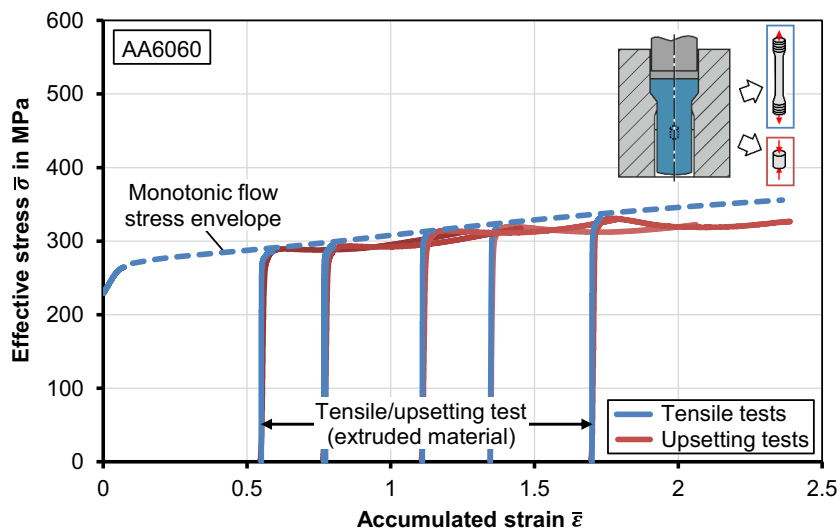
Figure 5.18: Effect of pre-strain on the tensile and compressive stress-strain curves of AA6060 after forward rod extrusion

In contrast to the investigated steels, AA6060 shows only minor anisotropic hardening phenomena. Of all investigated materials, it shows the lowest difference between the initial flow stresses under tension and compression and only weakly pronounced permanent softening. The results indicate that the existence as well as the intensity of all anisotropic work-hardening phenomena depends strongly on the material which was also reported by other researchers.

Bauschinger effect

The influence of the tensile pre-strain on the evolution of the Bauschinger coefficient for all investigated materials is illustrated in **Figure 5.19**. All materials show the expected drop of the Bauschinger coefficient at relatively low pre-strains. With exception of C15 all materials directly converge to a relatively constant level. C15 shows a rather irregular behavior, as the Bauschinger coefficient drops in the low strain regime, rises again above $\chi = 90$ % and then drops and saturates at about $\chi = 73\%$.
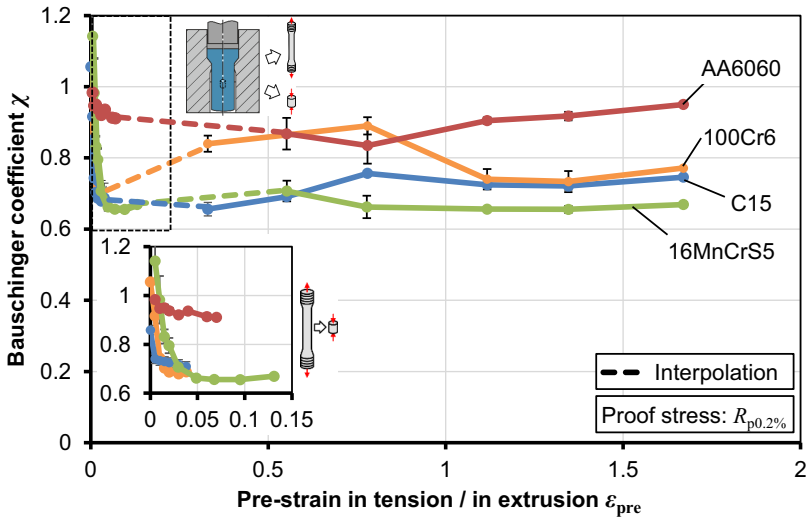
Figure 5.19: Influence of pre-strain on Bauschinger coefficients for various materials

A potential influence of outliers can be ruled out as a cause for this behavior, as the overall data scattering was very low as indicated by the error bars which symbolize the standard deviation over four specimens per data point. It is thus assumed, that the observed behavior is a material-specific property. Of all investigated materials AA6060 shows the least intense Bauschinger effect ($\chi > 85$ %).

The stress-difference curves of 100Cr6, C15 and AA6060 are shown in **Figure 5.20**.
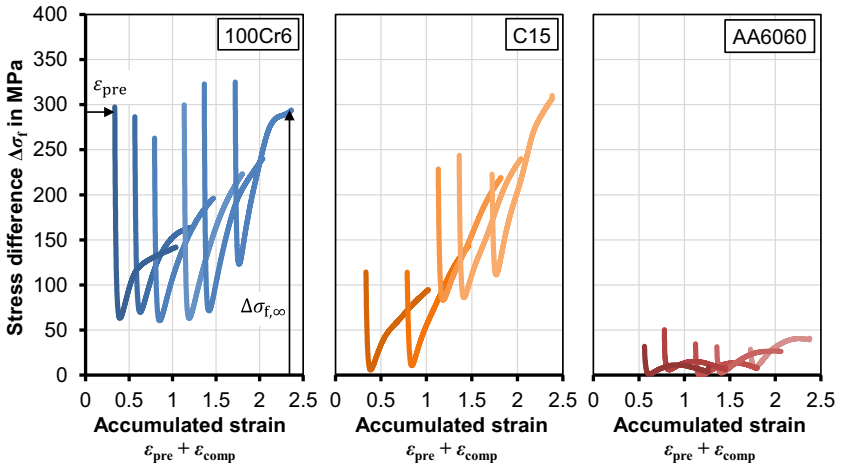
Figure 5.20: Tension-compression stress-difference curves as a function of the accumulated strain

In the case of 100Cr6 and C15, the existence of work-hardening stagnation is noticeable by the initial drop and the subsequent increase of the stress-difference curves, which can be observed for all investigated materials. The last point of the stress-difference curves marks the point at which permanent softening was evaluated (**Figure 5.21a**).
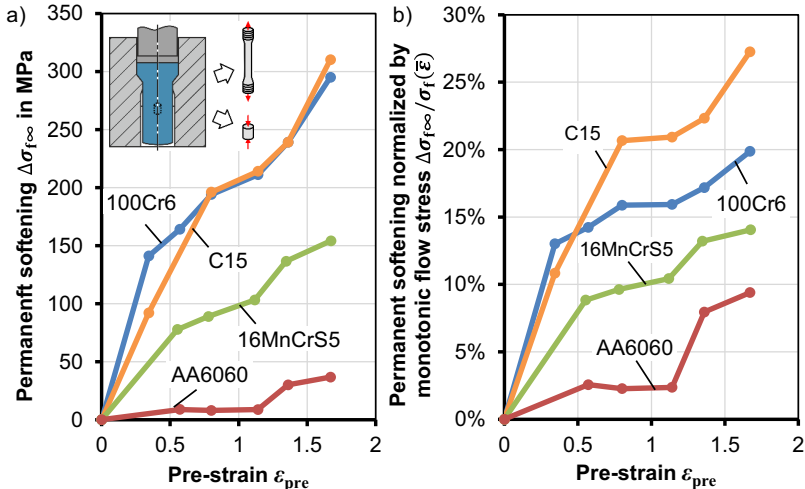
Figure 5.21: Influence of pre-strain on a) absolute permanent softening and b) permanent softening normalized by the flow stress under monotonic tension

All steels show a linear increase of permanent softening with the pre-strain. As none of the permanent softening curves converge in the investigated pre-strain regime, it can be assumed that the intensity of permanent softening may evolve even further at larger pre-strains. By normalizing the permanent softening values with the corresponding flow stress at the same accumulated strain, but under monotonic tension, the materials can be compared more easily (**Figure 5.21b**). All steels show a significant increase of permanent softening at small pre-strains. In contrast, the permanent softening of AA6060 does not increase significantly up to large pre-strains of $\varepsilon_{pre} > 1.3$ above which it shows a rapid increase. Nevertheless, even at the highest investigated pre-strain the normalized permanent softening of AA6060 is much lower than that of the investigated steels even when evaluated in terms of normalized values.

5.4 Results on the cross-hardening behavior

The influence of cross-loading sequences were investigated by coning torsion tests on cylindrical specimens extracted from forward extruded rods with $\varepsilon_{pre} = 0.56$. **Figure 5.22** shows the true stress-strain curves determined by torsion of annealed material and torsion of forward extruded material (16MnCrS5). In the latter case, the curve was translated by the corresponding pre-strain generated by extrusion. In both cases, the stress and strain were calculated from the torque and twisting angle data according to the Pöhlandt method. To compare the results at the varying strain regimes, the data generated by torsion of annealed material was extrapolated according to the Swift hardening law (parameters are given in the figure, see Table 4.5).
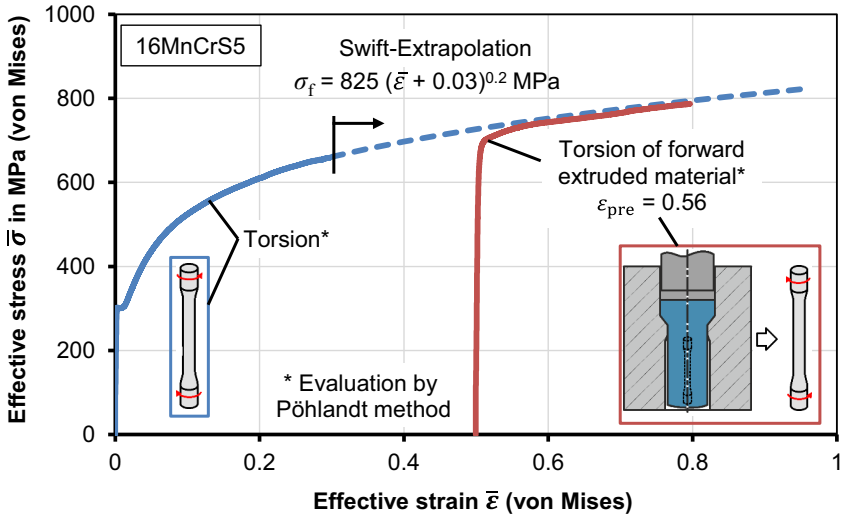
Figure 5.22: True stress-strain curves generated by torsion after forward extrusion

The results suggest, that 16MnCrS5 does not show any significant cross-hardening phenomena, which would typically lead to an overshoot of the stress-strain curve generated by torsion of extruded material as compared to the extrapolation of the stress-strain curve generated by monotonic torsion of annealed material. In fact, the initial shear flow stress of the pre-strained material is rather lower than the flow curve under monotonic torsion. With increasing strain, the flow curve approaches the flow curve generated by monotonic torsion. It is concluded, that the anisotropic work-hardening behavior of 16MnCrS5 does not include cross-hardening effects and thus the anisotropic work-hardening phenomena triggered under strain path reversals shown in the previous sections are dominant.

5.5 Summary

In this chapter the influence of strain path changes on the work-hardening behavior was explored by the example of three typical cold forging steels and one aluminum alloy.

Conventional as well as new methods to characterize the influence of strain path reversals as well as cross-loading sequences after initial plastic deformation were conducted and the results were compared. By comparison of different characterization methods, it was shown that the intensity of strain path reversal-related effects depends on the stress state. While all strain path reversal effects were visible under the tension-compression loading sequences as well as forward-reverse torsion of cylindrical specimens, no permanent softening was observed in forward-reverse in-plane torsion of 16MnCrS5.

It was found that the interrupted characterization procedure of tensile and compression tests on material pre-strained by forward extrusion is suitable to quantify the anisotropic work-hardening behavior of the investigated materials up to large strains and pre-strains, which are only limited by the achievable strains in forward extrusion. The investigations revealed that all anisotropic work-hardening phenomena including the Bauschinger effect, work-hardening stagnation and permanent softening are functions of the pre-strain. While the Bauschinger coefficient saturates at relatively small pre-strains for all investigated materials, the intensity of work-hardening stagnation and permanent softening increases with the pre-strain without showing any signs of saturation at larger pre-strains. Among the investigated materials the anisotropic hardening phenomena revealed under strain path reversals were most pronounced for the low carbon steel C15, and least pronounced for the aluminium alloy AA6060.

Lastly, by torsion of cylindrical specimens extracted from forward extruded material it was revealed that 16MnCrS5 does not show any significant signs of cross-hardening in the investigated pre-strain regime, which would typically cause an overshoot of the flow curve during subsequent orthogonal loading as compared to monotonic torsion. As a consequence, cross-hardening effects were not included in the constitutive modelling of the anisotropic work hardening behavior of 16MnCrS5.

6   Modeling anisotropic hardening in cold forging

In the first section constitutive material models are selected, implemented, and modified with the goal to capture the observed material behavior illustrated in the previous chapters. The capabilities and limits of the constitutive models are illustrated in terms of a parameter sensitivity study. In the second section, direct and inverse methods are applied to determine the material parameters of the case-hardening steel 16MnCrS5.

6.1   Constitutive models

The following models were used to model the work-hardening behavior of 16MnCrS5, focusing on the work-hardening behavior exhibited after strain path changes:

a) Isotropic hardening,
b) combined hardening according to Lemaître and Chaboche (1990),
c) combined hardening according to Yoshida and Uemori (2002),
d) Homogeneous anisotropic hardening (HAH) according to Barlat et al. (2011).

The basic model features are illustrated schematically in **Figure 6.1**.
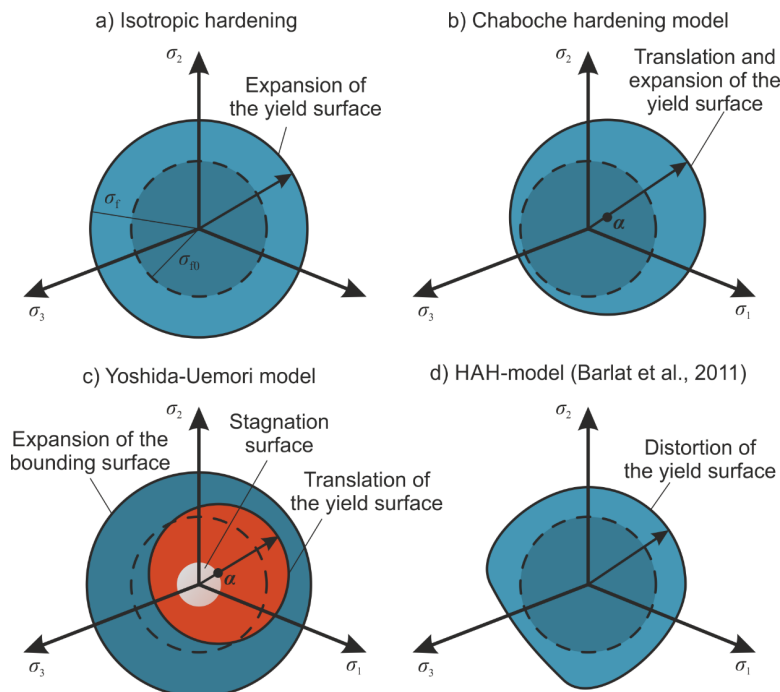
Figure 6.1: Schematic representations of the investigated hardening models

The investigated models possess increasing levels of complexity regarding the facets of work-hardening behavior they are capable of exhibiting. In the following, each model is addressed individually with regard to its implementation and necessary modifications to allow modelling of the work-hardening behavior observed in the previous chapters.

6.1.1 Isotropic hardening

Commonly, work-hardening is considered to evolve isotropically, i. e. independent of the loading direction or strain path. In the present scope, isotropic hardening was used as a reference for the more advanced kinematic and distortional hardening models. As isotropic hardening (Figure 6.1a) is the default work-hardening behavior in most commercial FEM-software packages including Abaqus/CAE, implementation was not necessary. A subroutine (UHARD.for) was used to define the parameterized evolution of the isotropic hardening component in terms of the relation

$$\sigma_{\text{f,iso}} = \underbrace{w C_{\text{iso}}(\bar{\varepsilon}^p + \varepsilon_0)^n}_{\substack{\text{Non-saturating} \\ \text{hardening component}}} + \underbrace{(1-w)R_{\text{sat}}\big(1 - e^{-k\bar{\varepsilon}^p}\big)}_{\substack{\text{Saturating} \\ \text{hardening component}}}. \tag{6.1}$$

The weighting factor $0 < w < 1$ controls the intensity of the non-saturating and the saturating hardening component. The saturating hardening term includes the saturated flow stress at infinite strains R_{sat} and the rate of saturation k. The non-saturating hardening term includes the parameters ε_0 and n, which are the shift parameter and the hardening exponent, respectively.

6.1.2 Chaboche combined hardening

The combined hardening model presented by Lemaître and Chaboche (1990) was utilized in this work (**Figure 6.1b**). The model, hence on referred to as "Chaboche model", is a combination of isotropic and kinematic hardening based on a generalized form of the kinematic hardening model first presented by Ziegler (1959).

In the Chaboche model, kinematic hardening in terms of the evolution law of the back-stress tensor $\boldsymbol{\alpha}$ evolves according to the relation

$$\dot{\boldsymbol{\alpha}} = C\dot{\bar{\varepsilon}}^p \frac{1}{\sigma_{\text{f0}}}(\boldsymbol{\sigma} - \boldsymbol{\alpha}) - \gamma \boldsymbol{\alpha}\dot{\bar{\varepsilon}}^p, \tag{6.2}$$

where C and γ are material parameters that control the intensity and rate of kinematic hardening and σ_{f0} is the initial radius of the yield surface. With increasing plastic strain, the kinematic hardening component of the model saturates to a value of C/γ after which the yield surface does not translate further and hardening hence on evolves in a purely isotropic fashion. The Chaboche model generally allows superposition of several back stresses $\boldsymbol{\alpha_i}$ whose evolution is controlled by their corresponding material parameters C_i and γ_i. In the present case, two back stress components were considered with $\gamma_2 = 0$,

which activates a non-saturating kinematic hardening component with a linear hardening modulus of C_2. This setting allows to capture the permanent softening observed for 16MnCrS5 after a strain path reversal, however, work-hardening stagnation cannot be modelled. As none of the materials investigated in this work exhibit a saturating work-hardening at large strains, the isotropic part of the model was generalized according to **Eq. (6.1)**.

6.1.3 Modified Yoshida-Uemori combined hardening

The combined hardening model presented by Yoshida and Uemori (2002) (hence on, referred to as Yoshida-Uemori model) is capable of modelling all known anisotropic work-hardening phenomena exhibited after strain path reversals with large pre-strains.

At the time of creation of this thesis, the Yoshida-Uemori model was not available in the FEM software Abaqus. The model was thus implemented utilizing a return map algorithm with a semi-implicit integration method presented by Ghaei et al. (2010), utilizing the user-defined Fortran subroutine UMAT.for. The UMAT-subroutine is called at the beginning of each iteration at each integration point. The components of the total strain tensor and the internal variables of the previous step are used as inputs. The user-defined subroutine then calculates the updated elastic and plastic strain increments as well as the updated internal variables. The internal variables of the Yoshida-Uemori model include the back stress tensors $\boldsymbol{\alpha}$ and $\boldsymbol{\beta}$ which account for the current centers of the yield and the bounding surface as well as their corresponding radii Y and B. The current radius of the stagnation surface is symbolized by R.

In its original form, the Yoshida-Uemori incorporates saturating isotropic hardening of the bounding surface. The evolution of isotropic hardening was generalized according to Eq. (6.1) as suggested by Yoshida et al. (2013) to account for the non-saturating work-hardening behavior at large strains observed for all investigated steels, including 16MnCrS5.

In the standard-form of the Yoshida-Uemori model, the rate of saturation of the isotropic hardening component of the bounding surface and its rate of translation are both controlled by the parameter k. It was found, however, that this coupling leads to a limited flexibility of the model with regard to the evolution of the ratio of isotropic and kinematic hardening at large pre-strains. Therefore, the model was modified by implementing a new material parameter k_2, which controls only the rate of kinematic hardening of the bounding surface, whereas the parameter k, controls the saturation rate of its isotropic hardening.

The implicit time integration scheme applied by Abaqus Standard requires the UMAT-subroutine to provide the material tangent at each iteration of the global integration scheme. Due to the modification of the isotropic hardening component, the derivative of Eq. (6.1) with respect to the plastic strain increment must be provided additionally.

While Ghaei and Green (2010) have also presented an approach for a fully implicit integration scheme of the Yoshida-Uemori model, the semi-implicit approach was chosen due to the simplified implementation procedure and the satisfactory compromise between precision and computation time. In the semi-implicit integration procedure, only the plastic strain increment is determined implicitly, while the other internal variables are determined explicitly. To minimize drift from the flow surface caused by the explicit integration scheme and assure robust convergence of the semi-implicit integration scheme, an automatic sub-stepping algorithm was implemented. After calculation of the updated plastic strain increment $\Delta\varepsilon^{\mathrm{p}}$ the value is checked against a pre-defined threshold value $\Delta\varepsilon^{\mathrm{p,max}}$. If the plastic strain increment exceeds this value at any given integration point, the iteration is started over with a reduced step size according to

$$\Delta t_{\mathrm{new}} \leftarrow \Delta t_{\mathrm{old}} \cdot \Delta\bar{\varepsilon}^{\mathrm{p,max}} \cdot c. \tag{6.3}$$

Herein, the value c refers the scaling factor that guarantees the plastic strain at the corresponding integration point to be below the threshold after a single iteration ($0 < c < 1$). In the present case, $\Delta\bar{\varepsilon}^{\mathrm{p,max}} = 0.001$ and $c = 0.9$ provided a satisfactory compromise between calculation time and robust convergence. While this straight-forward method does not yield perfect numerical efficiency, as the iteration is started over even if the plastic strain increments for individual elements is lower than the prescribed threshold, the simplicity of the approach with the given Abaqus functionalities in conjunction with an acceptable calculation time was reason enough for the approach to be adequate.

6.1.4 Homogeneous anisotropic hardening model

The HAH-model (**Figure 6.1d**) is a distortional hardening model that was first presented by Barlat et al. (2011) and extended frequently in the recent years, e. g. by to incorporating cross-hardening effects. For the sake of this thesis, the HAH-model was provided to the IUL by their inventors[1].

The HAH-model includes the following material dependent parameters:

- Material parameters connected to isotropic hardening as given in Eq. (6.1),
- exponent q controlling the flatness of the back of the yield surface,
- k_{b} controls the rate of rotation of the microstructure deviator,

---

[1] The HAH-model was provided to the Institute of Forming Technology and Lightweight Components by Professor Frédérick Barlat and his coworker Seong-Yong Yoon in terms of a Abaqus UMAT-subroutine. Considering the extensive amount of work that goes into implementing such an advanced constitutive model we are very thankful and highly appreciate the trust that goes along with this.

- the coefficients k_1, k_2 and k_3, which control the evolution of the new flow stress and the hardening rate after strain path reversal and
- k_4 and k_5 control the evolution of permanent softening.

In contrast to most kinematic hardening models, the HAH-model can capture changes of the work-hardening behavior over multiple load cycles. For a detailed description of the model and its implementational aspects please refer to the original publications, summarized in Section 2.1.3.

6.1.5 Parameter sensitivity study

The material parameters of all investigated constitutive models are summarized in **Table 6.1**. The models are sorted according to their corresponding number of material dependent parameters. All models incorporate an isotropic hardening component which is the weighted sum of a saturating and a non-saturating part according to Eq. (6.1).

Table 6.1: Material parameters of the investigated (modified) hardening models

Hardening model	Isotropic hardening parameters						Kinematic / distortional hardening parameters						#
	Non-saturating				Saturating								
Isotropic							-						6
Chaboche	w	C	ε_0	n	R_{sat}	k	C_1		γ_1		C_2		9
Yoshida-Uemori							c	B	b	h	k_2		11
HAH-model							q	k_1 k_2	k_3	k_4	k_5	k_{HAH}	13

To validate the models' functionality and illustrate their capabilities with regard to different anisotropic hardening phenomena, single element FEM-simulations were conducted for each model. To account for the load reversal behavior the load was reversed at specified pre-strains $\varepsilon_{\mathrm{pre}}$. Selected model parameters were varied based on fixed reference sets of generic model parameters taken from the literature, to illustrate their influence on the resulting anisotropic work-hardening behavior. In the following figures, the solid lines correspond to the work-hardening behavior exhibited under monotonic loading and the dashed lines indicate the work-hardening behavior exhibited after the strain path reversal. The direction of the black arrows indicate the effect of an increase of the corresponding model parameter.

Isotropic hardening

The effects of selected isotropic model parameters are shown in **Figure 6.5**. The parameter C scales the curves, the hardening exponent n defines the slope of the work-hardening curve and k controls the rate of saturation toward the hardening level R_{sat}. Per definition of isotropic hardening, the flow stress after strain path reversal equals the flow stress before strain path reversal yielding the conventional hardening model incapable of modelling the anisotropic work-hardening behavior of 16MnCrS5.
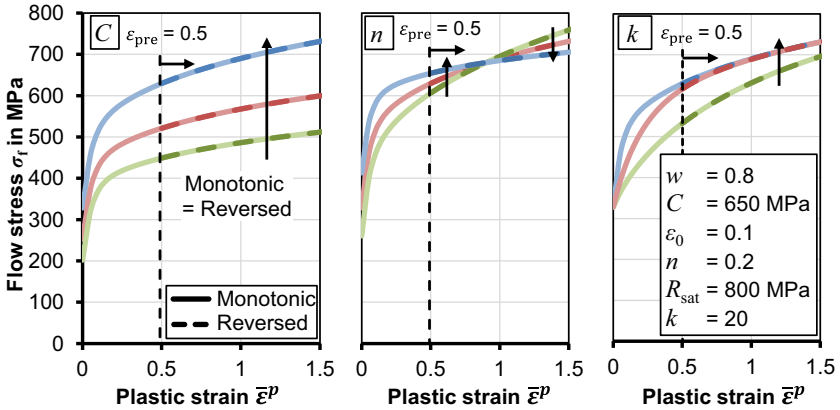
Figure 6.2: Effect of isotropic hardening parameters on the work-hardening behavior

Chaboche combined hardening

The effects of the Chaboche hardening parameters are illustrated in **Figure 6.6**. The ratio between C_1 and γ_1 controls the amount of kinematic hardening, whereas γ_1 additionally controls the rate of saturation of the back stress tensor, which causes a change of the initial hardening slope after strain path reversal.
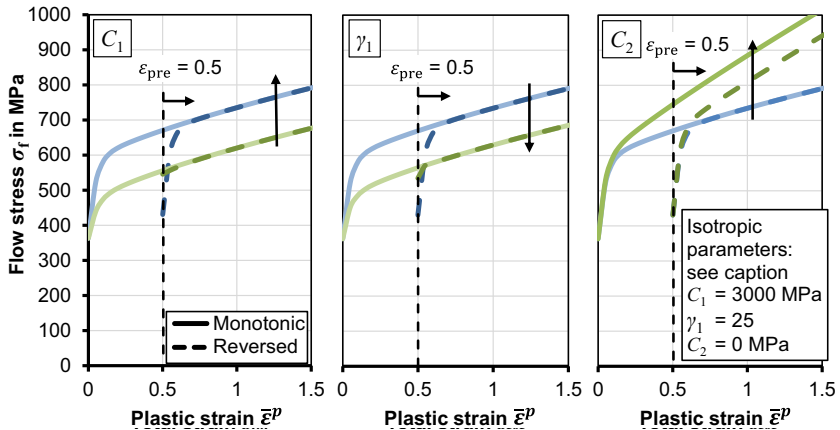
Figure 6.3: Effect of Chaboche parameters on the work-hardening behavior ($\sigma_{f0} = 328$ MPa, $w = 0.5$, $C = 350$ MPa, $\varepsilon_0 = 0.1$, $n = 0.7$, $R_{sat} = 200$ MPa, $k = 20$)

By applying an additional kinematic hardening component with a saturation rate $\gamma_2 = 0$, the saturation can be deactivated. This enables the model to capture permanent softening

to a certain degree. The amount of permanent softening depends on the amount of pre-strain weighted by the kinematic hardening slope C_2.

It is noted that in the combined hardening model, both the monotonic work-hardening curve as well as the reverse work-hardening curve are affected by the kinematic hardening component, as the overall hardening behavior is always a combination of both components. This property complicates the parameter identification procedure, as the isotropic and kinematic hardening components cannot be fit separately.

Yoshida-Uemori model

Figure 6.4 illustrates the influence of some selected Yoshida-Uemori hardening parameters on the resulting anisotropic work-hardening behavior. The parameter c controls the rate of translation of the yield surface toward the boundary surface, which causes a change in the hardening slope after load reversal. The initial boundary surface radius B scales the complete work-hardening curve (monotonic and reversed). The parameter h controls the intensity of work-hardening stagnation in terms of the width of the initial work-hardening plateau after load reversal. In analogy to the Chaboche model, both the work-hardening behavior under monotonic as well as under reverse loading are controlled by the isotropic and the kinematic hardening components.
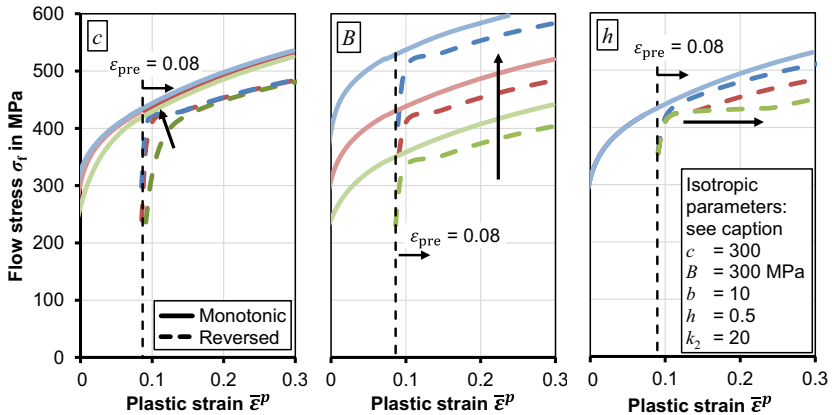
Figure 6.4: Effect of Yoshida-Uemori parameters on the resulting work-hardening behavior ($\sigma_{f,0} = 328$ MPa, $w = 0.8$, $C = 650$ MPa, $\varepsilon_0 = 0.1$, $n = 0.2$, $R_{sat} = 800$ MPa, $k = 20$)

HAH-model

The influences of the parameters k_1, k_4 and k_5 of the HAH-model are illustrated in **Figure 6.5**. The parameter k_1, prescribes the rate of hardening after strain path reversal and the parameters k_4 and k_5 control the amount of permanent softening.
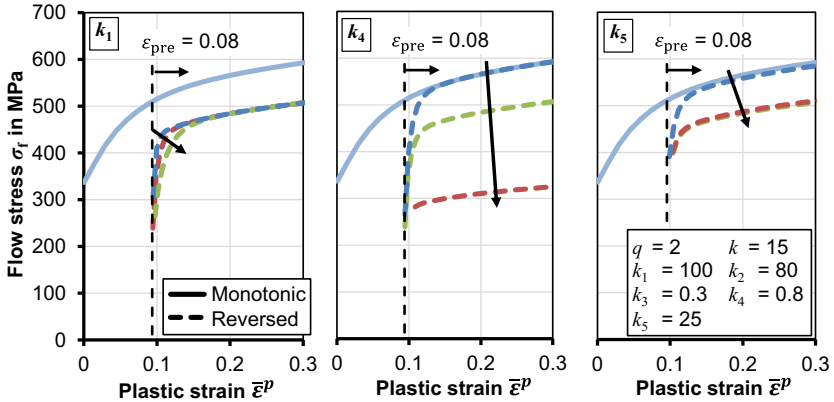
Figure 6.5: Effect of HAH-parameters on the work-hardening behavior ($\sigma_{f,0} = 328$ MPa, $w = 0.2$, $C = 650$ MPa, $\varepsilon_0 = 0.1$, $n = 0.2$, $R_{sat} = 800$ MPa, $k = 20$)

In contrast to the Yoshida-Uemori model, the work-hardening curve under monotonic loading is completely independent of the model parameters corresponding to the microstructure deviator which controls the behavior exhibited after strain path reversals, which makes handling of the model parameters quite convenient. In the provided form, the HAH-model was not capable to model work-hardening stagnation.

6.2   Parameter identification

The material parameters of all investigated constitutive models were determined with the goal to correctly model the anisotropic hardening behavior of 16MnCrS5, by applying a direct as well as an inverse identification procedure both of which are described in the following.

6.2.1   Direct parameter identification

Under the assumption of uniaxial stress the isotropic and Chaboche hardening models allow for the derivation of a closed form solution for the calculated flow stress as a function of the plastic strain. The material parameters of the models could thus be determined directly by fitting the analytical relations to the experimentally obtained hardening curves without the need to perform numerical simulations. In the following the procedure is described in detail.

Isotropic hardening

To determine the parameters of the isotropic hardening model, the experimental data obtained by tensile tests on elongated material (Figure 4.29) was prescribed in terms of a tabular relation between the flow stress and the plastic strain. The work-hardening

behavior under reverse loading was not considered in the adjustment of the isotropic hardening law, as isotropic hardening is not capable to model the corresponding work-hardening phenomena effects exhibited after a strain path reversal.

The error between the analytically and experimentally obtained work-hardening curves was calculated in terms of the mean squared error (MSE) according to

$$MSE = \frac{1}{n}\sum_{i=1}^{n}\left(|\sigma_{\text{f,sim}}(\bar{\varepsilon}_i^p)| - |\sigma_{\text{f,exp}}(\bar{\varepsilon}_i^p)|\right)^2. \tag{6.4}$$

Herein, n is the number of evaluated data points and $\sigma_{\text{f,sim}}$ and $\sigma_{\text{f,exp}}$ are the calculated and experimental flow stress values corresponding to the plastic strain $\bar{\varepsilon}_i^p$ at the i-th data point. The mean square error function was minimized by adjusting the material parameters via a MATLAB optimization environment.

Chaboche combined hardening

Assuming uniaxial loading the work-hardening behavior resulting from the Chaboche model can be determined analytically as

$$\sigma_{\text{f,sim}\pm} = |\sigma_{\text{f,iso}} + \alpha_{\pm}|. \tag{6.5}$$

Herein, σ_{f+} refers to the flow stress under uniaxial monotonic loading and σ_{f-} refers to the flow stress after a strain path reversal. The term $\sigma_{\text{f,iso}}$ corresponds to the current radius of the yield surface according to the isotropic hardening law given in Eq. (6.1).

The back stress under monotonic loading α_+ is determined in an explicit form by integration of the back stress evolution equation given in Eq. (6.2) resulting in

$$\alpha_+ = \frac{C_1}{\gamma_1}\left(1 - e^{-\gamma_1 \bar{\varepsilon}^p}\right) + C_2 \bar{\varepsilon}^p \tag{6.6}$$

The back stress component after load reversal α_-, which is a function of the pre-strain ε_{pre} before the strain path reversal is given by

$$\alpha_- = -\alpha_+(\varepsilon_{\text{pre}}) + 2\frac{C_1}{\gamma_1}\left(1 - e^{-\gamma_1(\bar{\varepsilon}^p - \varepsilon_{\text{pre}})}\right) + C_2\left(\bar{\varepsilon}^p - \varepsilon_{\text{pre}}\right), \tag{6.7}$$

where $\alpha_+(\varepsilon_{\text{pre}})$ is the yield surface translation previous to the load reversal. By inserting Eq. (6.6) and Eq. (6.7) in Eq. (6.5) the analytical relation can be used to adjust the model parameters of the Chaboche model in order to fit the numerical work-hardening data to the experimentally obtained monotonic and reverse flow stress data at prescribed pre-strains $\varepsilon_{\text{pre,i}}$.

The material parameters of the Chaboche model were optimized by minimizing the Mean-Square-Error function *MSE* according to Eq. (6.4) via the aforementioned MATLAB optimization environment.

6.2.2   Inverse parameter identification

In the cases of the Yoshida-Uemori model and the HAH-model, an inverse parameter identification procedure has been applied according to **Figure 6.6**.
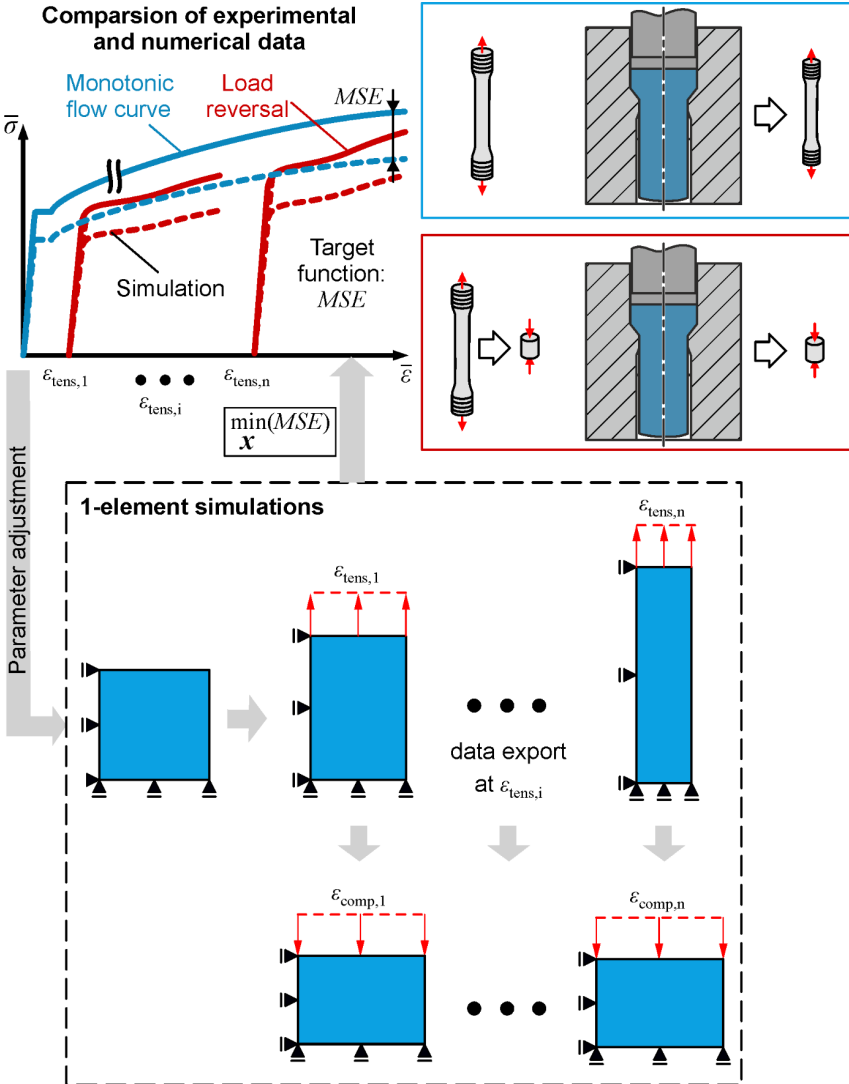

Figure 6.6: Parameter identification procedure

The material behavior is incorporated in terms of the Abaqus-specific Fortran-subroutine UMAT (user material), which is called by the single element model to calculate the resulting stress from prescribed strain data. The UMAT-files contain the corresponding material parameters in a parameterized form, i. e. as placeholders which can be found and replaced with actual values by the optimization environment.

Starting from an initial set of model parameters x_0, LS-Opt calls Abaqus via batch file operations and starts a single element simulation in which the top edge of the element is translated up and the element is elongated up to the maximum investigated pre-strain $\varepsilon_{tens,n}$. The additional restart-files are exported at pre-defined intervals, which contain the deformed configuration of the element at prescribed pre-strains $\varepsilon_{tens,i}$. The deformed single element models are then loaded in the opposite direction causing a strain path reversal at each pre-scribed pre-strain. After all simulations of a specific parameter set are completed, the batch file calls a Python-subroutine to extract the stress-strain data of each model, which is then compared to the experimental data by means of the mean square error function *MSE*. After determining a set of material parameters in terms of a D-optimal design space and finishing the simulations, the optimization algorithm analyzes the resulting response surfaces to determine appropriate parameter sets x_{i+1} for the next iteration. After each iteration, the parameter domains are reduced to ensure convergence of the solution. The applied parameter identification procedure is described in detail by Stander et al. (2005).

In the small pre-strain regime, the experimental data from upsetting tests on elongated material, and for the large pre-strain regime, the data from upsetting tests on cold extruded material was used. To ensure the correct solution under monotonic loading the data from tensile tests on extruded material was used according to Section 4.4.3. The pre-strains for each experimental data curve were determined by means of the effective average strains according to Section 4.3.1.

6.2.3 Results of the parameter identification

In this section, the results of the parameter identification are presented for all investigated material models. For the sake of a simplified illustration, the flow stress data in compression was fit to four selected flow curves with pre-strains of $\varepsilon_{ex,1} = 0.3$, $\varepsilon_{ex,2} = 0.5$, $\varepsilon_{ex,3} = 1.0$ and $\varepsilon_{ex,4} = 1.2$. The experimental data used to fit the material models are indicated by the dashed lines. The results of the numerically obtained curves with optimized material parameters are given as solid lines. It was assured, that all material models yield the same work-hardening behavior under monotonic tension.

Isotropic hardening

The work-hardening curves generated by the isotropic hardening model along with the optimized isotropic hardening parameters are shown in **Figure 6.7**. The experimental

curves obtained during subsequent compression were ignored for the optimization of the isotropic hardening parameters, to prevent an underestimation of the monotonic work-hardening curve.
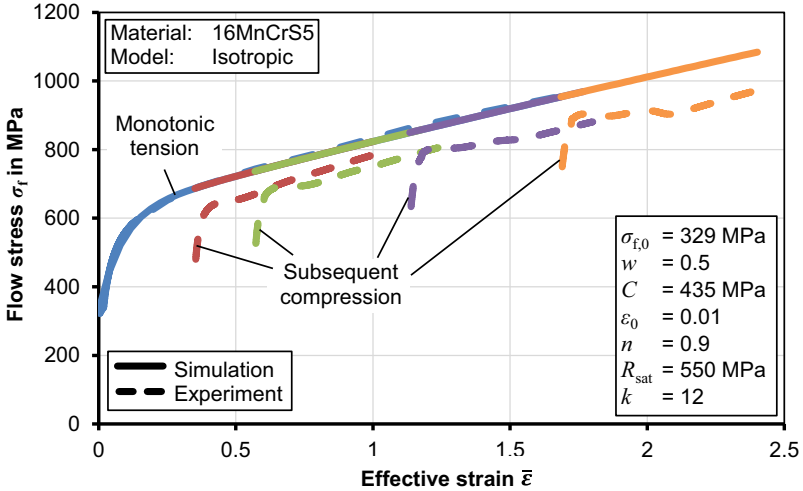
Figure 6.7: Experimental and numerical flow curves using isotropic work-hardening

In monotonic tension, the isotropic hardening model yields satisfactory results. The near-linear hardening of the monotonic flow curve is achieved by using a hardening coefficient n in the non-saturating hardening component close to 1, whereas the initial curvature is achieved by the saturating hardening component. As expected, under subsequent compression, the model overestimates the work-hardening curves significantly.

Chaboche hardening model

Two variants of the Chaboche hardening model were utilized. The first variant is the standard Chaboche hardening model with one back stress component (**Figure 6.8**). The second variant is extended by a second back stress component with $\gamma_2 = 0$, which deactivates the saturation of the corresponding kinematic hardening component and thus allows modelling of permanent softening (**Figure 6.9**).

Both model variants can capture the reduced yield stress under subsequent compression over the whole investigated pre-strain regime. However, considering only a single saturating kinematic hardening component leads to a fast convergence toward the monotonic work-hardening curve, which prevents modelling of both work-hardening stagnation and permanent softening.

The non-saturating kinematic hardening component leads to an irreversible drift of the yield surface during tensile loading, which causes permanent softening. However, the evolution of permanent softening with the pre-strain is not captured well.
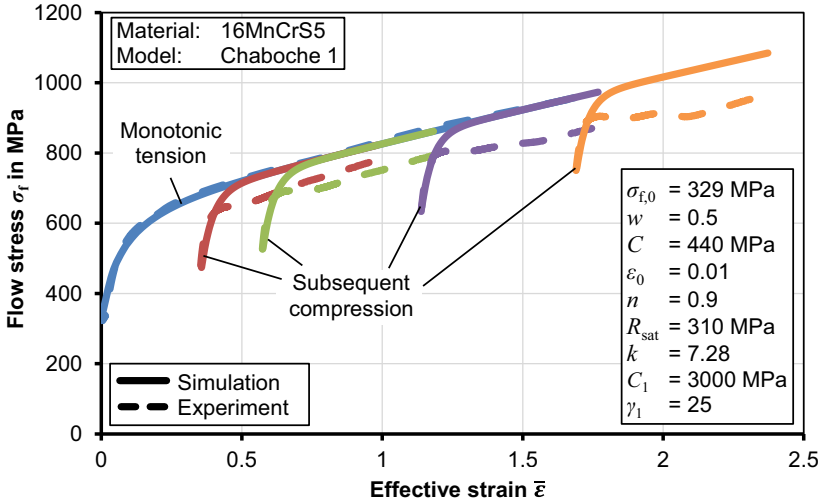
Figure 6.8: Experimental and numerical flow curves using the Chaboche work-hardening model with one back stress component (Chaboche 1)
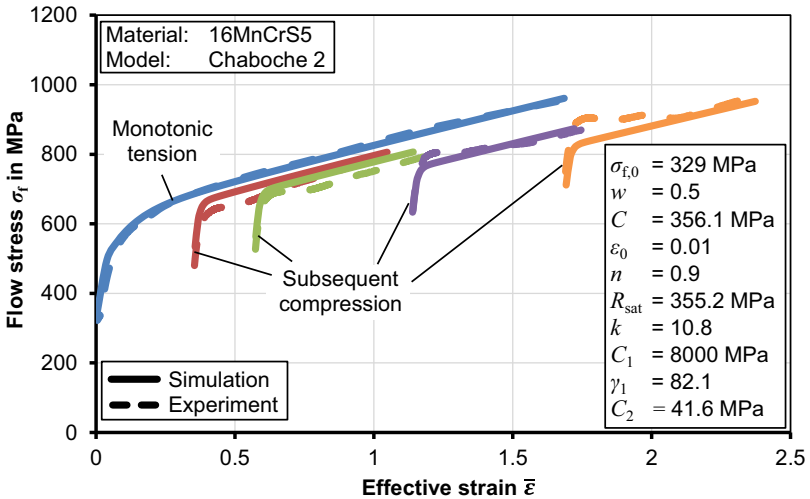
Figure 6.9: Experimental and numerical flow curves using the Chaboche work-hardening model with two back stress components (Chaboche 2)

The amount of permanent softening correlates to the pre-strain (multiplied by the kinematic hardening parameter C_2). As the pre-strain starts at zero, the model predicts low permanent softening at low pre-strains and more pronounced permanent softening at larger pre-strains. As each of the flow curves under subsequent compression was weighted equal, this leads to an underestimation of permanent softening in the small pre-strain regime and an overestimation in the large pre-strain regime.

Modified Yoshida-Uemori model

The results of the Yoshida-Uemori hardening model are shown in **Figure 6.10**. The model can capture all observed anisotropic hardening phenomena related to the strain path reversal with a high accuracy. These include the Bauschinger effect, transient hardening, work-hardening stagnation, and permanent softening.
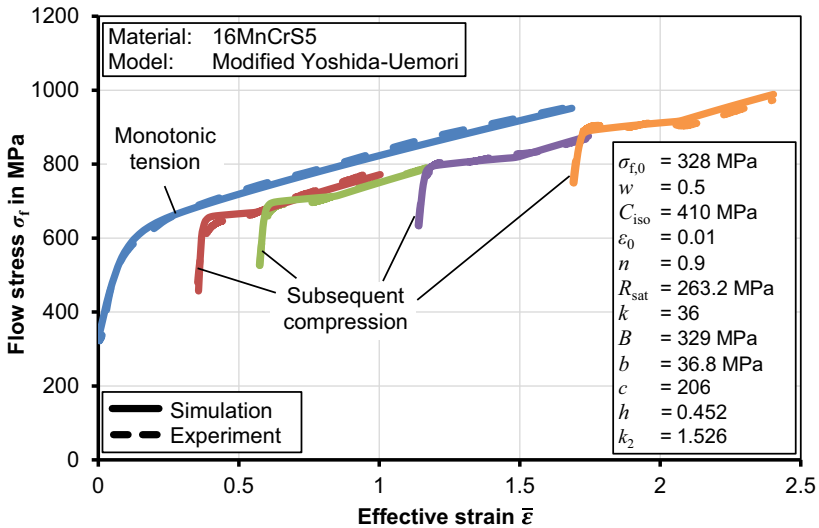
Figure 6.10: Experimental and numerical flow curves using the modified Yoshida-Uemori hardening model

In the original Yoshida-Uemori model the saturation rates of the isotropic and kinematic hardening of the bounding surface B are both described by the single model parameter k. With the original description, the experimentally observed evolution of permanent softening with the pre-strain could not be met well over the large pre-strain regime. For the sake of this thesis, the isotropic and kinematic hardening rates were thus uncoupled and a new parameter k_2 was introduced, which controls only the kinematic hardening rate of the bounding surface. The isotropic hardening rate of the bounding surface is still

controlled by the parameter k. This modification has led to an increased model flexibility with regard to the evolution of permanent softening at large pre-strains.

HAH-model

The results of the parameter identification for the HAH-model are shown in **Figure 6.11**. A unique property of the HAH-model is the capability to capture effects that only occur at multiple load cycles (e. g. tension-compression-tension). As the provided experimental data only accounts for single reverse cycles with large pre-strains, multiple material parameters of the model are redundant (q, k_{HAH}, k_2, k_3, k_5) and were thus taken from the literature. In the figure, the redundant parameters are indicated by the brackets.
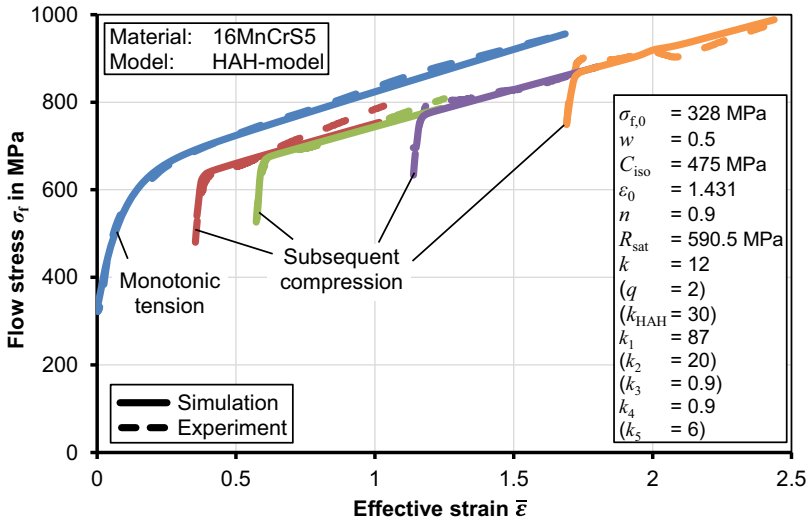
Figure 6.11: Experimental and numerical flow curves using the HAH-model

The HAH-model can successfully capture the Bauschinger effect, transient hardening, and permanent softening. However, in its original form, the HAH-model is not capable to capture the extensive work-hardening stagnation and the evolution of the work-hardening slope with the pre-strain. While the HAH-model yields significant improvements over isotropic hardening and the Chaboche combined hardening model with one back stress component. However, due to its relatively high calculation time and its inability to capture work-hardening stagnation, it was not considered for further investigations.

6.3 Summary

In this chapter, constitutive models of increasing complexity were selected and utilized to capture the material behavior of 16MnCrS5 exhibited under monotonic strain paths

up to large strains as well as under strain path reversal with large pre-strains. A summary of the models' capability to capture various work-hardening phenomena is given in **Table 6.2**.

Table 6.2: Comparison of constitutive models with regard to their capability to model various anisotropic work-hardening phenomena at large strains

Model	Bauschinger effect	Permanent softening	Work-hardening stagnation	Number of parameters	Calculation time*
Isotropic				6	1
Chaboche 1	✓			8	1
Chaboche 2	✓	(✓)		9	1
YU	✓	✓	✓	11	3**
HAH	✓	✓		13	6**

* The calculation time was determined by simulations of forward rod extrusion as described in Appendix B (extrusion strain $\varepsilon_{ex} = 0.5$, $2\alpha = 90°$, $r_{ex} = 3$ mm), isotropic hardening was defined as reference

** The YU- and HAH-model were not optimized with regard to numerical efficiency. The high calculation time is partly attributed to the global sub-stepping algorithm. A local sub-stepping algorithm, which is not in the scope of this thesis, expectedly leads to a significant reduction of calculation time

Of all investigated models, the modified Yoshida-Uemori model is the only model able to capture all work-hardening phenomena exhibited by 16MnCrS5. While the distortional HAH-model leads to a significant improvement over the Chaboche kinematic hardening model, its high calculation time and inability to model work-hardening stagnation in the available version have led to the exclusion of the model for the subsequent investigations. In the following chapter, the remaining hardening models were utilized to investigate the influence of individual anisotropic hardening phenomena on the process and product properties in cold forging.

7 Anisotropic hardening in single-stage cold forging processes

In this chapter, the influence of anisotropic work-hardening phenomena on the process and product properties is investigated by the example of basic cold forging processes. The investigated process and component properties include the forming forces, the flow stress distribution and forming-induced residual stresses. The simulation result are validated experimentally by the example of forward rod extrusion.

7.1 Investigated cold forging processes

The consequences of anisotropic hardening are investigated by the example of the two basic cold forging processes: forward rod extrusion (**Figure 7.1a**) and backward can extrusion (**Figure 7.1b**). The influence of the most important process parameters on the process and product properties were determined in terms of a parametric study (**Figure 7.1c**).
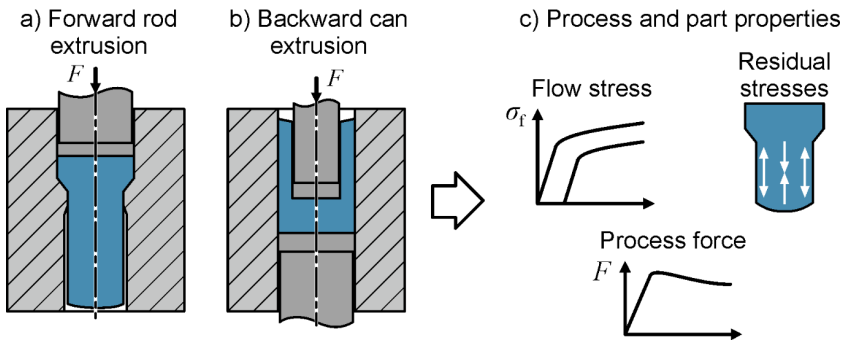
Figure 7.1: Investigated basic cold forging processes

To determine the influence of individual anisotropic work-hardening phenomena, the workpiece material behavior of 16MnCrS5 was modeled with the constitutive models presented in the previous section. To isolate influences of anisotropic hardening on the process and product properties, isotropic hardening was used as the reference. To assure convergence of the simulations even at large extrusion strains, the manual remeshing algorithm according to **Appendix C** was applied in the simulations whenever necessary.

7.1.1 Forward rod extrusion

Forward rod extrusion is investigated to represent a basic cold forging process. A process parameter variation was conducted with regard to the influence of the extrusion strain and the die cone angle on the resulting product and process properties considering isotropic and anisotropic hardening. The investigated process parameters are given in **Figure 7.2**. In order to capture the residual stress relaxation caused by small plastic

deformations during the ejection process, the dies and container were modeled as elastic objects and the ejection step has been simulated as well.

Varied parameters						
Extrusion strain $\varepsilon_{ex} = 2 \ln(d_0 / d_1)$				Die angle 2α		
0.3	0.5	0.7	1.0	60°	90°	120°

Fixed parameters			
Workpiece diameter d_0	Workpiece length l_0	Transition radii r_{ex}	Die land length l_{ex}
30 mm	71 mm	3 mm	3.5 mm
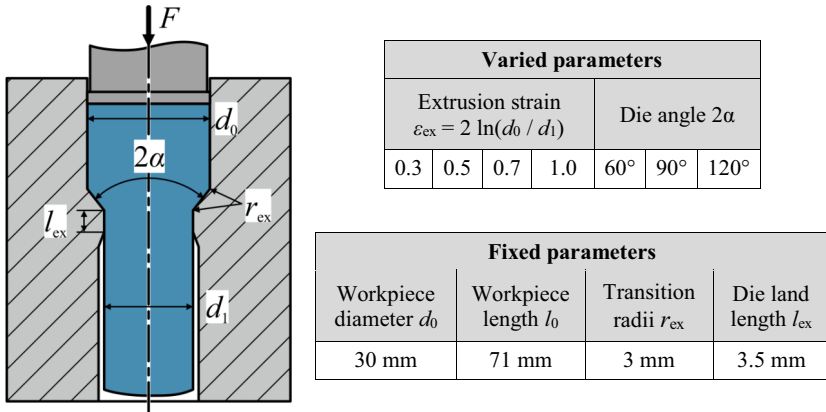
Figure 7.2: Investigated process parameters in forward rod extrusion

7.1.2 Backward can extrusion

Backward can extrusion was chosen as the second investigated basic cold forging process. In the case of backward can extrusion the relative area reduction ε_{bc} was varied according to **Figure 7.3**, to compare the influence of isotropic and anisotropic hardening on the resulting product and process properties. All other geometric parameters were kept fixed as shown in the figure.

Varied parameter		
Area reduction $\varepsilon_{bc} = d_i^2 / d_a^2$		
0.2	0.4	0.6

Fixed parameters			
Workpiece diameter d_a	Workpiece length l_0	Transition radii r_{ex}	Punch land length l_{bc}
30 mm	30 mm	2 mm	2.5 mm
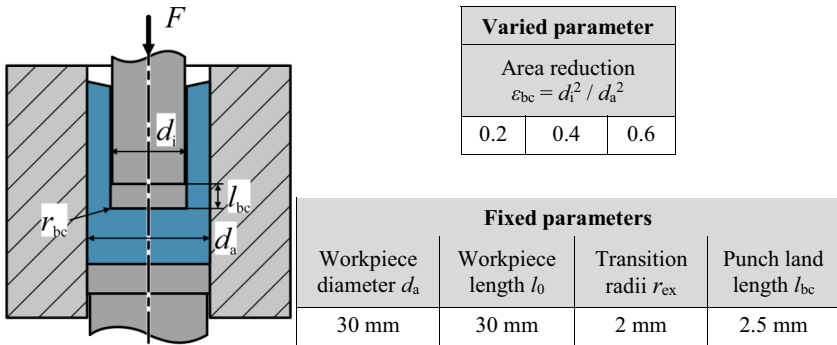
Figure 7.3: Investigated process parameters in backward can extrusion

To identify a potential effect of anisotropic hardening on the occurrence of new plastic strains during ejection, the backward movement of the ram and the ejection step have been modeled analogously to forward rod extrusion.

7.2   Influence of anisotropic hardening on component properties

7.2.1   Flow stress

Cold forging typically leads to an increase of the local flow stress of the workpiece, as the increase of the dislocation density leads to work-hardening, which affects the part's performance including its strength, hardness and fatigue life. When no intermediate heat-treatment is applied in multi-staged cold forming processes, the increase of local flow stress also affects the required forming forces in subsequent forming stages. The anisotropic hardening of 16MnCrS5 presented in the previous chapters is expected to have a significant impact on the flow stress distribution of the parts after cold forging.

If isotropic hardening is assumed, the local flow stress $\sigma_{f,iso}$ is directly related to the plastic strain $\bar{\varepsilon}^p$, either in terms of a tabular or analytical relation. In the present case, the combined Swift-Voce hardening relation was used according to the relation

$$\sigma_{f,iso}(\bar{\varepsilon}^p) = wC(\bar{\varepsilon}^p + \varepsilon_0)^n + (1-w)R_{sat}\left(1 - e^{-k\bar{\varepsilon}^p}\right), \qquad (7.1)$$

as described in Section 6.1.1. A visualization of the local flow stress distribution after forming is possible by means of a single contour plot, as the flow stress is a scalar value which does not depend on the type of stress state.

In the cases of the kinematic Chaboche and Yoshida-Uemori hardening models, the introduction of the yield surface translation, which is described by the back stress tensor $\boldsymbol{\alpha}$, leads to a more complex visualization of the local flow stress, as it depends on the type of stress state and the sign of the load ($\pm$).

Both of the aforementioned cases are illustrated by means of the yield locus (**Figure 7.4**), considering uniaxial tensile (+) and compressive (-) loading in xx-direction.
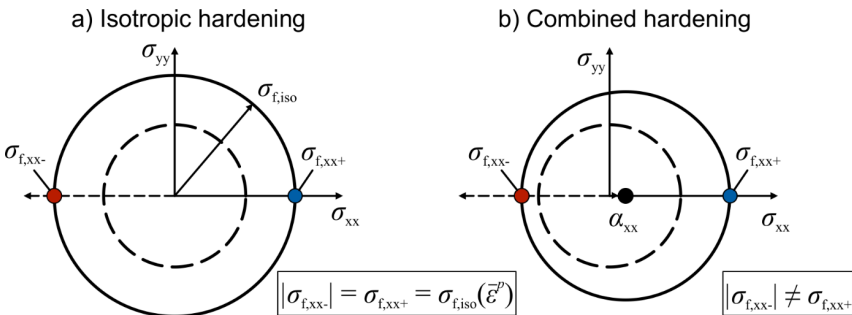
Figure 7.4: Flow stress determination in the yield locus for a) isotropic hardening and b) combined isotropic-kinematic hardening (von Mises yield criterion)

The flow stress is calculated with the von Mises yield condition according to

$$\sigma_{\text{Mises}}(\boldsymbol{\sigma} - \boldsymbol{\alpha}) - \sigma_{\text{f,iso}}(\bar{\varepsilon}^p) = 0 \tag{7.2}$$

$$\begin{aligned}
\Big[&\left((\sigma_{xx} - \alpha_{xx}) - (\sigma_{yy} - \alpha_{yy})\right)^2 + \left((\sigma_{yy} - \alpha_{yy}) - (\sigma_{zz} - \alpha_{zz})\right)^2 \\
&+ \left((\sigma_{zz} - \alpha_{zz}) - (\sigma_{xx} - \alpha_{xx})\right)^2 \\
&+ \left((\tau_{xy} - \alpha_{xy})^2 + (\tau_{xz} - \alpha_{xz})^2 + (\tau_{yz} - \alpha_{yz})^2\right)\Big]^{1/2} \\
&- \sigma_{\text{f,iso}}(\bar{\varepsilon}^p) = 0.
\end{aligned} \tag{7.3}$$

To calculate the flow stress for a given stress state, **Eq. (7.3)** must be solved for the corresponding component of the stress tensor, while all other components are set to zero. For each components of the stress tensor, there exist two solutions, which correspond to the two possible signs for each loading direction (tension/compression). Considering an arbitrary single component stress state this adds up to twelve flow stress values. The solutions of Eq. (7.3) for all single component stress states are given in **Appendix D**. In general, there exist two solutions for any possible stress state, corresponding to two points on opposite sides of the yield locus (Figure 7.4b).

The local flow stress distributions of forward extruded 16MnCrS5 rods are shown in **Figure 7.5**, assuming uniaxial loading in z-direction ($\sigma_{\text{f,zz}}$). For the combined hardening model, the flow stresses are shown under tensile (+) and compressive loading (-). As all three investigated kinematic hardening models yield nearly identical results with regard to the local flow stress after forming, only the results of the modified Yoshida-Uemori model are shown.
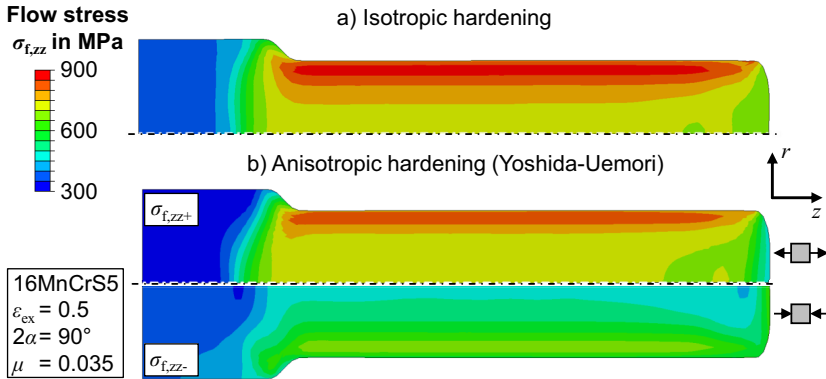
Figure 7.5: Flow stress distribution in forward extruded rods, considering a) isotropic and b) anisotropic hardening

All investigated anisotropic hardening models are capable to capture the flow stress difference under tensile and compressive loading observed in the material characterization experiments. As the material is predominantly stretched axially in forward extrusion,

the Bauschinger effect causes the material to have a much lower flow stress under subsequent axial compression, as compared to subsequent axial tension (in the core of the extrudate: $\sigma_{f,zz-} \approx 490$ MPa and $\sigma_{f,zz+} \approx 720$ MPa).

The local Bauschinger coefficient χ is calculated by dividing the local flow stress under compression and tension, which is a convenient measure to visualize the error in the flow stress prediction that is made by utilizing isotropic hardening models. Calculation of the stress direction-dependent Bauschinger coefficients when utilizing combined hardening models is summarized in **Appendix D**. The local Bauschinger coefficients considering axial loading χ_{zz} of forward extruded 16MnCrS5 rods are shown for various extrusion ratios in **Figure 7.6**. According to Eq. (7.3), there exist analogous plots as those shown in Figure 7.6 for any possible type of stress state (uniaxial stress, biaxial stress etc.) or loading direction (e.g. xx-direction).
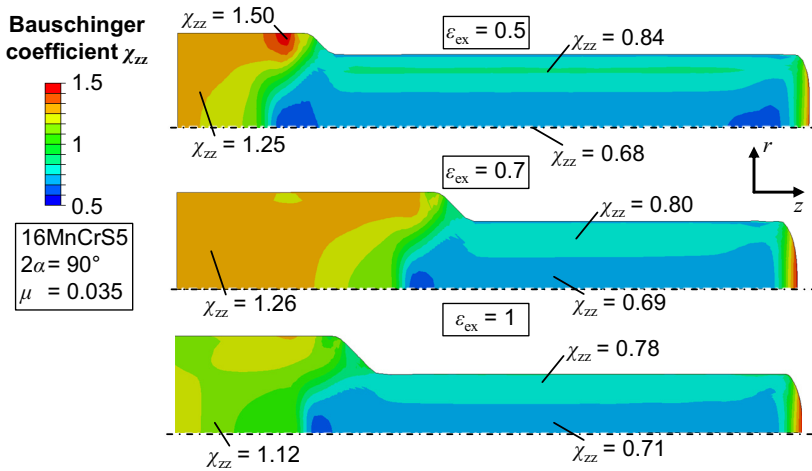
Figure 7.6: Influence of the extrusion strain on the Bauschinger coefficient χ_{zz} under subsequent axial loading (modified Yoshida-Uemori model)

In the core of the extrudates, the calculated Bauschinger coefficients correlate well with the real material behavior observed by tensile and upsetting tests on specimens extracted from the extrudates ($\chi_{zz,exp,core} = 0.69$), validating the parameter identification procedure presented in Section 6.2.2, which was done only by use of single element models. While the Bauschinger coefficient is lower than 1 in the shaft as the material is predominantly stretched, it is higher than 1 in the head region, where it is compressed. The results suggest, that the extrusion strain only has a minor impact on the Bauschinger coefficient.

The influence of the die cone angle 2α on the Bauschinger coefficient distribution is shown in **Figure 7.7** by the example of an extrusion strain of $\varepsilon_{ex} = 0.5$. The result suggest, that the Bauschinger coefficient becomes more inhomogeneous over the radius,

with increasing die cone angle, which is due to the material being slowed down and compressed in front of a steeper die shoulder, whereas in the core, the material flow and the Bauschinger coefficient are not affected. The die angle controls the hydrostatic pressure in the forming zone. However, a permanent change of flow stress due to the pressure was not observed in the experiments, which is in accordance with the simulations.
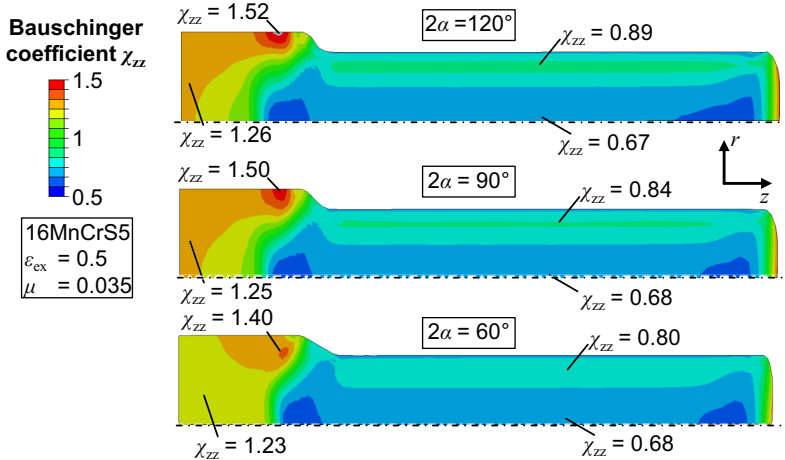
Figure 7.7: Influence of the die cone angle on the local Bauschinger coefficient χ_{zz} (modified Yoshida-Uemori model)

The local flow stress distributions of backward extruded cans under uniaxial loading in z-direction ($\sigma_{f,zz}$) are shown in **Figure 7.8**.
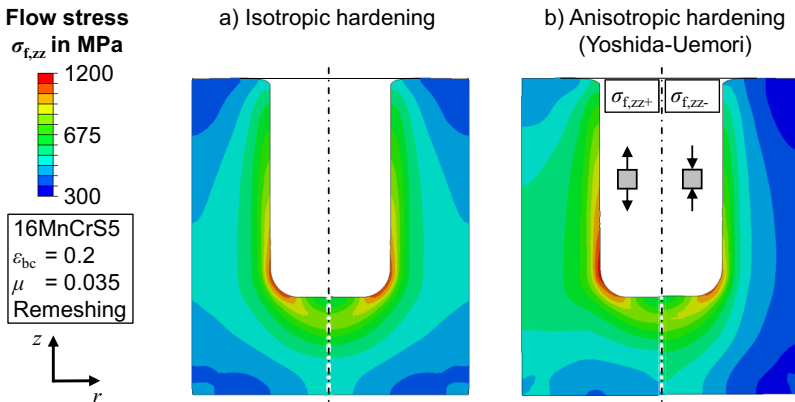

Figure 7.8: Flow stress distribution in backward extruded cans, considering a) isotropic and b) anisotropic hardening

Analogous to forward rod extrusion, the flow stress in the can wall under axial compressive loading is lower than the flow stress under axial tension loading, as the material in this region is predominantly axially stretched in the forming processes.

The area reduction in backward can extrusion controls the amount of strain in the can wall. The influence of the area reduction on the resulting Bauschinger coefficient is shown in **Figure 7.9**.
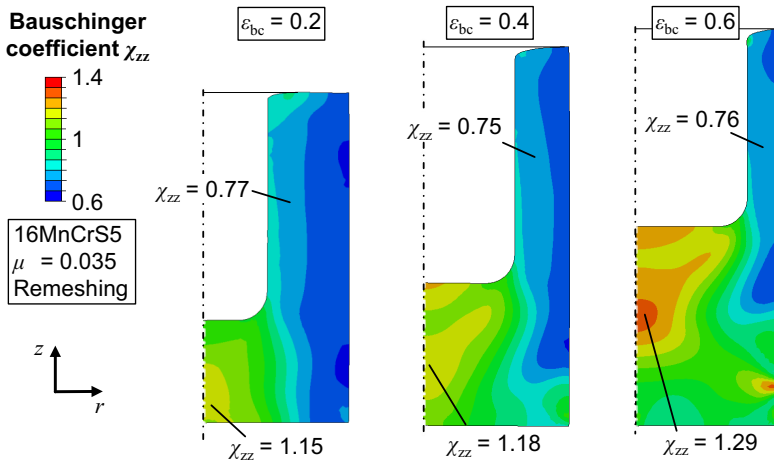
Figure 7.9: Influence of area reduction on the local Bauschinger coefficient χ_{zz} in backward can extrusion (modified Yoshida-Uemori model)

In the can wall, where the material has been stretched predominantly, the Bauschinger coefficient saturates at about $\chi_{zz} = 0.76$, whereas under the punch, the material is mainly compressed, leading to Bauschinger coefficients $\chi_{zz} > 1$.

7.2.2 Residual stresses

The evolution of residual stress in forward rod extrusion is shown in **Figure 7.10** by the example of an extrusion strain of $\varepsilon_{ex} = 0.5$, considering conventional isotropic hardening. As described in detail by Tekkaya (1986), residual stresses are generated due the occurrence of inhomogeneous elastic strains in the forming zone. In case of the axial residual zz-stress, this leads to high compressive stress in the core of the extrudate and positive residual stress towards the surface (**Figure 7.10a**). During ejection, a residual stress relaxation takes place, as new small plastic strains lead to an overall decrease of the elastic strain inhomogeneity (**Figure 7.10b**). After the extrudate is pushed out of the container, the friction forces are released and the part is fully unloaded, revealing the actual residual stress distribution.
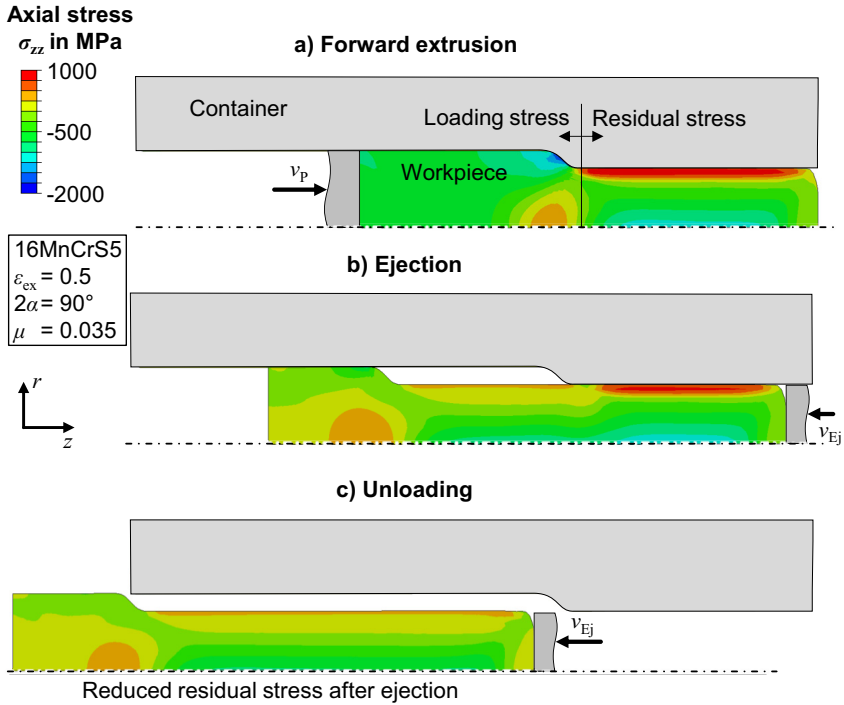
Figure 7.10: a) Residual stress built up during forward rod extrusion and b) relaxation during ejection (zz-stress, conventional isotropic hardening)

To identify the effect of the work-hardening formulation on the residual stress evolution, the axial stress distribution along the central line of the extrudate is shown during form-ing (**Figure 7.11**). In the forming stage, all anisotropic hardening models predict a lower axial residual stress in the core of the extrudate than the conventional isotropic harden-ing model. The Yoshida-Uemori model predicts the lowest axial stresses. The reason for the lowered residual stresses behind the forming zone, is the upsetting of the workpiece in the container, which causes a first stage-intrinsic strain path reversal. The strain path reversal is most pronounced towards to surface of the extrudate before the die shoulder, as the material is compressed most in this region. This leads to an alignment of work-hardening over the radius, even though the strains are highest at the surface, lowering the elastic-strain inhomogeneity over the radius. As Yoshida-Uemori model incorpo-rates the work-hardening stagnation after the strain path reversal the strain alignment is intensified.
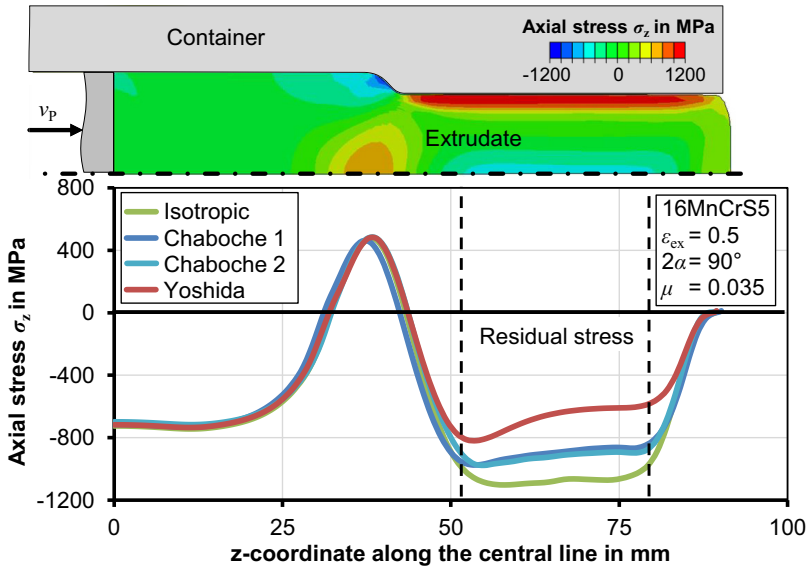
Figure 7.11: Axial stress distribution during forming in forward rod extrusion utilizing various work-hardening models

The influence of extrusion strain on the axial residual stress distribution over the squared radius (area) before ejection is shown in **Figure 7.12**. At all investigated extrusion strains, the conventional isotropic hardening model overestimates the residual stress distribution, especially in the core of the extrudate, whereas the Yoshida-Uemori model predicts the lowest axial residual stress distribution.
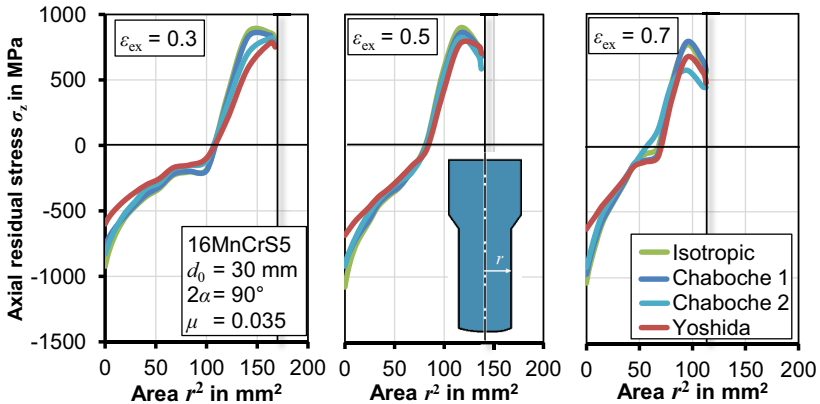
Figure 7.12: Effects of constitutive model and extrusion strain on calculated axial residual stress in forward rod extrusion (before ejection)

The anisotropic hardening models predict a lower flow stress under compression as compared to isotropic hardening leading to an increase of the strain increment during ejection and intensifying the residual stress relaxation above the die land **(Figure 7.13)**.
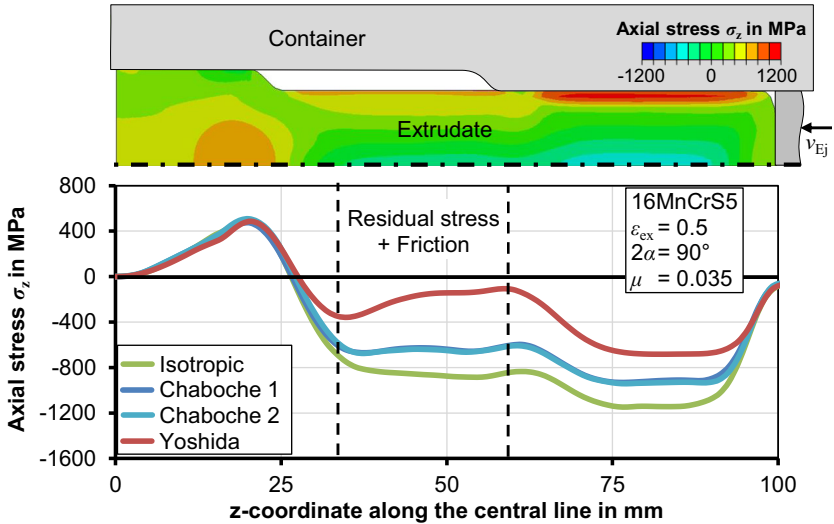
Figure 7.13: Axial stress evolution during ejection after forward rod extrusion as predicted by different constitutive models

The influence of the extrusion strain on the calculated axial residual stress distributions over the radius alongside experimental results are shown in **Figure 7.14** to **Figure 7.16**.
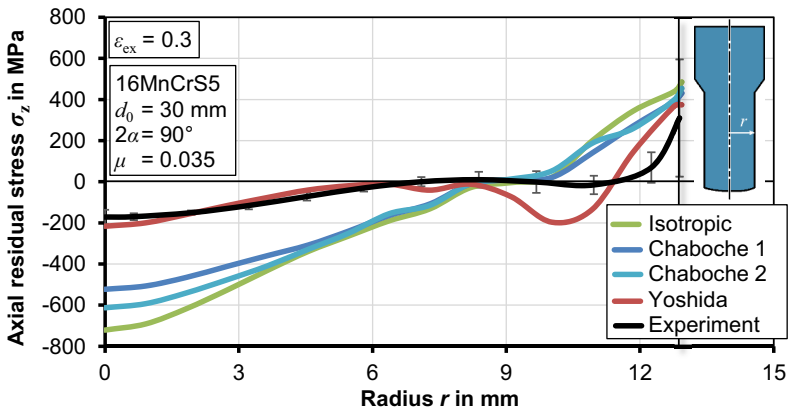
Figure 7.14: Effect of constitutive model on calculated axial residual stress after forward rod extrusion and experimental validation (ε_{ex} = 0.3, after ejection)
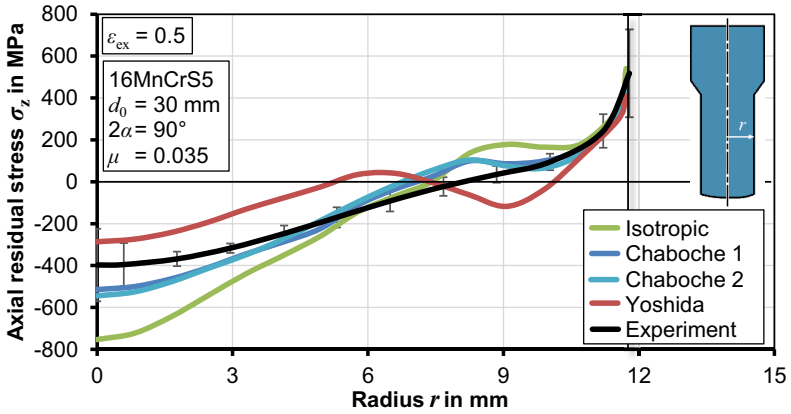
Figure 7.15: Effect of constitutive model on predicted axial residual stress after forward rod extrusion and experimental validation (ε_{ex} = 0.5, after ejection)
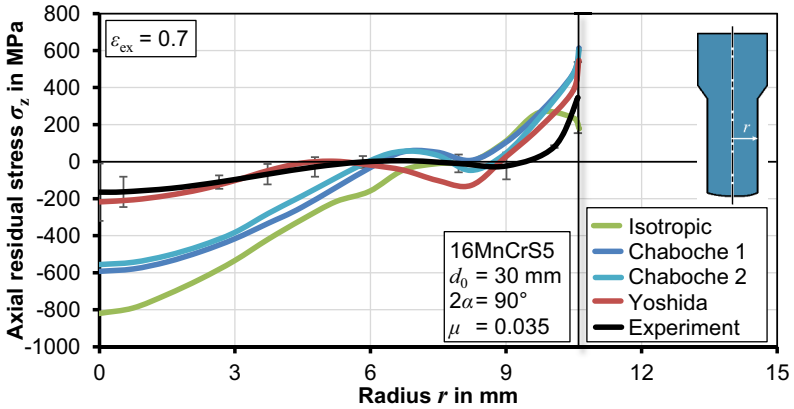
Figure 7.16: Effect of constitutive model on predicted axial residual stress after forward rod extrusion and experimental validation (ε_{ex} = 0.7, after ejection)

The anisotropic hardening models consistently predict a significantly lower residual stress level than the isotropic hardening model. While both Chaboche models maintain a similar trend as isotropic hardening, the axial stress distribution is completely altered when utilizing the modified Yoshida-Uemori model.

To validate the numerical results, the axial residual stress distributions were measured using the contour method as described by Prime and DeWald (2013). The error bars indicate the standard deviation of the contour method over six contour measurements per extrudate. Details regarding the experimental procedure to apply the contour method

to forward extruded rods are given in **Appendix E**. The experimental results for the extrudates with $\varepsilon_{ex} = 0.3$ and $\varepsilon_{ex} = 0.7$ coincide well with the results obtained with the Yoshida-Uemori model. While the general trend is also captured for $\varepsilon_{ex} = 0.5$, the existing deviations are assumed to be related rather to limitations of the contour method, which is known to yield only average results in the region of steep residual stress gradients, present e. g. at $r = 10$ mm. Nevertheless, all anisotropic hardening models yield a significant improvement of the predicted residual stress distribution as compared to conventional isotropic hardening which overestimates the residual stresses significantly at all investigated extrusion strains.

The intensified residual stress relaxation predicted by the Yoshida-Uemori model can be clarified through a thought experiment inspired by Tekkaya (1986) (**Figure 7.17a**). A cylinder is considered, which is subject to initial tensile axial residual stress $\sigma_{z,S,0}$ in the sheath region and compressive axial residual stress $\sigma_{z,C,0}$ in the core (acting on the same cross-sections). This initial stress distribution closely captures the actual residual stress distribution in a forward extruded rod after extrusion and before ejection. During ejection the shaft is compressed and the extrudate is formed again by a small additional plastic strain. In the core, plastic flow occurs first, as the compressive residual stress and loading stress add up, while the strain in the sheath first remains elastic due to the superposed tensile residual stress. Once the part is plastically formed over its complete cross-section, the mutual approach of the flow curves at different regions leads to a decrease of residual stress after unloading.
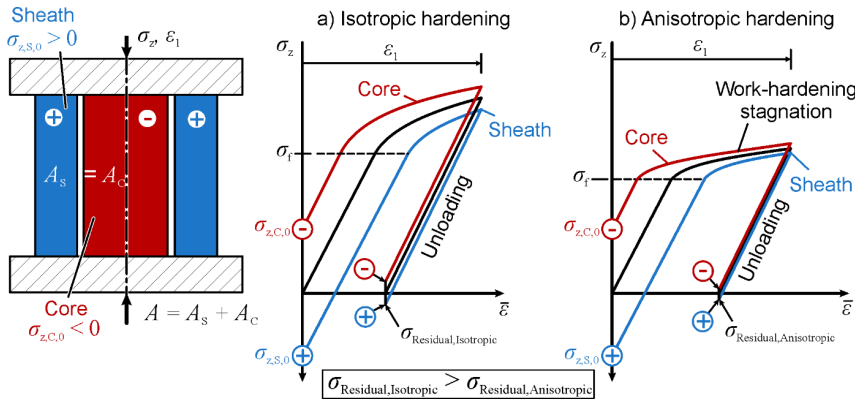
Figure 7.17: Thought experiment illustrating the residual stress relaxation during ejection after forward rod extrusion considering a) isotropic hardening and b) anisotropic hardening models (inspired by Tekkaya, 1986)

In the original thought experiment, the dominant stress leading to re-yielding during ejection was assumed to be tensile, which is true for isotropic hardening as the relaxation

of the die cavity leads to a second extrusion process. However, during ejection, the lower flow stress of the previously elongated material under subsequent compression and shear opposite to the original strain direction caused by anisotropic hardening, was expected to lead to an intensification of plastic deformation.

In order to verify this assumption, the plastic strain rate distributions during the ejection after forward rod extrusion were evaluated considering isotropic and anisotropic hardening models (modified Yoshida-Uemori). The corresponding strain rate distributions during steady-state ejection are shown in **Figure 7.18**.
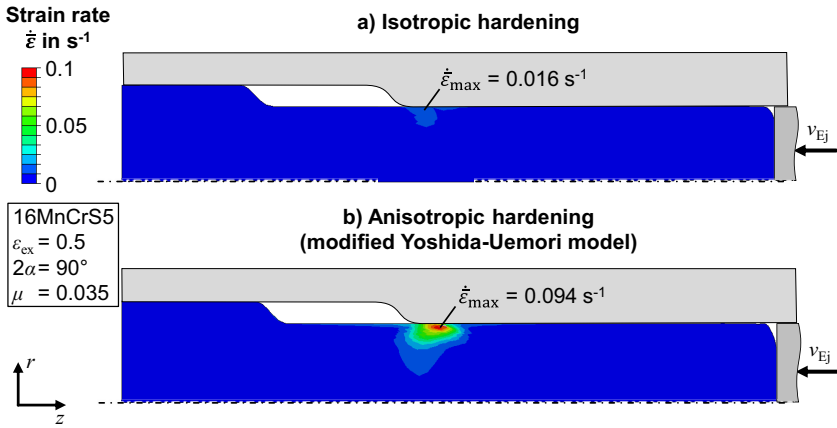
Figure 7.18: Influence of work-hardening formulation on the plastic strain rate distribution during steady-state part ejection

The results prove that the lowered flow stress opposite to the previous direction of elongation and shear, leads to an enlarged region of plastic flow in the case of the modified Yoshida-Uemori model. In addition, the maximum strain rate during ejection, which lies in the outer region of the workpiece close to the contact zone with the die, is significantly higher in the case of anisotropic hardening ($\dot{\bar{\varepsilon}}_{max} = 0.094$ s^{-1}) than in the case of isotropic hardening $\dot{\bar{\varepsilon}}_{max} = 0.016$ s^{-1}). The difference in strain rate between isotropic and anisotropic hardening raises the question, whether the geometry of the part - and more specifically - the diameter of the formed shaft is influenced by the intensified plastic flow. To verify this, the diameter of the simulated parts were evaluated and compared at the same point of the workpiece. In the case of isotropic hardening, the simulated diameter of the shaft after forming amounts to $D_1 = 23.438$ mm, whereas in the case of anisotropic hardening, a diameter of $D_1 = 23.435$ mm is determined. The small resulting deviation of less than 0.013 % lies within the margin of numerical error, concluding that the difference in the plastic strain accumulation between isotropic and anisotropic hardening

during ejection is mainly associated with redundant plastic work in the form of reverse shearing.

Based on the above observations, the thought experiment by Tekkaya is modified by incorporating the effect of the lowered effective flow stress and work-hardening stagnation triggered during the strain path reversal which is considered in the modified Yoshida-Uemori hardening model (**Figure 7.17b**). Besides, the fact that the plastic strain increment during ejection is higher in the case of anisotropic hardening. the work-hardening stagnation occurring in the early stages of plastic flow induced by the ejector, leads to a faster mutual convergence of the flow curves present in the sheath and core regions, which ultimately leads to a more pronounced residual stress relaxation.

The influence of the die cone angle 2α on the residual stress distribution is shown for the extrusion strain of $\varepsilon_{ex} = 0.5$ (**Figure 7.19**). All constitutive models predict a small increase of the axial residual stress with increasing die angle, which is in accordance with results from Tekkaya (1986). Higher die angles lead the material flow to be progressively restricted in front of the die shoulder, which causes an increase of the resulting strain inhomogeneity over the radius. However, at the same time, the slope of the flow curve decreases in the large strain regime, which counteracts the effect of the strain inhomogeneity to a certain degree. Regardless of the die angle, the Yoshida-Uemori-model predicts the lowest residual stresses.
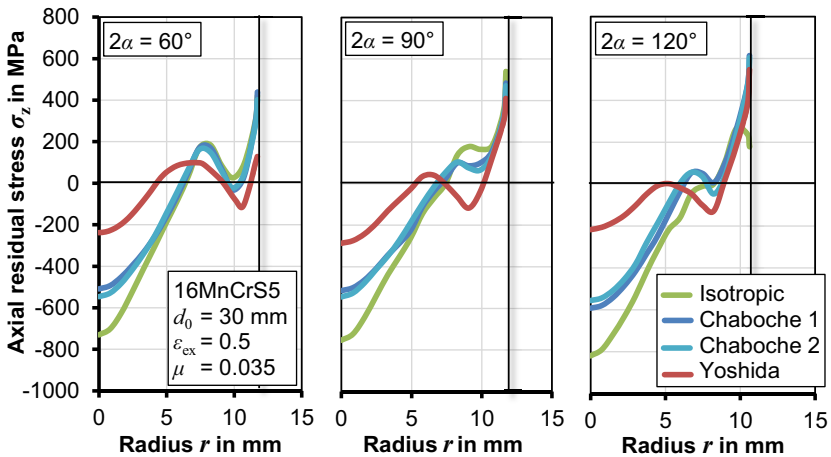
Figure 7.19: Influence of the die cone angle in forward rod extrusion on the residual stress distribution over the radius

The influence of the work-hardening formulation and the area reduction on the predicted axial residual stress after ejection in backward can extrusion is shown in **Figure 7.20**.
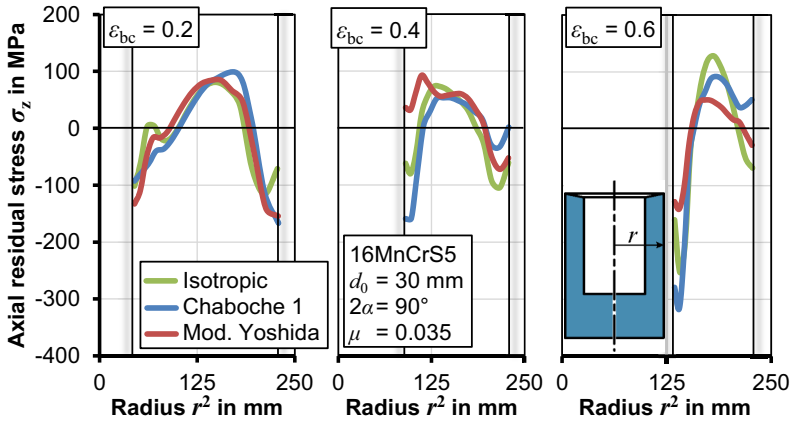
Figure 7.20: Effects of the work-hardening formulation and extrusion strain on the axial residual stress in backward can extrusion (can wall, after ejection)

As the results of both Chaboche models are similar, the Chaboche model with two back stress terms is suppressed for visualization purposes. For the lowest investigated area reduction $\varepsilon_{bc} = 0.2$, the influence of anisotropic hardening on the residual stress is negligible. For $\varepsilon_{bc} > 0.4$, the intrinsic strain path reversal between initial upsetting and subsequent backward extrusion leads to an increase of the strain inhomogeneity in the case of the Chaboche hardening model, causing an increase of the axial residual stresses. In contrast, the Yoshida-Uemori model, which simulates the work-hardening stagnation, leads to a decrease of the strain inhomogeneity upon the intrinsic strain path reversal causing a decrease of the axial residual stress.

7.3   Influence of anisotropic hardening on process forces

In the following, the influence of anisotropic hardening on the process forces are investigated, including the punch force and the ejector force. **Figure 7.21a** shows the influence of the work-hardening formulation and extrusion strain on the calculated punchstroke curves for forward extrusion. The maximum punch forces are summarized in **Figure 7.21b**.

The isotropic and anisotropic hardening models show only minor deviations, as the underlying strain paths are predominantly proportional. The differences are related to the upsetting of the billet in the container, which triggers a strain path reversal with a small compressive pre-strain of $\varepsilon_{pre} \approx 0.016$. The highest deviation between isotropic and combined hardening amounts to only 6 % ($\varepsilon_{ex} = 1$, Chaboche with two back stress terms).

The force-stroke curves of all models coincide well with the experimental measurements, however it is noted, that the friction coefficients were determined inversely to minimize the mutual deviation (see Appendix B for more details).
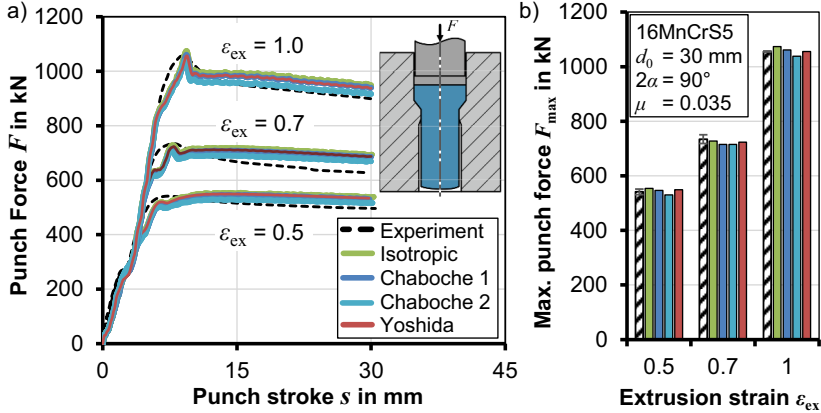
Figure 7.21: a) Punch force evolution in forward rod extrusion, comparison of constitutive models and experimental measurements, b) maximum punch forces

The ejector forces after forward rod extrusion are shown in **Figure 7.22**. In addition to the simulation results, experimentally obtained ejector forces are plotted for validation in terms of their maximum values, as the present machine setup did not allow for the measurement of the ejector stroke.
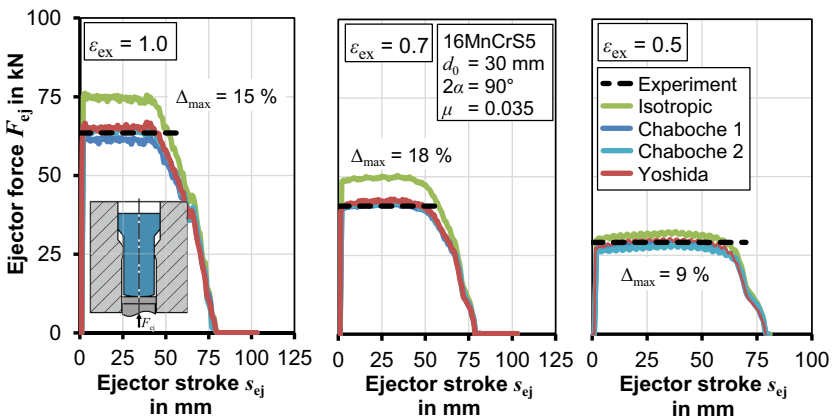
Figure 7.22: Calculated ejector forces after forward rod extrusion, comparison of isotropic and anisotropic hardening models and experimental validation

The anisotropic hardening models predict consistently lower ejector forces than the isotropic hardening model. All investigated anisotropic hardening models are in good agreement with the experimental measurements. The maximum difference between isotropic and anisotropic hardening amounts to $\Delta_{max} = 18\%$ ($\varepsilon_{ex} = 0.7$, Chaboche model with two back stress terms). The ejector forces are the result of the elastic springback of the container and die after the workpiece is unloaded. During ejection, the reduced diameter of the die leads to a second extrusion process with a small extrusion strain. In the previous section it was shown, that the anisotropic hardening evolving in the forming stage, leads to a lowered flow stress under reverse shearing, which is the explanation for the lowered ejection force. As the ejector force reduction is governed by the classical Bauschinger effect rather than work-hardening stagnation or permanent softening, all kinematic hardening models perform similarly well as compared to the experimental measurements as all models are capable of simulating the initial flow stress difference.

The influence of the different work-hardening formulations on the punch and ejector forces in backward can extrusion are shown in **Figure 7.23** and **Figure 7.24**.
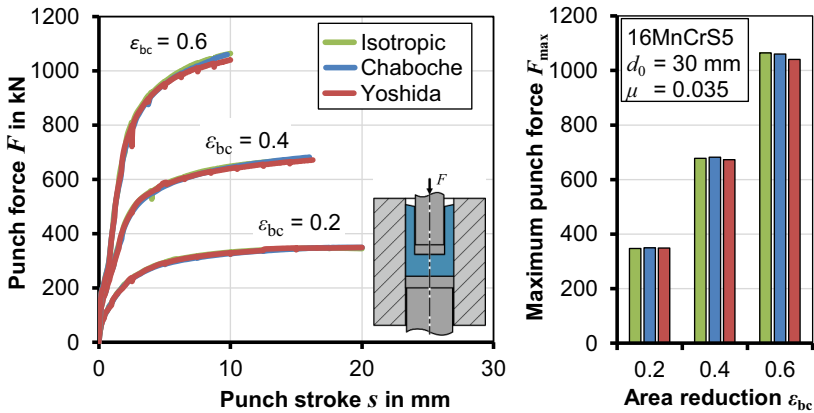
Figure 7.23: a) Punch forces in backward can extrusion, b) maximum punch forces, comparison of isotropic and anisotropic hardening models

Analogously to forward rod extrusion, the punch force is not significantly affected by anisotropic hardening, as the material is predominantly deformed in a proportional manner (axial tension and shear in the rz-plane). With increasing area reduction, the Yoshida-Uemori model predicts a lower punch force, as compared to the other models, which can be explained by the work-hardening stagnation and permanent softening exhibited after initial upsetting of the workpiece to fill the container. The largest difference between the punch forces predicted by the conventional isotropic and anisotropic hardening models amounts to 7 % ($\varepsilon_{bc} = 0.6$, Yoshida-Uemori).
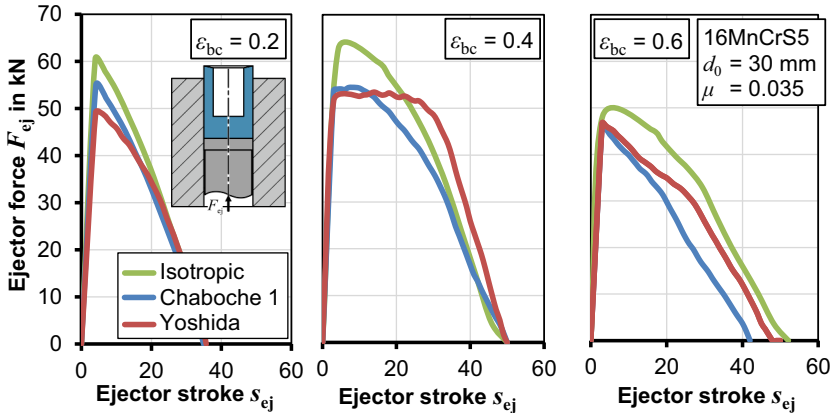
Figure 7.24: Calculated ejector forces in backward can extrusion, comparison of isotropic and anisotropic hardening models

In case of the ejector forces after backward can extrusion, the influence of anisotropic hardening is significant. In analogy to forward rod extrusion, the lowered flow stress after unloading and elastic springback of the container, leads to a lowered overall ejector force. The maximum difference between conventional isotropic hardening and the anisotropic hardening models amounts to 18 % ($\varepsilon_{bc} = 0.4$, Yoshida-Uemori).

7.4　Summary

It was shown, that the consideration of anisotropic hardening has a major impact on the predicted component properties and process forces in simulations of basic cold forging processes. The simulation results in terms of flow stress, residual stresses and process forces were validated experimentally, by the example of forward rod extrusion. **Table 7.1** summarizes the difference of component properties and process forces predicted by conventional isotropic hardening and the modified Yoshida-Uemori model.

Table 7.1: Deviations of process properties in cold forging processes between isotropic and anisotropic hardening models (16MnCrS5, $\sigma_{f,0}$ = 320 MPa)

Process	Yield strength $\sigma_{f,0}$	Residual stress σ_{zz}	Forces	
			Punch F	Ejector F_{ej}
Forward rod extrusion	25-39 %	1.6 $\sigma_{f,0}$	1-6 %	9-18 %
Backward can extrusion	25-29 %	0.6 $\sigma_{f,0}$	1-7 %	9-18 %

The influence of anisotropic hardening on the direction-dependent yield strength was not unexpected, as the results are the direct consequence of the experimentally observed

difference in the flow stress of pre-strained material under tensile and compressive load-
ing conditions, which were used to determine the material parameters of the anisotropic
hardening models as described in Section 6.2. It is important to note, however, that even
the tensile flow stress of cold extruded material, is affected by anisotropic hardening,
due to the occurrence of intrinsic local strain path reversals.

The flow stress anisotropy highly affects the resulting residual stresses after cold forg-
ing. While the more basic Chaboche work-hardening model leads to a mere reduction
of residual stresses, while maintaining the overall trend of conventional isotropic hard-
ening, the Yoshida-Uemori model which is able to capture all observed work-hardening
phenomena, causes a complete alteration of the residual stress field, both in forward rod
and backward can extrusion. The advanced model shows the best correlation with ex-
perimental results obtained by means of the contour method which was applied to for-
ward extruded rods with different extrusion strains.

For both investigated basic cold forging processes, the punch forces are affected only
weakly by anisotropic hardening, as no major intrinsic strain path reversals occur. All
investigated work-hardening formulations are in good accordance with experimental
force-stroke measurements during forward rod extrusion. During ejection, however, the
lowered flow stress caused by local strain path reversals after extrusion affects the pre-
dicted ejector forces for both forward rod extrusion and backward can extrusion. Con-
sequently, all anisotropic work-hardening models predict ejector forces that are signifi-
cantly lower than those predicted by conventional isotropic hardening. This observation
was validated by ejector force measurements after forward rod extrusion with different
extrusion strains.

In summary, anisotropic hardening significantly affects the predicted component prop-
erties as well as process forces, even for single-stage cold forging processes. At the same
time, the anisotropic hardening behavior is captured best by the modified Yoshida-
Uemori model implemented in the scope of this work. The model depends on a relatively
low number of material parameters and requires an acceptable calculation time even
with the large strains occurring in cold forging applications.

8 Anisotropic hardening in multi-stage cold forging processes

Parts are frequently produced by a sequence or combination of basic cold forming stages, mainly to produce more complex geometries or to reduce forming forces. In this chapter, different aspects regarding the influence of anisotropic work-hardening in cold forging sequences are explored. In the first section, the modified Yoshida-Uemori-model is applied to different types of cold forging sequences which include strain path reversals to determine their influence on the process forces. Further, it is investigated experimentally how a pre-compression of billets affects the process forces in subsequent forward extrusion. As a large part of cold forged parts are heat-treated between and after individual forming stages, the influence of heat-treatments on anisotropic hardening is assessed.

8.1 Influence of anisotropic hardening on process forces

In multi-stage and combined cold forging processes, anisotropic hardening is expected to have a significant impact on the resulting process forces. The following processes were evaluated to account for such effects:

- Combined cold forging: Forward extrusion and upsetting
- Multi-stage cold forging processes:
  - Forward extrusion and upsetting in two stages
  - Backward extrusion and subsequent flange upsetting

The investigated processes are illustrated in **Figure 7.1**.
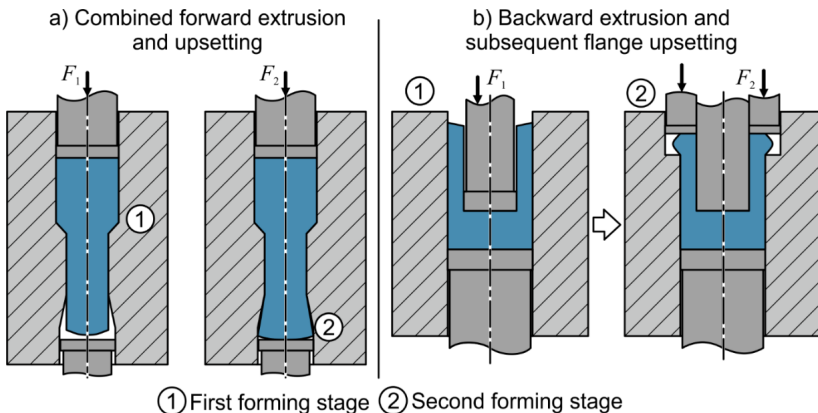
Figure 8.1: Investigated cold forging processes

The first investigated process combines forward rod extrusion and upsetting in a single uninterrupted process with one actively loaded punch (**Figure 8.2**).

① Forward extrusion parameters			
Extrusion strain $\varepsilon_{ex} = 2 \ln(d_0 / d_1)$	Die angle 2α	Workpiece diameter d_0	Workpiece length l_0
0.5	60°	30 mm	41 mm

② Upsetting parameters	
Transition radii r_{ex}	Undercut inclination 2β
3 mm	80°
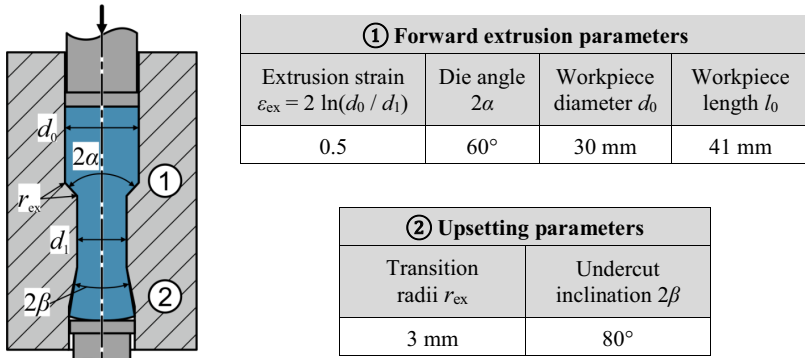
Figure 8.2: Process parameters in combined cold forging of an anchor bolt precursor

The process combination is inspired by the production of anchor bolt precursors used in civil engineering applications. In the industrial practice, cold forged anchor bolts are produced by use of lateral closing tools, which are pressed together under high forces during cold forging. After forming, the lateral closing force is released and the tools are opened to allow the removal of the semi-finished parts which would otherwise not be possible due to the generated undercuts. The combined cold forging process was simulated considering conventional isotropic hardening as well as the modified Yoshida-Uemori model. **Figure 8.3** shows the force-stroke curves during upsetting of the lower section. During the initial forward extrusion of the parts, there is no significant difference between isotropic and anisotropic hardening, thus the section is omitted.
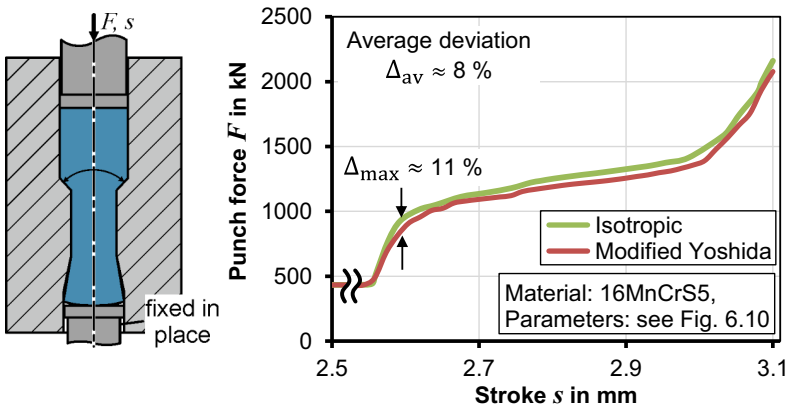
Figure 8.3: Simulation results on the influence of anisotropic hardening on the forming force in single-stroke anchor-forging

During the initial forward extrusion of the parts, there is no significant difference between isotropic and anisotropic hardening, thus the section is omitted. The maximum deviation between isotropic and anisotropic hardening occurs in the beginning of the upsetting stage and amounts to $\Delta_{max} = 11$ %. After this, the curves approach each other, as the punch force is increasingly driven by the growing friction forces at the container and die resulting from the restricted material flow at the lower punch. The force to overcome friction dominates the forces related to the plastic work in the second forming region, leading anisotropic hardening to have only a minor influence on the punch force. The average deviation between the simulated punch force curves predicted by isotropic and anisotropic hardening amount to $\Delta_{av} = 8$ %.

The first investigated multi-stage cold forging process is a variation of the anchor bolt forging process presented in the previous section (**Figure 8.4**). In this case the undercut is not produced by the restricted material flow caused by the fixed lower tool, but instead, the main punch stops and remains in place after the shaft is formed. In the second stage, the lower tool moves upwards, leading to the upsetting of the shaft and to the formation of the undercut (dashed box). Aside from the altered process kinematics, the geometric parameters are equal to those of the combined cold forging process to produce anchor bolts as investigated in the previous section.

① Forward extrusion parameters			
Extrusion strain $\varepsilon_{ex} = 2\ \ln(d_0 / d_1)$	Die angle 2α	Workpiece diameter d_0	Workpiece length l_0
0.5	60°	30 mm	41 mm

② Upsetting parameters	
Transition radii r_{ex}	Undercut inclination 2β
3 mm	80°
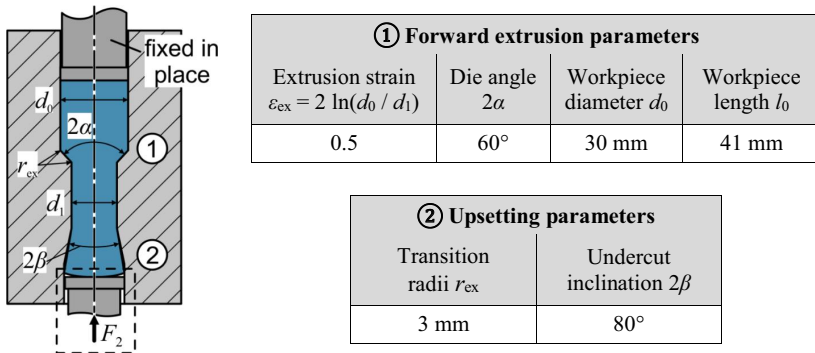
Figure 8.4: Process parameters in multi-stage cold forging of an anchor bolt precursor

The influence of anisotropic hardening on the process forces during the second stage of the multi-stage forming process to produce anchor bolt pre-cursors is shown in **Figure 8.5.** As in the case of the combined process variant, the maximum deviation occurs at the beginning of the upsetting stage and amounts to $\Delta_{max} = 20$ %. The higher deviation in the two-staged variant of the anchor forging process can be explained by the missing frictional forces and missing forces to maintain plastic flow in the forward extrusion stage, which lowers the impact of the plastic work in the second forming stage on the overall punch force. The permanent softening of 16MnCrS5 exhibited after the pre-

strain of $\varepsilon_{pre} = 0.5$ generated by the previous forward extrusion stage directly translates into a lowered punch force in the second forming stage with an average deviation of $\Delta_{av} = 11\ \%$ between isotropic and anisotropic hardening.
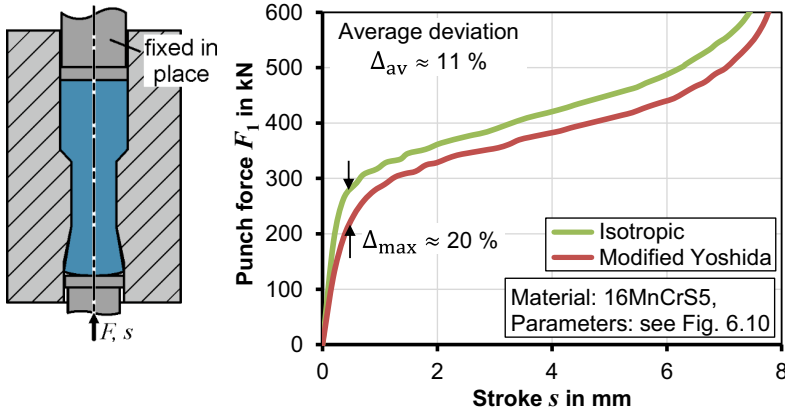
Figure 8.5: Simulation results on the influence of anisotropic hardening on the forming force in double-stroke anchor-forging

Lastly, a multi-stage forming process to create a cup with a flange is investigated. The process sequence consists of a backward can extrusion process and subsequent flange upsetting (**Figure 8.6**). In the backward can extrusion stage ① the material is sheared and elongated axially, whereas in flange upsetting ② the strain path is reversed and the material is compressed axially opposite to the previous elongation direction which corresponds to a full strain path reversal.

① **Backward extrusion parameters**			
Area reduction ε_{ex}	Workpiece diameter d_a	Workpiece length l_0	Transition radii r_{ex}
0.2	30 mm	51 mm	3 mm

② **Flange upsetting parameters**	
Flange diameter d_f	Flange height l_f
36 mm	5 mm
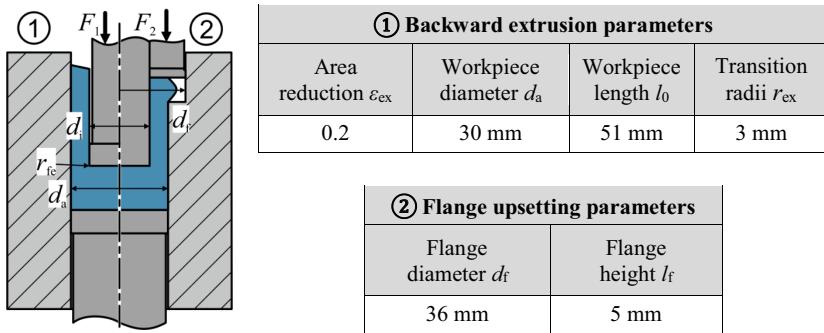
Figure 8.6: Process parameters in backward extrusion and subsequent flange upsetting

The influence of anisotropic hardening on the forming force in flange upsetting after backward extrusion is illustrated in **Figure 8.7**. The maximum deviation between the forming forces calculated by consideration of isotropic and anisotropic hardening occurs in the calibration stage of the process, during which the flange established contact with the outer ring of the die. The maximum deviation amounts to $\Delta_{max} = 19\,\%$. The average deviation amounts to $\Delta_{av} = 11\,\%$, which closely correlates with the permanent softening exhibited by 16MnCrS5 as illustrated in Section 5.3.2.
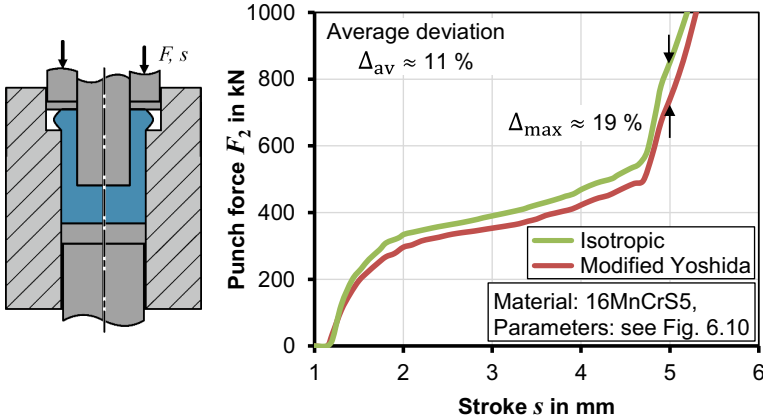
Figure 8.7: Simulation results on the influence of anisotropic hardening on the forming force in flange upsetting after backward can extrusion

To summarize this section, it was shown that the impact of anisotropic hardening on the process forces of multi-stage cold forming depends strongly on the process and tool kinematics. If the forming force in a subsequent forming stage is driven mainly by the plastic work necessary to cause the reverse plastic deformation, the lowered initial flow stress and permanent softening of the used material exhibited at the corresponding pre-strains translate directly into a reduction of the forming force. In these cases, a correct prediction of forming forces is not possible without the use of anisotropic hardening models. On the other hand, when the process forces during a subsequent forming stage are mainly driven by frictional forces or plastic work associated with forward plastic deformations, the influence of anisotropic hardening can be neglected in the process sequence design.

In this regard, it is emphasized that the identification of regions which experience strain paths that deviate significantly from monotonic or proportional loading is not always straight forward and may make necessary the utilization of strain path change indicators or the application of kinematic hardening models and observing the evolution of the back stress.

8.2   Influence of pre-compression before forward rod extrusion

In Section 5.3.5 it was shown that not only the flow stress is altered due to anisotropic hardening, but also the work-hardening at large reverse strains. For some materials, such as C15, the work-hardening potential seems to a lost completely for pre-strains of $\varepsilon_{pre} > 1.0$. This observations raises the question if a targeted pre-straining stage can lead to a reduction of the forming force in a subsequent forming stage if the strain path is reversed. In order to answer this question, billets were first pre-compressed and then forward extruded to identify a potential influence on the forming forces (**Figure 8.8**).
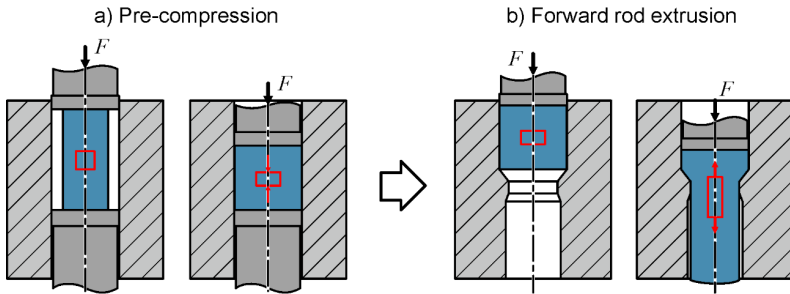
Figure 8.8:   Pre-straining by upsetting prior to forward extrusion (red rectangles illustrate the compression-tension strain path change)

The C15 billets were extracted from the as-received bars by turning. A container for backward can extrusion was used in combination with a forward extrusion punch to pre-compress the billets. The height and diameter of the pre-compression billets were chosen to realize a pre-strain of $\varepsilon_{ex} = 0.3$ by compression (**Figure 8.9a**). The pre-compressed billets were then forward extruded at an extrusion strain of $\varepsilon_{ex} = 1.5$ (**Figure 8.9b**).
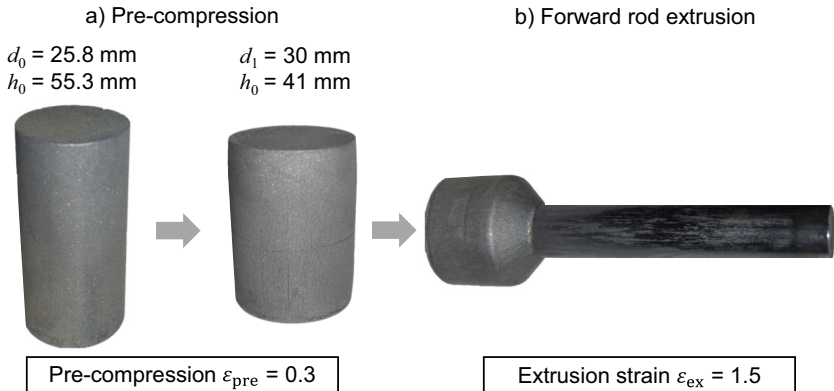
Figure 8.9: a) Pre-compression, b) forward rod extrusion of pre-compressed billets

To identify the influence of pre-compression on the forming forces in subsequent forward extrusion, additional billets were extracted from the as-received C15 bars with a volume equal to that of the pre-compressed billets. Both the forward extrusion experiments on annealed material and on pre-compressed material were repeated ten times each to account for data scattering and the resulting force-stroke curves were averaged over the corresponding set of measurements (**Figure 8.10**).
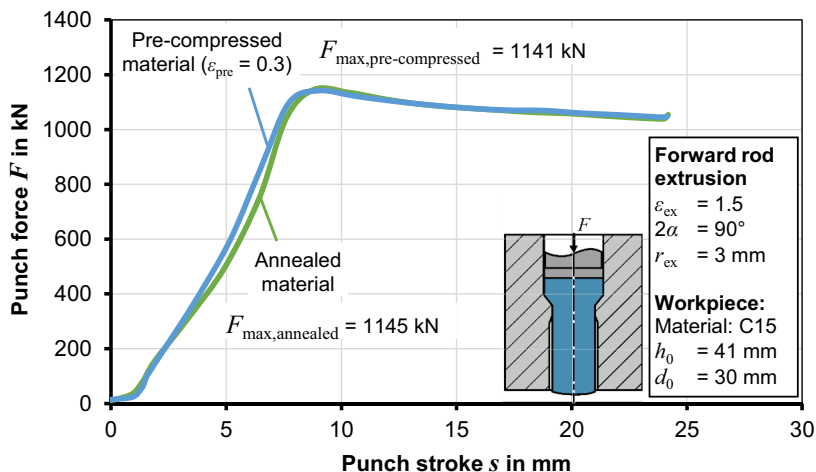
Figure 8.10: Punch force-stroke curves measured during forward rod extrusion of annealed and pre-compressed C15 billets

The additional pre-compression stage leads only to a small reduction of the punch force in forward extrusion as compared to the extrusion of annealed material (~ 0.4 %). To explain the rather small influence of pre-straining on the forming force in subsequent forward extrusion, the flow curves of annealed and pre-strained C15 are shown in **Figure 8.11**. Over the relevant strain regime up to $\varepsilon_{ex} = 1.5$, the average flow stress of annealed C15 amounts to 785 MPa, whereas the average flow stress of pre-strained C15 amounts to 766 MPa. The small difference of about 2.5 % explains the minor deviation in the required extrusion force. While the force reduction is too low to be exploited actively, the fact that the additional previous plastic deformation does not lead to an increase of the forming force in subsequent cold forming is counterintuitive to the conventional assumption that an increase in dislocation density must necessarily lead to an increase of the plastic work. A possible implication of these observations is, that in many cases in the industrial practice, annealing stages after pre-compression may not be necessary to reduce the forming forces in subsequent cold forging stages. This may be especially important in cold forging of drawn wires, which are often upset before the actual forming operations to increase the billet diameter.
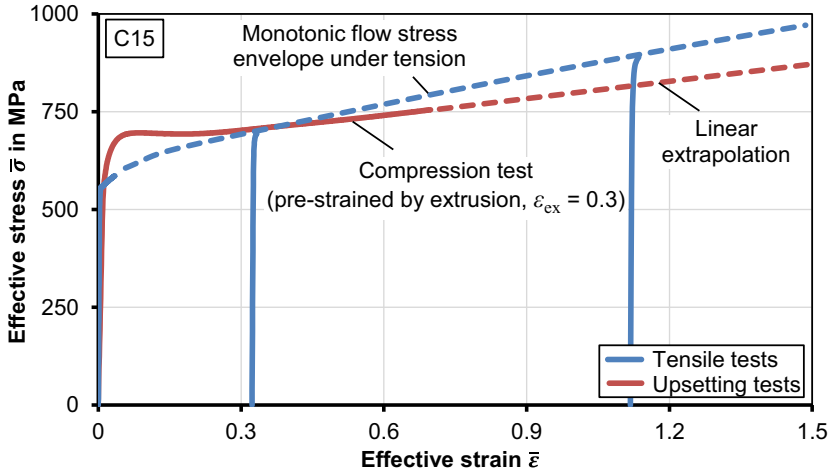
Figure 8.11: Flow curves of annealed C15 and pre-strained C15 after strain path reversal

8.3 Influence of heat-treatment on anisotropic hardening

A large fraction of cold forged parts are heat-treated in between forming stages to reduce the accumulated work-hardening which leads to a reduction of forming forces and tools loads in subsequent forming stages. Furthermore, parts are heat-treated after the process sequence, to increase the strength or reduce residual stresses. **Table 8.1** lists the most common heat-treatments applied to cold forged steels. With exception of stress-relieve annealing, the target of all listed procedures is the reduction of dislocation density and recrystallization, potentially erasing the effects of (anisotropic) work-hardening.

Table 8.1: Most common heat-treatments of cold forged steels (Lange et al., 2008)

Heat-treatment	Temperature	Goal
Stress-relieve annealing	400-500 °C, slow cooling	Decrease of residual stresses
Recrystallization annealing	Depends on dislocation density and material	Softening between forming stages
Soft annealing	680-700 °C, subsequent cooling within the heater	Improving formability by transformation of lamellar into globular cementite
Normalizing	30-50 °C above A_{C3}, subsequent cooling at air	Intensive softening between forming stages

According to Lange et al. (2008), in the industrial practice cold forged parts are stress-relieve annealed at about 500 °C, however, a residual stress reduction starts even below

500 °C. Depending on the parts diameter, the parts are typically annealed for 1-2 hours and then cooled slowly, to prevent the occurrence of new residual stresses.

To investigate the influence of heat-treatments on the anisotropic work-hardening, tensile and compression test specimens were extracted from forward extruded parts (16MnCrS5, $\varepsilon_{ex} = 1.0$). The specimens were heated in a convection furnace to temperatures of $T_{hold} = 400, 500, 600$ and 650 °C and held for 2 hours. The specimens were cooled to room temperature over the course of 5 hours (**Figure 8.12**).
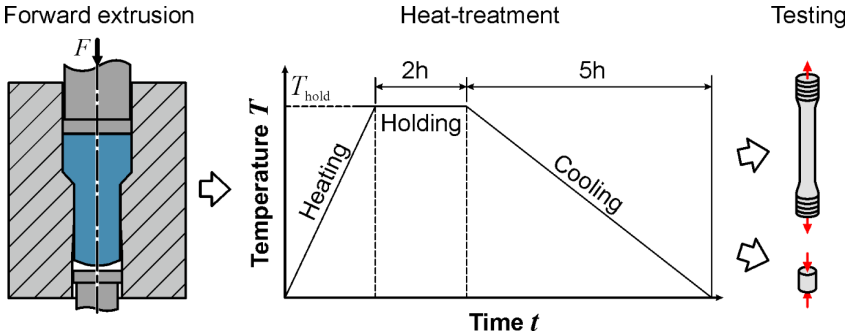
Figure 8.12: Applied methodology to analyze the influence of heat-treatments on anisotropic hardening of forward extruded specimens

The influence of the holding temperature on the flow curves obtained under tensile and compressive loading after the heat-treatment is shown in **Figure 8.13**.
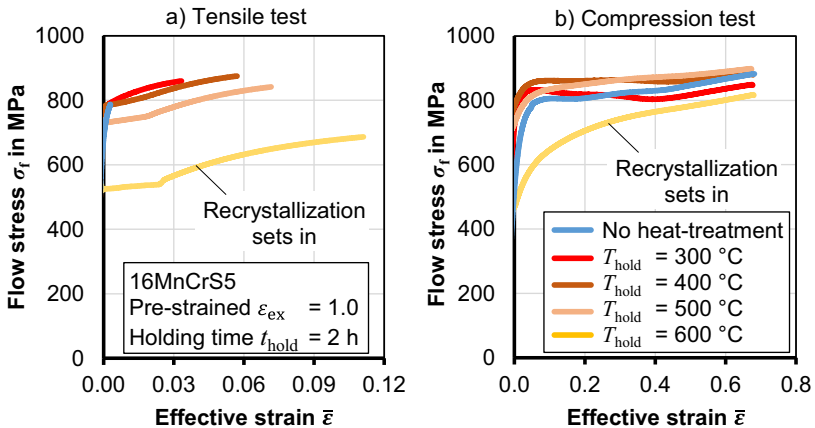
Figure 8.13: Effect of heat-treatment on the flow curves of specimens extracted from cold extruded rods under a) monotonic loading and b) strain path reversal

Below holding temperatures of 400 °C, the tensile flow stress is increased slightly. At 500 °C, the flow curve starts to drop visibly and the beginning of recrystallization is marked by the first appearance of a Lüders plateau. The plateau grows significantly at the highest applied holding temperature of 600 °C. At this point, recrystallization effects set in, lowering the complete flow curve significantly. In contrast, under compression holding temperatures up to 500°C first lead to an increase of the flow. Only at the highest applied holding temperature of 600 °C the flow curve under compression drops drastically. The following conclusions can be drawn from the observations:

- For temperatures below 500 °C recovery occurs, which can be explained by the combination of dislocation diffusion and the relieve of short-range internal stresses as described by Aran and Demirkol (1981). The reduction of short-range internal stresses leads to a decrease of the flow curve under compression, and thus to an overall reduction of tension-compression anisotropy generated during forward extrusion.
- At temperatures above 500 °C recrystallization sets in, causing an overall reduction of dislocation density, regardless of the strain path. In this case, both the flow curves under tension and compression are reduced and move closer together.

In addition, the above results underline that individual anisotropic hardening phenomena are affected differently at different holding temperatures:

- The classical Bauschinger effect and transient hardening diminish at temperatures below 500 °C, as short-range residual stresses are released in this temperature range, which are commonly considered the origin of the Bauschinger effect at small reverse strains.
- Work-hardening stagnation and permanent softening persist visibly up to holding temperatures of 600 °C, as these effects are associated rather with a polarization of dislocation structures, which are removed only with the formation of new grains.

Similar observations were made by Hasegawa et al. (1976) for pure aluminium. Up to temperatures of 250 °C he observed a reduction of anisotropic hardening effects associated with small reverse strains, i. e. the Bauschinger effect and transient hardening, and an increase of anisotropic hardening effects associated with large reverse strains, i. e. work-hardenings stagnation and permanent softening.

To minimize the flow stress anisotropy of cold forged parts, stress-relieve annealing at low temperatures can be considered to reduce the intensity of the Bauschinger effect in terms of the initial tension-compression anisotropy. If further forming operations follow, which include strain path reversals, no intermediate heat-treatments should be applied, in order to exploit the reverse flow stress reduction at large reverse strains.

8.4   Summary

In this chapter, the influence of anisotropic hardening in multi-stage cold forging processes was investigated. By comparison of numerically determined forming forces utilizing isotropic hardening and the modified Yoshida-Uemori model the influence of strain path reversals on the forming forces was determined for various multi-stage cold forging processes. The results of the investigation are summarized in **Table 8.2**.

Table 8.2: Deviations of process forces in multi-stage cold forging processes considering isotropic and anisotropic hardening models (Material: 16MnCrS5)

Process sequence	Punch force deviation in %	
	Average	Maximum
Combined cold forging (Anchor bolt)	8	11
Multi-stage forging (Anchor bolt)	11	20
Multi-stage forging (Flanged can)	11	19

The forming force to produce an anchor bolt precursor by combined forward rod extrusion and upsetting is only weakly affected by anisotropic hardening, as a large part of the punch force is dominated by the work to overcome the friction between the workpiece and die surfaces and the forming work associated with the first forming stage. In the case of the investigated multi-stage forming processes, in which the initially cold forged material is subsequently deformed by a second active tool, the punch force is affected more significantly by anisotropic hardening, as it is mainly controlled by the work to form the material opposite to the previous deformation direction. In these cases, the permanent softening observed in the non-monotonic characterization of 16MnCrS5 correlates directly with the forming force reduction compared with isotropic hardening.

The targeted pre-compression of billets in an enclosed container was investigated as a possible measure to reduce the forming forces in subsequent forward extrusion by the example of C15, which was shown to lose its work-hardening potential after a strain path reversal. While the resulting force reduction was too low to be exploited actively, the mere fact that pre-compression does not lead to an increase of the forming force in subsequent extrusion is counterintuitive. A possible implication is that some parts in the industrial practice may not need to be annealed after pre-compression, which is often applied to increase the diameter of as-received billets.

Lastly, the influence of heat-treatments on the anisotropic hardening after cold extrusion was investigated by annealing forward extruded specimens at different temperatures. It was shown, that the Bauschinger effect and transient softening vanish in the temperature range between 300 °C and 600 °C. The observations can be explained by the relaxation

of short-range residual stresses, which are commonly considered the origin of the classical Bauschinger effect and transient hardening. The work-hardening stagnation and permanent softening generated during forward rod extrusion persist up to holding temperatures of 600 °C, above which recrystallization triggers the formation of new grains leading to the removal of dislocation structure polarization.

9 Conclusion and outlook

9.1 Conclusion

A new experimental method was developed to quantify the anisotropic hardening behavior of different metals focusing on the influence of strain path reversals at large pre-strains. By performing uniaxial tensile tests on specimens extracted from forward extruded parts, large strain flow curve points up to true effective strains of 1.7 can be obtained. By performing compression tests on forward extruded materials, the previous strain path is reversed, which allows to characterize the large strain anisotropic work-hardening behavior. The applicability of the new characterization methods was verified experimentally, analytically and numerically. The methods were applied to three steels and one aluminium alloy, and the results were compared to those of conventional characterization methods. In the shared strain regime there exists a high correlation with the results of conventional methods, however, the reachable strains and pre-strains are extended significantly. The observations on the large strain anisotropic work hardening phenomena can be summarized as follows:

- At large strains, the flow curves of all materials transition from a degressive into a linear increase. This is in accordance with results of Langford and Cohen (1969) for iron alloys and by Varma and LeFevre (1980) for aluminium alloys, who explained the transition with a change of the dominant hardening mechanism,
- after strain path reversals, all materials exhibit the classical Bauschinger effect, transient hardening, work-hardening stagnation and permanent softening,
- the intensity of anisotropic hardening effects depends strongly on the material,
- all strain path reversal related work-hardening phenomena intensify with the pre-strain, showing no signs of saturation up to the highest achieved pre-strain of 1.7,
- torsion tests of forward extruded 16MnCrS5, corresponding to an orthogonal strain path change, revealed no signs of cross-hardening.

The experimental results on the large strain anisotropic-work-hardening behavior of 16MnCrS5 obtained by the new methods were used to select, modify and fit various constitutive hardening models for the application in cold forging simulations. The results of the investigations include the following aspects:

- An automatic parameter identification procedure was applied successfully to identify the material parameters of all investigated hardening models,
- the large strains monotonic hardening behavior can be captured with sufficient accuracy with all investigated constitutive models, including conventional isotropic hardening, by using a combination of Swift- and Voce-type hardening,
- isotropic hardening does not allow to model the anisotropic hardening phenomena revealed by any of the investigated materials,

- the combined isotropic-kinematic hardening model by Chaboche is able to model the initial drop of the flow stress observed after a strain path reversal,
- a modified version of the Yoshida-Uemori isotropic-kinematic hardening model was implemented, which is able to capture all observed anisotropic hardening phenomena, with an acceptable numerical efficiency.

The models were applied to simulations of the basic cold forging processes "forward rod extrusion" and "backward can extrusion". The following insights were obtained:

- By comparison with conventional isotropic hardening, the influence of anisotropic hardening phenomena on the forming forces and resulting part properties in cold forging could be isolated successfully,
- all combined isotropic-kinematic hardening models are able to correctly predict the anisotropic flow stress distribution and corresponding local Bauschinger coefficients within cold extruded parts,
- the residual stresses in the cold forged parts are highly affected by anisotropic hardening, due to intrinsic strain path changes,
- the Yoshida-Uemori model predicts the lowest residual stresses, as the work-hardening stagnation considered in the model leads to a significant reduction of the elastic strain inhomogeneity during part ejection, which was explained by a thought experiment originally introduced by Tekkaya et al. (1985),
- the punch forces are not affected by anisotropic hardening, however, compared to isotropic hardening the ejector forces are significantly lower.

Lastly, the consequences of anisotropic work-hardening for the process sequence design in cold forging was analyzed. The results can be summarized as follows:

- In multi-stage cold forging processes, where significant material regions experience a strain path reversal, the forming forces in the second stage are significantly reduced due to anisotropic hardening; the permanent softening observed in the material characterization translates directly into the reduced process force,
- a targeted pre-compression, comparable to initial coining or upsetting, leads to reduced forming forces in subsequent cold forging, if the strain path is reversed; this can be utilized to skip heat-treatments in between two forming stages,
- by performing heat-treatments on cold forged specimens, the Bauschinger effect and transient hardening are erased at temperatures below 500 °C (holding time of 2 hours); work-hardening stagnation and permanent softening continue up to the beginning of recrystallization at temperatures of 600 °C and above.

The developed methodology to consider anisotropic hardening can be applied to any cold forging process or process sequence to increase the prediction accuracy of forming simulations and bring closer the vision of a performance prediction under service loads.

9.2 Outlook

The new characterization methods to quantify the anisotropic hardening behavior of metals revealed that the intensity and evolution of individual anisotropic hardening effects strongly depends on the material. In the future, the phenomenological observations regarding the large strain anisotropic hardening behavior should be explained on the micro-scale e.g. by TEM analyses (transmission electron microscopy), allowing the investigations of the dislocation structures and their polarization which are considered the driver of large strain anisotropic hardening phenomena such as work-hardening stagnation and permanent softening.

While the focus of this work was on the anisotropic hardening phenomena exhibited after full strain path reversals, torsion tests on forward extruded material were also successfully applied to identify a possible influence of cross-loading sequences. While no such effects could be found in the case of 16MnCrS5, it is not out of question that other materials may show the expected overshoot of the flow curve after a previous lateral deformation. To investigate this further, additional materials should be characterized with regard to potential cross-hardening effects, which can then be considered in the simulation by advanced constitutive models such as the HAH-model.

The flow curve is generally known to be a function of the temperature and strain rate. Both the applied monotonic characterization methods as well as the characterization methods to quantify anisotropic hardening effects can be adapted simply by conducting the mechanical tests on pre-strained specimens at elevated temperatures or strain rates to quantify the influence of temperature and strain rate on the intensity of anisotropic hardening phenomena. In the present thesis, the loading sequence of tension with subsequent compression was focused. As an additional influencing factor on the intensity of anisotropic hardening, the order of loading should be analyzed in the future.

In this work, two-stage cold forging sequences were investigated, which include a single strain path reversal. In the literature it is reported for some materials, that the intensity of anisotropic hardening phenomena also depends on the number of forward-reverse loading cycles. To analyze the influence of the number of load cycles on the work-hardening behavior, the developed characterization methods must be adapted to allow for multiple loading cycles. In addition to this, constitutive models must be utilized, which have the flexibility to consider the influence of the number of loading cycles on the work-hardening behavior. Such models, however, would naturally rely on a larger number of material parameters and complex material characterization methods.

References

Abel, A., Ham, R.K., 1966. The cyclic strain behaviour of crystals of aluminum-4 wt.% copper-i. The bauschinger effect. Acta Metallurgica 14 (11), pp. 1489–1494.

Aran, A., Demirkol, M., 1981. Effect of heat treatment on the Bauschinger effect for a medium carbon steel. Materials Science and Engineering 47 (2), pp. 89–92.

ASTM International, 2013. ASTM E8/E8M - Standard Test Methods for Tension Testing of Metallic Materials, ASTM International, West Conshohocken, PA.

Avitzur, B., 1968. Analysis of Central Bursting Defects in Extrusion and Wire Drawing. Journal of Engineering for Industry 90 (1), p. 79.

Awiszus, B., Kleditzsch, S., Härtel, S., 2009. Untersuchung numerischer Einflussgrößen bei der Simulation von Drückwalzprozessen. UFTscience 2, pp. 1–6.

Baltov, A., Sawczuk, A., 1965. A rule of anisotropic hardening. Acta Mechanica 1 (2), pp. 81–92.

Banabic, D., Bunge, H.-J., Pöhlandt, K., Tekkaya, A.E, 2000. Formability of Metallic Materials - Plastic Anisotropy, Formability Testing, Forming Limits, Springer-Verlag, Berlin, Heidelberg.

Barlat, F., Gracio, J.J, Lee, M.-G., Rauch, E.F, Vincze, G., 2011. An alternative to kinematic hardening in classical plasticity. International Journal of Plasticity (27), pp. 1309–1327.

Bauschinger, J., 1886. Über die Veränderung der Elastizitätsgrenze und die Festigkeit des Eisens und Stahls durch Strecken und Quetschen, durch Erwärmen und Abkühlen und durch oftmals wiederholte Beanspruchungen. Mittheilungen aus dem Mechanisch-Technischem Laboratorium 13.

Berns, M., 1977. Verzug von Stählen infolge Wärmebehandlung. Materialwissenschaft und Werkstofftechnik 8 (5), pp. 149–157.

Boger, R.K, 2006. Non-monotonic strain hardening and its constitutive representation. Dissertation, Ohio State University, Columbus, USA.

Boger, R.K, Wagoner, R.H, Barlat, F., Lee, M.G, Chung, K., 2005. Continuous, large strain, tension/compression testing of sheet material. International Journal of Plasticity 21 (12), pp. 2319–2343.

Bouvier, S., Haddadi, H., Levée, P., Teodosiu, C., 2006. Simple shear tests: Experimental techniques and characterization of the plastic anisotropy of rolled sheets at large strains. Journal of Materials Processing Technology 172 (1), pp. 96–103.

Bridgman, P.W, 1945. Effects of High Hydrostatic Pressure on the Plastic Properties of Metals. Reviews of Modern Physics 17 (1), pp. 3–14.

Carl Bechem GmbH, 2020. www.bechem.de. Retrieved on 02.08.2021.

Chaboche, J.L, 1986. Time-independent constitutive theories for cyclic plasticity. International Journal of Plasticity 2 (2), pp. 149–188.

Chaboche, J.L, 2008. A review of some plasticity and viscoplasticity constitutive theories. International Journal of Plasticity 24 (10), pp. 1642–1693.

Dafalias, Y.F, Popov, E.P, 1976. Plastic Internal Variables Formalism of Cyclic Plasticity. Journal of Applied Mechanics 43 (4), p. 645.

Deutsches Institut für Normung e. V., 2003. DIN 8580 - Manufacturing processes - Terms and definitions, division, Beuth Verlag GmbH, Berlin.

Deutsches Institut für Normung e. V., 2003. DIN 8582 - Manufacturing processes forming - Classification; Subdivision, terms, Beuth Verlag GmbH, Berlin.

Deutsches Institut für Normung e. V., 2003. DIN 8583-6 - Manufacturing processes forming under compressive conditions - Part 6: Extrusion; Classification, subdivision, terms and definitions, Beuth Verlag GmbH, Berlin.

Deutsches Institut für Normung e. V., 2007. DIN EN 573-3 - Chemische Zusammnesetzung und Form von Halbzeugen - Teil 3: Chemische Zusammensetzung und Erzeugnisformen.

Deutsches Institut für Normung e. V., 2016. DIN 50106 - Testing of metallic materials - Compression test at room temperature, Beuth Verlag GmbH, Berlin.

Deutsches Institut für Normung e. V., 2016. DIN 50125 - Testing of metallic materials - Tensile test pieces, Beuth Verlag GmbH, Berlin.

Deutsches Institut für Normung e. V., 2020. DIN EN ISO 6892-1 - Metallic materials - Tensile testing - Part 1: Method of test at room temperature, Beuth Verlag GmbH, Berlin.

Dieter, G.E, 1961. Mechanical Metallurgy, McGraw-Hill, New York, USA.

Doege, E., Meyer-Nolkemper, H., Saeed, I., 1986. Fließkurvenatlas metallischer Werkstoffe - Mit Fließkurven für 73 Werkstoffe und einer grundlegenden Einführung, Hanser Verlag, München.

Edwards, E.H, Washburn, J., 1954. Strain hardening of latent slip systems in zinc crystals. JOM 6 (11), pp. 1239–1242.

Eggertsen, P.-A., Mattiasson, K., 2009. On the modelling of the bending–unbending behaviour for accurate springback predictions. International Journal of Mechanical Sciences 51 (7), pp. 547–563.

Ellermann, A., 2013. Der Bauschingereffekt bei vergüteten, bainitischen und normalisierten Zuständen der Stähle 42CrMoS4 und 100Cr6. Dissertation, Kassel University Press, Kassel.

European Commission, 2021. https://www.bmu.de/en/topics/climate-adaptation/climate-protection/eu-climate-policy. Retrieved on 10.09.2021.

Farren, W.S, Taylor, G.I, 1925. The heat developed during plastic extension of metals. Proceedings of the Royal Society A: Mathematical, Physical and Engineering 107 (743), pp. 422–451.

Feldmann, H.D, 1959. Fließpressen von Stahl, Springer-Verlag, Berlin, Heidelberg.

Fields, D.S, Backofen, W.A, 1957. Determination of Strain Hardening Characteristics by Torsion Testing. Proceeding of American Society for Testing and Materials, pp. 1259–1272.

Frederick, C.O, Armstrong, P.J, 2007. A mathematical representation of the multiaxial Bauschinger effect. Materials at High Temperatures 24 (1), pp. 1–26.

Galdos, L., Agirre, J., Mendiguren, J., Argandona, E.S de, Otegi, N., Trinidad, J., 2019a. Mixed isotropic–kinematic hardening model for cold forging simulation of an industrial bolt. Proceedings of the 52nd ICFG Plenary Meeting.

Galdos, L., Agirre, J., Otegim, N., Mendiguren, J., Argandona, E.S de, 2019b. Hardening Characterization of Cold Forging Steel by means of Compression and Torsion Tests. 8th Manufacturing Engineering Society International Conference.

Ghaei, A., Green, D.E, 2010. Numerical implementation of Yoshida–Uemori two-surface plasticity model using a fully implicit integration scheme. Computational Materials Science 48 (1), pp. 195–205.

Ghaei, A., Green, D.E, Taherizadeh, A., 2010. Semi-implicit numerical integration of Yoshida–Uemori two-surface plasticity model. International Journal of Mechanical Sciences 52 (4), pp. 531–540.

Gil Sevillano, J., van Houtte, P., Aernoudt, E., 1980. Large strain work hardening and textures. Progress in Materials Science 25 (2-4), pp. 69–134.

Hahn, F., 2003. Untersuchung des zyklisch plastischen Werkstoffverhaltens unter umformnahen Bedingungen, Technischen Universität Chemnitz. Dissertation.

Han, K., van Tyne, C.J, Levy, B.S, 2005a. Bauschinger Effect Response of Automotive Sheet Steels. In: Xia, Z.C., Stoughton, T., Oetjens, T., Liu, S.D., Worswick, M. (Eds.), Sheet/Hydro/Gas Forming Technology and Modeling. SAE International, USA.

Han, K., van Tyne, C.J, Levy, B.S, 2005b. Effect of strain and strain rate on the Bauschinger effect response of three different steels. Metallurgical and Materials Transactions A 36 (9), pp. 2379–2384.

Hasegawa, T., Yakou, T., Karashima, S., 1975. Deformation behaviour and dislocation structures upon stress reversal in polycrystalline aluminium. Materials Science and Engineering 20 (2), pp. 267–276.

Hasegawa, T., Yakou, T., Shimizu, M., 1976. The Effect of Deformation Temperature on the Bauschinger Effect in Polycrystalline Aluminium. Transactions of the Japan Institute of Metals.

Havranek, J., 1984. The Effect of Pre-Drawing on Strength and Ductility in Cold Forging. Advanced Technology of Plasticity 2 (2), pp. 845–850.

Hering, O., 2020. Schädigung in der Kaltmassivumformung. Dissertation, TU Dortmund University, Shaker Verlag, Düren.

Hering, O., Tekkaya, A.E, 2020. Damage-induced performance variations of cold forged parts. Journal of Materials Processing Technology 279, 116556.

Hilleke, S., Baumgart, P., 2010. Neueste Versuchsergebnisse an höchstfesten Aluminiumlegierungen und anschließenden Hartbeschichtungen. 25. Jahrestreffen der Kaltmassivumformer.

Hockett, J.E, Sherby, O.D, 1975. Large strain deformation of polycrystalline metals at low homologous temperatures. Journal of the Mechanics and Physics of Solids 23 (2), pp. 87–98.

Hoffmann, H., Spur, G., Neugebauer, R. (Eds.), 2012. Handbuch Umformen, Carl Hanser Verlag, München.

Hu, Z., Rauch, E.F, Teodosiu, C., 1992. Work-hardening behavior of mild steel under stress reversal at large strains. International Journal of Plasticity 8 (7), pp. 839–856.

ICFG, 1991. Lubrication aspects in cold forging of carbon steels and low alloy steels - International Cold Forging Group - Document (8/91).

Isogawa, S., 2016. Latest Precision Forging in Japan, Proceedings of the 49th ICFG, pp. 120–126.

Jennison, H.C, 1930. Certain Types of Defects in Copper Wire Caused by Improper Dies and Drawing Practice. Proceedings of the Institute of Metals Division AIME (89).

Jia, L.-J., 2014. Integration algorithm for a modified Yoshida–Uemori model to simulate cyclic plasticity in extremely large plastic strain ranges up to fracture. Computers & Structures 145, pp. 36–46.

Krause, U., 1963. Vergleich verschiedener Verfahren zum Bestimmen der Formänderungsfestigkeit bei Raumtemperatur. Stahl und Eisen 1 (83), pp. 1626–1640.

Krieg, R.D, 1975. A Practical Two Surface Plasticity Theory. Journal of Applied Mechanics 42 (3), p. 641.

Kuwabara, T., Nagata, K., Nakako, T., 2001. Measurement and Analysis of the Bauschinger Effect of Sheet Metals Subjected to In-plane Stress Reversals. International Conference of Advanced Materials and Processing Technology, pp. 407–414.

Landgrebe, D., 2000. Bestimmung der Formänderungsgrenzen durch duktiles Werkstoffversagen bei Kaltumformverfahren mit Hilfe der FEM. Dissertation, Shaker Verlag, Aachen.

Lange, K., 1988. Umformtechnik Handbuch für Industrie und Wissenschaft, Springer-Verlag, Berlin, Heidelberg.

Lange, K., Kammerer, M., Pöhlandt, K., Schöck, J., 2008. Fließpressen - Wirtschaftliche Fertigung metallischer Präzisionswerkstücke, Springer-Verlag, Berlin, Heidelberg.

Langford, G., Cohen, M., 1969. Strain Hardening of Iron by Severe Plastic Deformation. Transactions of the ASM (62), pp. 623–638.

Lee, J., Lee, J.-Y., Barlat, F., Wagoner, R.H, Chung, K., Lee, M.-G., 2013. Extension of quasi-plastic–elastic approach to incorporate complex plastic flow behavior – application to springback of advanced high-strength steels. International Journal of Plasticity 45, pp. 140–159.

Lee, J.-Y., Lee, J.-W., Lee, M.-G., Barlat, F., 2012. An application of homogeneous anisotropic hardening to springback prediction in pre-strained U-draw/bending. International Journal of Solids and Structures 49 (25), pp. 3562–3572.

Lemaître, J., Chaboche, J.-L., 1990. Mechanics of solid materials, Cambridge University Press, Cambridge, UK.

Ludwik, P., 1909. Elemente der Technologischen Mechanik.

Ma, L., 2007. Effect of pre-drawing on formability during cold heading, McGill University, Library and Archives Canada, Ottawa, Canada.

Macherauch, E., Wohlfahrt, H., Wolfstieg, U., 1973. Zur zweckmäßigen Definition von Eigenspannungen. Härterei-Technische Mitteilungen 28 (3), pp. 201–211.

Mahato, J.K, De, P.S, Sarkar, A., Kundu, A., Chakraborti, P.C, 2014. Effect of Prestrain and Stress Rate on Bauschinger Effect of Monotonically and Cyclically Deformed OFHC Copper. Procedia Engineering 74, pp. 368–375.

Marciniak, Z., Kolodziesjki, J., 1972. Assessment of sheet metal failure sensitivity by method of torsion the rings. Proceedings of the 7th Biennual Congress IDDRG, pp. 61–64.

Margolin, H., Hazaveh, F., Yaguchi, H., 1978. The grain boundary contribution to the Bauschinger effect. Scripta Metallurgica 12 (12), pp. 1141–1145.

Masing, G., 1923. Zur Heynschen Theorie der Verfestigung der Metalle durch verborgene elastische Spannungen. In: Harries, C.D. (Ed.), Wissenschaftliche Veröffentlichungen aus dem Siemens-Konzern, III. Band 3. Springer-Verlag, Berlin, Heidelberg.

Mcallen, P., Phelan, P., 2005. Ductile Fracture by Central Bursts in Drawn 2011 Aluminium Wire. International Journal of Fracture 135 (1-4), pp. 19–33.

Miki, T., Toda, M., 1988. Evaluation of Work Hardening and Bauschinger Effect of Steels under Cold Forging by the Half-value Breadth of X-ray Diffraction Profile. Journal of the Society of Materials Science Japan 38 (427), pp. 398–403.

Mróz, Z., 1967. On the description of anisotropic workhardening. Journal of the Mechanics and Physics of Solids 15 (3), pp. 163–175.

Mughrabi, H., 1983. Dislocation wall and cell structures and long-range internal stresses in deformed metal crystals. Acta Metallurgica 31 (9), pp. 1367–1379.

Muster, W.J, Hochhaus, C., 1983. Eigenspannungen. Technische Rundschau Bern (75), pp. 32–33.

Narita, S., Hayakawa, K., Kubota, Y., Harada, T., Uemori, T., 2017. Effect of Hardening Rule for Spring Back Behavior of Forging. Procedia Engineering 207, pp. 167–172.

Narita, S., Uemori, T., Hayakawa, K., Kubota, Y., 2016. Effect of Hardening Rule on Analysis of Forming and Strength of Multistage Cold Forged Bolt without Heat Treatment. Journal of the JSTP 57 (670), pp. 1070–1076.

Nehl, E., 1983. Untersuchungen zum Halbwarmfließpressen von Automatenstählen, Springer-Verlag, Berlin, Heidelberg.

Ningbo Anchors, 2021. https://www.anchor-fasteners.com/product/wedge-anchor-bolt-automatic-cold-forging-machine-no-material-wasted. Retrieved on 11.03.2021.

Orowan, E., 1959. Causes and effects of internal stresses. In: Freudenthal, A.M. (Ed.), Internal stresses and fatigue in metals, Causes and effects of internal stresses. Elsevier, New York, USA, p. 71.

Ossenkemper, S., 2018. Verbundfließpressen in konventionellen Fließpresswerkzeugen. Dissertation, TU Dortmund University, Shaker Verlag, Herzogenrath.

Peiter, A., 1966. Eigenspannungen I. Art: Ermittlung und Bewertung, Triltsch, Düsseldorf.

Pöhlandt, K., 1979. Beitrag zur Aufnahme von Fließkurven bei hohen Umformgraden - Seminar "Neuere Entwicklungen in der Massivumformung", Forschungsgesellschaft Umformtechnik mbH, Stuttgart.

Pöhlandt, K., Tekkaya, A.E, Lach, E., 1983. Prüfung des plastischen Verhaltens metallischer Werkstoffe in Torsionsversuchen. Materialwissenschaft und Werkstofftechnik 14 (6), pp. 181–189.

Prager, W., 1945. Strain Hardening Under Combined Stresses. Journal of Applied Physics 16 (12), pp. 837–840.

Prime, M.B, 2001. Cross-Sectional Mapping of Residual Stresses by Measuring the Surface Contour After a Cut. Journal of Engineering Materials and Technology 123, pp. 162–168.

Prime, M.B, DeWald, A.T, 2013. The Contour Method. In: Schajer, G.S. (Ed.), Practical Residual Stress Measurement Methods. Wiley-Blackwell, pp. 109–138.

Roll, K., Tekkaya, A.E, 1993. Numerische Verfahren der Prozeßsimulation in der Umformtechnik. In: Lange, K. (Ed.), Umformtechnik Handbuch für Industrie und Wissenschaft, Band 4: Sonderverfahren, Prozeßsimulation, Werkzeugtechnik, Produktion 4. Springer-Verlag, Berlin, Heidelberg, pp. 330–435.

Sachs, G., 1927a. Der Nachweis Innerer Spannungen in Stangen und Rohren. Zeitschrift für Metallkunde (19), pp. 352–357.

Sachs, G., 1927b. Zur Theorie des Ziehvorgangs. Zeitschrift für Angewandte Mathematik und Mechanik 7, pp. 235–236.

Schmitt, J.H, Aernoudt, E., Baudelet, B., 1985. Yield loci for polycrystalline metals without texture. Materials Science and Engineering 75 (1-2), pp. 13–20.

Schmoeckel, D., 1973. Entwicklung eines Fließpressteils zur Serienreife. Industrie-Anzeiger 63 (95), pp. 1469–1472.

Schmoeckel, D., 1976. Betrachtung der Wirtschaftlichkeit des Kaltfließpressens. Draht 27, pp. 37–45.

Scholtes, B., Voehringer, O., Macherauch, E., 1980. Die Auswirkung des Bauschingereffekts auf das Verformungsverhalten technisch wichtiger Vielkristalle. Steel Research (56).

Schultheis, V., 2007. Oszillierendes Umformen mit direkt angetriebenen Umformmaschinen. Dissertation, Shaker Verlag, Aachen.

Semiatin, S.L. (Ed.), 2005. ASM Handbook - Metalworking: Bulk Forming - Volume 14A.

Shi, M.F, Zhu, X., Xia, C., Stoughton, T., 2008. Determination of Nonlinear Isotropic/Kinematic Hardening Constitutive Parameters for AHSS Using Tension and Compression Tests. Proceedings of the Numisheet 2008, pp. 137–142.

Siebel, E., 1924. Kräfte und Materialfluss bei der bildsamen Formänderung. Bericht des Walzwerkausschusses des Vereins Deutscher Eisenhüttenleute (37).

Siebel, E., 1932. Die Formgebung im Bildsamen Zustande - Theoretische Grundlagen der Technischen Formgebungsverfahren, Verlag Stahleisen GmbH, Düsseldorf.

Sillekens, W.H, 1992. Backward can extrusion and materials behaviour. Dissertation, Eindhoven University of Technology, Eindhoven, Netherlands.

Sillekens, W.H, Dautzenberg, J.H, Kals, J.A.G., 1988. Flow Curves for C45 Steel at Abrupt Changes in the Strain Path. CIRP Annals - Manufacturing Technology 37 (1), pp. 213–216.

Sillekens, W.H, Dautzenberg, J.H, Kals, J.A.G., 1991. Strain Path Dependence of Flow Curves. CIRP Annals - Manufacturing Technology 40 (1), pp. 255–258.

Singer, F., 1934. Verfahren zur Vorbehandlung von Eisen- und Stahlwerkstücken für die spanlose Formgebung, z.B. das Ziehen, Stecken und Walzen - Patent DE673405C.

Sleeswyk, A.W, Kassner, M.E, Kemerink, G.J, 1986. The Effect of Partial Reversibility of Dislocation Motion. In: Gittus, J., Zarka, J., Nemat-Nasser, S. (Eds.), Large Deformations of Solids: Physical Basis and Mathematical Modelling. Springer-Verlag, Dordrecht, pp. 81–98.

Sowerby, R., Uko, D.K, Tomita, Y., 1979. A review of certain aspects of the Bauschinger effect in metals. Materials Science and Engineering 41 (1), pp. 43–58.

Soyarslan, C., Tekkaya, A.E, Akyuz, U., 2008. Application of Continuum Damage Mechanics in discontinuous crack formation: Forward extrusion chevron predictions. Zeitschrift für Angewandte Mathematik und Mechanik 88 (6), pp. 436–453.

Spitzig, W.A., Sober, R.J., Richmond, O., 1975. Pressure dependence of yielding and associated volume expansion in tempered martensite. Acta Metallurgica 23 (7), pp. 885–893.

Stander, N., Craig, K.J, Mllerschn, H., Reichert, R., 2005. Material identification in structural optimization using response surfaces. Structural and Multidisciplinary Optimization 29 (2), pp. 93–102.

Stoltz, R.E, Pelloux, R.M, 1976. The Bauschinger effect in precipitation strengthened aluminum alloys. Metallurgical Transactions A 7 (9), pp. 1295–1306.

Suh, Y.S, Agah-Tehrani, A., Chung, K., 1991. Stress analysis of axisymmetric extrusion in the presence of strain-induced anisotropy modeled as combined isotropic-kinematic hardening. Computer Methods in Applied Mechanics and Engineering 93 (2), pp. 127–150.

Sun, L., Kim, J.H, Wagoner, R.H, 2009. Non-Proportional Hardening Of Dual Phase Steels And Its Constitutive Representation. IDDRG International Conference, pp. 119–130.

Swift, H.W, 1952. Plastic instability under plane stress. Journal of the Mechanics and Physics of Solids 1 (1), pp. 1–18.

Tabor, D., 2000. The hardness of metals, Oxford University Press, Oxford, UK.

Tan, Z., Magnusson, C., Persson, B., 1994. The Bauschinger effect in compression-tension of sheet metals. Materials Science and Engineering: A 183 (1-2), pp. 31–38.

Tekkaya, A.E, 1986. Ermittlung von Eigenspannungen in der Kaltmassivumformung. Dissertation, Universität Stuttgart, Springer-Verlag, Berlin, Heidelberg.

Tekkaya, A.E, Allwood, J.M, Bariani, P.F, Bruschi, S., Cao, J., Gramlich, S., Groche, P., Hirt, G., Ishikawa, T., Löbbe, C., Lueg-Althoff, J., Merklein, M., Misiolek, W.Z, Pietrzyk, M., Shivpuri, R., Yanagimoto, J., 2015. Metal forming beyond shaping: Predicting and setting product properties. CIRP Annals - Manufacturing Technology 64 (2), pp. 629–653.

Tekkaya, A.E, Ben Khalifa, N., Hering, O., Meya, R., Myslicki, S., Walther, F., 2017. Forming-induced damage and its effects on product properties. CIRP Annals - Manufacturing Technology 66 (1), pp. 281–284.

Tekkaya, A.E, Gerhardt, J., Burgdorf, M., 1985. Residual Stresses in Cold-Formed Workpieces. CIRP Annals - Manufacturing Technology 34 (1), pp. 225–230.

Tekkaya, A.E, Lange, K., 2000. An Improved Relationship between Vickers Hardness and Yield Stress for Cold Formed Materials and its Experimental Verification. CIRP Annals - Manufacturing Technology 49 (1), pp. 205–208.

Tekkaya, A.E, Pöhlandt, K., Lange, K., 1982. Determining Stress-Strain Curves of Sheet Metal in the Plane Torsion Test. CIRP Annals - Manufacturing Technology 31 (1), pp. 171–174.

Thuillier, S., Rauch, E.F, 1994. Development of microbands in mild steel during cross loading. Acta Metallurgica et Materialia 42 (6), pp. 1973–1983.

Tozawa, Y., 1979. Plastic deformation behavior under conditions of combined stress. In: Koistinen, D.P., Wang, N.-M. (Eds.), Mechanics of Sheet Metal Forming. Springer-Verlag, Boston, MA, pp. 81–109.

Tozawa, Y., Kojima, M., 1971. Effect of Pre-Deformation Process on Limit and Resistance in Upsetting Deformation. Journal of Japan Society for Technology of Plasticity 12, pp. 174–182.

Varma, S.K, LeFevre, B.G, 1980. Large wire drawing plastic deformation in aluminum and its dilute alloys. Metallurgical and Materials Transactions A 11 (6), pp. 935–942.

Verein Deutscher Ingenieure, 1981. VDI 3171 - Upsetting and Preforming, Beuth Verlag GmbH, Berlin.

Verhoeven, F., 1966. Internal Reports no. 503910/2/66 and 503910/5/66. N.V. Bekaert, C.V.O.

Voce, E., 1956. A practical strain-hardening function. Metallurgica (51), pp. 219–226.

Volkmuth, J., 1996. Eigenspannungen und Verzug. Härterei-Technische Mitteilungen (51), pp. 145–154.

Wagoner, R.H, Lim, H., Lee, M.-G., 2013. Advanced Issues in springback. International Journal of Plasticity 45, pp. 3–20.

Wernicke, S., Hahn, M., Gerstein, G., Nürnberger, F., Tekkaya, A.E, 2021. Strain path dependency in incremental sheet-bulk metal forming. International Journal of Material Forming 14 (4), pp. 547–561.

Wilson, D.V, 1965. Reversible work hardening in alloys of cubic metals. Acta Metallurgica 13 (7), pp. 807–814.

Yin, Q., Brosius, A., Tekkaya, A.E, 2011. Modified plane torsion tests for sheet metal characterization. Steel Research International, Special Edition: 10th International Conference on Techology of Plasticity, pp. 696–701.

Yin, Q., Soyarslan, C., Isik, K., Tekkaya, A.E, 2015a. A grooved in-plane torsion test for the investigation of shear fracture in sheet materials. International Journal of Solids and Structures 66, pp. 121–132.

Yin, Q., Tekkaya, A.E, Traphöner, H., 2015b. Determining cyclic flow curves using the in-plane torsion test. CIRP Annals - Manufacturing Technology 64 (1), pp. 261–264.

Yoon, S.Y, Choi, H.S, Yoon, J.W, Barlat, F., 2018. FE implementation of HAH model using FDM-based stress update algorithm for springback prediction of AHSS sheets. Journal of Physics Conference Series 1063, 012021.

Yoshida, F., Hamasaki, H., Uemori, T., 2013. Modeling of anisotropic hardening of sheet metals. In: Yoon, J.W., Stoughton T.B., Rolfe B., Beynon, J.H., Hodgson P. (Eds.), AIP Conference Proceedings 1567. AIP Publishing, pp. 482–487.

Yoshida, F., Uemori, T., 2002. A model of large-strain cyclic plasticity describing the Bauschinger effect and workhardening stagnation. International Journal of Plasticity 18 (5-6), pp. 661–686.

Yoshida, F., Uemori, T., Fujiwara, K., 2002. Elastic–plastic behavior of steel sheets under in-plane cyclic tension–compression at large strain. International Journal of Plasticity 18 (5-6), pp. 633–659.

Yoshida, F., Urabe, M., Toropov, V.V, 1998. Identification of material parameters in constitutive model for sheet metals from cyclic bending tests. International Journal of Mechanical Sciences 40 (2-3), pp. 237–249.

Yoshino, M., Shirakashi, T., 1997. Flow-stress equation including effects of strain-rate and temperature history. International Journal of Mechanical Sciences 39 (12), pp. 1345–1362.

Zhu, Y.X, Liu, Y.L, Li, H.P, Yang, H., 2013. Springback prediction for rotary-draw bending of rectangular H96 tube based on isotropic, mixed and Yoshida–Uemori two-surface hardening models. Materials & Design 47, pp. 200–209.

Ziegler, H., 1959. A modification of Prager's hardening rule. Quarterly of Applied Mathematics 17 (1), pp. 55–65.

Zimerman, Z., Avitzur, B., 1970. Analysis of the Effect of Strain Hardening on Central Bursting Defects in Drawing and Extrusion. Journal of Engineering for Industry 92 (1), p. 135.

Zoch, H.-W., 2006. From Single Production Step to Entire Process Chain – the Global Approach of Distortion Engineering. Materialwissenschaft und Werkstofftechnik 37 (1), pp. 6–10.

Zucko, M., Pöhlandt, K., Pyzalla, A., Reimers, W., Kockelmann, H., 1997. Berechnung der Umformeigenspannungen beim Fließpressen und Vergleich mit experimentellen Ergebnissen. Materialwissenschaft und Werkstofftechnik 28 (9), pp. 417–423.

Appendix A: Forward rod extrusion experiments

Cylindrical workpieces with a length of $l_0 = 71$ mm and a diameter of $d_0 = 30$ mm were extracted from the as-received materials in the form of bars with diameters between 30 and 40 mm. To improve the adhesion of lubricant to the workpieces, the parts were sandblasted at a pressure of 6 bar by use of a mineral melting-chamber granulate with a grain diameter between $0.25 - 1.4$ mm. The parts were ultrasonically cleaned in an ethanol bath and air dried. The parts were then heated up to 90 °C and immersed in an aqueous solution of the solid lubricant Beruforge 191. Beruforge 191 is a MoS2-containing coating lubricant with low particle size that has a high pressure-stability and withstands large surface expansions without the need of zinc phosphates. The lubricant can be used up to temperatures of $T = 500$ °C (Carl Bechem GmbH, 2020). After coating, the water evaporates, leaving the actual lubricant on the parts.

All extrudates were produced on a triple-acting hydraulic deep drawing press of the type SMG HZPUI 260/160-1000/1000. The machine setup is shown in **Figure A.1**.
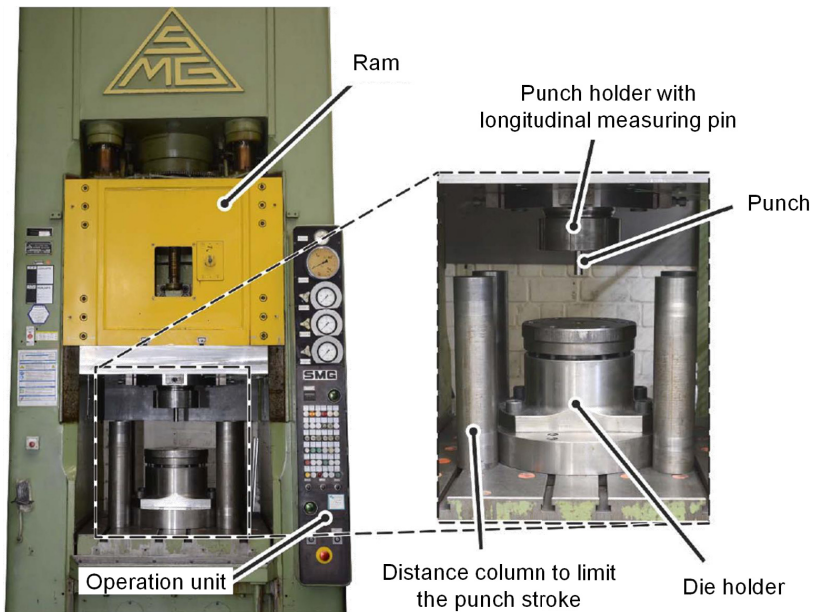
Figure A.1: Extrusion press and die setup (Ossenkemper, 2018)

To use the press for cold forging applications, the ram and the blank holder forces are coupled with a coupling plate, leading to a total force of 2,600 kN. The total extrusion force is measured with a piezoelectric longitudinal measuring pin, positioned above a

pressure plate, which is located within the punch holder directly above the punch. During extrusion, the measuring pin records the elastic strain of the pressure plate which can then be transformed into force values. The maximum punch stroke of the hydraulic press was limited by four distance columns which are located around the die setup. The exact height is controlled by additional distance plates which are positioned on top of the columns. All extrusion experiments were conducted with a constant punch velocity of $v_p = 10$ mm/s. After forming, the parts are pushed out of the die and the container under high forces by an ejector. **Figure A.2** shows forward extruded 16MnCrS5 parts with different extrusions strains.

Material:	16MnCrS5
Tool radii:	$r_{ex} = 3$ mm
Extrusion strain:	$\varepsilon_{ex} = \ln(d_0^2/d_1^2)$
Die angle:	$2\alpha = 90°$

$\varepsilon_{ex} = 0.1$ $\varepsilon_{ex} = 0.2$ $\varepsilon_{ex} = 0.3$ $\varepsilon_{ex} = 0.5$ $\varepsilon_{ex} = 0.7$ $\varepsilon_{ex} = 1.0$ $\varepsilon_{ex} = 1.2$ $\varepsilon_{ex} = 1.5$
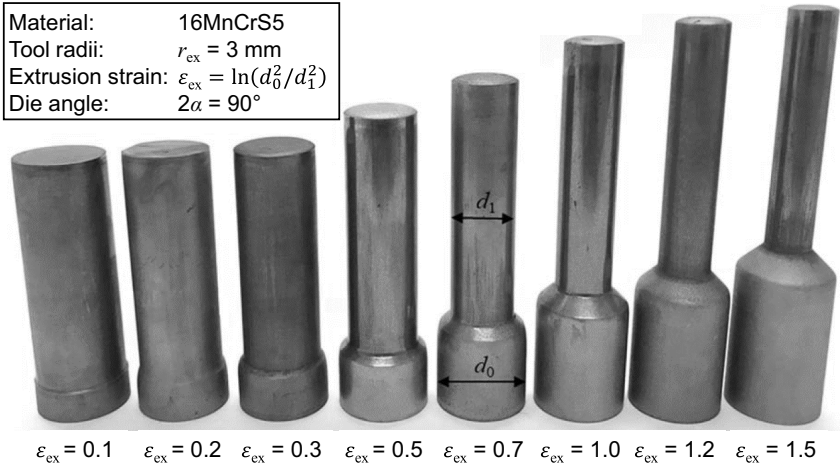
Figure A.2: Forward extruded 16MnCrS5 parts with various extrusion strains
            (adapted from Hering, 2020)

Appendix B: Finite element simulation of cold forging processes

The FEM program Abaqus CAE (Version 6.13-4) was used for the conduction of all numerical investigations. The main reason for this choice is the straight-forward implementation of user-defined material models (Abaqus internal keyword UMAT). As the results in this thesis rely heavily on numerical investigations, the necessary steps of the FEM model setup will be described in the following section.

Forward rod extrusion and reduction

The workpiece was modelled as an elastic-plastic object. To correctly simulate the residual stress reduction during part ejection, according to Tekkaya (1986) the die was simulated as an elastic object with a Young's modulus of $E_{die} = 210$ GPa and a Poisson's ratio $v_{die} = 0.3$. The model assembly at different process stages is shown in **Figure B.1**.
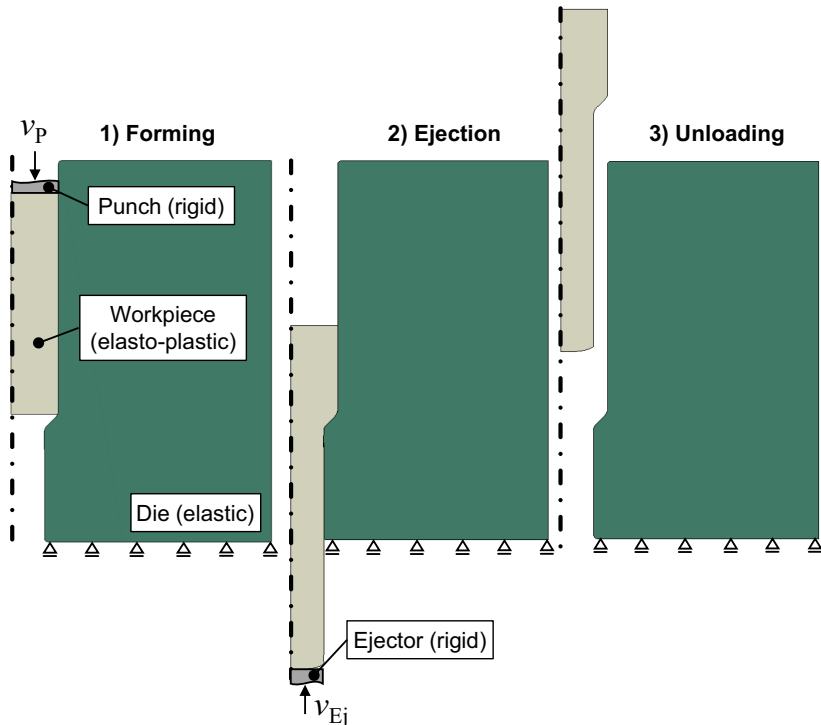

Figure B.1: Model assembly of forward rod extrusion at different simulation stages

In the first stage, the workpiece is pushed into the die and reduced in diameter. In the second stage, the workpiece is unloaded and then loaded at the bottom edge into the opposite direction, to eject the part from the die. In the third stage, the part is unloaded

numerically by deactivating all boundary conditions (except the symmetry condition) and an additional equilibrium calculation is conducted. The punch movement was applied directly by prescribing a constant ram velocity v_P to the top edge of the workpiece. Same applies to the ejection velocity v_{Ej} at the bottom edge of the formed workpiece. The y-translation of the die at the bottom edge is set to zero.

The flow curve of 16MnCrS5 was determined by means of the procedure presented in Section 4.4.3. The work-hardening was assumed as isotropic for the determination of the friction coefficients, as the material does not experience significant cyclic deformations. The effect of the temperature increase during cold forging on the current flow stress was neglected due to its minor influence on the resulting local workpiece properties after forming ($\Delta T \approx 250\ °C$ for $\varepsilon_{ex} = 1.5$, see Section 4.3.1.

The workpiece was meshed with 2D-axisymmetric 4-node quadrilateral elements with reduced integration (CAX4R). To determine a suited mesh size that yields a good compromise between result quality and calculation time, a mesh convergence study was performed. As the calculated residual stresses are most sensitive with regard to the mesh quality, they were used as the target quantity in the mesh convergence study. The necessary number of elements was determined by the example of forward rod extrusion ($\varepsilon_{ex} = 0.7$, $2\alpha = 90°$ $r_{ex} = 3$ mm, $\mu = 0.035$). The influence of the number of elements on the strain and residual stress distribution over the extrudate radius after extrusion and unloading are shown in **Figure B.2**.
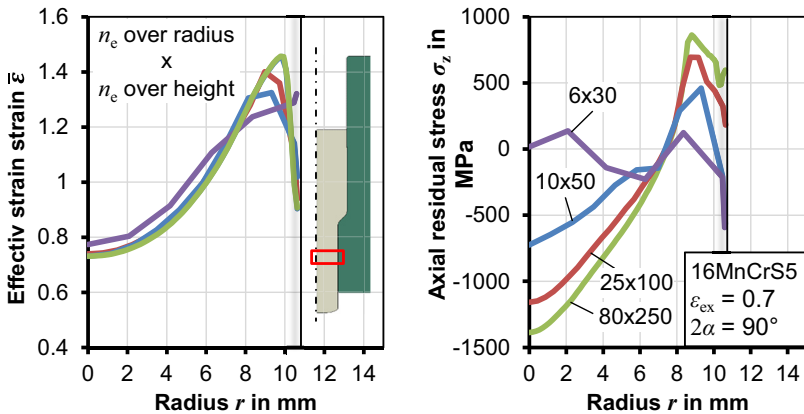
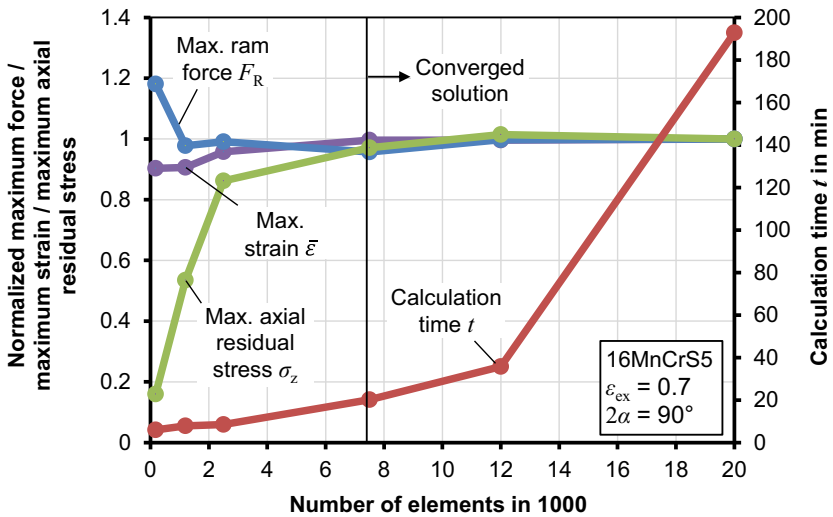**Figure B.2:**   Influence of the number of elements on the resulting effective strain and axial residual stress over the extrudate radius after unloading

As expected, both effective strain and stress depend strongly on the number of elements both over the extrudate length and the extrudate radius. This is mainly due the influence of the mesh density on the resolution of the workpiece curvature at die shoulders and

the effect of extensive element shearing toward the surface, which becomes more pronounced with larger elements.

To conclude the results of the mesh convergence study, the influence of the mesh density on the maximum punch force, the maximum strain and the maximum axial residual stress after forming and unloading are depicted in **Figure B.3**. To allow better comparison all values are normalized by their corresponding value at the highest investigated number of elements (80x250 = 20,000). While the punch force converges at 2,000 elements, the strain and residual stress converge at 7,500 elements. As the calculation time increases from 20 minutes to about 200 minutes between the two settings, the solution lower element number was considered sufficient. The corresponding mesh density of 7 elements/mm^2 was fixed for all simulations and only increased in cases where no stable solution could be achieved otherwise.

Figure B.3: Influence of the number of elements on the maximum ram force, maximum strain and maximum axial residual stress after unloading and corresponding calculation time

As the dies were defined to deform only elastically, the mesh density of the die is less critical. As a result, about 4,800 elements were used. The die mesh is more refined at the die shoulders, as this is the location of the highest elastic deflections during extrusion. In regions further away, the mesh density is reduced significantly to speed up calculation time. A representative die mesh for $\varepsilon_{ex} = 0.7$ is shown in **Figure B.4**.
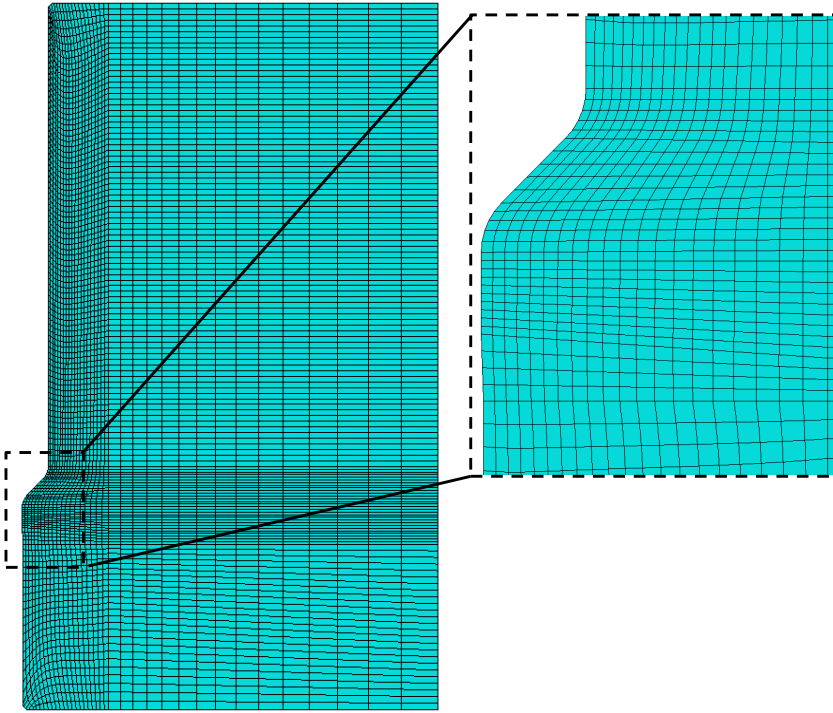
Figure B.4: Representative mesh for the die and container in forward rod extrusion
($\varepsilon_{ex} = 0.7$, $2\alpha = 90°$ $r_{ex} = 3$ mm, $\mu = 0.04$)

The node-to-surface contact algorithm was utilized to model the contact between the die and the workpiece. To simulate the friction between the workpiece and the die, the Coulomb friction model was used. The friction coefficient was changed iteratively to assure the best possible fit between simulated and the experimentally obtained ram forces for all investigated extrusion ratios. The friction coefficient was determined as $\mu < 0.035$, which leads to a good correlation between experimental and numerical results over the whole range of investigated extrusion ratios (**Figure B..5**).

The highest deviations occur at the lower extrusion ratios, as the absolute values of the ram forces are lowest (~31 % deviation). The deviations can be attributed to a variety of factors that are neglected in the simulation, including the pressure-dependence of the friction coefficient, statistical scattering of the experimental ram force measurements (partly attributed to the change in forming conditions over time due to heating and lubrication of the die) as well as the influence of the temperature on the flow stress. As all these factors have only a minor influence on the part's properties, which are the focus

of this thesis, the deviations are considered insignificant as the general trend of the ram forces is captured accurately.
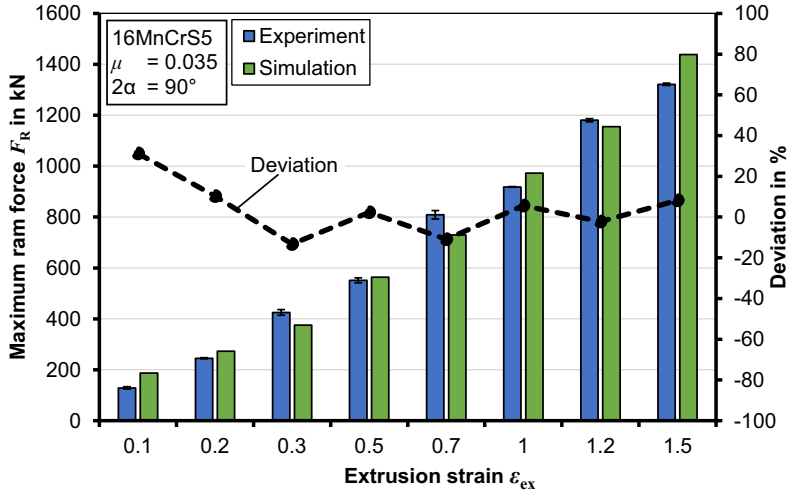
Figure B.5: Comparison of numerical and experimentally obtained ram forces for three different extrusion ratios

Backward can extrusion

The process of backward can extrusion is divided into three process stages, namely: forming, punch removal and ejection as illustrated in **Figure B.6**.
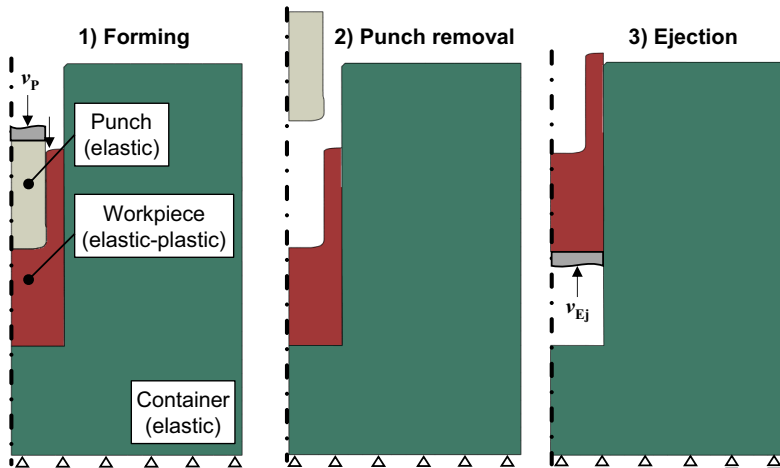
Figure B.6: Simulation stages in back ward can extrusion

For backward can extrusion, the mesh density was set equal to that determined for forward rod extrusion (~7 elements/mm^2). As backward can extrusion introduces extreme shearing to some workpiece regions, which cannot be overcome by a mere increase of the mesh density, a manual remeshing algorithm was utilized for the conduction of backward can extrusion simulations, which is presented in detail in Appendix C.

Multi-stage and combined cold forging

For the multi-stage and combined cold forging processes presented in Section 8.1, the simulation settings were applied analogously to the previous sections. The mesh density was set to ~7 elements/mm^2 according to the convergence study applied for forward rod extrusion. For all multi-stage and combined cold forging processes the manual remeshing algorithm was applied according to Appendix C, whenever extensive element distortions have occurred.

Appendix C: Manual remeshing algorithm in Abaqus Standard

In the simulation of cold forging applications by means of FEM, some workpiece regions undergo significant plastic deformations. In some cases these deformations can cause extensive mesh distortions, which can cause a degradation of the calculated local field quantities. This can ultimately lead to a premature termination of the simulation as the calculated solution diverges from the real solution. In addition, mesh distortions can lead to an occurrence of negative element Jacobians (i. e. the element becomes concave), which prevents further mapping between the elements current shape and its corresponding reference unit element. The most common method to tackle problems caused by extensive mesh distortion in bulk forming simulations, is the usage of automatic remeshing algorithms, which detect local mesh degradations and assign a new, regularized mesh to the deformed structure, while preserving the calculated field quantities up to this point. Abaqus Standard (implicit), however, does not include an in-built automatic remeshing capability. Instead, a manual remeshing algorithm was implemented and applied to critical simulations, in which mesh distortions have led to a premature stop. The manual remeshing procedure applied in this work is visualized in **Figure C.1**.
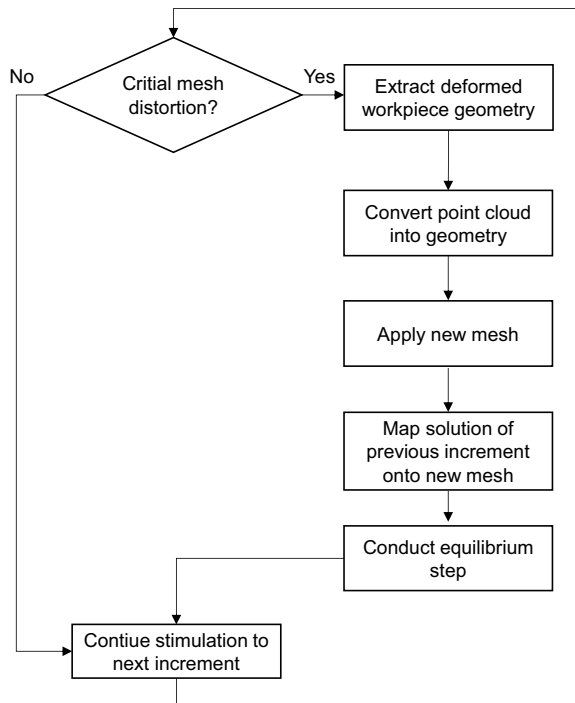
Figure C.1: Manual remeshing algorithm utilized for critical simulations

In a first step, the mesh quality is assessed in terms of critical element distortions. Whenever a deformed element yields a corner angle smaller than 30° or larger than 120°, the manual remeshing algorithm was triggered. In a first step, the deformed workpiece geometry is imported from the result database (odb-file) of the previous step. The imported file contains the deformed mesh geometry in terms of nodal coordinates and an element connectivity list. To apply the general Abaqus meshing capabilities to the deformed configuration, the elements are transformed into geometry data, which approximates the nodal coordinates with analytical functions. A new regularized mesh is manually applied to the deformed geometry and the boundary conditions and interaction properties are reapplied to the model. The Abaqus keyword MAP SOLUTION is utilized, to map the results of the last increment before the critical mesh degradation onto the new mesh. As the mapping introduces some interpolation errors, an equilibrium calculation is conducted before continuation of the actual simulation. The manual remeshing procedure is repeated whenever necessary until the simulation is finished.

The application of the manual remeshing algorithm is illustrated by the example of backward can extrusion. **Figure C.2** shows a situation at which the manual remeshing algorithm was applied to prevent subsequent result degradation due to excessive element distortion in the forming zone.
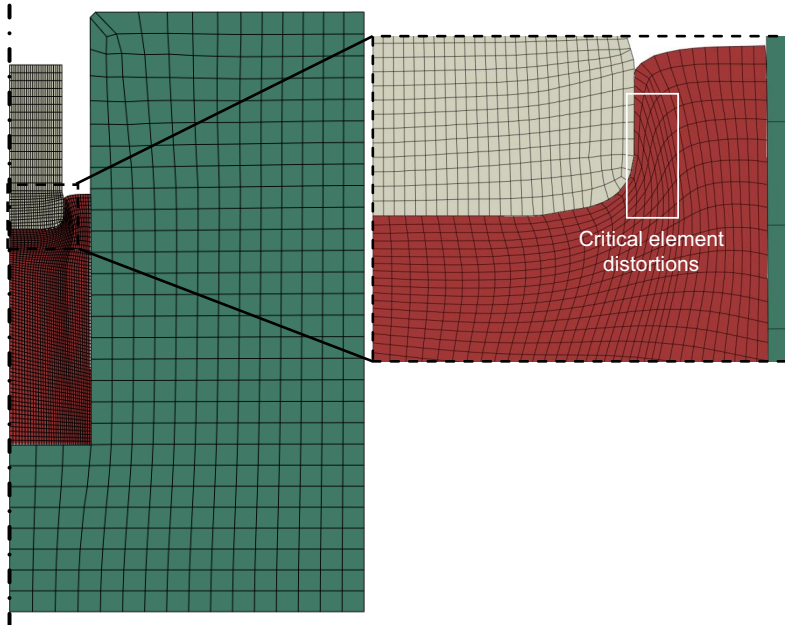

Figure C.2: Situation during backward can extrusion during which the manual remeshing algorithm is applied to prevent degradation of the result quality

In the demonstrated case, the remeshing algorithm was applied after a punch stroke of 5 mm and multiple times after that at punch stroke increments of 2.5 mm. Remeshing introduces several additional sources of error including

- manual conversion of the nodal points from the deformed mesh into a parameterized geometry that can be remeshed,
- restoring the contact conditions between the tools and the workpiece and
- interpolation errors caused by remeshing.

Any changes of the result quality in between individual remeshing steps were investigated carefully to assure that the solution is not altered by the remeshing process.

The influence of five remeshing stages on the resulting punch force is illustrated in **Figure C.3**. The results show no significant discontinuities in the punch force, which is a first indicator that remeshing does not falsify the calculated results.
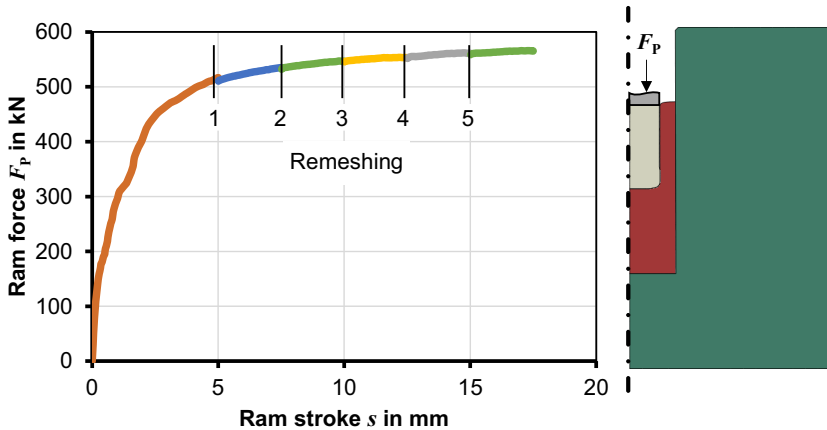
Figure C.3: Influence of manual remeshing steps on the resulting force-stroke curve

Local quantities like effective strains and residual stresses are more sensitive to numerical errors. To check a potential influence of remeshing on those quantities, a contour plot of the axial stress distribution as well as the axial stress and effective strain distribution are shown in **Figure C.4**. The stresses and strains were evaluated before remeshing as well as after remeshing and the corresponding initial balance calculation.

The results suggest that the manual remeshing algorithm does not introduce any significant alterations to the local field quantities. It is noted, however, that any potential alterations that may be caused by remeshing were always traced carefully for all simulation in which remeshing was necessary to achieve a stable solution.
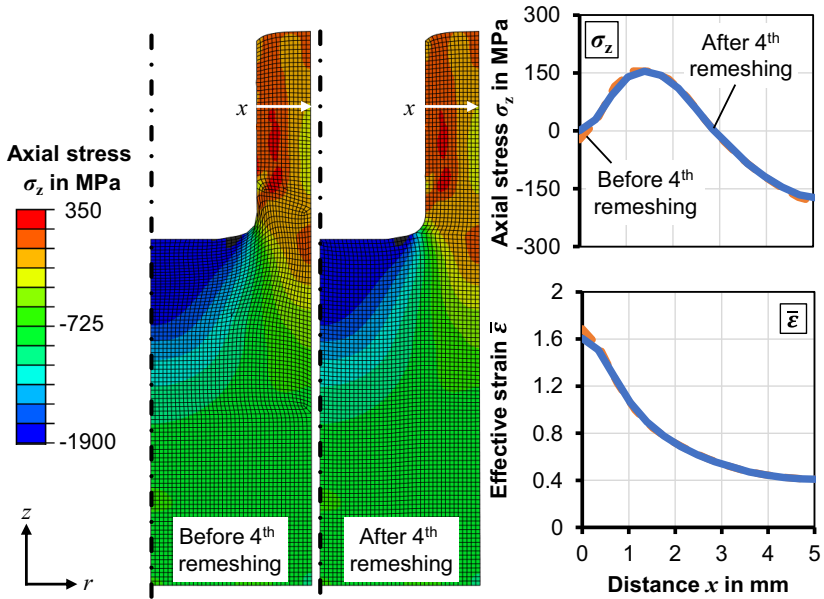
Figure C.4: Axial residual stress and effective strain distribution before and after remeshing (backward can extrusion, workpiece loaded, tools are suppressed for illustration purposes)

The manual remeshing algorithm was applied to the following simulations, which otherwise would not have yielded reliable results:

- Forward rod extrusion with extrusion strains $\varepsilon_{ex} \geq 1.2$
- Backward can extrusion
- Combined forming process: Forward extrusion and upsetting
- Multi-stage forming process: Backward can extrusion and flange upsetting

In all above cases, the application of the manual remeshing algorithm enabled the simulations to finish without any obvious result quality degradations.

Appendix D: Flow stress calculation for kinematic hardening models

The yield surface translation in kinematic hardening models is described by the back stress tensor $\boldsymbol{\alpha}$. The flow stress is calculated using the von Mises yield condition according to

$$\sigma_{\text{Mises}}(\boldsymbol{\sigma} - \boldsymbol{\alpha}) - \sigma_{\text{f,iso}}(\bar{\varepsilon}^p) = 0 \tag{D.1}$$

$$\left[\left((\sigma_{xx} - \alpha_{xx}) - (\sigma_{yy} - \alpha_{yy})\right)^2 + \left((\sigma_{yy} - \alpha_{yy}) - (\sigma_{zz} - \alpha_{zz})\right)^2 + \right.$$
$$\left((\sigma_{zz} - \alpha_{zz}) - (\sigma_{xx} - \alpha_{xx})\right)^2 + \left((\tau_{xy} - \alpha_{xy})^2 + (\tau_{xz} - \alpha_{xz})^2 + \right. \tag{D.2}$$
$$\left. \left(\tau_{yz} - \alpha_{yz})^2\right)\right]^{1/2} - \sigma_{\text{f,iso}}(\bar{\varepsilon}^p) = 0.$$

Herein, $\sigma_{\text{f,iso}}$ corresponds to the current radius of the yield locus, taking into account isotropic hardening. To calculate the flow stress for any given stress state, **Eq. (D.2)** is solved for the corresponding component of the stress tensor, while all the other components are set to zero. For each single stress component, there exist two solutions of the above equation, which correspond to the two possible signs for each loading direction (e. g. tension / compression). Considering all possible uniaxial stress states this adds up to a total of twelve flow stress values.

The solutions of Eq. (D.2) for all uniaxial stress states are given in the following:

$$\sigma_{\text{f,xx}\pm} = \alpha_{xx} - \frac{\alpha_{yy} + \alpha_{zz}}{2}$$
$$\pm \frac{1}{2}\left(-12\alpha_{xy}^2 - 12\alpha_{xz}^2 - 3\alpha_{yy}^2 + 6\alpha_{yy}\alpha_{zz} - 12\alpha_{yz}^2 - 3\alpha_{zz}^2 \right. \tag{D.3}$$
$$\left. + 4\sigma_{\text{f,iso}}^2\right)^{1/2}$$

$$\sigma_{\text{f,xx}\pm} = \alpha_{yy} - \frac{\alpha_{xx} + \alpha_{zz}}{2}$$
$$\pm \frac{1}{2}\left(-12\alpha_{xy}^2 - 12\alpha_{xz}^2 - 3\alpha_{xx}^2 + 6\alpha_{xx}\alpha_{zz} - 12\alpha_{yz}^2 - 3\alpha_{zz}^2 \right. \tag{D.4}$$
$$\left. + 4\sigma_{\text{f,iso}}^2\right)^{1/2}$$

$$\sigma_{\text{f,zz}\pm} = \alpha_{zz} - \frac{\alpha_{xx} + \alpha_{yy}}{2}$$
$$\pm \frac{1}{2}\left(-12\alpha_{xy}^2 - 12\alpha_{xz}^2 - 3\alpha_{xx}^2 + 6\alpha_{xx}\alpha_{yy} - 12\alpha_{yz}^2 - 3\alpha_{yy}^2 \right. \tag{D.5}$$
$$\left. + 4\sigma_{\text{f,iso}}^2\right)^{1/2}$$

$$\sigma_{f,xy\pm} = \alpha_{xy} \pm \frac{\sqrt{3}}{3}\left(-\alpha_{xx}^2 + \alpha_{xx}\alpha_{yy} + \alpha_{xx}\alpha_{zz} - 3\alpha_{xz}^2 - \alpha_{yy}^2 + \alpha_{yy}\alpha_{zz}\right.$$
$$\left. - 3\alpha_{yz}^2 - \alpha_{zz}^2 + \sigma_{f,iso}^2\right)^{1/2} \tag{D.6}$$

$$\sigma_{f,yz\pm} = \alpha_{yz} \pm \frac{\sqrt{3}}{3}\left(-\alpha_{xx}^2 + \alpha_{xx}\alpha_{yy} + \alpha_{xx}\alpha_{zz} - 3\alpha_{xy}^2 - \alpha_{yy}^2 + \alpha_{yy}\alpha_{zz}\right.$$
$$\left. - 3\alpha_{xz}^2 - \alpha_{zz}^2 + \sigma_{f,iso}^2\right)^{1/2} \tag{D.7}$$

$$\sigma_{f,xz\pm} = \alpha_{xz} \pm \frac{\sqrt{3}}{3}\left(-\alpha_{xx}^2 + \alpha_{xx}\alpha_{yy} + \alpha_{xx}\alpha_{zz} - 3\alpha_{xy}^2 - \alpha_{yy}^2 + \alpha_{yy}\alpha_{zz}\right.$$
$$\left. - 3\alpha_{yz}^2 - \alpha_{zz}^2 + \sigma_{f,iso}^2\right)^{1/2} \tag{D.8}$$

Due to the quadratic form of **Eq. (D.3)** to **(D.8)**, there exist two separate solutions for each uniaxial stress state (indicated by $\pm$). For example, the flow stress under uniaxial tensile loading in xx-direction is indicated by $\sigma_{f,xx+}$, whereas the flow stress under uniaxial compressive loading in xx-direction is indicated by $\sigma_{f,xx-}$. Consequently, there exist six Bauschinger coefficients χ, i. e. one for each uniaxial stress state (**Table D.1**).

Table D.1: Bauschinger coefficients, calculated from the directional flow stresses

χ_{xx}	χ_{yy}	χ_{zz}	χ_{xy}	χ_{xz}	χ_{yz}
$\dfrac{\left\vert\sigma_{f,xx-}\right\vert}{\sigma_{f,xx+}}$	$\dfrac{\left\vert\sigma_{f,yy-}\right\vert}{\sigma_{f,yy+}}$	$\dfrac{\left\vert\sigma_{f,zz-}\right\vert}{\sigma_{f,zz+}}$	$\dfrac{\left\vert\sigma_{f,xy-}\right\vert}{\sigma_{f,xy+}}$	$\dfrac{\left\vert\sigma_{f,xz-}\right\vert}{\sigma_{f,xz+}}$	$\dfrac{\left\vert\sigma_{f,yz-}\right\vert}{\sigma_{f,yz+}}$

A Bauschinger coefficient of $\chi = 1$ means, the flow stress in a given load direction is independent of the sign of the load, whereas a Bauschinger coefficient $\chi = 0.5$ would mean, the flow stress under compression is half of the flow stress under tension.

Appendix E: Residual stress determination via contour method

The contour method by Prime (2001) was applied to determine the residual stress field in forward extruded parts to validate the numerical results. Besides neutron diffraction-based methods and the Sachs boring method (1927a), the contour method is among the few methods to obtain a residual stress distribution over a macroscopic body, while being more time- and cost-efficient as compared to the other methods and relying only on a few assumptions (e. g. ideal cutting conditions). The basic process principle of the contour method is illustrated in **Figure E.1**.
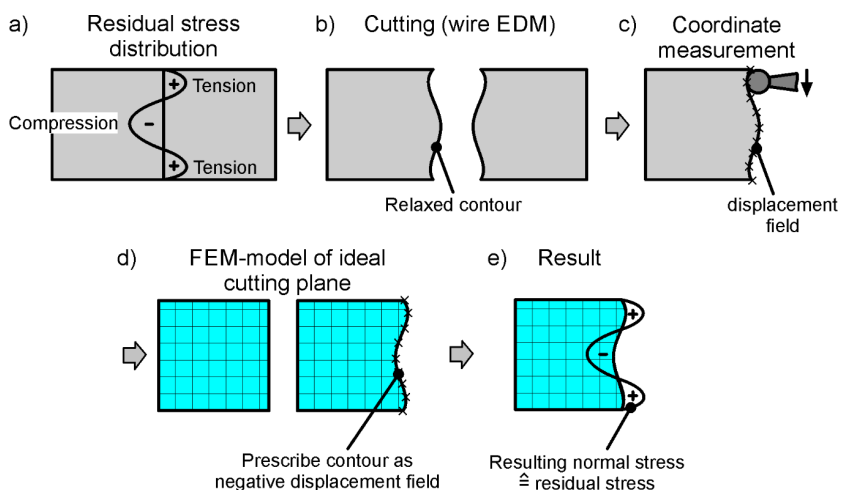
Figure E.1: Basic principle of the contour method to determine residual stresses

A body is considered, which is subject to initial residual stresses (**Figure E.1a**). If the body is cut into two halves along the plane normal to the residual stress direction of interest, the separation results in a residual stress relaxation leading to an elastic spring back of the cut surfaces (**Figure E.1b**). Wire-cutting electrical discharge is recommended to prevent the alteration of the relaxed surfaces which would be influenced by mechanical cutting methods. The relaxed surface contour is measured and the data is processed to achieve a displacement field, hence the name of the method (**Figure E.1c**). Due to the scatter of the experimentally measured surface contour point cloud as well as surface tilting the data is smoothed and processed further to obtain the contour, e. g. in terms of an analytical expression with respect to the coordinates. A FEM-simulation model is set up, considering the geometry of interest with an ideally plane cutting surface (**Figure E.1d**). By applying the reversed displacement field to the cutting plane as a boundary condition, the resulting stresses equal the residual stress field (**Figure E.1e**).

To investigate the axial residual stress distribution in the forward extruded parts, a clamping setup was designed, allowing positioning of the extrudates and preventing dropping of the cut halves which could cause potential cutting errors (**Figure E.2**).

a) Clamping setup

Upper clamp

Cutting plane

Extrudate

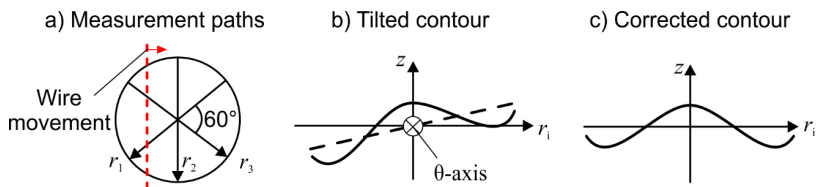Lower clamp

b) Wire-cut EDM

Wire
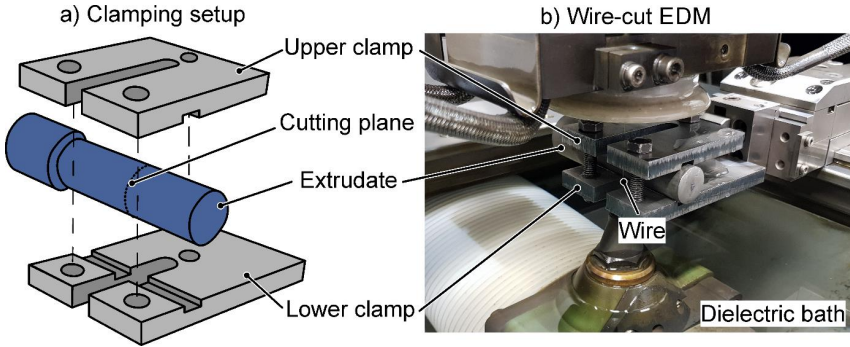
Dielectric bath

Figure E.2: Wire-cut EDM of cold extruded rods: a) Clamping setup, b) Experimental setup before immersion with the dielectric fluid

The extrudate is clamped with the device and its orientation is marked on the part to keep track in the subsequent process stages. The clamping setup is immersed in bath consisting of a dielectric fluid. The cutting wire is translated along the plane of interest and cuts the extrudate in two halves. The cutting parameters are given in **Table E.1**.

Table E.1: Wire-cut parameters

Wire diameter in mm	Wire tension in N	Cutting speed in mm min^{-1}	Flushing nozzle injection pressure in bar	Roughness R_a in µm
0.25	12	3.84	13	2.8

The contour of the cut surfaces is measured by means of a tactile coordinate measurement system Zeiss PRISMO VAST 5 HTG with a resolution of 1 µm. Each extrudate half was measured along three linear radial paths r_i orientated at angles of 60°, making up a total of six contour paths per extrudate (**Figure E.3a**).

a) Measurement paths

Wire movement

60°

r_1 r_2 r_3

b) Tilted contour

z

r_i

θ-axis

c) Corrected contour

z

r_i

Figure E.3: Coordinate measurement of cold extruded rods and data correction procedure with respect to a tilted contour

Each measured contour was post-processed to account for tilting of the cut surfaces with respect to the ideal cutting plane (**Figure E.3b**). To achieve this, the data was rotated around the θ-axis to attain a symmetric contour with respect to the extrudate's z-axis (**Figure E.3c**). Each contour is approximated by a polynomial of sixth degree to smooth the data scattering caused by the surface roughness generated during wire-cutting.

Finally, the processed contour data of each extrudate is applied to an idealized FEM-model of the cut extrudate in terms of a negative displacement field on the initially ideal cutting plane. The simulations were setup as axisymmetric FEM-models in Abaqus Standard. The material behavior was assumed elastic with a Young's modulus of $E = 210,000$ MPa and a Poisson's ratio of $v = 0.3$. The resulting normal stress distributions on the cutting plane equal the forming-induced residual stress field present in the extrudate before wire-cutting.

The results for parts with three extrusion strains are shown in **Figure E.4**. The error bars indicate the standard deviation of six contour measurements per extrusion strain.
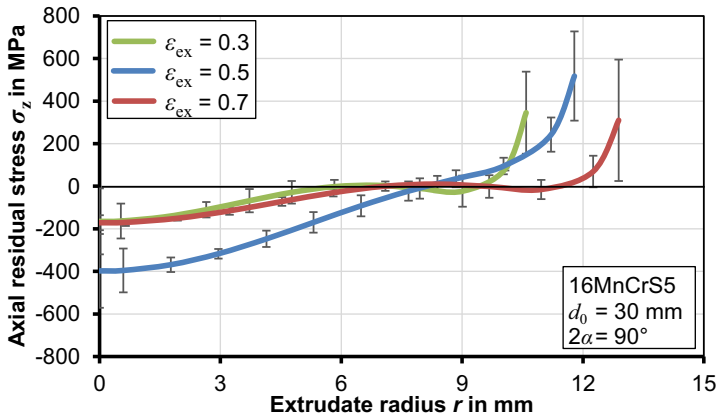
Figure E.4: Axial residual stress distribution for three different extrusion ratios as obtained by the contour method

In the core of the extrudates, there exists a compressive residual stress, whereas, towards the surfaces the material is subject to positive residual stress. Qualitatively, the results of the contour method match well with the expected axial residual stress distributions. Even the slight drop shortly before the rapid increase toward the surface is captured by the method. In this region, the data scattering is high, due to the rapid change of the residual stress. Consequently, the contour method is expected to yield only averaged results in this region. The contour method can be applied to determine radial and tangential residual stress fields simply by changing the cutting plane, respectively.

Curriculum Vitae

General:

Name	Felix Kolpak
Time and place of birth	19.08.1991, Duisburg
Nationality	German

Education:

09/2002– 08/2011	Landfermann-Gymnasium, Duisburg
08/2011	Abitur (German High School Diploma)
10/2011 – 03/2014	Undergraduate Program, Mechanical Engineering, TU Dortmund University
03/2015	Bachelor of Science, Mechanical Engineering
03/2015 – 10/2016	Graduate Program, Mechanical Engineering, TU Dortmund University
10/2016	Master of Science, Mechanical Engineering

Scholarships and Prizes:

06/2016	IMU-Scholarship (Industrieverband Massivumformung)
03/2018	Scholarship for the participation of the ISPF-seminar in Nagoya, Japan
09/2019	ICFG International Prize 2019, Donostia-San Sebastian, Spain

Career:

06/2014 – 09/2015	Student assistant, IUL, TU Dortmund
09/2015 – 11/2016	Research assistant, IUL, TU Dortmund
11/2016 – 01/2022	Research associate (Department of bulk metal forming), IUL, TU Dortmund University
since 01/2022	Team leader (Department of profile and sheet metal forming), IUL, TU Dortmund University

Aus der Dortmunder Umformtechnik sind im Shaker Verlag bisher erschienen:

A. Adelhof: Komponenten einer flexiblen Fertigung beim Profilrunden.
ISBN 3-86111-601-4

G. Reil: Prozeßregelung numerisch gesteuerter Umformmaschinen mit Fuzzy
Logic.   ISBN 3-86111-862-9

F. Maevus: Rechnerintegrierte Blechteilefertigung am Beispiel des
Gesenkbiegens.   ISBN 3-8265-0104-7

R. Warstat: Optimierung der Produktqualität und Steigerung der Flexibilität
beim CNC-Schwenkbiegen.   ISBN 3-8265-1170-0

H. Sulaiman: Erweiterung der Einsetzbarkeit von Gesenkbiegepressen durch
die Entwicklung von Sonderwerkzeugen.   ISBN 3-8265-1443-2

Ch. Smatloch: Entwicklung eines numerisch einstellbaren Werkzeugsystems für
das Tief- und Streckziehen.   ISBN 3-8265-1465-3

T. Straßmann: Prozeßführung für das Walzrunden auf der Basis Neuronaler
Netze.   ISBN 3-8265-1966-3

L. Keßler: Simulation der Umformung organisch beschichteter Feinbleche und
Verbundwerkstoffe mit der FEM.   ISBN 3-8265-2256-7

E. Szücs: Einsatz der Prozeßsimulation bei der Entwicklung eines neuen
Umformverfahrens - der Hochdruckblechumformung.   ISBN 3-8265-3119-1

S. Chatti: Optimierung der Fertigungsgenauigkeit beim Profilbiegen.
ISBN 3-8265-3534-0

F. Haase: Eigenspannungen an dünnwandigen Bauteilen und
Schichtverbunden.   ISBN 3-8265-4312-2

N. Austerhoff: Integrierte Produkt- und Prozeßgestaltung für die Herstellung
von Blechbiegteilen.   ISBN 3-8265-6613-0

D. Arendes: Direkte Fertigung gerundeter Aluminiumprofile beim
Strangpressen.   ISBN 3-8265-6442-1

R. Kolleck: Finite-Element-Simulation wirkmedienbasierter
Blechumformverfahren als Teil einer virtuellen Fertigung.   ISBN 3-8265-6566-5

T. Weidner: Untersuchungen zu Verfahren und Werkzeugsystemen der
wirkmedienbasierten Blechumformung.   ISBN 3-8265-6602-5

W. Homberg: Untersuchungen zur Hochdruckblechumformung und deren
Verfahrenskomponenten.   ISBN 3-8265-8684-0

M. Rohleder: Simulation rückfederungsbedingter Formabweichungen im Produktentstehungsprozess von Blechformteilen.   ISBN 3-8265-9977-2

V. Hellinger: Untersuchungen zur Methodik der Berechnung und Herstellung von leichten Stützkernverbunden.   ISBN 3-8322-0104-1

A. Klaus: Verbesserung der Fertigungsgenauigkeit und der Prozesssicherheit des Rundens beim Strangpressen.   ISBN 3-8322-0208-0

B. Heller: Halbanalytische Prozess-Simulation des Freibiegens von Fein- und Grobblechen.   ISBN 3-8322-0923-9

A. Wellendorf: Untersuchungen zum konventionellen und wirkmedienbasierten Umformen von komplexen Feinstblechbauteilen.   ISBN 3-8322-2435-1

C. Klimmek: Statistisch unterstützte Methodenplanung für die Hochdruck-Blechumformung.   ISBN 3-8322-2994-9

R. Krux: Herstellung eigenschaftsoptimierter Bauteile mit der Hochdruck-Blechumformung und Analyse der induzierten Eigenspannungen.
ISBN 3-8322-3551-5

S. Jadhav: Basic Investigations of the Incremental Sheet Metal Forming Process on a CNC Milling Machine. ISBN 3-8322-3732-1

C. Beerwald: Grundlagen der Prozessauslegung und -gestaltung bei der elektromagnetischen Umformung. ISBN 3-8322-4421-2

A. Brosius: Verfahren zur Ermittlung dehnratenabhängiger Fließkurven mittels elektromagnetischer Rohrumformung und iterativer Finite-Element-Analysen. ISBN 3-8322-4835-8

R. Ewers: Prozessauslegung und Optimierung des CNC-gesteuerten Formdrückens. ISBN 3-8322-5177-4

T. Langhammer: Untersuchungen zu neuen Konzepten für PKW-Kraftstoff-behälter. ISBN 3-8322-5300-9

M. Schikorra: Modellierung und simulationsgestützte Analyse des Verbundstrangpressens. ISBN 3-8322-5506-0

M. Schomäcker: Verbundstrangpressen von Aluminiumprofilen mit endlosen metallischen Verstärkungselementen. ISBN 978-3-8322-6039-2

N. Ridane: FEM-gestützte Prozessregelung des Freibiegens.
ISBN 978-3-8322-7253-1

R. Shankar: Surface Reconstruction and Tool Path Strategies for Incremental Sheet Metal Forming. ISBN 978-3-8322-7314-9

U. Dirksen: Testumgebung für Prozessregelungen zum Drei-Rollen-Profilbiegen mit virtuellem und realem Biegeprozess.
ISBN 978-3-8322-7673-7

D. Risch: Energietransfer und Analyse der Einflussparameter der formgebundenen elektromagnetischen Blechumformung.
ISBN 978-3-8322-8360-5

M. Marré: Grundlagen der Prozessgestaltung für das Fügen durch Weiten mit Innenhochdruck. ISBN 978-3-8322-8361-2

D. Becker: Strangpressen 3D-gekrümmter Leichtmetallprofile.
ISBN 978-3-8322-8488-6

V. Psyk: Prozesskette Krümmen - Elektromagnetisch Komprimieren - Innenhochdruckumformen für Rohre und profilförmige Bauteile.
ISBN 978-3-8322-9026-9

M. Trompeter: Hochdruckblechumformung großflächiger Blechformteile.
ISBN 978-3-8322-9080-1

H. Karbasian: Formgenauigkeit und mechanische Eigenschaften pressgehärteter Bauteile. ISBN 978-3-8322-9250-8

M. J. Gösling: Metamodell unterstützte Simulation und Kompensation von Rückfederungen in der Blechumformung. ISBN 978-3-8322-9355-0

H. Pham: Process Design for the Forming of Organically Coated Sheet Metal.
ISBN 978-3-8440-0309-3

B. Rauscher: Formschlüssig verbundene Metall-Kunststoff-Hybridbauteile durch Integration von Blechumformung und Spritzgießen.
ISBN 978-3-8440-0655-1

T. Cwiekala: Entwicklung einer Simulationsmethode zur zeiteffizienten Berechnung von Tiefziehprozessen.
ISBN 978-3-8440-0701-5

M. Hermes: Neue Verfahren zum rollenbasierten 3D-Biegen von Profilen.
ISBN 978-3-8440-0793-0

N. Ben Khalifa: Strangpressen schraubenförmiger Profile am Beispiel von Schraubenrotoren.
ISBN 978-3-8440-0969-9

J. Kolbe: Thermisch beschichtete, faserverstärkte Polymerwerkzeuge für die Umformung höherfester Blechwerkstoffe.
ISBN 978-3-8440-1353-5

L. Kwiatkowski: Engen dünnwandiger Rohre mittels dornlosen Drückens.
ISBN 978-3-8440-1381-8

T. Kloppenborg: Analyse- und Optimierungsmethoden für das Verbundstrangpressen.
ISBN 978-3-8440-1384-9

A. Schuster: Charakterisierung des Faserverlaufs in umgeformten Stählen und dessen Auswirkung auf mechanische Eigenschaften.
ISBN 978-3-8440-1581-2

A. Jäger: Strangpressen von Aluminiumprofilen mit prozessintegrierter umformtechnischer Weiterverarbeitung.
ISBN 978-3-8440-1654-3

M. M. Hussain: Polymer Injection Sheet Metal Forming – Experiments and Modeling.
ISBN 978-3-8440-2041-0

M. S. Aydın: Efficient Parameter Characterization for Hardening and Yield Locus Models for Sheet Metals.
ISBN 978-3-8440-2118-9

A. Canpolat: Experimentelle und numerische Bewertung der Fließortbestimmung mittels Kreuzzugversuch.
ISBN 978-3-8440-2126-4

V. Güley: Recycling of Aluminum Chips by Hot Extrusion.
ISBN 978-3-8440-2476-0

D. Pietzka: Erweiterung des Verbundstrangpressens zu höheren Verstärkungsanteilen und funktionalen Verbunden.
ISBN 978-3-8440-2538-5

M. Haase: Mechanical Properties Improvement in Chip Extrusion with Integrated Equal Channel Angular Pressing.
ISBN 978-3-8440-2571-2

Q. Yin: Verfestigungs- und Schädigungsverhalten von Blechwerkstoffen im ebenen Torsionsversuch.
ISBN 978-3-8440-2839-3

C. Becker: Inkrementelles Rohrumformen von hochfesten Werkstoffen.
ISBN 978-3-8440-2947-5

R. Hölker: Additiv hergestellte Werkzeuge mit lokaler Innenkühlung zur Produktivitätssteigerung beim Aluminium-Strangpressen.
ISBN 978-3-8440-3149-2

C. Weddeling: Electromagnetic Form-Fit Joining.
ISBN 978-3-8440-3405-9

A. Güner: In-situ stress analysis with X-ray diffraction for yield locus Determination.
ISBN 978-3-8440-3414-1

A. Güzel: Microstructure Evolution during Thermomechanical Multi-Step Processing of Extruded Aluminum Profiles.
ISBN 978-3-8440-3428-8

S. Hänisch: Verzugsanalyse kaltmassivumgeformter und wärmebehandelter Bauteile.
ISBN 978-3-8440-3761-6

A. Foydl: Strangpressen partiell verstärkter Aluminiumprofile.
ISBN 978-3-8440-3875-0

A. Weinrich Mora: Das Freibiegen mit inkrementeller Spannungsüberlagerung.
ISBN 978-3-8440-4221-4

S. Cai: Tailored and double-direction pressure distributions for vaporizing-foil Forming.
ISBN 978-3-8440-4255-9

G. Sebastiani: Erweiterung der Prozessgrenzen inkrementeller Blechumform-verfahren mittels flexibler Werkzeuge.
ISBN 978-3-8440-4359-4

C. Pleul: Das Labor als Lehr-Lern-Umgebung in der Umformtechnik. Entwicklungsstrategie und hochschuldidaktisches Modell.
ISBN 978-3-8440-4569-7

H. Hassan: Springback in deep drawing – Accurate prediction and reduction.
ISBN 978-3-8440-4924-4

L. Chen: An Investigation of Failure Mechanisms in Forming of Monolithic and Composite Sheets.
ISBN 978-3-8440-5168-1

L. Hiegemann: Glattwalzen beschichteter Oberflächen.
ISBN 978-3-84440-5419-4

G. Georgiadis: Hot stamping of thin-walled steel components.
ISBN 978-3-8440-5435-4

S. P. Afonichev: Numerische Simulation der Umformung von Sandwichblechen unter Berücksichtigung großer Krümmungen.
ISBN 978-3-8440-5471-2

D. May: Globally Competent Engineers. Internationalisierung der Ingenieurausbildung am Beispiel der Produktionstechnik.
ISBN 978-3-8440-5615-0

H. Chen: Granular medium-based tube press hardening.
ISBN 978-3-8440-5701-0

G. Grzancic: Verfahrensentwicklung und Grundlagenuntersuchungen zum Inkrementellen Profilumformen.
ISBN 978-3-8440-5889-5

S. Alkas Yonan: Inkrementelle Kaltumformung von Thermoplasten.
ISBN 978-3-8404-6026-3

P. Sieczkarek: Inkrementelle Blechmassivumformung.
ISBN 978-3-8440-6118-5

S. Ossenkemper: Verbundfließpressen in konventionellen Fließpresswerkzeugen.
ISBN 978-3-8440-6175-8

K. Isık: Modelling and characterization of damage and fracture in sheet-bulk metal forming.
ISBN 978-3-8440-6278-6

S. Gies: Thermische Spulenverluste bei der elektromagnetischen Blechumformung.
ISBN 978-3-8440-6468-1

C. H. Löbbe gen. Brüggemann: Temperaturunterstütztes Biegen und Wärmebehandeln in mehrstufigen Werkzeugen.
ISBN 978-3-8440-6485-8

J. Lueg-Althoff: Fügen von Rohren durch elektromagnetische Umformung – Magnetpulsschweißen.
ISBN 978-3-8440-6558-9

C. Dahnke: Verbundstrangpressen adaptiver Leichtbaukomponenten aus Aluminium und Formgedächtnislegierungen.
ISBN 978-3-8440-6630-2

O. K. Demir: New test and interpretation of electromagnetic forming limits of sheet metal.
ISBN 978-3-8440-6986-0

M. Schwane: Entwicklung und Eigenschaften von Längspressnähten beim Aluminiumstrangpressen.
ISBN 978-3-8440-6994-5

R. Meya: Schädigungskontrolliertes Blechbiegen mittels
Druckspannungsüberlagerung.
ISBN 978-3-8440-7510-6

O. Hering: Schädigung in der Kaltmassivumformung: Entwicklung,
Auswirkungen und Kontrolle.
ISBN 978-3-8440-7525-0

H. Traphöner: Erweiterung der Anwendungsgrenzen des ebenen
Torsionsversuchs.
ISBN 978-3-8440-7737-7

O. Napierala: Tiefzieh-Verbundfließpressen: Analyse, Bauteileigenschaften
und Potentiale.
ISBN 978-3-8440-7856-5

S. Wernicke: Inkrementelle Blechmassivumformung belastungsangepasster
Funktionsbauteile.
ISBN 978-3-8440-7980-7

D. Staupendahl: 3D Profile Bending with Five Controlled Degrees of Freedom.
ISBN 978-3-8440-8006-3

S. Heibel: Schädigung und Versagensverhalten hochfester Mehrphasenstähle.
ISBN 978-3-8440-8269-2